8-6-2007

Dust within the Central Regions of Seyfert Galaxies

Rajesh Deo

Dust Within the Central Regions of Seyfert Galaxies

by
Rajesh Deo
Under the Direction of D. Michael Crenshaw

ABSTRACT

We present a detailed study of mid-infrared spectroscopy and optical imaging of Seyfert galaxies with the goal of understanding the properties of astronomical dust around the central supermassive black hole and the accretion disk. Specifically, we have studied *Spitzer Space Telescope* mid-infrared spectra of 12 Seyfert 1.8-1.9s and 58 Seyfert 1s and 2s available in the *Spitzer* public archive, and the nuclear dust morphology in the central 500 pc of 91 narrow and broad-line Seyfert 1s using optical images from the *Hubble Space Telescope*. We have also developed visualization software to aid the understanding of the geometry of the central engine. Based on these studies, we conclude that the nuclear regions of Seyfert galaxies are fueled by dusty spirals driven by the large-scale stellar bars in the host galaxy. The accumulation of dusty gas in the central kiloparsec leads to enhanced star formation. In this case, the circumnuclear starburst and the central engine compete for dominance in the heating of the circumnuclear dust. Emission from the heated dust is most clearly seen in the mid-infrared. We find that the spectra of Seyfert 2s show the most variety in the continuum shapes due to different starburst contri-

butions. We find that the spectra of Seyfert 2s that are devoid of starburst contribution are dominated by a single thermal component at a temperature of $T \sim 170$ K. We also find that the mid-IR continua of Seyfert 1.8/1.9 galaxies are more like those of starburst-dominated Seyfert 2s than Seyfert 1s, contrary to expectations. We discuss the implications of these findings in the context of the Unified Model of AGN and the secular evolution of Seyfert nuclei.

Index Words: astronomy, galaxies, spectroscopy, infrared, mid-infrared, dust, active galaxies, Seyfert galaxies, torus, nuclear spirals, narrow-line region, Spitzer Space Telescope, Hubble Space Telescope.

Dust Within the Central Regions of Seyfert Galaxies

by

Rajesh Deo

A DISSERTATION

Presented in Partial Fulfillment of the Requirements for

the Degree of

Doctor of Philosophy

in the

College of Arts and Sciences

Georgia State University

2007

Dust Within the Central Regions of Seyfert Galaxies

by

Rajesh Deo

Major Professor:	Prof. D. Michael Crenshaw
Committee:	Prof. Douglas R. Gies
	Prof. Steven B. Kraemer
	Prof. H. Richard Miller
	Prof. William H. Nelson
	Prof. Paul J. Wiita

Electronic version approved:

Office of Graduate Studies
College of Arts & Sciences
Georgia State University
July, 2007

I would like to dedicate this dissertation to the memory of my father, and to my mother who has struggled against all odds in her life, so that I can comprehend this world.

Acknowledgments

This dissertation has benefited from a number of people at the Department of Physics and Astronomy at Georgia State University (GSU). First and foremost of all, I would like to thank my dissertation adviser, Prof. D. Michael Crenshaw for accepting me to work with him, bearing my shortcomings, teaching me important lessons and believing in me in the time of my need. I sincerely admire his ability to be critical without being overbearing, to believe in simple common-sense explanation first before invoking more complicated approaches and to strip a problem down to its bare essentials. I hope I can reproduce such simplicity in my future work. I would like to greatly thank Prof. S. B. Kraemer; he generously provided us with his *Spitzer* data on Seyfert 1.8/1.9s and without his good criticism of my research, there would not have been the important results that I present in this dissertation.

I sincerely thank all the astronomy faculty at GSU who have instructed me. I would particularly like to thank Prof. Douglas Gies, who helped by contacting Prof. Ron Buta at the University of Alabama in regard to my questions about Hubble classification of galaxies. I would like to thank Prof. Buta for providing us access to the "De Vaucouleur's Atlas of Galaxies" in its electronic form, as the Georgia State Library does not have a copy of the Third Revised Catalog of Galaxies. Prof. Hal McAlister kindly sent me for the Michelson Summer School during the summer of 2003 where I was introduced to the new field of optical interferometry, and I am very thankful to him for that. Prof. Paul Wiita has been a source of encouragement

to a generation of graduate students of Indian origin, and his expertise in astrophysics was the main reason I chose to come to GSU over other schools; he has been helpful in many ways since then. I would like to thank Prof. Bill Bagnuolo, for the occasional discussions about image processing algorithms and Fourier transforms. I would also like to thank our department chair, Prof. H. Richard Miller, for decreasing my lab teaching duties while I took care of the departmental cluster of Linux machines. I am greatly indebted to him, as he personally helped me in finding accommodation when I first came to Atlanta from India. I am also very grateful to Prof. Todd Henry for his excellent planetary system class.

I would like to thank the previous senior graduate students and system managers, John McFarland and Dave Berger. I would like to thank John McFarland in particular for the large number of scripts and utility tools he wrote to manage the network of Linux machines. These tools were of great help when the task of maintaining systems was given to me. I would also like to thank our department systems administrator, Duke Windsor, for letting me maintain the Astronomy cluster of Linux machines and pursuing our requests for new hardware as quickly as possible when needed. Foremost of all, I would like to thank the entire Astronomy community at GSU for bearing with my approach to systems administration.

A number of fellow graduate students have helped me in my tasks at GSU. In particular, collaborations with Alvin Das, Jay Dunn and Nick Collins at CUA have resulted in authorship on four papers and I am grateful to them. I would like to thank former graduate student Ginny McSwain for her guidance during graduate courses and matters of a career in Astronomy. I would like to thank Weichun Jao and Alvin Das for giving me a copy of their dissertation templates. I would like to thank Deepak Raghavan for the occasional discussions on the finer points of programming in IDL. Finally, I would like to thank all the rest of the graduate students, past and present, for making my experience an enjoyable one at GSU.

Contents

List of Tables

List of Figures

Abbreviations

AGN ..... Active Galactic Nuclei

BBB ..... Big Blue Bump

BCD ..... Blue Compact Dwarf

BLR ..... Broad-Line Region

BLRG ..... Broad-Line Radio Galaxy

BPT ..... Baldwin, Phillip, and Terlevich Diagram

BQS ..... Bright Quasar Survey

DISM ..... Diffuse Inter-Stellar Medium

DS ..... Dust Spiral

ENLR ..... Extended Narrow-Line Region

EP ..... Excitation Potential

EW ..... Equivalent Width

FHWM ..... Full Width at Half Maximum

FR ..... Fanaroff-Riley Class

GD ..... Grand-Design

GO ..... General Observer

GTO ..... Guaranteed Time Observer

HST ..... Hubble Space Telescope

IDL ..... Interactive Data Language

ILR ..... Intermediate Line Region

IP ..... Ionization Potential

IRAC ..... InfraRed Array Camera

IRS ..... InfraRed Spectrograph

ISM ..... Inter-Stellar Medium

ISO ..... Infrared Space Observatory

LOS ..... Line of Sight

MBH ..... Massive Black Hole

MIPS ..... Multi-band Infrared Photometer for Spitzer

NED ..... NASA Extragalactic Database

NLR ..... Narrow-Line Region

NLRG ..... Narrow-Line Radio Galaxy

NLS1 ..... Narrow-line Seyfert 1

PA ..... Position Angle

PAH ..... Poly-cyclic Aromatic Hydrocarbons

PCA ..... Principle Component Analysis

PDR ..... Photo-dissociation Region

PSF ..... Point Spread Function

QSO ..... Quasi-Stellar Object

Quasar ..... Quasi-Stellar Radio Source

SED ..... Spectral Energy Distribution

SMART ..... Spectral Modeling, Analysis and Reduction Tool

SMBH ..... Super-Massive Black Hole

UIB ..... Unidentified Infrared Bands

VSG ..... Very Small Grain

WFPC2 ..... Wide Field Planetary Camera 2

Chapter 1

Introduction to Active Galaxies

This dissertation deals with active galaxies and the properties of dust in their nuclear environments. Generally, most astronomers may think "why study dust?" It extincts[1] and reddens the light coming from the astronomical object of interest, thus making the task of interpreting the data more difficult. But dust in astronomical scenarios is indeed very useful and can be a great probe of the nebulosity. Dust in astronomical settings is in the form of minute micron-size or smaller particles as well as inorganic and organic molecules. These particles effectively absorb short-wavelength (optical/ultraviolet) radiation and emit that energy in the infrared band. This process makes astronomical dust particles great probes of physical conditions within the nebula. It has been known for a long time that dusty molecular clouds are the birthplaces of the future generations of stars. These stellar nurseries are the places where the physics of the astronomical dust has been studied the most. Mostly dust particles are thought to originate in the atmospheres of evolved red giant or supergiant stars.

In this dissertation, we shall focus on the location, geometry and physical nature of the dust in the central 500 pc of active galaxies. In particular,

[1]Extincts is a verb and specifically in the case of astronomical dust, the dust absorbs as well as scatters the radiation, leading to "dimming" of starlight.

we will look at (1) the geometry of the dust distribution with respect to the narrow-line region (NLR) and host galaxy, (2) the phenomenon of dusty nuclear spirals and nuclear stellar bars, and (3) the study of the elusive dusty torus using infrared spectroscopy. These three research themes are distinct, and I shall elaborate on their connections as we go along through this dissertation. The dissertation is divided into three parts, each one dealing with one of the three themes mentioned above.

We begin with this chapter, where I shall introduce the basic properties of active galaxies as they are known. We shall see the anatomy of an active nucleus, review the various classes of AGN and look at some historical perspectives on active galaxies. I will pay particular attention to Seyfert galaxies and describe the important results for this class of AGN from the literature. I will end this chapter with a brief description of the three main themes mentioned above. I will describe the goals of each effort and then provide a brief summary of results from these efforts.

1.1 Active Galaxies

The words "active galactic nuclei" (AGN) are used to describe the nuclear regions of active galaxies. The key word here is "active", meaning that there are tremendous amounts of astrophysical activity going on in the nuclear regions of some galaxies. The activity includes an extremely bright ($\sim 10^{42}$–10^{47} erg s^{-1}) point-like source of radiation, large-scale (up to 700 pc) mass outflows from the nucleus and variable continuum emission in all wavebands from X-rays to radio. Associated with this nuclear activity, one often finds enhanced star formation rates within the central kiloparsec of active galaxies. Active galaxies were originally noted as galaxies having a stellar appearing nucleus in their optical images. Originally active galaxies were studied in the optical and radio wavebands; thus many classifications are based on their morphological and spectral appearance in these regimes. First, we shall look

at the components of an active nucleus as based on the current body of research, and then we will look at their properties in different wavebands that lead to various classes.

1.1.1 Anatomy of an Active Nucleus

The basic model of an active nucleus is quite simple. The key component or the "engine" of the system is a supermassive black hole (SMBH) with a swirling flattened disk of matter around it. This "accretion" disk radiates strongly in all wavebands except radio. This accretion disk–black hole system is responsible for converting the incoming matter to energy. As the matter falls closer and closer to the black hole, friction and dissipative forces heat up the inflow and the resulting radiation escapes from the surfaces of the disk. The SMBH is humongous in size and mass, compared to its stellar cousins (Cygnus X-1 binary system hosts a black hole of 8.5 $M_{\odot}$). It is typically as massive as 10^{6}–$10^{9.5}$ $M_{\odot}$. The gas and dust from the nearby regions (a few parsec) in the galaxy fuel the SMBH. The infalling matter has a significant amount of rotational angular momentum. Hence, instead of falling radially inward toward the black hole, it settles in a disk of gas and dust, which we call the accretion disk. As the matter spirals in this disk of gas, inner layers of the disk rub against the outer layers. The resulting friction, shear and collisions between the cloudlets of gas and dust heat up the infalling gas. The gas radiates this energy away into near-infrared, optical, UV, and soft X-ray bands. As the gas heats up, it also loses the angular momentum and spirals inward to the black hole. Different parts of the accretion disk radiate in different wavebands. The innermost parts produce the soft X-ray and extreme UV radiation. The middle regions produce the UV and the optical radiation, while the very outer parts will likely produce near-infrared radiation. Overall, simple accretion disk models are expected to be thermal structures. Above the accretion disk, in the inner regions, a hot coronal gas is expected to be present, which emits in the hard X-ray band. Accretion disk

models are subject to a number of physical parameters, such as the viscosity of the matter, but the simplest scaling is provided by relating the actual matter accretion rate ($\dot{M} = dM/dt$) to the Eddington rate for spherical accretion ($\dot{M}_E$).

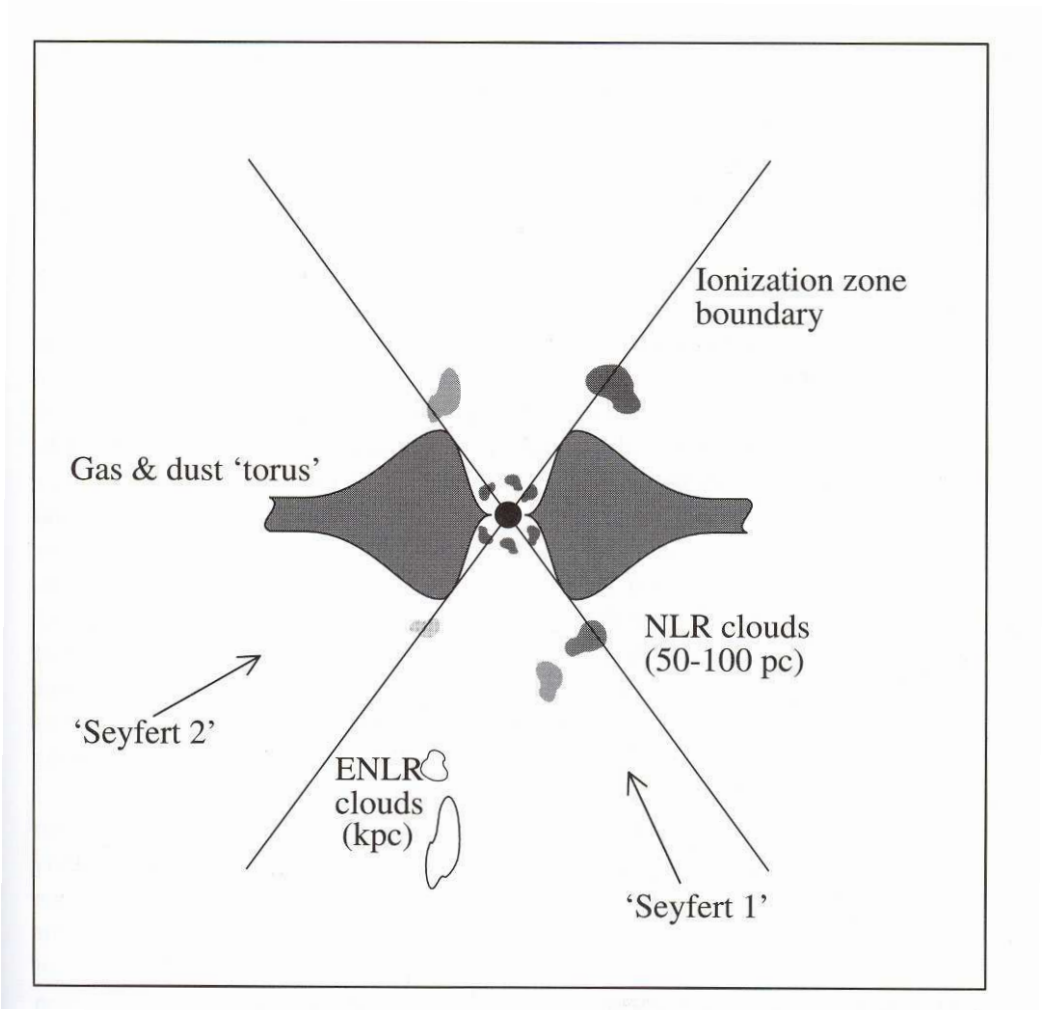

Figure 1.1: A schematic diagram (Peterson 1997) showing the various structural components in a low mass active nucleus.

The geometry of an active nucleus is axisymmetric for the most part. Thus, above and below the accretion disk–black hole component, the broad-

line emitting clouds of gas are expected to be present. The presence of the broad-line region (BLR) is inferred from the spectra of type 1 AGN which tend to show broad and permitted emission lines. These two components, the accretion disk, and the BLR, are well within a parsec of the central black hole. It is expected that a region of space filled with dusty molecular clouds surrounds this "central engine". This region is envisioned as having a torus-shaped geometry. The central theme of this dissertation is the investigation into the nature of the dusty medium within this region of space around the central engine and further out to a distance of about1 kpc. Along the symmetry axis of this system are regions partially filled with clouds of gas and dust. These regions are ionized by the hard radiation from the central engine. These regions appear to be in the shape of a bicone, with the apex of the bicone centered on the location of the central engine. This is the narrow-line region (NLR). The narrow permitted and forbidden lines in the optical/UV spectra of AGN arise from this region of space. A detailed study of high resolution spectra of these NLRs have revealed that the clouds forming this structure are in outflow from the nucleus (Crenshaw et al. 2003b). The NLR sizes typically range from $\sim$ 500 pc to 1000 pc. The NLR, the BLR, the dusty torus and the central engine composed of the accretion disk, corona, and the SMBH form the active nucleus within an active galaxy. Apart from these main components, other structures or variations of the outflow are also found. For example, radio-loud objects tend to show strong relativistic jets of plasma being driven along the symmetry axis of the system. These powerful jets often travel exceedingly large distances of several hundreds of kilo-parsecs compared to the scale of a few parsecs involved in the rest of the components of the nucleus. Also, gas in the host galaxy on scales of several kilo-parsecs that is ionized by the active nucleus has come to be known as the extended narrow-line region (ENLR). A schematic model of the AGN and its scales is shown in Figure 1.1.

1.1.2 Taxonomy of AGN

Since the pioneering work by Carl Seyfert (Seyfert 1943), a number of AGN types have been classified. Sometimes classifications differ because of the type of detection method employed to put a given galaxy into a specific class. Thus it is possible for a galaxy to be classified in more than one way and have different labels for its type. There are two main approaches used: optical spectral classification and photometric/morphological classification using radio emission from AGN. AGN are also put into different boxes based on the characteristics of their variable emission in the optical or the radio regime. A large part of the discussion here is taken from Peterson (1997), Kembhavi & Narlikar (1999) and Binney & Merrifield (1998). We will discuss the following classes:

- Seyfert galaxies
- Liners
- Quasars and QSOs
- Broad-line and Narrow-line Radio Galaxies
- BL Lac Objects and Optically Violent Variables

Seyfert Galaxies

Seyfert galaxies are the most common type of intermediate luminosity ($M_B > -21.5 + 5\log h_0$)[2] active galaxies in the nearby Universe. The classification of Seyfert galaxies is based on their optical spectra. Khachikian & Weedman (1974) divided the Seyfert nuclei into two main classes: Seyfert 1s and Seyfert 2s. Type 1 Seyferts show broad permitted emission lines arising in the BLR close to the SMBH. Type 1 Seyferts also show permitted and forbidden narrow emission lines, which arise in the NLR much farther away from the

[2] $h_0 = H_0/c$ where H_0 is the Hubble's constant and c the speed of light

SMBH. Type 2 Seyferts only show the permitted and forbidden narrow lines; the broad component is absent in unpolarized light. In all sub-classes of Seyfert galaxies, the narrow-lines typically show widths of $\sim$ 500 km s^{-1}, much higher than emission-line width in non-AGN galaxies, while the broad-lines show widths of $\gtrsim$ 1000 km s^{-1}.

Osterbrock (1981) further divided type 1 Seyferts into 1.5, 1.8 and 1.9s, based on the strength of the broad-line components in their optical spectra. In Seyfert 1.5 spectra, the broad and narrow components of the Balmer-lines can be easily distinguished, with the narrow core on top of the broad wings from the BLR. Seyfert 1.8s show weak broad wings on the permitted Hα and Hβ lines. Seyfert 1.9s on the other hand show broad wings only on the Hα lines. The absence of broad emission lines in type 2 Seyferts indicates that the broad line emission is extincted or diminished, possibly by an intervening dust screen. Seyfert nuclei of both types tend to show strong and variable hard X-ray emission and also emit strongly in the infrared.

Morphologically, Seyfert galaxies are almost always early Hubble type (Sa, SBa, SBb) gas-rich spiral disk galaxies (Adams 1977). Seyfert 2 galaxies tend to show more disturbed morphology than Seyfert 1s (Adams 1977; Hunt & Malkan 2004). Large-scale stellar bars induced by merger/interactions with smaller dwarf satellites have been suggested (Simkin et al. 1980) to provide efficient fueling of Seyfert nuclei. Morphological surveys (De Robertis et al. 1998) do not find an excess of large-scale interactions among large Seyfert galaxies. About 1% of all spiral galaxies are Seyferts, thus making them the second most common of all active galaxies in the local Universe after LINERS.

In addition to the strong emission lines, the Seyfert spectra often have weak stellar absorption features due to late-type giant stars in the host galaxy. In Seyfert 1s, the absorption lines are relatively weak, as the lines are diluted by the strong non-thermal continuum. On the other hand, the AGN continuum is very weak in the typical Seyfert 2 galaxy and a detailed

deconvolution is needed to remove the host galaxy spectrum. Confusion due to stellar continua in spectra of Seyfert 1.8/1.9s may make them appear as Seyfert 2s; hence great caution must be taken when classifying Seyfert 2 spectra.

Another source of confusion can arise from comparison with LINER galaxies (see the next subsection). The spectra of Seyfert 2s and Liners appear similar, but there are important differences, which if overlooked can result in misclassification. Most LINER spectra are dominated by low-ionization species such as [N II] $\lambda\lambda 6716, 6731$, [S II] $\lambda\lambda 6548, 6583$, [O II] $\lambda 3727$ and [O I] $\lambda 6300$. Further, the [O III] $\lambda 5007/\mathrm{H}\beta$ ratio is much greater in Seyfert 2s than in LINER galaxies.

Another important observation is that some galaxies show strongly variable broad-lines in their spectra. The Seyfert type of these objects changes over a span of a few years (Tohline & Osterbrock 1976). For example, when a Seyfert 1 nucleus is in a very faint state, the broad bases on the Balmer-lines will almost disappear. If there is an additional strong stellar component in the spectrum, the spectrum will appear similar to a Seyfert 2 spectrum. However, close examination of spectra almost always shows that the broad wings never completely go away (Peterson 1997). This indicates the presence of common physical properties associated with the standard model in all Seyfert 1s and Seyfert 2s. These broad-line and continuum variability properties of Seyfert galaxies have been used to great effect to study the properties of the BLR (Peterson 1993; Peterson et al. 2004).

Liners

Most nearby AGN are Liners, which stands for low-ionization narrow emission line regions. The term was introduced by Heckman (1980a), who studied this phenomenon first. The LINER spectra resemble Seyfert 2 spectra, except that high ionization lines like [O III] $\lambda 5007$ are relatively weak. Ho et al. (1994) showed that low-luminosity AGN (mostly Liners) are present in nearly

half of all spiral galaxies. It was suggested that LINER-like activity in the nuclei of galaxies could be due to extensive star formation and ionization of gas due to O-B associations. Baldwin et al. (1981) showed that it is possible to separate HII region galaxies, planetary nebulae, and nuclei photo-ionized by a featureless continuum, based on intensity ratios of *two* pairs of lines. The ratio of line intensities for a pair of nearby lines is sensitive to the shape of the ionizing continuum and thus can be used a diagnostic of whether the photo-ionization is due to a collection of blackbodies or a power-law ionizing spectrum. Veilleux & Osterbrock (1987) applied this method while choosing pairs of lines close to each other in wavelength, thus reducing the effects of reddening. This "Baldwin, Phillips, and Terlevich (BPT)" diagram is shown in Figure 1.2.

In the optical, it is possible to distinguish Liners from Seyfert 2s by their low values of [O III] λ5007/Hβ relative to [N II] λ6583/Hα, while they have larger values of [N II] λ6583/Hα than most HII region galaxies. Furthermore, the presence of strong [O I] λ6300 is considered an indication that the photo-ionization in LINER nuclei occurs due to a flat power-law spectrum.

In a large survey, Ho (1996) showed that Liners are extremely common in the present epoch, comprising approximately 1/3 of all galaxies with $B_T \leq$ 12.5 mag. He suggests that if most Liners are non-stellar in origin then they are the dominant constituents of the AGN population. He also showed that a substantial fraction of Liners contain BLRs, yielding direct evidence, at least in these objects, of a physical link between Liners and classical Seyfert 1 nuclei and QSOs.

Quasars/QSOs

The terms quasar and QSO are now used interchangeably to refer to objects whose spectra are similar to those of Seyferts, but exhibit much higher bolometric luminosities. Quasars/QSOs form the most luminous subclass of AGNs, with nuclear magnitudes of $M_B < -21.5 + 5\log(h_0)$. The powerful

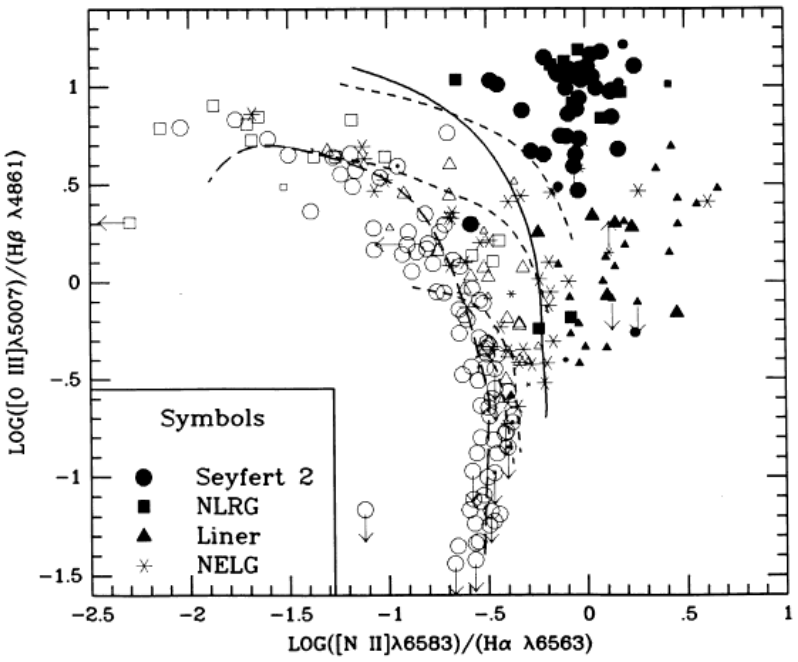

Figure 1.2: The BPT diagram from Veilleux & Osterbrock (1987), the symbols are filled circles: Seyferts, filled squares: NLRGs, filled triangles: Liners, asterisks: NELGs, open circles: HII regions, open circle with dot: nuclear HII region, open triangle: starburst galaxy, open square: HII galaxy. The dashed lines shows HII region photo-ionization models, and the solid line separates AGNs from HII regions.

double-lobed radio sources that originally defined the quasar class form only about 5-10% of the total population of quasars. A large majority of quasars are 'radio-quiet'. Quasars distinguish themselves from Seyfert galaxies on Palomar Sky Survey plates by being stellar-appearing with no clear evidence of a surrounding galaxy. Quasar spectra are remarkably similar to Seyfert galaxies, except that (a) stellar absorption features are very weak and difficult to detect, and (b) the narrow lines are generally weaker relative to the broad lines compared to Seyfert galaxies. A typical QSO spectrum is shown below.

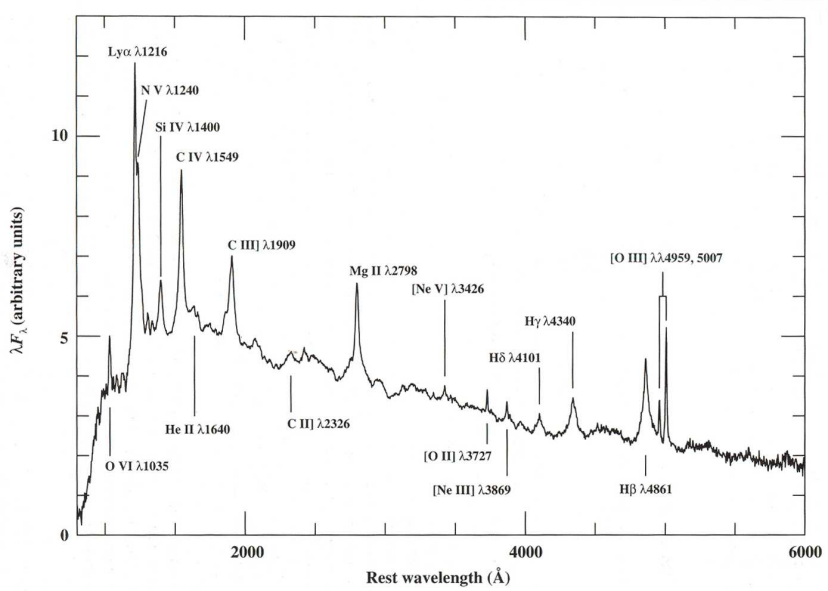

Figure 1.3: Average quasar spectrum from Peterson (1997, Fig 2.2)

Advances in radio interferometry in early 1970s led to sub-arcsec resolution, enabling detailed maps of radio emission to be made. This allowed classification of the radio morphology of quasars and radio galaxies. The morphology is often described broadly in terms of two components, 'extended' (*i.e.,* spatially resolved) and 'compact' (*i.e.,* unresolved at $\sim 1''$). Sometimes, the terms 'lobe-dominated' and 'core-dominated' are used. The defining characteristic of a quasar/QSO is its broad spectral energy distribution (SED). In the radio, the SED is crudely described in terms of a power-law, often written as $F_\nu \propto \nu^{-\alpha}$. Lobe-dominated sources tend to show steep radio spectra, while core-dominated ones show flat spectra with $\alpha \leq 0.5$. Fanaroff & Riley (1974) divided the extended radio structures into two separate luminosity classes: Class I (FR I) sources are weaker radio sources that are brightest in the center with decreasing surface brightness towards the edges. These FR I sources are still jet-dominated and the jet is brightest in the inner half.

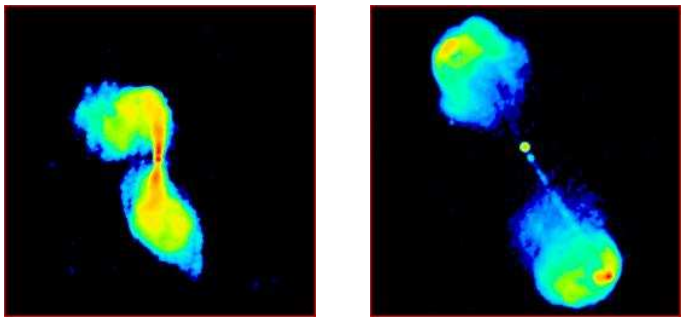

Figure 1.4: Fanaroff-Riley Classes: FR I – 3C 272, FR II – 3C 47; Source: `http://www.jb.man.ac.uk/atlas/dragns.html`

The more luminous class II (FR II) sources are limb-brightened (*i.e.,* lobe-dominated) at the edges of the radio structures. All radio-loud quasars are FR II sources. Examples of these two classes are shown in Figure 1.4. A radio luminosity division between these classes is given by Bridle & Perley (1984) at $L_\nu(1.4\text{GHz}) = 10^{32}$ erg s^{-1} Hz^{-1}.

Broad-Line and Narrow-Line Radio Galaxies

Apart from the presence of strong radio emission in quasars, there are two types of strong radio galaxies which show spectra similar to those of Seyfert galaxies. These are called broad-line radio galaxies (BLRGs) and narrow-line radio galaxies (NLRGs). They are the 'radio-loud' counterparts of Seyfert 1s and Seyfert 2s, respectively. One important difference from 'radio-quiet' Seyferts is that they tend to occur in elliptical galaxies rather than spirals.

Blazars: BL Lac Objects and OVVs

All AGN show continuum variability from X-ray to radio wavelengths, but some show extreme continuum variability. BL Lacertae is the prototype of such extreme variability behavior. BL Lac was first discovered as an extremely variable "star" in optical photometric monitoring. The typical changes are $\Delta m \gtrsim 0.1$ mag on time scales as short as a day. Such objects

are termed "Blazars", which are divided into BL Lac objects and Optically Violent Variables (OVVs). All known blazars are radio sources and tend to have high polarizations that vary both in magnitude and position. Urry et al. (1991) showed that BL Lacs are relativistically beamed FR I sources and the OVVs are beamed FR II sources.

1.1.3 AGNs studied in this dissertation

Having seen the varied classes of AGN in the last section, we will focus on the properties of two special categories of Seyfert galaxies: the Seyfert 1.8/1.9s and the narrow-line Seyfert 1s (NLS1s).

Seyfert 1.8/1.9s

In § 1.1.2, we saw that Osterbrock (1981) broke the Seyfert 1 class into sub-classes 1.2, 1.5, 1.8 and 1.9. This sub-classification of Seyfert 1s is based on the strength of the narrow-components of the Balmer permitted lines as compared to the strength of the broad-components. As we progress from type 1 to 1.5 the narrow-component becomes more and more clearly separated from the broad wings. Seyfert 1.8s show weak broad wings on the permitted Hα and Hβ lines, while Seyfert 1.9s show broad wings only on the Hα lines.

Osterbrock in his original 1981 paper proposed that the BLRs in these systems suffer strong extinction due to dust, which leads to steep Balmer decrements [3] in these systems. Goodrich & Osterbrock (1983) studied Mrk 704 and Mrk 1066, and suggested that the BLR might be seen edge-on in these objects. Osterbrock & Dahari (1983) expanded the sample of Seyfert 1.8/1.9s with further identifications. Lawrence & Elvis (1982) studied the soft and hard X-ray emission from different classes of Seyferts to understand if there is a continuum of Seyfert types and suggested that obscuration of

[3]The ratio of flux of Hα to the flux of Hβ is termed the Balmer decrement, as usually the bluer $H\beta$ flux is weaker if there is reddening due to dust.

the BLR plays a big role. They found that X-ray selected Seyfert galaxies were more edge-on than optically selected Seyfert galaxies from Keel (1980). They also suggested that more attention should be paid to spectroscopic classifications of Seyfert galaxies with weak broad Hα. To test the obscuration hypothesis of Lawrence & Elvis (1982), Rudy & Willner (1983) measured the Paschen-α line for a Seyfert 1.9 galaxy V Zwicky 317 in the near-IR and determined that the line was too weak to suffer the modest extinctions ($E(B-V) \approx 1$) derived from the Hα/Hβ ratio. They suggested radiative transfer effects in the BLR as an alternative and that the BLR in Seyfert 1.8/1.9s may have lower densities, temperatures and optical depths than those of Seyfert 1s, hence hypothesizing that the BLRs in these systems can be strong Lyα emitters. Further efforts by Rudy, Cohen and collaborators (Rudy et al. 1985, 1988), revealed a few intermediate Seyfert galaxies that could be explained by these radiation transfer effects. However, they also noticed intermediate Seyferts which could be explained by reddening alone, thus leaving this issue unresolved. Early infrared photometry (*e.g.,* Rudy & Rodriguez-Espinosa 1985) of Seyfert 1.8/1.9s revealed the presence of a strong contribution from starlight and weaker overall infrared contribution due to the non-stellar core as compared to Seyfert 1s.

Further, in a literature compilation of Balmer decrements, [O III] strengths, infrared fluxes and polarizations, Rudy (1984) suggested that dust in the NLR plays a major role in the infrared emission at 10 μm. This was based on a correlation between $L(10\ \mu\mathrm{m})$/L(Hα) *vs.* [OIII]/Hβ. He also notes that the sample used is biased against edge-on galaxies as in Keel (1980), thus the observed variations in parameters he compiled must be due to dust close to the active nucleus. A further study of host galaxy axial ratio (b/a) and Balmer decrement from narrow and broad components by de Zotti & Gaskell (1985) highlighted the importance of extinction due to the host disk.

Initial studies (Tohline & Osterbrock 1976) hinted at the variability of Seyfert type in Seyfert 1.8/1.9s. Goodrich (1989a) studied spectropolarime-

try of Seyfert 1.8/1.9s and the broad-line variability in NGC 2622, NGC 7603, and Mrk 1018. Goodrich concluded that the variations in the broad lines were due to changes in the line of sight optical depth of the obscuring dust. Goodrich (1990) further tried to distinguish between competing theories mentioned above to explain the weak broad lines in Seyfert 1.8/1.9s by using Pa$-\alpha$ measurements. However he concluded that while some are consistent with dust reddening, others are consistent with the optical-depth/ionization-parameter explanation (Rudy & Willner 1983). Quillen et al. (2000) reported 1.6 μm variability timescales of a few hours to a few weeks in Seyfert 1.5-2 systems and suggested that the variability of near-infrared continuum at 1.6 μm in Seyfert 1.8/1.9s implied dust sublimation radii of $\sim$ 1 pc (Barvainis 1987).

Goodrich (1995) presented a spectral survey of Seyfert 1.8/1.9 galaxies and compared the spectra with previous studies of emission-line variability. He concluded that NGC 7603, Mrk 993, and Mrk 1018 show variability consistent with changes in the reddening to the BLR. However, Goodrich notes that NGC 2622 (Mrk 1218), which showed variability consistent with reddening changes in earlier studies, has declined in brightness, but has done so in a manner inconsistent with a simple change in reddening. He also notes that the variability in Mrk 883 and UGC 7064 is inconsistent with reddening changes, and may to due to real changes in the ionizing flux in the BLR.

Thus, the important problem that has remained unsolved so far is that the Balmer decrement in some Seyfert 1.8/1.9s can be characterized by obscuration due to dust, but in other Seyfert 1.8/1.9s that show presence of broad Lyα in their UV spectra, one has to invoke radiation transfer effects, as suggested by Rudy, Cohen and collaborators. In the mid-infrared, the effects of dust on NLR line ratios will be minor, and it may be possible to resolve this issue. Further, it is not clear if the obscuring dust is in the form a parsec scale torus, a 100 pc scale clumpy torus, or an outflowing dusty wind at the base of the NLR, where the galactic matter runs into the photo-ionized wind

from the accretion disk.

Narrow-Line Seyfert 1s

Another sub-class of Seyfert 1s that we study in this dissertation is narrow-line Seyfert 1s (NLS1s). This sub-classification is based on the following optical spectral properties:

- The narrow permitted lines are only slightly broader than the forbidden lines from the NLR;
- The [OIII]/Hβ ratio is generally smaller than 3;
- Fe II emission complexes, expected to come from a high-density region, are observed, in contrast with Seyfert 2s;
- However, full width at half maximum (FWHM) of Hβ is less than 2000 km s^{-1}, in contrast to broad-line Seyfert 1s;

The first three of these criteria were defined in Osterbrock & Pogge (1985), while the last criterion is due to Goodrich (1989b). The presence of an unobscured high-density region, in particular, places these AGN firmly in the Seyfert 1 category.

The NLS1s were first recognized by Osterbrock & Dahari (1983) as peculiar objects due to their very narrow Balmer lines like some Seyfert 2s and their strong Fe II emission blends like broad-line Seyfert 1s (BLS1). An example of the optical spectrum of an NLS1 (Mrk 42) is shown in Figure 1.5. As can be noted in the figure, the Hβ line is narrow, but stronger than [O III]. The Fe II blends are notable in the NLS1 spectra. The weakness of the Fe II blends and the weak broad bases are a source of confusion in low S/N optical spectral classification of Seyfert 1s.

Based on better spectra, Halpern & Oke (1987) suggested that NLS1s such as I Zw 1 could be strong X-ray sources. Grupe et al. (1994) showed

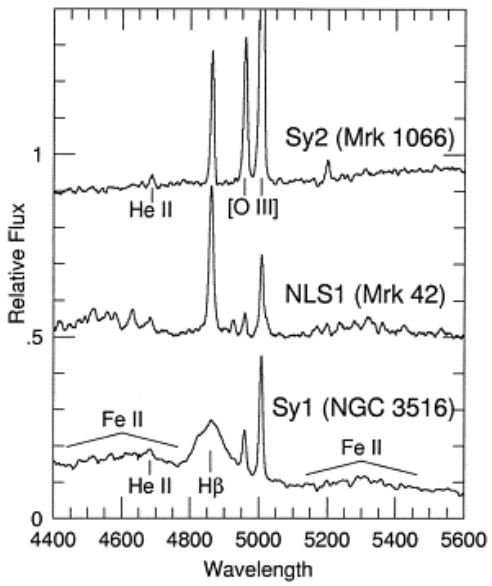

Figure 1.5: Example Seyfert Spectra from Pogge (2000): NLS1 (Mrk 42), Seyfert 1 (NGC 3516), Seyfert 2 (Mrk 1066)

that $\sim 50\%$ of the soft-X-ray selected AGN from the ROSAT All Sky Survey are NLS1s. A further study by Boller et al. (1996) confirmed that NLS1s are strong soft X-ray emitters and are highly variable in the soft X-ray regime. The X-ray photon index[4] (Γ) for NLS1s is ~ 2.19 whereas most Seyfert 1s show a value of ~ 1.73. Boller et al. (1996) suggested that NLS1 nuclei could be analogous to strong-soft states of galactic black holes (Pounds et al. 1995). They also suggested that NLS1s nuclei may be viewed mostly pole-on, or they could have smaller black hole masses and/or more distant BLRs that could lead to the narrow-permitted lines observed. Mason et al. (1996) studied NLS1 RE-J1034+396 and noted that the narrow (FWHM ~ 1000 km s^{-1}) Hβ has a weak broad component (FWHM ~ 2500 km s^{-1}) and suggested that the observed narrow permitted lines may arise from an intermediate

[4]In X-ray astronomy, fluxes are generally represented as number of photons per unit energy per unit time, the "photon" index is thus the index of the power law that describes that emergent photon counts as a function of frequency.

region between the BLR and the NLR. The signature of the BLR in NLS1 systems could remain hidden due to low S/N spectra and/or host galaxy contamination.

The strong interest in researching NLS1s is driven in part by the need to find the physical driver for the existence of the Boroson-Green eigenvector 1 (Boroson & Green 1992) for AGN, which was derived using principal component analysis (PCA). The eigenvector is a result of the anti-correlation between line strengths of Fe II and [O III], and the correlation between the FWHM of Hβ and the peak of [O III]. The PCA analysis confirms that strong Fe II, weak [O III] and narrow Hβ lines are the defining characteristics of the NLS1 class. Mathur (2000) proposed that the high accretion rates estimated for NLS1s (Pounds et al. 1995) could be due to smaller black hole masses in NLS1s. An alternative to this picture is proposed by Murayama et al. (2001), where the BLR is flattened in NLS1s and is viewed preferentially pole-on, leading to enhanced soft X-ray variability due to beaming and narrow Hβ components.

Thus, we see that NLS1s offer many puzzles about the nature of AGN. If these are indeed young AGN with high accretion rates, perhaps the host galaxy environment of NLS1s may be conductive to formation and growth of SMBHs. This is the topic researched in Chapter 3 of this dissertation.

1.1.4 The Unified Model of AGN

The fundamental concept behind the 'unified model' of AGN is the commonly held belief in science that any description of a physical phenomenon should be as simple as possible. The existence of common properties among a population of different AGN sub-classes drives the need to have a common 'unified' model for AGN. As we saw in § 1.1.1, the basic components that make up the active nucleus appear to be similar in their physical properties. Just like stellar models are composed of a few key parameters such as the mass, age and the metallicity of the star, current research posits that there

will be a few basic parameters that govern the nature and appearance of all AGN. Two such parameters recognized are the bolometric luminosity of the AGN and the orientation of the line-of-sight (LOS) of the observer to the symmetry axis of the AGN. It is recognized that AGN appear to have axial rather than spherical symmetry and the inclination angle at which we look at the system govern the observed properties of the system to a certain degree. There is also strong evidence that basic physical properties of an active nucleus, such as the mass of the central SMBH and the matter accretion rate, governs the emergent continuum spectrum and related properties. Thus it is likely that a pragmatic 'unified model' will incorporate real physical diversity through changes in a few basic parameters coupled with observer-dependent parameters such as orientation, resolution and perhaps other limitations of the observing process. On the size scale of the NLR (tens to hundreds of parsecs), there is clear evidence for an axial symmetry, in the form of biconical NLR outflow. However there is considerable uncertainty about the geometry of the dusty obscuration in the equatorial plane at the apex of the NLR outflows. In this dissertation, we are mainly concerned with estimation of constraints on this dusty geometry.

Simple Unification

The original idea of using orientation as a unification parameter goes back to Osterbrock (1978), who suggested that dense gas and dust along an equatorial plane may be obscuring the BLR; thus Seyfert 2 galaxies only show narrow emission lines arising from the NLR. In the case of extreme AGN, such as blazars, it was suggested (Blandford & Rees 1978) that we may be observing these systems nearly along the radio jet axis, leading to the observed flux being dominated by the beamed component. These observations show that the key elements in a simple unified scheme are the obscuring torus and the observed radio flux. In this simple scheme, the Seyfert 1s and BLRGs are distinguished from their counterparts, Seyfert 2s and NLRGs, by

Table 1.1: A Simple Unification Scheme

Radio	Orientation	
Properties	Face-On	Edge-On
Radio Quiet	Seyfert 1s	Seyfert 2s
	QSO 1s	QSO 2s/ULIRGs ?
Radio Loud	BL Lac	FR I
	BLRG	NLRG
	OVV	FR II

the orientation of the obscuring torus (or for that matter the orientation of the radio jet) to the LOS. This simple scheme shown in Peterson (1997) is presented in Table 1.1 (see also Figure 1.1).

Optical spectroscopy shows that observationally there are two main types of Seyfert galaxies. Due to the relatively similar nature of narrow line profiles in both type of Seyferts, and the variability of broad-lines in some Seyfert 1s, it was expected that the lack of broad-lines in Seyfert 2s is due to dust attenuation along the LOS to the central source in Seyfert 2s. The problems with this concept are: (1) the featureless continuum in Seyfert 2s is still more or less a power-law, which it should not be if the power-law continuum from the central source is heavily reddened; (2) Seyfert 2 galaxies are only about one magnitude fainter than Seyfert 1 galaxies, implying that the continua in Seyfert 2s are only a magnitude fainter or so than in Seyfert 1s, but the broad emission lines are *completely* extinguished. Even in Seyfert 1.8/1.9s, whose spectra appear like those of Seyfert 2s and show variability in their broad-line fluxes, use of high signal-to-noise spectra and careful subtraction of the host galaxy spectrum show that the broad bases on permitted emission lines never completely vanish. This implies that Seyfert 2s may not just be Seyfert 1s in faint states.

Even though the presence of equatorial dust obscuration can explain the lack of broad-lines in Seyfert 2s, it does not explain the presence of a power-law AGN continuum in Seyfert 2s. The spectropolarimetry study of some

nearby type 2 Seyferts like NGC 1068 (Antonucci & Miller 1985) showed that the broad emission lines can be observed using polarized light from the source. The polarization is assumed to be due to a scattering region filled with high energy electrons above the torus. This important discovery was used to put forth the torus hypothesis, hinting at the fact that there is underlying uniformity to the central engine of an AGN and any observed changes are the effect of looking at the central engine from different lines of sight. This scattering region is the key component of the torus model, without which the continuum in Seyfert 2s will not appear like a power-law. This basic idea lead to the formation of the Unified Model of AGN (Antonucci 1993). The model posits that the dichotomy for each class of AGN is a result of strong obscuration by dust in the equatorial plane. Specifically, the dust is arranged in a torus-like structure around the central engine and shields the BLR for lines of sight close to the equatorial plane of the system. The viewing angle to the BLR and the central source, defines the optical spectral type of the AGN being observed. In this framework (see Figure 1.1), Seyfert 1s are observed mostly pole-on, thus allowing "seeing of the BLR", while Seyfert 2s are observed mostly edge-on, thus allowing us to view only the NLR.

In NGC 1068, the continuum polarization is $\sim 16\%$ after removal of significant starlight contribution to the spectrum. This polarization can occur via scattering, either due to dust or due to free electrons. Code et al. (1993) showed that the continuum polarization in NGC 1068 stayed constant at $\sim 16\%$ in the near-UV band. Combined with the original measurements by Miller & Antonucci (1983) in the optical, it was concluded that only electrons (and not dust) can provide a wavelength independent scattering mechanism over the large wavelength region of UV and optical observations. A number of observations have shown that at least some of the Seyfert 2s contain hidden Seyfert 1 nuclei (Antonucci 1993, and references therein). Since the observational case for polarization is strong in some Seyfert 2s, it is possible

to ask whether this behavior is present in all Seyfert 2s and whether or not all of them host an obscured BLR.

Tests of Unification

It should be possible to test for various concepts (or parameters) of unification in a robust way using large samples of AGN, if and only if, *all* the AGN are derived from the same parent population. Since the radiation from AGN is strongly anisotropic, it is clear that orientation plays a role. In a true parent population of AGN, these orientations will be truly random. There are a couple of general ways in which one may build such tests:

- We can count the total number of each type of AGN in a volume-limited sample. The properties of the dominant type will then highlight the properties of the parent population and hint towards properties that lead to unification. A problem with this approach is defining the volume that samples the parent population properly and avoiding selection effects.

- Another approach is to use a property that is, due to its physical nature, independent of observer's orientation with respect to the central source. Various possibilities include: extended radio emission, hard X-ray emission, far-infrared emission of host galaxies and emission from the NLR. Each of this approaches have their difficulties, but probably the most promising ones are hard X-ray observations and emission from the NLR.

- Another approach is to investigate the energy budget of the narrow-emission lines from the NLR and compare it to the input energy from the continuum source. This can be done in practice, but depends closely on the filling factor of the NLR clouds, the size of the emitting region on each cloud and other properties such as the dust content of the NLR.

- Yet another approach is to compare the total infrared luminosity from the central source to its total hard X-ray luminosity (see, Lutz et al. 2004, for a recent attempt), since the total IR luminosity of the torus should be equal to the total high-energy luminosity that it intercepts. Recent studies with *Spitzer* (Buchanan et al. 2006) have shown that the emission due to the torus is anisotropic until about ≈ 20 μm, but this result may be subject to other selection effects such as presence of dominant circumnuclear star formation within the galaxy sample.

Over the last two decades a number of tests have been done using such ideas. It is generally agreed that there are two main types of AGN, the radio-quiet (Seyfert 2s, Seyfert 1s and QSOs) and the radio-loud (FR Is, BL Lacs, FR IIs and Quasars). Within these two classes, the arguments in favor of Seyfert Unification are:

- Some Seyfert 2s can be shown observationally to be obscured Seyfert 1s, via spectropolarimetry (Antonucci 1993).

On the other hand, there is also some evidence against it:

- The continua of Seyfert 2 galaxies are in general *not* polarized (Cohen et al. 2000) and the polarization seems to be concentrated within the NLR knots (*e.g.,* see Kishimoto et al. 2002).

- Miller & Goodrich (1990) showed that for a torus opening angle of 30^{o}, and for NLR bicones lying in the plane of sky, continuum polarizations should reach 50% in edge-on tori. However this is clearly not seen; the maximum polarization noted in NGC 1068 is about 16% (Antonucci & Miller 1985).

- For a long time the non-detection of radio-quiet QSO 2s was considered a problem with radio-quiet unification theory. Discovery of a population of obscured AGN with *Spitzer* that are observable in mid-IR but

not observable in hard X-rays with *Chandra* (*i.e.,* they are Compton-thick) provides strong support for unification models of radio-quiet AGN. However the properties of these postulated radio-quiet QSO 2s sources are not clear. For example, recent mid-IR spectra of some QSO 2s (Sturm et al. 2006) actually appear similar to spectra of type 1 PG quasars in the $5 - 12$ μm range. Further, there are several speculative possibilities such as the obscuring tori are more flattened and/or they 'recede', in high-luminosity sources, because of the more intense radiation field that destroys dust close to the central source. The *Spitzer* spectra at least appear to have ruled out the possibility that these obscured sources are ULIRGs as they do not show evidence for silicate or ice absorption features commonly seen in ULIRG sources.

The radio-loud objects are primarily composed of two components, a steep-spectrum extended source (radio lobes) and a highly beamed flat-spectrum core. In VLBI measurements, the flat-spectrum cores get resolved into linear jet-like structures which are, for the most part, one-sided due to relativistic beaming effects. Observations of radio-loud sources and their description via this simple two-component idea are contradictory and need unification via orientation effects to explain them.

Urry et al. (1991) showed that lower-power FR I radio sources are the parent population of BL Lac objects, with BL Lacs being the beamed FR Is, based on number density of flux-limited samples in optical, X-ray and radio regimes. Many properties of BL Lacs match with those of FR I sources such as very weak emission line spectra. Padovani & Urry (1992) further proposed that the parent population of OVVs are FR II sources based on the distribution of Lorentz factors estimated for both classes. Also, OVVs show strong optical emission lines and also show strong evidence for cosmological evolution, much like FR II sources. OVVs are thus likely to be beamed FR IIs.

Thus overall, some basic connections between certain broad classes of AGN have been made:

- The primary difference between a Seyfert nucleus and a quasar nucleus is the luminosity of the central source.
- There is dust obscuration in the equatorial region of AGN and this is most convincingly shown in case of Seyfert 1s and Seyfert 2s, suggesting that Seyfert 2s harbor hidden Seyfert 1 nuclei. A similar situation is possible for NLRGs and BLRGs.
- Blazars are radio-loud AGNs in which our line of sight is close to the radio jet, leading to relativistic beaming effects.

Apart from these ideas, the study of other basic parameters such as the radio power, the mass of the SMBH and the relative accretion rate will provide directions to a common unified model for all AGN. It is however amply clear that two types of effects dominate the observed properties; (1) the intrinsic physical properties of the source and (2) orientation of the observer's line of sight.

1.1.5 Astronomical dust and its properties

In this section we take a bit of a diversion and look at the basic properties of astronomical dust. This is essential, as further ahead we will work with the fundamental quantities we define here.

Astronomical dust is not the same stuff as what we call dust on Earth. Astronomical dust is rather made up of clusters of organic and inorganic molecules and chemical compounds. Solid-state materials like graphite also make up a fraction of the dust composition. Thus dust in astronomical scenarios is actually much like the smog or organic pollutants in modern cities. It similarly absorbs and reddens light from objects of interest. Dust is formed when large red giant stars throw vast quantities of hot gas streaming

out of their envelopes. Dust particles condense out of this gas as it travels farther away from the surface of the star. The realization by Trumpler in the 1920s that dust prevents a clear view of our Galaxy was one of the great milestones in astronomy. The key to his realization was the fact that dust not only scatters visible radiation, but it absorbs radiation with wavelengths smaller than the size of the dust particles and in the process gets heated and re-emits this energy as infrared radiation. The scattering of light by dust particles is evident in reflection nebulae, where the spectrum of the reflection nebulae actually shows features in the spectrum of the star illuminating the nebula.

Dust grains are effective absorbers of photons whose wavelengths are comparable to, or smaller than, the size of the dust grains. Dust grains are typically larger than about 100 nm. Due to this, dust effectively absorbs UV radiation. Most of the energy emitted by hot stars is in the optical and UV region, and hence effectively heats the dust grains. Moreover, the massive young stars born in star forming regions burn their fuel quickly and barely come out of their dusty cocoons. The overall effect of these processes is that dust absorbs most of the stellar radiation, converting it to infrared. This process makes most galaxies strong emitters in the far-IR. The absorption of ambient star light warms the dust grains to about $\sim$ 10 K in the diffuse ISM.

Extinction and Reddening

The scattering and absorption processes dim the light from distant stars. This dimming is termed 'extinction'. The extinction (A_X) in some waveband X is given as:

$$A_X = m(X) - m_0(X) \tag{1.1}$$

where, $m(X)$ is the observed magnitude with extinction and $m_0(X)$ is the magnitude that should have been measured if there was no extinction.

The 'reddening' or color excess, $E(X-Y)$ in some color $X-Y$ is defined to be the difference between the observed color $m(X)-m(Y)$ and the intrinsic color $m_0(X)-m_0(Y)$, thus:

$$E(X-Y) = [m(X)-m(Y)] - [m_0(X)-m_0(Y)] = A_X - A_Y \qquad (1.2)$$

Since color is generally defined such that shorter wavelengths are on the left and the strength of the interstellar extinction generally decreases from short to long wavelengths, $E(X-Y)$ will be a positive number. The most common type of extinction cited is A_V and the most common type of reddening cited is $E(B-V)$. It is customary to convert A_λ to A_V for a given λ when reporting extinction values.

If the distance to a star is known independently, it is possible to obtain A_X by estimating the absolute magnitude of the star from its MK spectral class, by using the formula for distance modulus.

$$m_X - M_X = A_X + 5\log d - 5 \qquad (1.3)$$

Thus, measurements of stars of known MK class, and therefore, known intrinsic colors in two wavebands, yields $E(B-V)$.

A comprehensive review of classic studies of extinction in the UBV system for stars in the Galaxy is given in Savage & Mathis (1979) and Whittet (1992). All major early studies focused on O and B stars as they are ideal for studies of extinction. There are three reasons for this: (1) O-B stars are highly luminous and can be seen over large distances, which also helps to provide a large enough dust column to study extinction; (2) their emission is intrinsically blue and mostly in the UV, hence their light is most susceptible to extinction; (3) the spectra of O and B stars are distinctive, which helps to classify them accurately.

The Extinction Curve

The amount of extinction and reddening depends on the column density of dust along the line of sight and it is very different for different lines of sight. The naive assumption that the dust particles are the same in all regions, though not entirely correct in realistic situations, is a good first start. If we assume that the type of the dust particle is the same in the regions of interest, then the ratio of the extinctions at any two wavelengths is the same for any lines of sight to that region. The variation of this ratio for a given line of sight over the wavelength region of interest is called the extinction curve.

The extinction curve peaks in the UV and falls off to both infrared and X-ray regimes. The curve shows three bumps or features, one at 217 nm, and other two at 9.7 μm and 18 μm. The feature at 217 nm in the UV is possibly due to tiny graphite grains of the size of ~ 50 atoms. The latter features are due to Si–O bonds in silicate grains. In the optical, the extinction curve does not rise as sharply as it does in the UV. This is attributed to the presence of very small dust grains along lines of sight giving rise to the extinction curve in the UV. The slope of the extinction curve is quantified by the parameter:

$$R_V = \frac{A_V}{A_B - A_V} = \frac{A_V}{E(B-V)} \tag{1.4}$$

For a steeply rising curve, $R_V \simeq 3$, and $R_V \simeq 5$ for a slowly-rising curve. For the Galaxy, classical studies of extinction derived $R_V \simeq 3.1$. However, it is very likely that R_V is very different for different lines of sight. In AGN environments, typically $R_V \gtrsim 3.1$ and the extinction curve rises sharply in the UV, indicating presence of very small grains (Savage & Mathis 1979).

Radiation by Dust

Dust reprocesses the short-wavelength radiation to higher wavebands and much can be learned about the environment from re-radiation by dusty struc-

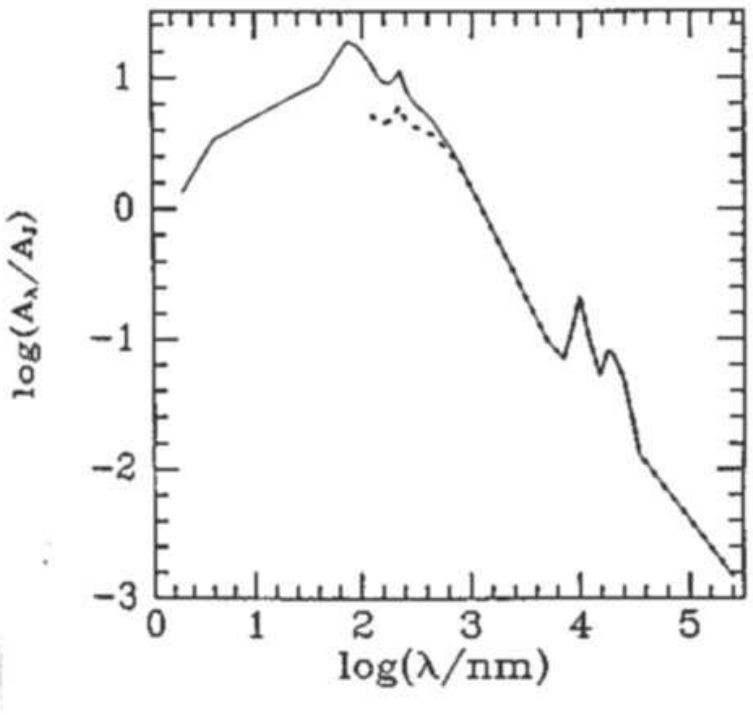

Figure 1.6: Extinction Curve from Mathis (1990), as plotted in Binney & Merrifield (1998, Fig 3.17), the solid curve shows the expected form for lines of sight that pass through the diffuse ISM, while the dashed line shows a line of sight through a thick molecular cloud.

tures. Very good examples of such environments are reflection nebulae, the diffuse interstellar medium (DISM) and dust within AGN. The key to understanding dust re-radiation is Kirchhoff's law. Kirchhoff's law states that if a body of temperature T absorbs a fraction Q_ν of the radiation of frequency ν, then the emissivity at its surface is $Q_\nu B_\nu(T)$, where $B_\nu(T)$ is the Planck function. In the context of a radiative transfer framework, this leads to:

$$I_\nu(\tau_\nu) = I_\nu(0)e^{-(1+K_s/K_a)\tau_\nu}, \text{ for } B_\nu \to 0 \tag{1.5}$$

where τ_ν is the optical depth at frequency ν, $K_a(\nu)$ is the absorption cross-section of the dust grains and K_s is the emission cross-section due to scattering in a specified direction. The extinction at frequency ν is then given as,

$$A_\nu = -2.5 \log_{10} \frac{I_\nu(\tau_\nu)}{I_\nu(0)} = 1.086(1 + K_s/K_a)\tau_\nu \tag{1.6}$$

This simple relationship between A_ν and τ_ν leads to the use of τ_V as an effective measure of amount of extinction involved. However, the actual extinction A_V may not be related as simply to the actual optical depth due to the contribution from scattering. Alternatively, $E(B-V) = A_V/R_V$ is often used.

The above relation holds for dust which does not emit significantly at a given ν. This will be the case in the visual band for cold dust at $T \sim 10$ K. In the case when dust emits strongly at the frequency of interest (*e.g.,* in the infrared), the extinction estimated from measurements of τ_ν will be greater.

The Dust-to-Gas Ratio

Bohlin et al. (1978) showed empirically that the column density of Hydrogen $N(H_{tot})$, in all its forms (atomic or molecular), is linearly related to the line of sight reddening, $E(B-V)$.

$$N(H_{tot}) = 5.8 \times 10^{25} E(B-V) \text{ m}^{-2} \text{ mag}^{-1} \tag{1.7}$$

$$N(H_{tot}) = 1.9 \times 10^{25} A_V \text{ m}^{-2} \text{ mag}^{-1}, \text{ for} R_V \simeq 3.1 \tag{1.8}$$

Based on IUE spectra, Shull & van Steenberg (1985) updated the value of $N(HI)$ to $5.1 \times 10^{25} E(B-V)$ m^{-2} mag^{-1}. To the first approximation then, this implies that a given mass of gas contains a characteristic mass of dust, independent of whether it is molecular or atomic. Thus the value of $E(B-V)/N_H$ characterizes the dust/gas ratio.

Dust Grain Sizes and PAH

Extinction is caused by a combination of absorption and scattering of radiation by dust. The fraction of extinction which is caused by the scattering is called albedo. Dust grains do not scatter radiation isotropically and small-angle forward scattering dominates. In the B-band the albedo is expected to be ~ 0.6. Grains much smaller than 500 nm do not scatter light as much and tend to do it isotropically. Grains that are a fraction of a micron in size radiate fairly efficiently and tend to stay at a temperature of about $T \simeq 20$ K in the diffuse ISM. This emission peaks in the submm-regime near 150 μm, as is evident in many galaxies that have a peak in their SED in this region.

IRAS observed the infrared sky in four bands centered on 12 μm, 25 μm, 60 μm, and 100 μm. IRAS made the important observation that even in the mid-infrared band at 12 μm and 25 μm, there was considerable emission from diffuse interstellar dust. This observation led to radical changes in the models of interstellar dust grains. It is now accepted that the interstellar medium (ISM) includes extremely small grains, containing $\lesssim 100$ atoms, in addition to 'classical' dust grains, ~ 0.1 μm in size and containing $\gtrsim 10,000$ atoms. These small grains are heated stochastically by UV photons from stars. Typically a UV photon with energy of $\sim$ 10 eV will heat a small grain to a temperature $\sim$ 1000 K; when this grain cools, it will emit most of this energy in the near-IR continuum. On average, a large collection of these stochastically-heated small dust grains will likely give rise to a strong near-IR continuum. Strong evidence for stochastic heating of dust grains is seen in reflection nebulae (Sellgren 1984). One of the important distinguishing factors about emission due to stochastic-heating is that the blackbody spectrum of the emitted radiation does not shift to cooler temperatures (or gets reddened) with increasing distance from the source, though the emission may be reduced due to the reduced probability of a UV photon exciting the small grain at farther distances from the source. It has been suggested that these small dust grains could be polycyclic aromatic hydrocarbons (PAHs)

(Leger & Puget 1984). These molecules are considered to be linked benzene rings to which other species of atoms have attached themselves, forming a variety of configurations.

A detailed analysis of the diffuse interstellar emission has been done by Draine & Li (2001) and Li & Draine (2001). The most recent models of interstellar dust (Draine & Li 2007) have a combination of silicate, graphite and PAH grains.

1.2 Overview of this dissertation

We will now look at the three main themes of this dissertation: (1) Geometrical modeling of NLR orientations with respect to their dusty host-galaxy disks; (2) *HST/WFPC2* optical imaging of dusty nuclear spirals in Seyfert galaxies; (3) *Spitzer/IRS* mid-infrared spectroscopy of Seyfert galaxies. The motivations of these research themes, and the ensuing main results are covered in this section, as an early overview of the complete dissertation. Each part is further described in detail in individual chapters ahead. The major aspect of this dissertation is understanding the nature of dust obscuration in Seyfert galaxies. Since it is readily evident that dust plays an important role in how we see type 1 and type 2 sources, a detailed understanding of properties of nuclear dust distributions is necessary.

1.2.1 Geometrical modeling of NLR orientation

The first project was to use the Interactive Data Language[5] (IDL) to build a program that can simulate the geometry of the NLR outflows with respect to the host galaxy disk.

The motivation for the development of this software tool was the results presented by Clarke et al. (1998). Clarke et al. had developed a statistical

[5]Interactive Data Language is developed by ITTVIS, Inc. formerly Research Systems, Inc.

approach to estimating the angle between the axis of the radio jet and the normal to the host galaxy plane. Naively one might expect that the central accretion disk, the radio outflow/jet, and the host galaxy disk share the same axis of symmetry, and are aligned preferentially in the same direction. Further, the Unified model suggests that the dichotomy between type 1 and type 2 sources is dependent on the inclination angle the line of sight of the observer makes with the direction of the radio jet. Smaller angles lead to type 1 like properties, while larger angles lead to type 2 like properties.

Investigation of any alignment between the radio outflow/jet and the host galaxy disk can be done with Seyfert galaxies as their host galaxies are easily visible, in contrast to radio-loud quasars at high redshifts. The downside of using Seyfert galaxies is that their radio outflows are not particularly strong and well collimated. Clarke et al. came up with a 3-D geometrical system that defined the necessary geometric constraints between different components of the active nucleus, such as the inclination and position angle of the radio jet, and the inclination and position angle of the host galaxy disk. They attempted to determine the angle β between the direction of the radio jet and the normal to the host galaxy plane. Although the inclination angle of the radio jet is not generally known, they were able to determine a minimum β angle and look at the distribution of this angle over a large sample of Seyfert 1 and 2 galaxies. They conclude that the radio jets are oriented randomly with respect to the normal to the host galaxy plane, confirming the results of Schmitt et al. (1997). Thus they find that the accretion disk does not necessarily align itself with the plane of the host galaxy. Further, Kinney et al. (2000) based on a larger sample of uniformly selected Seyfert galaxies, showed that the orientation of the radio jet with respect to the normal to the host galaxy plane is random. Schmitt et al. (2003) indicate that, based on the survey of [O III] emission in *HST* images of Seyfert galaxies, there is no correlation between the orientation of the extended NLR outflow and the host galaxy major axis.

Our software simulates the geometrical system with constraints as defined in Clarke et al. (1998). The tool is interactive, so that a user can view the model as projected on the sky and then freely move the model in three dimensions to visualize the geometry. The important differentiator in our efforts here are that we are using the symmetry axis of the NLR outflow instead of the symmetry axis of the radio jet. The NLR outflows are much more prominent in Seyfert galaxies than are radio jets. It is more probable that the opening angle of the biconical NLR outflow is constrained by the opening angle of the torus, as the torus encircles the central source. Thus, measuring the opening angle of the NLR outflow in a number of Seyfert galaxies will allow us to understand the interaction between the NLR outflows and their host galaxies. Furthermore, we can actually determine the inclination angle of the NLR bicones from the outflow kinematics, thereby fully constraining the geometry of an individual source. A result of these efforts to model the geometry of 12 Seyfert NLR outflows was reported in Deo & Crenshaw (2003) where we used kinematic model constraints from J. Ruiz's thesis (CUA) on slitless spectroscopy of NLRs in Seyferts. Das et al. (2005, 2006) further improved the kinematical method with high resolution long slit data for NGC 4151 and NGC 1068 and have used this program to model the NLR and the host disk geometry. We have also used this program to investigate the reddening of the NLR by a dusty disk in the plane of the host galaxy, as we will show later (see also Collins et al. 2005).

1.2.2 HST Imaging of Nuclear Spirals in NLS1s

The main motivation for this study is the phenomenon of **narrow-line Seyfert 1s**. These Seyfert galaxies are classified as type 1 Seyferts with the FWHM of broad $H\beta$ line $\gtrsim 500$ km s^{-1} but $\lesssim 2000$ km s^{-1}. It has been suggested that the narrow-width of the emission lines for such Seyfert 1 galaxies is due to their intrinsically smaller black hole masses (Pounds et al. 1995), leading to smaller rotational broadening of BLR lines. The question

we seek to answer is, does the host morphology of narrow-line Seyfert galaxies show any peculiarity suggestive of putative smaller black hole masses and higher Eddington ratios? (Simkin et al. 1980) suggested that merger-induced formation of large-scale stellar bars can fuel large amounts of gas and dust to the central regions of Seyfert galaxies. Crenshaw et al. (2003a) noted that the hosts of 19 NLS1s from a sample of Seyfert 1s by Malkan et al. (1998) and the *HST* archive showed a higher frequency of large-scale ($>$ 1 kpc) stellar bars than that found in broad-line Seyfert 1s (BLS1s), suggesting that efficient fueling due to bars was plausible. We have used the sample from Crenshaw et al. (2003a) and have now studied the morphology of the nuclear regions ($\sim$ 500 pc) of these *HST* images. The images are mostly optical WFPC/2 images in the wide band filter F606W, although some of the images are taken with the F547M filter. We reduced, calibrated and performed cosmic-ray rejection on the raw images. The resulting images were studied and classified according to the morphological type of the host galaxy. We used a technique called 'structure mapping' (Pogge & Martini 2002) to enhance the dusty structures in the image and then classified the nuclear morphology.

Martini & Pogge (1999) and Pogge & Martini (2002) showed that the circumnuclear regions of Seyfert galaxies and many other normal galaxies have mini-spirals of gas and dust embedded inside the large-scale spiral of the host galaxy. Due to the limited resolution of ground-based telescopes, nuclear spirals were not discovered until the late 1990s and were first discovered with *HST* images. There are two main types, the two-armed grand-design structure and the multi-armed flocculent structure. We find that the NLS1s preferentially have grand design structure and this is due to the presence of a strong large-scale stellar bar. The large-scale stellar bar induces spiral shocks which travel inward in a gas disk. In the inner 500 pc these shocks curve to form a two armed spiral. Numerical simulations Maciejewski et al. (2002); Maciejewski (2004b) and recent IFU observations Fathi et al. (2006)

of the spirals support this picture.

We saw in the last section that the accretion disks of Seyfert galaxies are not necessarily aligned with the host galaxy disks as suggested by the orientation of the weak radio jets. This misalignment can be caused by a number of theoretical effects related to the structure of the accretion disk, the spin of the SMBH and the pattern of inflow of matter to the accretion disk. Suggestions that the NLR outflow is controlled by the dust obscuration in the central parts of a Seyfert galaxy imply that it is plausible that the pattern of inflow can affect the geometry of the NLR and hence classification of Seyfert galaxies into type 1s and type 2s. The presence of different nuclear dust morphologies in type 1 objects indicates that there could be an evolutionary scenario that converts a NLS1 to a BLS1. It is seen from our study and those of Martini et al. (2003b) that grand-design spirals tend to occur in barred galaxies, while tightly-wound multi-arm structures occur in galaxies without bars. From our study we find that BLS1s tend to show the tightly-wound type of nuclear spirals. One way for a NLS1 to convert to a BLS1 is to grow the stellar bulge of the galaxy along with the black hole mass. This would then lead to the dissolution of the large-scale bar, thus allowing the two-armed spiral in the central region of the NLS1 to wind more, finally producing a tightly-wound multi-arm structure.

The important point of this study is that the nuclear regions of Seyfert galaxies, whether Seyfert 1s or Seyfert 2s, host a large amount of gas and dust. In the case of high Eddington ratio systems like NLS1s, the inflow is clearly driven by the large-scale bars. The presence of such large quantities of dusty gas also provides the necessary material that can form the dusty obscuration in the very inner region ($\lesssim$ 10 pc) of the nucleus. The position angle of the major axis of the nuclear spiral disks does not necessary match the position angle of the large-scale disk, and it is possible that there could be trends between the position angle of the NLR outflow and the nuclear disk. The nuclear disks are expected to be feeble and not necessarily self-gravitating,

but it is possible that in the presence of a large enough concentration of matter or a external driving force like a stellar bar, they will affect the orientation of the active nucleus.

1.2.3 Spitzer Spectroscopy of Seyfert 1.8-1.9s

After the imaging project, I worked on the mid-infrared spectra of Seyfert 1.8/1.9 galaxies from *Spitzer Space Telescope* observations (S. Kraemer, PI) using the infrared spectrograph (IRS) in the wavelength range 5-38 μm. Goodrich (1995) had shown that some Seyfert 1.8/1.9s show variations in the flux of the broad Balmer line wings consistent with changes in the reddening of the BLR. Thus, these objects are likely to be viewed at intermediate angles with respect to the torus axis, and since they do not fully extinguish the nucleus as in Seyfert 2s, provide a probe of the nature of the dust obscuration in the torus. The primary motivation to study Seyferts with *Spitzer* spectroscopy is to understand the characteristics of the dusty torus and the surrounding dusty regions. We have supplemented this sample of 12 Seyfert 1.8/1.9s with publicly available Seyfert 1 and 2 spectra from the *Spitzer* archives. Overall we have 69 Seyferts where mid-IR low resolution spectra have been studied.

Since the NLR gas is photoionized by the continuum emission from the central engine, the ionization structure of the NLR is a very good probe of the power of the central engine. Recent studies of the intrinsic absorption in NLR cloud complexes (Crenshaw et al. 2003b) have shown that the NLR is an outflowing wind from the central engine. The NLR is also seen as a conical structure in high resolution *HST* images Schmitt et al. (2003) with the apex near the central engine. This implies that the orientation of the axis of the NLR can define the orientation of the accretion disk. Some torus models (Konigl & Kartje 1994; Elitzur & Shlosman 2006) have predicted that the torus may be the outer region of the accretion disk itself and the BLR and the NLR are the outflowing winds coming off the accretion disk as well. A further

issue is the presence of dust within the NLR clouds, which was recognized fairly early (Rudy 1984). Here, we use the *Spitzer* spectroscopy as a diagnostic of the mid-infrared emission from the central engine and the NLR to probe the structure, location and scale height of the dust torus. Another important factor that should not be overlooked is that the active nucleus is buried in a large spiral galaxy. The average scale height of spiral galaxies in the inner kiloparsec is $\sim$ 100 pc (Binney & Merrifield 1998). Thus, it is quite likely that dusty clouds and starbursts external to the active nucleus will affect the intrinsic infrared spectra of the nuclear dust distribution. Thus, separating all these components is essential if we want to constrain the properties of the dust distribution within 100 pc of the central engine. The first step towards doing this is to estimate the background starburst contribution to a given mid-IR Seyfert spectrum. Only after one has calibrated and removed this component from the spectra can we begin to estimate the contribution due to dust at various temperatures and the underlying non-thermal mid-IR continuum, if it exists. The mid-IR *Spitzer* spectra are proving to be very useful in terms of study of the photo-ionization of the NLR, as the waveband is rich in narrow emission lines. We have estimated a few spectral diagnostics based on prominent narrow-lines and these results are reported in Chapter 5 onwards.

Chapter 2

Geometry of the Narrow-Line Region

In this chapter, we will look at the study of the orientation of the NLR with respect to the inclination of the disk of the host galaxy. The primary goal of this study was to develop a computer program to visualize the geometry of the active nucleus in a given host galaxy.

There are several important uses of such a program. For example, it is useful to visualize the inclination of the NLR with respect to the inclination of the host galaxy disk and with respect to the inclination of the nuclear dust disk of the host galaxy. Differences in position angles and inclinations between the major axis of the host galaxy and the major axis of the nuclear disk suggest disturbances in the nuclear region driven by gravitational forces in the host galaxy. Their relative geometry to the NLR outflow can provide hints about how the nuclear regions can be fueled and the dominant process that leads to efficient fueling. In the study discussed in this chapter, we assume that the inner nuclear dust disks are aligned with the outer disk of the host galaxy. This assumption may not be true, and we plan to investigate this in future. Further, the visualization allows one to see which side of the host galaxy disk is closer to the observer's line of sight (LOS) and therefore

which side of the NLR bicone is expected to be extincted by the dust in the host galaxy. Finally, the visualization serves as a good schematic of the geometry of the active nucleus. A direct application of such a tool is to constrain the nuclear geometry of large number of active galaxies and then estimate the distribution of inclination angles of the NLR. Such a distribution of inclination angles, estimated per AGN type, will test the limits of the hypothesis that the inclination of the LOS to the axis of symmetry of the nucleus strongly affects the classification of the active nucleus.

The geometry of the active nucleus is suspected to be strongly axially symmetric. The axis of the NLR outflow therefore likely defines the symmetry axis for the active nucleus. This is true only if the symmetry axis of the obscuring torus at the base of the conical NLR matches the axis of symmetry of the accretion disk. Thus in the discussions that follow, we assume that the plane of the accretion disk lies in the equatorial plane of the torus and the biconical NLR is perpendicular to this plane and gets cut in half at the equatorial plane of the torus.

2.1 Previous Studies

The motivation and framework of this work is taken from Clarke et al. (1998). They developed a statistical approach to estimating the angle between the axis of the radio jet and the normal to the host galaxy plane. Seyfert galaxies are known to be weak radio emitters, but they have faint extensions within their NLRs that look like weak radio jets. Some radio-loud AGN have strong classical radio jets. Investigation of any alignment between such weak radio outflow and the host galaxy disk is possible in Seyfert galaxies as their host galaxies are easily visible, in contrast to high-redshift radio-loud quasars where the jet can be seen much more easily but the host galaxy is often difficult to resolve. Clarke et al. came up with a 3-dimensional (3-D) system that defined the necessary geometrical constraints between the inclination

and position angle (PA) of the radio jet and the inclination and position angle of the host galaxy disk. They attempted to determine the angle (called 'β') between the direction of the radio jet and the normal to the host galaxy plane. Although the inclination angle of the radio jet is not generally known, they were able to determine a minimum β angle and look at the distribution of this angle over a large sample of Seyfert 1s and Seyfert 2s. They concluded that the radio jet directions were distributed randomly with respect to the normal to the host galaxy planes, confirming previous results of Schmitt et al. (1997). Thus they conclude that the accretion disks in Seyfert galaxies do not necessarily align with the planes of the host galaxies.

Using high-resolution narrow-band ([O III] λ5007, WFPC2 with F502N filter) imaging with *HST* , Schmitt & Kinney (1996) observed that the sizes of NLRs in Seyfert 1s are much smaller than NLR sizes of Seyfert 2s. They proposed that Seyfert 1s may have their torus axis aligned close to the normal to the galaxy plane, while the torus axis in Seyfert 2s may lie at an intermediate angle between the normal to the host galaxy plane and the plane of the host galaxy. As the amount of gas intercepted by the nuclear radiation will be less perpendicular to the plane, Seyfert 1s should show less extended NLRs than Seyfert 2s. To check this hypothesis, Schmitt et al. (1997) compared the distribution of the position angles of the radio jets and the position angles of the host galaxy major axes. They found that Seyfert 1s are less likely to show extended radio structure along the host galaxy major axis, while Seyfert 2s have these radio structures distributed in all possible directions. Keel (1980) had suggested that there is a paucity of edge-on Seyfert 1s. Further, Maiolino & Rieke (1995) argue that intermediate Seyfert types 1.8/1.9s are likely to be Seyfert 1 nuclei embedded in edge-on host galaxies, where the additional obscuration due to the dust and gas in the host galaxy contributes to the lack of broad emission-lines, while many Seyfert 1s nuclei are found preferentially in face-on systems. Schmitt et al. (1997) suggest that the lack of extended radio structures aligned with the host galaxy major

axis in Seyfert 1s agrees with results of Keel (1980) and Maiolino & Rieke (1995).

As mentioned above, Clarke et al. (1998) using the dataset gathered by Schmitt et al. (1997) showed that given the inclination i of the host galaxy, and the difference (δ) between P.A. of the radio jet and the P.A. of the major axis of the host galaxy disk, it is possible to estimate a minimum value of angle β. From this analysis, they concluded that the distribution of β angles are different for Seyfert 1s and Seyfert 2s at a 96% confidence level, which contradicts the Unified model scenario. Seyfert 1s favor low values of β, while Seyfert 2s favor high values of β. However, Nagar & Wilson (1999) argue that a bias in the distribution of host galaxy inclination i can lead to apparent differences in β distributions of Seyfert 1s and Seyfert 2s. They further argue that there is no difference in β distributions of the two types. Kinney et al. (2000) selected a sample of Seyfert 1s and Seyfert 2s based on their 60 μm fluxes and warm infrared colors. They show that the distributions of β are the same for Seyfert 1s and Seyfert 2s, if it is assumed that a galaxy appears as a Seyfert 1 when the angle between the LOS and the radio jet is less than ϕ_c and that the galaxy inclination i is smaller than some angle i_c. Thus they conclude that this orientation restriction on the model to generate statistically acceptable fits indicates that at least to first order, orientation effects dominate the interpretation of AGN properties.

Schmitt et al. (2001), using the far-infrared selected sample, performed statistical tests for the unified model. They show that samples selected using isotropic properties provide strong support for the orientation idea of the Unified Model. However, they note the lack of edge-on Seyfert 1s as compared to Seyfert 2s, in agreement with Keel (1980) and Maiolino & Rieke (1995). They interpret this as suggesting that dust and gas along the host galaxy disk can play an important role in hiding the Seyfert 1 nuclei from direct view. Crenshaw & Kraemer (2001) suggested that the dusty "lukewarm" absorbers postulated to explain the saturated UV absorption lines in UV

spectra of Seyfert 1s are related to the dusty clouds in the host galaxy at distances of $\sim$ 100 pc or more. They also showed that for a large sample of Seyfert 1s the continuum reddening (as measured by UV color) tends to increase with inclination of the host galaxy. These observational evidences provide strong hints that, apart from the postulated existence of the compact molecular torus at distances $\sim$ 1 pc, the presence of dusty clouds in the host galaxy at distances of $\gtrsim$ 100 pc can provide orientation dependent effects that mimic the effects of the parsec-scale torus.

Thus, when studying a particular Seyfert galaxy in detail, it would be good to have a tool that will help simulate the geometry of the active nucleus in relation to the position of the dusty nuclear disk of the host galaxy. Radio structures in Seyfert galaxies are weak and the NLR provides a strongly visible structure to estimate the orientation of the torus. Further, it is possible to more tightly constrain the geometry of the NLR via spectroscopic mapping along its length, because accurate inclinations for individual AGN are becoming available via bicone fits to radial velocities measured for individual clouds (Das et al. 2006, 2005). In the sections below we describe the program that satisfies such a need.

2.2 The Design of the Program

We have developed an IDL program based on the geometrical constraints developed in Clarke et al. (1998) to visualize the geometry of the NLR and the host galaxy disk with respect to the LOS. This geometry is shown in Figure 2.1. In the figure, the X-Y plane defines the plane of the galaxy. The X'-Y' plane defines the plane of the sky. The Z-axis is the normal to the galaxy plane and Z'-axis is the LOS. The bicone is tilted from the normal the galaxy plane by angle β, which we wish to estimate. The angle δ is the difference in position angle of the bicone axis as projected on the plane of the sky and the position angle of the photometric major axis of the galaxy as

measured on the plane of the sky. The angle between the LOS and the bicone axis is ϕ (inclination angle of the bicone). The angle ϕ defines the nature of the observed properties of the nucleus, in the framework of the unified model. The angle β is therefore the angle between the normal to accretion disk and the normal to the host galaxy disk. This is assuming that the NLR outflow is perpendicular to the accretion disk plane and the symmetry axis of the accretion disk matches the symmetry axis of the NLR bicone, which is presumably fixed by the interior torus. In the figure, the photometric major axis of a galaxy is along the X axis. There is a mirror symmetry about the Y-Z plane, which can be removed by observationally determining which side of the bicone is towards us. This can be done by fitting the kinematics of the NLR and then extracting the inclination from the biconical model fits. Apart from that, there is 180^o ambiguity in determining the closer side of a host galaxy disk. This is normally resolved by using a galactic rotation curve and the assumption that spiral arms trail the rotation (Kinney et al. 2000). The direction of the dusty spiral arms help to resolve this ambiguity.

The mathematical setup is as given in Clarke et al. (1998), which we reproduce here, the major difference being that we use the NLR axis instead of the axis of the radio emission. The coordinate system is setup as described above. In this coordinate system, the unit vector in the direction of the LOS is,

$$k_{LOS} = (0, -\sin i, \cos i) \tag{2.1}$$

If we denote the unit vector along the NLR symmetry axis as k_{NLR}, then the vector intersects a unit sphere centered on the origin and lies on a latitude defined by the angle β. The angle between k_{NLR} and k_{LOS} defines a great circle on the unit sphere. The difference δ between the PA of the major axis of the galaxy (along X-axis) and the PA of the NLR axis, is constrained between 0 and 90^o. Given δ and inclination i, the unit vector k_{NLR} can then

be written using direction cosines as,

$$\begin{aligned} k_{NLR} &= (k_{NLR_x}, k_{NLR_y}, k_{NLR_z}) \\ &= (\cos\delta \sin\phi, \\ &\quad \sin\delta \cos i \sin\phi - \sin i \cos\phi, \\ &\quad \sin\delta \sin i \sin\phi + \cos i \cos\phi), \end{aligned} \tag{2.2}$$

where ϕ is the angle between k_{LOS} and k_{NLR} and lies in the range $-180^o < \phi < 180^o$. This leads to the mirror symmetry about the apparent minor axis of the galaxy (Y'-axis). Thus the NLR axis may lie on one of the two great circles which are reflections of each other in the Y-Z plane. To remove this ambiguity, we need to know which side of the NLR is close to us. As mentioned above, this can be done by fitting a kinematical bicone model to the NLR kinematics (Das et al. 2005, 2006). The angle β between the k_{NLR} and Z-axis is then obtained from Eq. 2.2 as,

$$\begin{aligned} \cos\beta &= k_{NLR_z} \\ &= \sin\delta \sin i \sin\phi + \cos i \cos\phi \end{aligned} \tag{2.3}$$

The only relevant values of ϕ are those which give $0^o < \beta < 90^o$, thus, this means that ϕ lies in the range $\phi_1 < \phi < \phi_1 + 180^o$, where ϕ_1 is given as,

$$\phi_1 = \tan^{-1}\left(\frac{-\cot i}{\sin\delta}\right) \tag{2.4}$$

which then lies in the range $90^o > \phi_1 > 0^o$. If $\phi < 0^o$, then the NLR is projected against the half of the galaxy that is farther away from us. We can figure out which side of the host galaxy disk is close to us by tracing dusty spiral arms within optical images of the galaxy. The side of the galaxy with less pronounced dusty features will be farther away from us due to contamination from the light of the bulge. This allows us to remove the

ambiguity in ϕ.

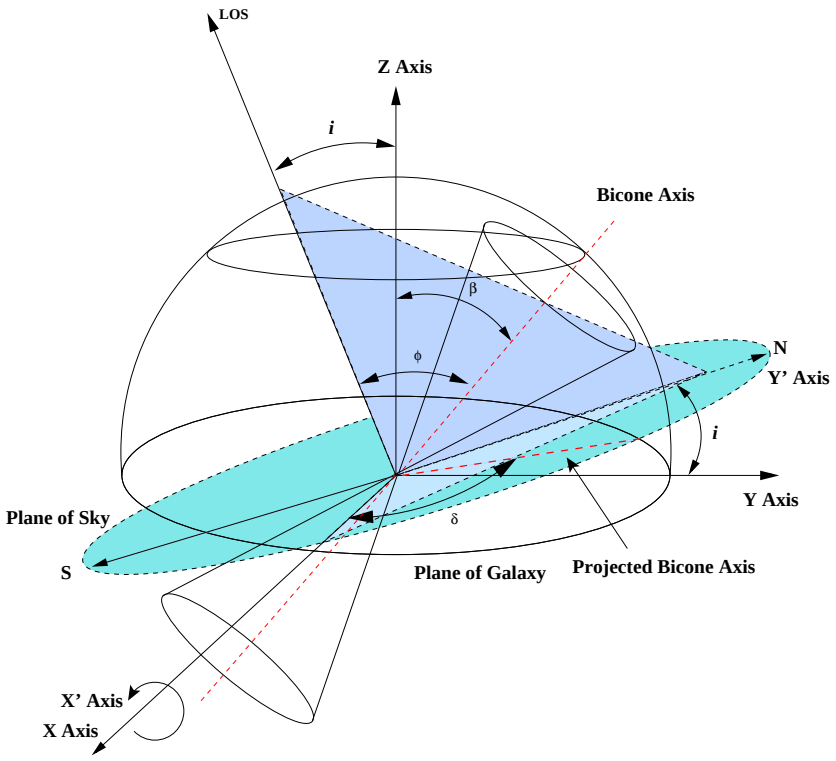

Figure 2.1: Geometrical model of NLR orientation with respect to the normal to the host galaxy disk.

The program is written in IDL and has a graphical user interface (GUI). The user inputs the position angle (P.A.$_{\rm gal}$) and inclination ($i_{\rm gal}$) of the host galaxy, the position angle (P.A.$_{\rm bicone}$) and inclination (ϕ) of the NLR bicone, and the half-opening angle ($H.A._{\rm bicone}$) of the NLR. Using these values and the geometrical constraints described below, the software simulates a thin nuclear host disk, a torus and the NLR bicones, and then positions these 3-D surfaces in the coordinate system as shown in Figure 2.1. The program then orients the system such that North is up and East to the left in the view-port of the user, just as it would be on sky. After this point, the user can use the mouse pointer to move the entire model in 3-D by dragging it.

All components of the model can be transformed in three fundamental ways: translation, scaling and rotation about an arbitrary axis. The safest option among these is scaling, as the others will change the geometrical constraints we have put in the model. The entire system can be rotated around any axis to simulate different lines of sight. For example, one can view the galactic disk edge-on, to see how the NLR bicone is oriented with respect to the disk.

The geometrical definitions and constraints on the system are given below.

- Inclination of the host galaxy disk, $i_{\rm gal}$, is zero when face-on.
- Inclination of the bicone axis, ϕ, increases away from the line of sight.
- Position angle of the major axis of galaxy is such that P.A.$_{\rm gal}$ + 90$^{\rm o}$ points along the minor axis of the host galaxy on the side of the disk that is closer to the observer.
- Position angle of the bicone axis is such that the cone along the given position angle points away from the observer.
- All angles used are positive and measured counter-clockwise.

The main parameters computed are $|\delta|$, the difference between the position angle of the galactic major axis and the bicone axis, and β, the angle between the bicone axis and the normal to the galactic disk.

A detailed description of the usage of the program is given in Appendix A. An example of the visualization created by the program and the program GUI is shown in Figure 2.2.

2.3 Applications of the Program

This program was originally used to look at the distribution of β angles for a sample of 12 Seyfert galaxies taken from Ruiz et al. (2005). The inclination angle and the half-opening angle of the bicone were estimated from

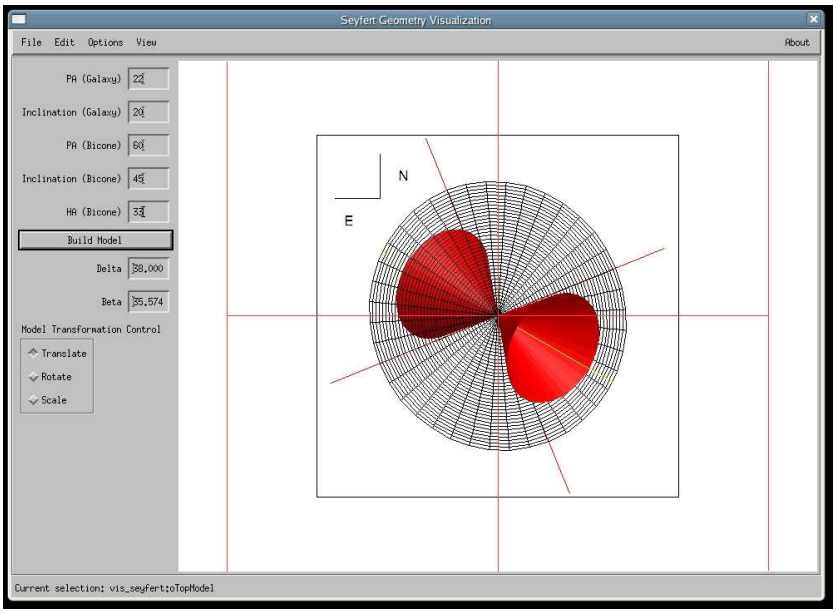

Figure 2.2: Example of the GUI of the program and a model of NGC 4151 NLR geometry

HST slitless spectroscopy with *HST* of the [O III] λ5007 emission knots (Ruiz et al. 2005). These estimates are based on modeling of the NLR kinematics using the biconical models described in Crenshaw et al. (2000) and Crenshaw & Kraemer (2000). Measuring radial velocities from slit-less spectroscopy is difficult and hence there are large uncertainties in these measurements. Nevertheless, the results of this simple modeling effort are shown in Figure A.2 in Appendix A along with a user's manual for the program.

Long-slit spectroscopic mapping of the NLR, however, results in much better estimates of $i_{\rm bicone}$ and δ. Das et al. (2005, 2006) using such observations with the *HST*/STIS spectrograph determined accurate estimates of the position angle, inclination angle and the half-opening angle of the NLR bicones in NGC 4151 and NGC 1068 (see Table 2.1). Our program was used to demonstrate visually that at least one edge of the biconical NLR in both NGC 4151 and NGC 1068 lies close to the galactic disk and for a sufficiently

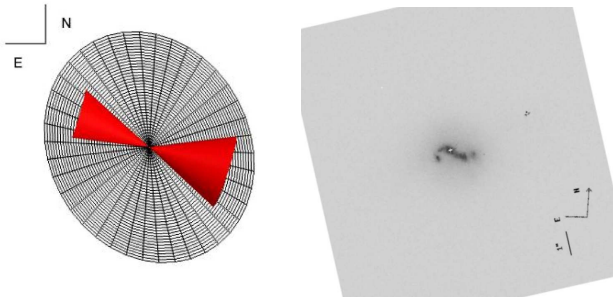

(a) Mrk 3 (Collins et al. 2005)

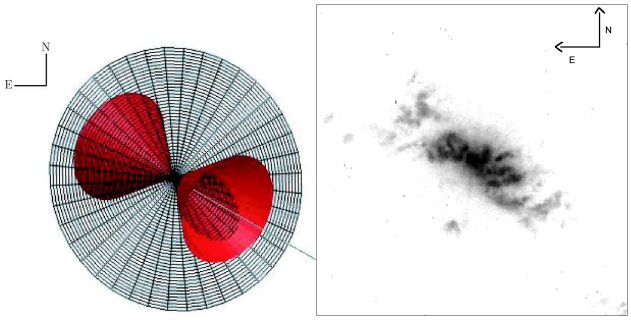

(b) NGC 4151 (Das et al. 2005)

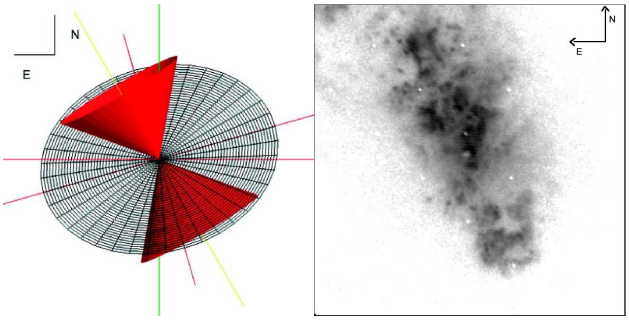

(c) NGC 1068 Das et al. (2006)

Figure 2.3: Geometrical NLR Models for Mrk 3 (Collins et al. 2005), NGC 4151 (Das et al. 2005) and NGC 1068 (Das et al. 2006), the right side shows *HST*/WFPC2 F502N images showing the NLR in the light of [O III].

Table 2.1: Visualization parameters for NGC 4151, NGC 1068 and Mrk 3

Object Name	Galaxy P.A.	Galaxy Incl.	Bicone P.A.	Bicone Incl.	Bicone Half Angle	Closer side of Gal. Disk	δ	β
(1)	(2)	(3)	(4)	(5)	(6)	(7)	(8)	(9)
MRK 3[c]	28	33	72	95	25	E	44	72
NGC 4151[a]	22	20	60	45	33	SW	38	36
NGC 1068[b]	106	40	30	95	40	NE	76	56

Notes: The columns 2–6 form the input parameters for the visualization program and 7–9 are the results. Bicone parameters constrained with kinematics from: Das et al. (2005), NGC 4151; Das et al. (2006), NGC 1068; (Collins et al. 2005), Mrk 3

thick inner galactic disk, will likely intersect the disk, leading to reddening of the NLR and formation of the ENLR as suggested by Evans et al. (1993).

Collins et al. (2005) observe an extinction gradient (Figure 2.4) in the NLR of Mrk 3 increasing from west to east (at position angle 71°) in both line and continuum emission of STIS UV spectra of Mrk 3. They infer from this reddening gradient that the host galaxy disk is tilted toward the observer in the east and the line of sight to the eastern cone intersects more dust in the plane of the galaxy than that to the western cone. The program presented here was used to visualize this geometry in the Mrk 3 nucleus and validate these conclusions of Collins et al. (2005).

In these few individual cases, we have shown that the NLR and host galaxy normal are not aligned, consistent with findings of Schmitt et al. (1997). Based on these studies of NLR orientations and estimates of reddening from UV spectroscopy, it is highly likely that NLRs in at least some intermediate (1.5, 1.8 and 1.9) Seyfert galaxies are reddened due to dust within the host galaxy. The outflow and orientation of the bicone with respect to the disk leads to a less-extincted view of the cone closest to us, which explains why integrated [O III] profiles are almost always blueshifted and/or

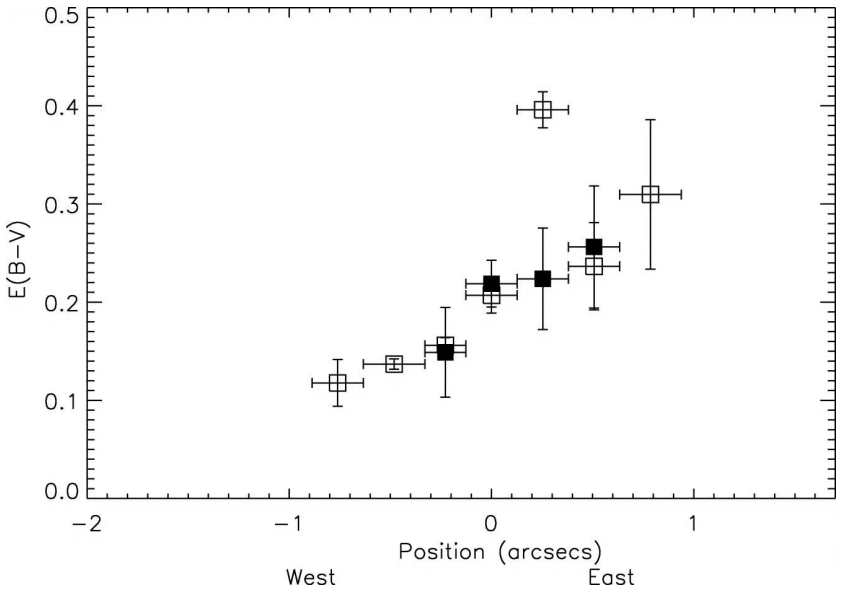

Figure 2.4: Extinction gradient within NLR of Mrk 3 along the slit (positioned NE to SW along the NLR), from west to east (Collins et al. 2005), compare with model of Mrk 3 in Figure 2.3. Vertical bars show the uncertainty in E(B - V), and horizontal bars show the angular size of the measured bin. Open squares represent redshifted components and filled squares represent blueshifted components. There is a clear extinction gradient increasing from west to east in the NLR.

asymmetric to the blue (Veilleux 1989; De Robertis & Shaw 1990; Rice et al. 2006).

Chapter 3

HST Imaging of Nuclear Spirals in NLS1s

An active nucleus needs a steady inflow of gas and dust to fuel the nuclear activity seen so evidently in all spectral ranges. What is the source of this fueling flow of gas and dust? The obvious answer is that it comes from the surrounding galaxy. But exactly how the SMBH is fueled is not yet clear. Based on analogy to Galactic stellar black holes, it is clear that the matter forms an accretion disk around the SMBH, but how it gets there is difficult to understand. The main difficulty in understanding the physical processes involved in fueling AGN is that the matter in the galaxy has a significant angular momentum. How the matter loses this angular momentum as it travels closer and closer to the SMBH is not known in detail.

3.1 Secondary bars and nuclear spirals

Two processes have been suggested for local AGN. One possibility involves tidal interactions and/or mergers with neighboring galaxies as suggested originally by Toomre & Toomre (1972) and Adams (1977). However, recent studies of environments of Seyfert galaxies (De Robertis et al. 1998, and

references therein) show no evidence for a statistical excess in number of companion galaxies or recent merger events in Seyfert galaxies compared to normal galaxies. Krongold et al. (2001) studied the host galaxies and environments of 26 NLS1s using digitized sky survey plates to look for the presence of companions that may induce heightened nuclear activity. They noted that the NLS1s show a paucity of companion galaxies (like Seyfert 1s). Another possibility that has received considerable attention is gas inflow along a stellar bar. Simkin et al. (1980) suggested that this could effectively drive large amounts of gas and dust to the central kiloparsec. Theoretical studies (Prendergast 1983; Shlosman et al. 1990; Athanassoula 1992) show that disk gas can get shocked along the leading edges of the stellar bar and thus lose angular momentum. This loss of angular momentum leads to inflow along the leading edges of the stellar bar. However most observational studies (Heckman 1980b; Simkin et al. 1980; Ho et al. 1997; Mulchaey & Regan 1997; Regan & Mulchaey 1999) have found similar fractions of large-scale stellar bars in Seyfert and normal galaxies. Crenshaw et al. (2003a) noted that the stellar bar fraction for Seyfert galaxies in these studies varied from $\sim 30\% - 80\%$, due to selection effects, such as whether samples contained luminous or average spirals. Further, bar classification suffers from confusion with weak oval structures in disks of spiral galaxies. Thus, while gas may be transported to inner kilo-parsec via large-scale stellar bars ($\gtrsim 1$ kpc), there are other factors that influence the further transport of gas to parsec scales.

The study of the central few tens of parsecs of nearby galaxies was only possible after the COSTAR corrected *HST* and the installation of the second generation of the Wide Field Planetary Camera (WFPC2). Until then, resolving structure in nuclei of nearby galaxies was very difficult from ground-based studies due to the glare of the central nucleus and limited resolution. The ability to model gas dynamics in the central parsec was also limited until the early 1990s due to computational limitations on the finest size of the grids in hydrodynamical models. Much progress has been made since then

and we summarize some of it below.

3.1.1 Secondary/Nuclear bars

Shlosman et al. (1990) suggested that the gravitational potential of a strong stellar bar can drive gas to within ~ 1 kpc of the active nucleus. They noted that the transport of gas will be halted at the inner Lindblad resonance (see, Figure 3.1) and the infalling gas will form a gaseous disk of matter inside the inner Lindblad resonance. The Lindblad resonances (the iILR, oILR and OLR markers in Figure 3.1) are the places in the host galaxy disk where the angular speed of the bar (Ω_p) equals the angular speed of the spiral arms ($\Omega \pm \kappa/2$ for a two-armed spiral, Binney & Merrifield 1998). As demonstrated in Figure 3.1, normally there are two resonances, one outer (the OLR) and one inner (the ILR). The outer resonance generally leads to formation of the outer ring observed in early-type galaxies. The inner resonance leads to formation of an inner ring of material in disk galaxies. At these resonances, the gas and dust pile up and that often leads to star formation. Often the inner Lindblad resonance is split into two resonances, the inner inner Lindblad resonance (iILR) and the outer inner Lindblad resonance (oILR). Buta & Combes (1996) present a comprehensive review of these resonance patterns in ordinary galaxies. It has been suggested (Maciejewski 2004b, and references therein) that AGN host galaxies may lack the iILR, thus favoring inflow of gas to the inner regions.

Shlosman et al. (1990) suggested that if there are non-axisymmetric gravitational instabilities in the gas disk within the inner kiloparsec, then a secondary gaseous bar pattern can develop on sub-kiloparsec scales. This may drive the gas down to scales of a few parsec. Maiolino et al. (2000) discovered a secondary bar-like structure within 100 pc of the nucleus of Circinus, the closest (~ 8 Mpc) Seyfert 2 galaxy. However, a search for gaseous secondary bars showed that these are not common and mini nuclear spirals are the dominant population (Regan & Mulchaey 1999; Martini & Pogge 1999;

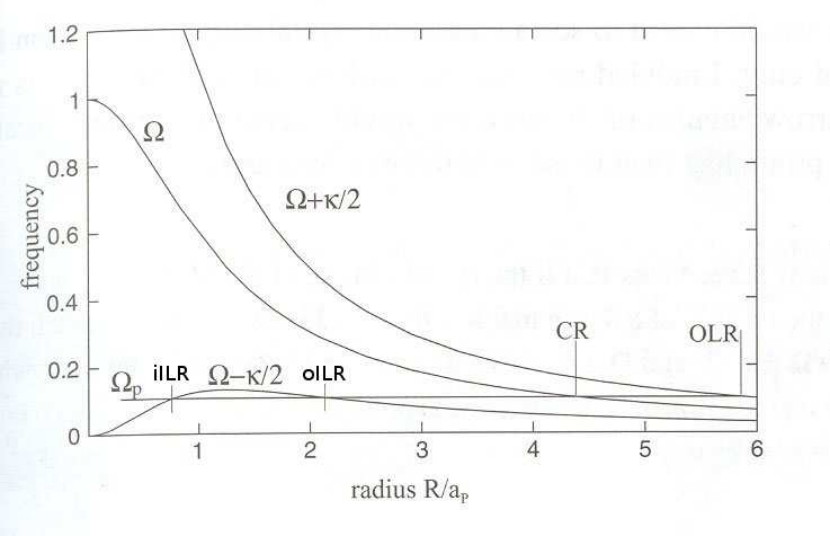

Figure 3.1: Lindblad Resonances in a two-armed spiral disk galaxy: OLR–Outer Lindblad Resonance, CR–Corotation radius of the bar rotating with angular speed Ω_p. Ω is the angular speed in the galaxy at a given characteristic radius R/a_p. $\Omega \pm \kappa/2$ gives the angular speeds of the spiral arms, where κ is the angular speed of the spiral pattern, a_p is the major axis of the bar pattern, and R is the radial distance from the galactic center.

Pogge & Martini 2002) at the centers of nearby Seyfert galaxies. It also appears that *stellar* secondary bars may not be that uncommon in normal galaxies (Erwin & Sparke 2002; Laine et al. 2002). For a review of the theoretical and observational studies of stellar secondary bars see Shlosman (2002). The current view seems to be that the nuclear dust disks within the inner kiloparsec may be self-gravitating and foster formation of stellar secondary bars; however, the response of the gas in the disk to the presence of the secondary stellar bar may be much different from its response to the large-scale bar. It is not clear yet whether the stellar secondary bar forms along with the nuclear dust spiral, but they are almost always associated with the presence of a large-scale bar. Further, their major axes are perpendicular to the major axis of large-scale bars.

3.1.2 Nuclear Spirals

As mentioned above, a search for gaseous secondary bars via dust absorption in nuclei of Seyfert galaxies revealed instead the presence of dusty nuclear spirals. Early studies with *HST* (Regan & Mulchaey 1999; Martini & Pogge 1999; Pogge & Martini 2002) used color maps and optical broad-band images to search for nuclear structures. These studies concentrated on Seyfert 2 galaxies (mainly the CFA sample) as the glare of the central nucleus is not present. Several of these studies used the *HST* Near-Infrared Camera and Multi-Object Spectrometer (NICMOS) images and WFPC2 optical broad-band images to form color maps to trace the dust distribution. Pogge & Martini (2002) used WFPC2 F606W[1] or F547M images and employed image-enhancement techniques to sharpen the structures in the inner kilo-parsec. They called this technique 'structure mapping'. We will describe this technique in detail later in this Chapter. Martini et al. (2003a) used a large sample of Seyfert 1s (24), Seyfert 2s (49), Liners (6) and inactive (44) galaxies from their HST program and showed that nuclear dust spirals are the most common type of morphology in the centers of Seyfert galaxies and normal galaxies alike. They classified the nuclear morphology into the following sub-classes: grand-design (two armed spirals, GD), tightly-wound spirals (multiarm spirals, TW), loosely-wound spirals (multiarm but not as tightly-wound, LW), chaotic spiral (single-armed or slightly chaotic spirals, CS), chaotic (amorphous with no clear spiral structure, C) and smooth disks with no dusty enhancements (N). Examples of their scheme are shown in Figure 3.2.

Further, Martini et al. (2003b) formed sub-samples of their original sample to remove selection effects due to host galaxy properties such as disk luminosity, inclination and Hubble type. Their main conclusion was that the grand-design and the loosely-wound nuclear dust spirals were associated with

[1]F606W is a wide-band optical filter on *HST* for WFPC2, while F547M is a medium-band optical filter.

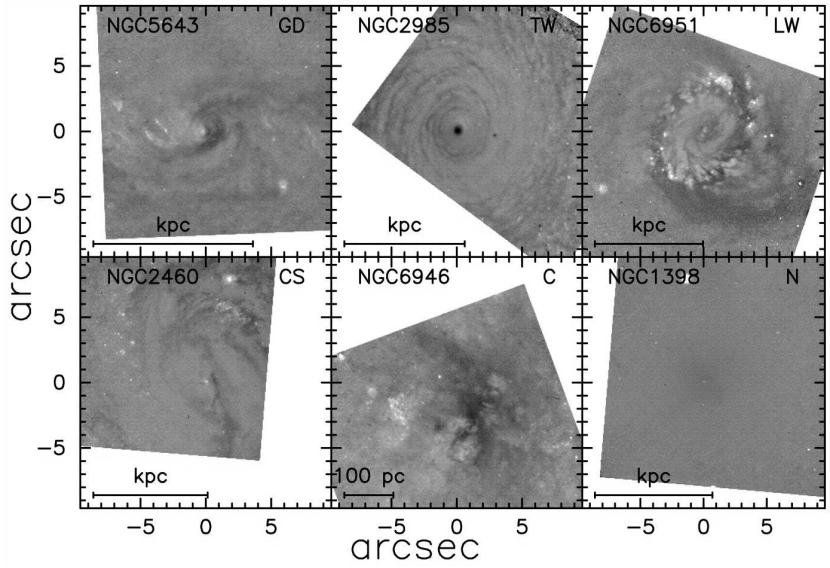

Figure 3.2: Examples of Nuclear Dust Morphology from Martini et al. (2003a): Dusty structures are dark and stellar emission is white. GD–Grand design, TW–Tightly Wound, LW–Loosely wound, CS–Chaotic Spiral, C–Chaotic/Amorphous dust structures, N–No obvious circumnuclear dust structure.

galaxies hosting large-scale bars, while the tightly-wound dust spirals were associated with galaxies that did not host large-scale bars. This difference confirmed earlier observations and theoretical calculations that the grand-design spirals are results of bar-driven inflow. The spiral arms in these GD dust spirals are extensions of the dusty leading edges of the large-scale stellar bars. Martini et al. (2003b) also note that there is a statistically significant excess of dusty structures within nuclei of Seyfert galaxies as compared to nuclei of inactive galaxies.

Hunt & Malkan (2004) use *HST*/NICMOS imaging of 250 active and inactive galaxies and argue that H II/starburst galaxies show the most disturbed morphology, while normal inactive galaxies and Liners show the least disturbed morphology in the circum-nuclear environment. They also show that Seyfert 2s have more disturbed isophotes than any other category of

galaxy and early-type Seyfert 2s are more disturbed than early-type Seyfert 1s. According to them, these morphological differences suggest that the differences between Seyfert 1s and Seyfert 2s are not simply due to orientation of the viewing angle to the central engine. Further, Hunt & Malkan (1999) showed that Seyferts and Liners together show a large fraction of resonance rings, with Liners showing inner rings more often than Seyferts, which show outer rings more often. Using this result, Hunt & Malkan (2004) propose that Liners may be 'starved AGN'. The inner ring at the ILR blocks the inflow of matter from the outer galaxy, thus effectively reducing the fueling rate for active nuclei in Liners. Further, Maciejewski (2004b) suggests that presence of a SMBH modifies the gravitational potential in the circumnuclear region enough to remove the presence of the inner Lindblad resonance in some galaxies. This effect will allow penetration of bar-driven spiral shocks deep into the nucleus and facilitate fueling. Current observational studies, however, have not yet shown if this is indeed the case.

These results are encouraging and indicate that fuel can be transported from scales of several kiloparsec to scales of a few parsec in Seyfert galaxies, but whether the grand-design spirals are efficient in transporting fuel is not clear yet. Neither it is clear how the gas inflow occurs in multi-arm tightly-wound spirals.

3.2 Narrow-line Seyfert 1s and AGN fueling

We saw in § 1.1.3 that Osterbrock & Pogge (1985) coined the term *Narrow-Line Seyfert 1s* (NLS1s) to denote Seyferts 1s with spectra generally like those of classical Seyfert 1s (strong Fe II, [O III] λ5007, λ4959 relatively weak compared to hydrogen Balmer series) but with permitted line widths much narrower than typical Seyfert 1s. Goodrich (1989b) specified that all NLS1s have FWHM(Hβ) < 2000 km s^{-1}. The PCA analysis of Boroson & Green (1992) confirmed that strong Fe II, weak [O III] and narrow Hβ lines are the

defining characteristics of the NLS1 class in the optical regime. The current paradigm to explain the nature of AGN activity in NLS1s is that the nuclei host SMBH of relatively modest mass ($\leq 10^7\ M_\odot$) that are being fed at or close to the Eddington accretion rate (Pounds et al. 1995). This view is supported by recent observational results that indicate that NLS1s possess significantly smaller black hole masses than their broad-line counterparts, and yet have luminosities similar to BLS1s (Mathur et al. 2001; Wandel 2002; Peterson et al. 2004). In this scenario, the narrow-line widths are simply due to the smaller black hole mass.

As we saw in the last section, in order to fuel an active nucleus, matter must be transported all the way from kiloparsec scales to the central engine. Thus the matter must lose almost all of its angular momentum via some process. One possibility involves mergers or tidal interactions with neighboring galaxies; however Krongold et al. (2001) showed that there is no significant difference between NLS1s and BLS1s and inactive galaxies in terms of companion objects. They suggested instead that the host galaxies of NLS1s are smaller in size and have smaller bulges indicating a smaller black hole mass.

Another process that has received considerable attention is gas inflow along a galactic stellar bar (Simkin et al. 1980). However most observational studies have found similar fractions of bars in Seyferts and normal galaxies (Heckman 1980b; Simkin et al. 1980; Ho et al. 1997; Mulchaey & Regan 1997; Mulchaey et al. 1997). Since there is strong evidence that most normal galaxies contain inactive SMBH (Kormendy & Richstone 1995), this indicates that while gas may be transported to the inner kiloparsec via large-scale stellar bars, there are other factors that contribute to the presence of nuclear activity. We saw in the last chapter that many imaging studies (Martini et al. 2003a, and references therein) with *HST* detected nuclear dust spirals instead of nuclear dust bars.

If the high accretion rate paradigm for NLS1s is correct, it suggests that the fueling of the AGN is more efficient in NLS1s than in their BLS1 counter-

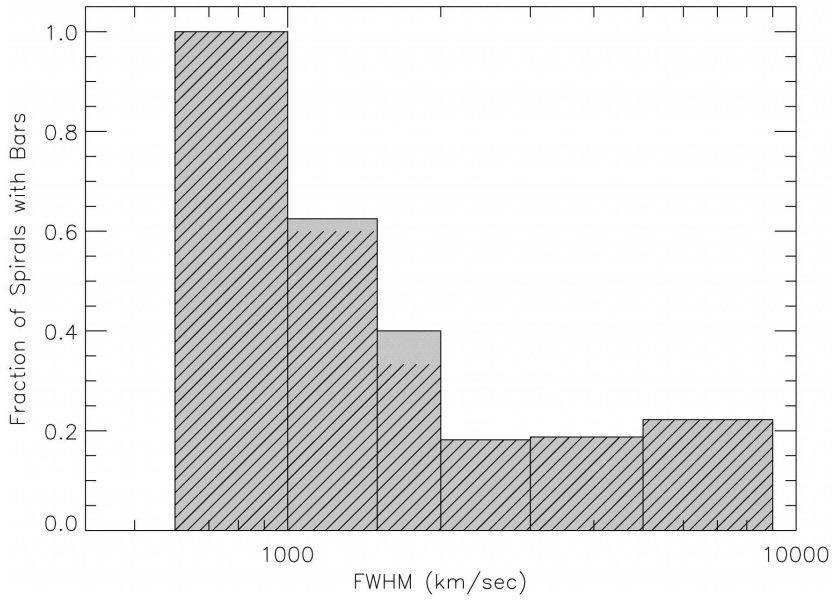

Figure 3.3: Histogram of the fraction of Seyfert 1s spirals with large-scale bars as a function of FWHM of the broad component of $H\beta$ from Crenshaw et al. (2003a). Shaded region is for the full sample in CKG03 and hatched region is for the sub-sample of 91 Seyfert 1s from Malkan et al. (1998). The dividing line between NLS1s and BLS1s is 2000 km s^{-1}.

parts. Crenshaw et al. (2003a) (hereafter, CKG03) showed that NLS1 nuclei are hosted mostly in barred Seyfert galaxies as compared to BLS1 nuclei: 65% of the NLS1s have bars, while only 25% of BLS1s have bars. This division is seen very nicely in their Figure 3 (reproduced here as Figure 3.3). These large-scale stellar bars typically begin at ~ 1 kpc from the nucleus and extend to $5-10$ kpc. However they did not study the inner regions (< 1 kpc) of the BLS1s and NLS1s, where establishing a connection between Seyfert 1 type and inner morphology would be even more crucial for understanding the fueling of the active nucleus.

The motivations for the research described here came from the need to understand the nuclear structures that exist within the central regions of NLS1s. There are no previous studies comparing NLS1 and BLS1 samples for differ-

ences in nuclear morphology. Several early studies (Martini & Pogge 1999; Regan & Mulchaey 1999) were focused mainly on Seyfert 1.8 to Seyfert 2 galaxies. Pogge & Martini (2002) and Martini et al. (2003a) included about equal numbers of Seyfert 1s and 2s and investigated the differences between Seyfert 1s and 2s. We note that in surveys of nuclear regions of both active and normal galaxies with *HST* (Martini & Pogge 1999; Regan & Mulchaey 1999; Pogge & Martini 2002; Martini et al. 2003b) and ground-based imaging studies (Erwin & Sparke 2002), it was found that nuclear dust spirals are seen in similar frequencies in *both* active as well as inactive galaxies. Further, Martini et al. (2003a) find that barred galaxies (either active or inactive) preferentially show a grand-design type of nuclear morphology, while unbarred ones show tightly-wound nuclear spirals. Since host galaxies of NLS1s are found to be barred from CKG03, we might expect to see grand-design as the preferred nuclear morphology for NLS1s. The results to be presented in this chapter have been published in Deo et al. (2006).

3.3 Sample Selection

Our sample contains the *HST* broadband (primarily F606W) Wide Field Planetary Camera 2 (WFPC2) images of Seyfert 1 galaxies obtained in the snapshot survey of Malkan et al. (1998). This is a uniform sample of 91 Seyfert 1 galaxies with $z \leq 0.039$. A typical exposure time for each snapshot was 500s, and nearly all of the galaxies were centered on the PC chip, which has a resolution element of $\sim 0.''1$. The galaxies with their properties are listed in Table 3.1.

The number of NLS1s in this sample is small (13/91); we excluded Mrk 335, as it appears as a point source in the WFPC2 image, leaving 12 NLS1s out of 91 Seyfert 1s. CKG03 had added five additional NLS1s at higher redshifts from the study of Véron-Cetty et al. (2001) (see Table 1 in CKG03). As we do not have enough resolution at distances of four of these objects to

study nuclear morphology, we did not consider them. We also exclude UGC 05025 which is a NLS1 with z of 0.026 as the F814W exposure time is just 80 secs and the nuclear region is not well exposed. However we note that this galaxy is barred. Some galaxies in the sample did not have their nuclear regions within the PC detector; following is a list of these: F1146 (WF2), PKS 0518-458 (WF4), WAS 45 (WF4), UM 614 (WF2). All of these galaxies are BLS1s and their lower resolution WF images do not have any appreciable impact on our final conclusions. Further, we decided to not include IR 1319-164 (BLS1) in our analysis as most of the galaxy is outside the PC chip in the WFPC2 field of view on the sawtooth side. Thus finally we ended up with 75 BLS1s and 12 NLS1s where nuclear morphology can be studied at the resolution afforded by the PC detector.

We compiled the redshift (z), major axis to minor axis ratio (b/a), the Hubble stage (T) and the absolute blue magnitude, (M_B^0) from the NASA Extra-galactic Database (NED) for the entire sample. The M_B^0 is computed from the corrected asymptotic blue magnitude B_T^0 (which is corrected for interstellar extinction and the K-correction). We used $B_T^0 - M_B^0 = 5 \log cz/H_0 + 25$, with $H_0 = 71$ km s^{-1} Mpc^{-1} (Spergel et al. 2003). The value of B_T^0 was not available in NED for some of the galaxies, so these galaxies do not have a M_B^0 value assigned in Table 3.1. There were galaxies for which we had to assign a value to the numerical Hubble stage index (T), this value was assigned by looking at the morphological classification given as part of the basic data for an object in NED and the table describing the coding of morphological types in the Third Reference Catalog of Bright Galaxies (de Vaucouleurs et al. 1991, hereafter RC3). We have also used The de Vaucouleurs Atlas of Galaxies (Buta et al. 2002, published by Cambridge University Press in 2006) to assign these values as the RC3 Catalog images were not available to us. The values of B_T^0 were selected only from RC3 for consistency. The axial ratios (b/a) were chosen from the RC3 data section provided in NED.

Table 3.1. Nuclear Morphology and Host Galaxy Parameters.

Name	Redshift	b/a^h	Hubble^h Stage	$M_B^{0\,h}$	Seyfert 1 Class	Large-scale Morph.	Nuclear Morph.
(1)	(2)	(3)	(4)	(5)	(6)	(7)	(8)
ESO 215-G14	0.019	0.70	3.0		BLS1	SB	DS (GD)
ESO 323-G77	0.015	0.67	-2.2	-20.92	BLS1	SB	DS (FL), NR
ESO 354-G4	0.033	0.82	2.7	-21.53	BLS1	S	DS (FL)
ESO 362-G18	0.013	0.67	-0.3	-20.12	BLS1	S	DS (FL)
ESO 438-G9	0.024	0.70	2.2	-21.41	BLS1	SB	DS (GD)
F 51	0.014	0.56	2.8	-20.20	BLS1	SB	DS (?)
F 1146[b]	0.032	0.62	3.0		BLS1	S	DL
HEAO 1-0307-730	0.028	0.50	1.0		BLS1	SB	ND
HEAO 1143-181	0.033	0.88	90.0		BLS1	I	A
HEAO 2106-099[d]	0.027	0.60	0.0		BLS1	P	ND
IC 1816	0.017	0.86	2.4	-20.62	BLS1	SB	DS (?)
IC 4218	0.019	0.23	1.0	-20.89	BLS1	S	DL
IC 4329A	0.016	0.29	-0.7	-20.51	BLS1	S	DL
IR 1249-131[f]	0.014	0.58	3.0		NLS1	S	DS (GD), NR
IR 1319-164[e]	0.017	0.80	3.0		BLS1	S	-
IR 1333-340	0.008	0.60	-2.0	-19.24	BLS1	S	DL
MCG 6-26-12	0.032	0.13	4.7		NLS1	SB	DS (GD)
MCG 8-11-11	0.020	0.71	1.0	-21.54	BLS1	SB	DS (?)
Mrk 6	0.019	0.63	-0.5	-20.05	BLS1	S	DL
Mrk 10	0.030	0.39	3.0	-22.62	BLS1	S	ND
Mrk 40	0.020	0.43	-2.0		BLS1	?	ND
Mrk 42	0.024	0.98	2.0	-20.00	NLS1	SB	DS (GD), NR
Mrk 50	0.023	0.60	-2.0	-20.05	BLS1	S	DS (FL)
Mrk 79	0.022	1.00	3.0	-21.52	BLS1	SB	DS (GD)
Mrk 279	0.031	0.56	-2.0	-21.15	BLS1	S	DS (FL)
Mrk 290	0.029	0.89	-5.0	-20.37	BLS1	E	ND
Mrk 334	0.022	0.70	99.0	-20.83	BLS1	S	DS (?), SBS
Mrk 335[d]	0.025	1.00	0.0		NLS1	P	-
Mrk 352	0.015	0.50	-2.0	-19.52	BLS1	E	ND
Mrk 359	0.017	0.83	0.0	-20.44	NLS1	SB	DS (GD)
Mrk 372	0.031	0.80	1.0	-21.23	BLS1	S	DS (FL)
Mrk 382	0.034	0.92	4.0	-20.94	NLS1	SB	DS (?)
Mrk 423	0.032	0.56	3.0	-21.01	BLS1	S	DS (FL)
Mrk 471	0.034	0.67	1.0	-21.57	BLS1	SB	DS (GD)
Mrk 493	0.031	0.83	3.0	-21.13	NLS1	SB	DS (GD), NR

Table 3.1—Continued

Name	Redshift	b/a^h	Hubble^h Stage	$M_B^{0\,h}$	Seyfert 1 Class	Large-scale Morph.	Nuclear Morph.
(1)	(2)	(3)	(4)	(5)	(6)	(7)	(8)
Mrk 516	0.028	0.83	4.0	-20.36	BLS1	S	DS (FL)
Mrk 530	0.029	0.67	3.0	-21.84	BLS1	S	DS (FL), NR
Mrk 543	0.026	1.00	6.0	-20.23	BLS1	S	DS (FL)
Mrk 590	0.027	0.91	1.3	-21.61	BLS1	S	DS (FL)
Mrk 595	0.028	0.68	1.0	-21.00	BLS1	S	DS (FL)
Mrk 609	0.032	0.90	1.0		BLS1	S	DS (FL)
Mrk 699^d	0.034	0.87	-4.0	-20.16	NLS1	E	ND
Mrk 704	0.029	0.57	1.0	-20.55	BLS1	SB	A
Mrk 744	0.010	0.59	1.0	-20.16	BLS1	S	DS (?), NR
Mrk 766	0.012	0.80	1.0	-19.73	NLS1	SB	DS (GD)
Mrk 817	0.033	1.00	4.0	-21.36	BLS1	SB	DS (GD)
Mrk 833	0.039	0.75	90.0		BLS1	I	A
Mrk 871	0.034	0.50	0.0	-21.29	BLS1	S	DL
Mrk 885	0.026	0.57	3.0	-20.41	BLS1	SB	DS (GD)
Mrk 896	0.027	0.73	3.0		NLS1	SB	DS (GD), NR
Mrk 915	0.025	0.30	3.0		BLS1	S	DS (GD)
Mrk 1040	0.016	0.21	4.0	-21.92	NLS1	S	DL
Mrk 1044	0.016	0.86	1.0		NLS1	SB	DS (FL), SBS
Mrk 1126	0.010	1.00	1.0		BLS1	SB	DS (GD)
Mrk 1218	0.028	0.50	3.0	-20.83	BLS1	SB	DS (GD)
Mrk 1330	0.009	0.74	3.0	-21.47	BLS1	SB	DS (GD)
Mrk 1376	0.007	0.24	1.0	-20.09	BLS1	S	DL
Mrk 1400	0.029	0.50	1.0		BLS1	S	DS (?)
Mrk 1469	0.031	0.36	3.0		BLS1	S	DL
MS 1110+2210	0.030	0.86	-4.0		BLS1	E	ND
NGC 235	0.022	0.54	-2.0	-20.87	BLS1	S	DS (FL)
NGC 526A	0.018	0.53	-2.0		BLS1	I	DL
NGC 1019	0.024	0.90	3.5	-20.86	BLS1	SB	DS (GD), NR
NGC 1566	0.004	0.80	4.0	-20.98	BLS1	S	DS (FL)
NGC 2639	0.011	0.61	1.0	-21.14	BLS1	S	DS (FL)
NGC 3227	0.003	0.67	1.0	-19.33	BLS1	SB	DL
NGC 3516	0.009	0.77	-2.0	-20.76	BLS1	SB	DL
NGC 3783	0.009	0.89	1.5	-20.86	BLS1	SB	DS (FL)
NGC 4051	0.002	0.75	4.0	-18.89	NLS1	SB	DS (GD)
NGC 4235	0.007	0.21	1.0	-20.46	BLS1	S	DL

Table 3.1—Continued

Name (1)	Redshift (2)	b/a^h (3)	Hubble^h Stage (4)	$M_B^{0\,h}$ (5)	Seyfert 1 Class (6)	Large-scale Morph. (7)	Nuclear Morph. (8)
NGC 5252	0.022	0.56	-2.0	-20.91	BLS1	S	DS (?)
NGC 5548	0.017	0.93	0.0	-21.47	BLS1	S	DS (FL)
NGC 5674	0.025	0.91	5.0	-21.55	BLS1	SB	DS (GD)
NGC 5940	0.033	1.00	2.0	-21.60	BLS1	SB	DS (GD)
NGC 6104	0.028	0.82	3.0	-21.39	BLS1	SB	DS (?)
NGC 6212	0.030	0.76	3.0	-20.58	BLS1	S	DS (FL), NR
NGC 6860	0.015	0.62	2.6	-20.80	BLS1	S	DS (FL)
NGC 7213	0.006	0.90	1.0	-20.89	BLS1	S	DS (FL)
NGC 7314	0.006	0.46	4.0	-20.93	BLS1	S	DS (FL)
NGC 7469	0.017	0.73	1.0	-21.64	BLS1	S	DS (?), NR
II SZ 10[g]	0.034	0.60	4.0		BLS1	S	ND
PKS 0518-458[c]	0.034	0.69	-2.0	-19.84	BLS1	E	ND
TOL 1059+105	0.034	0.45	-1.0	-20.66	BLS1	S	ND
TOL 2327-027	0.033	0.68	2.7		BLS1	SB	DS (GD), NR
UM 146	0.017	0.77	3.0	-20.42	BLS1	S	DS (?)
UGC 3223	0.018	0.57	1.0	-21.32	BLS1	SB	DS (FL)
WAS 45[c]	0.024	1.00	3.0	-20.92	BLS1	SB	DS (GD), NR
UGC 10683B	0.031	0.50	1.0		BLS1	SB	DS (?)
UGC 12138	0.025	0.88	1.0	-21.33	BLS1	SB	DS (GD)
UM 614[b]	0.033	0.52	-1.0	-20.88	BLS1	S	ND
X 0459+034[a]	0.016	0.82	-4.0		BLS1	E	A

Note. — All images except as noted were taken with F606W filter. Large-scale galactic morphology classes are, S: spiral, SB: barred spiral, E: elliptical, I: irregular, P: point source and ?: not classified. Primary nuclear morphology classes are, ND: no significant dust, DS: dust spiral, DB: dust bar, A: amorphous structures, DL: large-scale dust lane, NR: Nuclear Ring and SBS: Star-burst (nuclear) Spiral. Secondary nuclear morphology classes are; GD: grand-design spiral, FL: flocculent multi-arm spiral and ?: for no secondary classification.

[a]Observed with the F814W filter.

[b]Galaxy positioned in WF2 chip

[c]Galaxy positioned in WF4 chip

[d]Not included in Figure 3.5.

[e]Excluded from analysis, see § 3.3.

[f]Other name: NGC4748

[g]The MAST fits header entry for this galaxy mentions it as II ZW 10 which is incorrect.

[h]Data values were selected from NED for these columns. Some values for the Hubble stage T were reassigned using classifications from The de Vaucouleurs Atlas of Galaxies (Buta et al. 2002). The coding of morphological types is given in Table B.1.

Table 3.2. Host Galaxy Properties of the Sample.

Parameter	All (87) Median	All (87) Mean	All (87) σ	NLS1 (12/87) Median	NLS1 (12/87) Mean	NLS1 (12/87) σ	BLS1 (75/87) Median	BLS1 (75/87) Mean	BLS1 (75/87) σ
Redshift (z)	0.024	0.022	0.01	0.024	0.022	0.01	0.024	0.023	0.01
Inclination i (deg.)	46.37	43.70	19.36	36.87	41.58	20.92	47.93	44.31	18.87
Hubble Stage (T)	1.0	1.3	2.3	3.0	2.1	2.4	1.0	1.2	2.3
M_B^0 (mag.)	-20.88	-20.80	0.69	-20.16	-20.40	0.93	-20.89	-20.86	0.64

Table 3.1 shows our sample and its properties. The first column gives the name of the galaxy, the second column gives the redshift of the galaxy from CKG03, and the third column gives the RC3 axial ratio (b/a). The fourth column gives the numerical Hubble stage index (T). The fifth column gives the corrected absolute blue magnitude (M_B^0) computed as given above. The sixth column gives the Seyfert 1 class, *i.e.,* whether the galaxy is a NLS1 or a BLS1. The seventh column gives the large-scale morphology as classified in this study. The eighth column gives the nuclear morphology classification for each galaxy (these are explained later in this chapter). Three galaxies had main morphology classifications that could not be defined. These are HEAO 2106-098 (point source), Mrk 40 (?) and Mrk 335 (point source). IR 1319-164 was not included in the analysis as most of the galaxy is outside the PC field of view. This resulted in a sample of 87 Seyfert 1s where both large-scale and nuclear structures could be classified.

We tested the sample for selection biases that may have been introduced due to the heterogeneous nature of our sample. Figure 3.4 shows the histogram of the four host galaxy parameters. The histogram with solid boundary line shows the BLS1 sample (75/87 objects), while the shaded histogram with dashed boundary line shows the NLS1 sample (12/87 objects). In Table 3.2 we list the representative numbers that describe the sample. The spreads (σ) reported are standard deviations for the sample in question.

The sample as a whole (87 Seyfert 1s) has a median Hubble stage index of 1.0, moderately high inclinations of 46.37^o and median redshift of 0.024. When we break up the sample into NLS1s and BLS1s based on their H_β

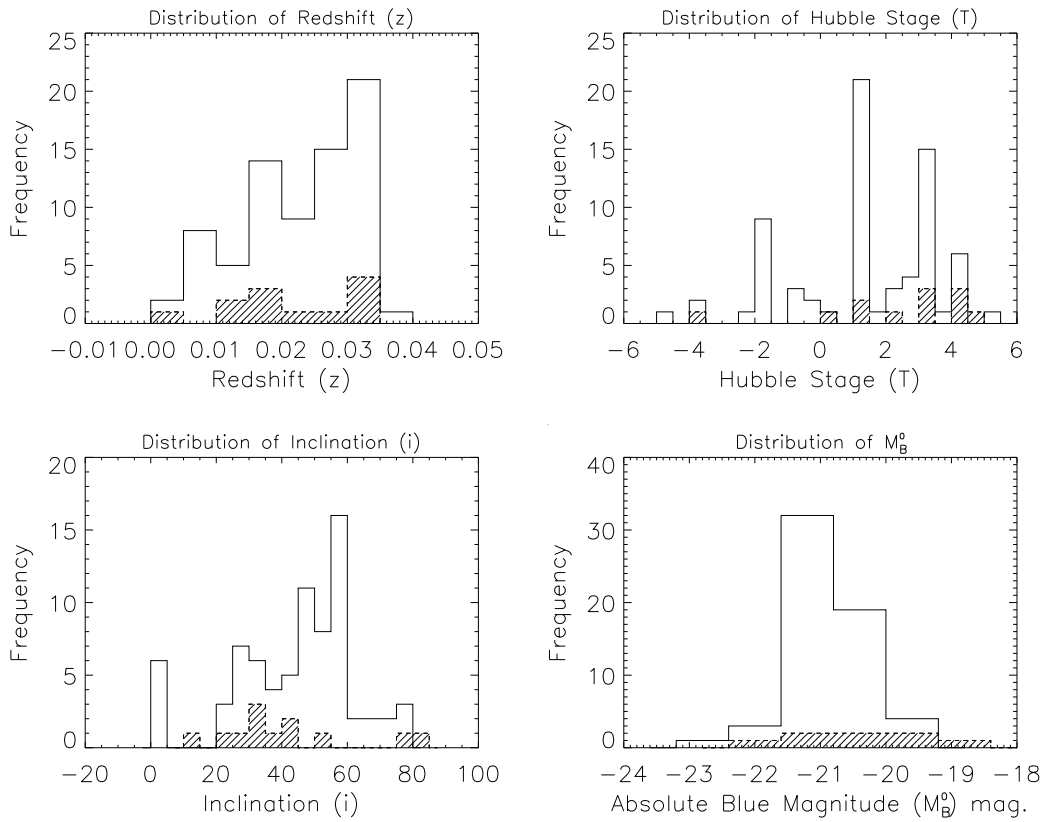

Figure 3.4: Host Galaxy Properties of the Sample: Histograms of four host galaxy parameters: the redshift (z), the galaxy inclination (i) in degrees, numerical Hubble stage index (T) and the absolute blue magnitude (M_B^0) for the NLS1 (shaded histogram) *vs.* BLS1 sample.

FWHM, we see that the NLS1s are slightly more face-on and have a median T of 3.0 as compared to BLS1s which are more edge-on and have a median T of 1.0. The NLS1s are also 0.73 mag. less luminous than BLS1s in the median, which is close to the standard deviation of both groups. All of the differences are smaller than the quoted spreads of the sample. However, we discuss their possible impact towards the end of § 3.5.

3.4 Image Analysis and Classification

We retrieved raw images from the *HST* archives, which were calibrated with the standard HST pipeline. Since this was a snapshot survey, we only had single frames per galaxy and hence we employed a routine written in IDL to detect and remove cosmic rays. This routine is written specifically for handling WFPC2 data and is tuned for the PC chip. The routine scans the input image for pixels affected by cosmic rays and iteratively discards them, replacing them with average values of pixels in a box centered on the pixel being discarded. The routine also estimates the sky background simultaneously by selecting various peripheral sections of the input image. This option can be turned off in case the galaxy covers the whole PC detector, which is the case for most images. Various parameters of the routine control the selection of scanning box size and how to distinguish a faint star from a cosmic ray hit. We also replaced bright foreground stars within the image with a square area from the opposite side of the image, with the line joining the two sections passing through the center of the galaxy. We made sure that none of these areas contained any dust structures. It should be noted that none of these foreground stars were close to the centers of the galaxies being studied. This process was required so that the image enhancement process used (see ahead) would not be affected by the presence of areas of large intensity apart from the central point source. Since we are looking for dust structures near the nuclear source in Seyfert 1s, the cleaner the image, the better the contrast enhancement. Residual cosmic rays were examined and cleaned by eye using a combination of IRAF and IDL tools.

We have employed the method used by Pogge & Martini (2002) to enhance the contrast of dusty structures. This process has been called "structure mapping" and is based on the Richardson-Lucy (R-L) deconvolution process. It highlights marginally resolved structures, as the first-order smooth structures are removed. One starts with a good estimate of the *HST* point spread function (PSF, tuned for the WFPC2 CCD detectors) and uses it to

perform an operation similar to unsharp masking via division. One divides the original image with a PSF-convolved version of the original image, finally multiplying the resulting image with the transpose of the PSF. This operation is shown below.

$$\text{Structure Map} = \frac{\text{Image}}{\text{Image} \otimes \text{PSF}} \otimes \text{PSF}^t \tag{3.1}$$

where PSF^t is the transpose of the PSF and the $\otimes$ represents a convolution operation. The convolutions can be done efficiently in Fourier space with FFTs and we implemented a simple IDL routine to perform the above operations. This results in an image which contains the high spatial frequency components enhanced in contrast. The resultant image forms the second-iteration corrector image in a R-L deconvolution process (see Pogge & Martini 2002). It is crucial that a properly matched PSF be used to generate these structure maps. Thus, custom WFPC2 PSFs were required for each snapshot image.

We used 2-D Gaussian fits to the saturated cores of the Seyfert 1s to determine the location of the central source on the chip, and then generated the PSFs by using the TinyTim software (Krist & Hook 1999). The form of the *HST* WFPC2 PSF depends on the following parameters in order of importance: (1) filter used for the observations (*e.g.,* F606W), (2) the location on the WF or PC detector, (3) the secondary mirror focus position, and (4) the color of the object being observed. The latter two parameters were not of great importance, as the final structure map did not show significant improvement in quality when these parameters were tweaked. Most of the galaxy centers were not near any of the available observed stellar PSFs for WFPC2 from the MAST archives, hence using TinyTim was the only way to get reasonable PSFs.

PSF subtraction of the central point source was also attempted but we decided to not use the resulting images to construct structure maps. To attempt subtraction, the artificial PSFs where scaled to the intensity of the

central source (estimated via Gaussian fits) and then embedded in image sections the same size as the original image being worked on. Artificial random noise was added to these image sections to mimic the background noise in the real images. Many images had saturated cores and we estimated best fit 2-D profiles by looking at 1-D cross-sections through the core and fitting the wings to estimate the intensity scale factor. The fits were also judged based on the quality of output structure maps. Since the structure maps are quite sensitive to large variations in brightness levels in pixels, performing PSF subtraction and then forming a structure map from the resulting image was not practical.

Examples of final processed structure maps are shown in Figure 3.5 and Figure 3.6. The structure maps for the entire sample are presented in Appendix B along with the reasoning for individual nuclear classifications.

For each galaxy, we construct the structure map of a 600 $\times$ 600 pixel region of the PC chip, which avoids the over-scan regions. Each figure shows the nuclear regions of the structure maps zoomed to appropriate size to facilitate display of nuclear structure. Each image shows the size of the region in arc-seconds on the vertical axis, as well as the corresponding projected size of the image in kiloparsecs (assuming $H_0 = 71$ km s^{-1} Mpc^{-1}, see Spergel et al. 2003) in the top title. The structure map images are bounded by lower and upper thresholds to display faint structures properly. The images are also color inverted. Dusty, high extinction areas appear white, while emission regions appear dark. Compass markers indicate the North and East directions on the image. The color bar at the bottom is provided as a guide to how the brightness and contrast of the image was stretched between the applied upper and lower thresholds.

3.4.1 Nuclear Morphology Classification

Prof. Crenshaw and I independently classified the nuclear structures within $\sim$ 1 kpc without prior knowledge of the Seyfert type (*i.e.,* BLS1 or NLS1)

or the main galaxy morphology. We looked at the original image as well as the structure map in the process. We chose the following notation for our classification: DS for nuclear dust spiral, DB for nuclear dust bar, A for amorphous dust clouds, DL for large-scale dust lane passing in front of the central source and ND for no significant dust structure. We also noticed that several galaxies showed star-forming rings inside the central kiloparsec and in two cases (Mrk 334 and Mrk 1044), star-forming nuclear spiral arms. We called the starburst nuclear spirals SBS and the nuclear rings NR. Further, we classified the dust spirals (DS) into two secondary classes: GD for two arm grand-design spirals and FL for flocculent multi-armed spirals. The nuclear dust spirals which could not be classified into these two classes were bunched together with the notation "?" for their secondary classification. We call a nuclear dust spiral "grand-design" (GD) if it has two distinct symmetric dust spiral arms. Examples (see Figure B.1) include Mrk 1126, Mrk 42 and Mrk 766. TOL 2327-027 is a spectacular example of this class. The flocculent dust spirals (FL) were defined to be those that showed more than two distinct spiral arms peppered with puffy gas and dust clouds. This class essentially bunches together the classes TW and LW from Martini et al. (2003a). Examples of this class include: ESO 323-G77, ESO 354-G4, Mrk 1330, Mrk 590 and Mrk 609. NGC 2639 is a good example of the multi-arm nature of these spirals. There were other cases with only a single dust arm visible (*e.g.,* MCG8-11-11, NGC 6104, Mrk 744), where the galaxy has a high inclination that prevented a clean classification (*e.g.,* F51), or where the image showed slightly chaotic grand-design like structure with a hint of a dust bar-like structure (*e.g.,* IC 1816, Mrk 334, UM146). These were not given any special secondary classification and were grouped together in a category called "?". Our class A (amorphous) corresponds to class C (for chaotic) from Martini et al. (2003a). In the final classification, we cross-checked and reassigned appropriate classes to the few cases where we originally disagreed. Appendix B lists all the galaxies, their nuclear classification and a summary

of main features noted in the images.

Also, during the classification process we noticed that a few of the galaxies had been previously classified as a spiral (class S) in CKG03, when on inspection of structure-mapped images and WFPC2 mosaics, we realized that they were barred spirals (class SB). For example, in the PC2 image of ESO 215-G44 in Malkan et al. (1998), the large-scale bar is not obvious, but can be seen clearly in a structure map. Other such cases have been recorded in the Appendix. These galaxies have since been reclassified as SB in Table 3.1. In CKG03, they had concluded that excluding point sources, ellipticals, irregular and unclassified (main morphology class) galaxies (12 out of 97): 34% (29/85) of spiral Seyfert 1s are barred, and of these 65% (11/17) of NLS1s are barred, and 26% (18/68) of BLS1s are barred, indicating a high fraction of barred host galaxies for NLS1s. With our revised classification, we now conclude from the CKG03 sample of 97 Seyfert 1s that, excluding point sources, ellipticals, irregular and unclassified (main morphology class) galaxies (12 out of 97), we now have: 47% (40/85) of spiral Seyfert 1s are barred, 76% (13/17) of NLS1 host galaxies are barred and 40% (27/68) of BLS1 host galaxies are barred. Thus the incidence of large-scale bars in NLS1s is still much larger than that in BLS1s.

3.5 Results

In Table 3.1, we give the results of our nuclear dust classifications. Column 7 gives the large-scale morphology based on the structure maps and WFPC2 mosaic images (see CKG03 for the original classifications). Column 8 gives the nuclear morphology classification for each galaxy. Within the parenthesis in column 8 is the secondary nuclear classification. Galaxies that were not given a formal secondary dust spiral classification are included in the category "?".

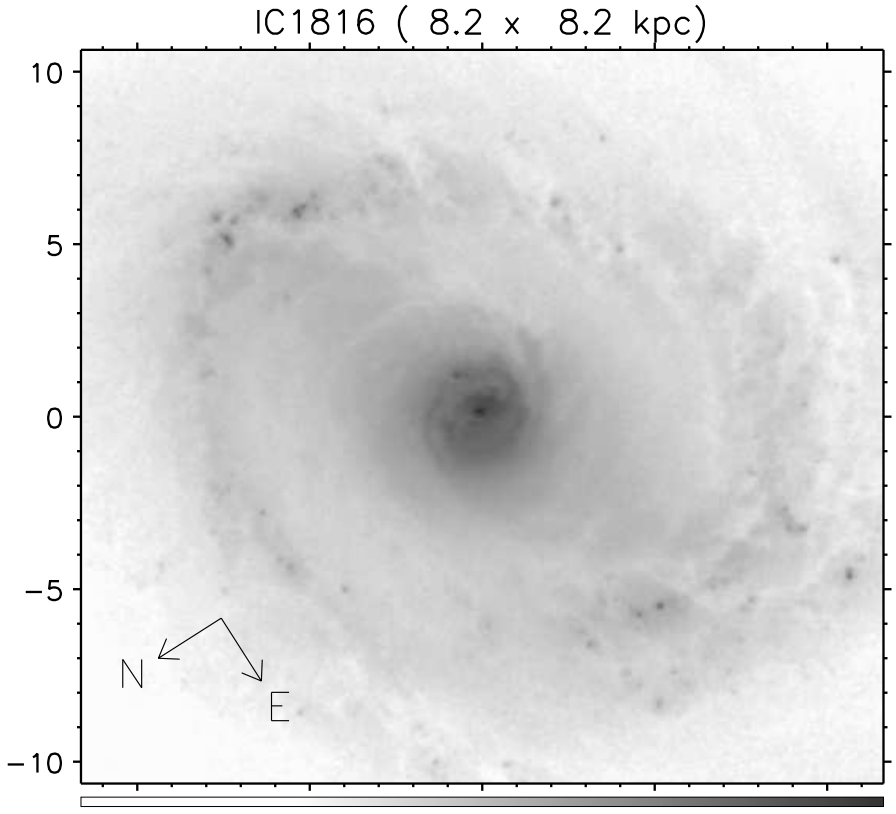

Figure 3.5: Representative Structure Maps of Seyfert 1s and classification of their nuclear dust structures; light areas are dusty, dark areas are stellar emission. Shown above is IC 1816, a grand-design dust spiral (Category: GD).

Table 3.3. Frequency of Primary Nuclear Dust Structures

Galaxy Class[a]	No Dust	Dust Spiral[c]	Dust Bar	Amorph.	Dust Lane	Nuclear[d] Ring
Seyfert 1s (87)[b]	0.11 (10 ± 3.0)	0.69 (60 ± 4.3)	0.00 (0)	0.05 (4 ± 2.0)	0.15 (13 ± 3.3)	0.16 (14 ± 3.4)
NLS1s (12)	0.08 (1 ± 1.0)	0.83 (10 ± 1.3)	0.00 (0)	0.00 (0)	0.08 (1 ± 1.0)	0.42 (5 ± 1.7)
BLS1s (75)	0.12 (9 ± 2.8)	0.67 (50 ± 4.1)	0.00 (0)	0.05 (4 ± 2.0)	0.16 (12 ± 3.2)	0.12 (9 ± 2.8)
Barred Spirals (36)	0.03 (1 ± 1.0)	0.89 (32 ± 1.9)	0.00 (0)	0.03 (1 ± 1.0)	0.06 (2 ± 1.4)	0.32 (8 ± 2.5)
Spirals (42)	0.10 (4 ± 1.9)	0.67 (28 ± 3.1)	0.00 (0)	0.00 (0)	0.24 (10 ± 2.8)	0.11 (6 ± 2.3)

[a]Given as fractions; number of galaxies in each group is given in parenthesis, along with binomial errors.

[b]Out of a total of 91 Seyferts, 87 have both nuclear and large-scale morphological type defined.

[c]Dust spirals are further classified into Grand Design and Flocculent types, see Table 3.4.

[d]The nuclear ring category also includes the two nuclear spirals showing starburst spiral arms, Mrk 334 and Mrk 1044, for simplicity.

Table 3.4. Frequency of Nuclear Dust Spirals and Starburst Rings

Galaxy Class[c]	Nuclear Spiral Morphology[a] Grand Design[b]	Flocculent[b]	Undefined[b]
Seyfert 1s (60)	0.40 (24 ± 4.0)	0.40 (24 ± 3.8)	0.20 (12 ± 3.1)
NLS1s (10)	0.80 (8 ± 1.3)	0.10 (1 ± 1.0)	0.10 (1 ± 1.0)
BLS1s (50)	0.32 (16 ± 3.3)	0.46 (23 ± 3.5)	0.22 (11 ± 2.9)
Barred Spirals (32)	0.69 (22 ± 2.6)	0.12 (4 ± 1.9)	0.19 (6 ± 2.2)
Spirals (28)	0.07 (2 ± 1.4)	0.71 (20 ± 2.4)	0.21 (6 ± 2.2)

[a]Given as fractions; number of galaxies in each group is given in parenthesis, along with binomial errors.

[b]Nuclear spiral classification: these are galaxies that show dust spirals as their primary nuclear morphology.

[c]The numbers in parenthesis in this column come from column 3 in Table 3.3, *e.g.,* out of 87 Seyfert 1s in Table 3.3, 60 have dust spirals.

Table 3.3 and Table 3.4 shows the frequencies of these classes as fractions; number counts for galaxies are given in parenthesis along with one sigma uncertainties assuming a binomial distribution (since all the classes are independent and each structure is either present in the galaxy or not). The distributions are given for the entire sample of 87 Seyfert 1s, as a function of class (NLS1 *vs.* BLS1) and as a function of the host galaxy morphology (barred spirals *vs.* unbarred spirals). Table 3.4 shows the distributions for GD, FL and the undefined ("?") categories of dust spirals. All of the entries in this table come from the galaxies that show dust spirals (Table 3.3, column 3) as their primary nuclear morphology.

Figure 3.7 shows bar plots for each class of nuclear structure. For each graph, the vertical axis is frequency of the structure and the horizontal axis has the various classes as in Table 3.3. On the top of each bar is the fraction corresponding to the class being presented. The plots compare barred *vs.* unbarred Seyfert galaxies and NLS1s *vs.* BLS1s.

We do not see nuclear dust bars, in agreement with Pogge & Martini (2002). Erwin & Sparke (2002, 2003) demonstrate how stellar secondary bars can be uniquely identified with help of isophotal analysis and unsharp-masking. Since structure mapping is similar to unsharp-masking, we could

have noticed the presence of secondary stellar bars, but we did not detect any.

Table 3.3 and Figure 3.7 show that 83% of NLS1s and 67% of BLS1s have nuclear dust spirals, implying that nuclear spirals are the favored morphological features, in agreement with Martini et al. (2003b). In Table 3.4, we see that 80% (8/10) of NLS1s with nuclear dust spirals have grand-design type nuclear spirals as compared to 32% (16/50) for BLS1s with nuclear dust spirals. We also see that 69% (22/32) of barred spirals with nuclear dust spirals have grand-design structure, compared to 7% (2/28) in the unbarred spirals. Since the sample of Seyferts with barred galaxy morphology is more than doubled by adding barred BLS1 (27/75) to the NLS1 (9/12) sample, and yet the percentage of grand-design nuclear dust spirals (22/32, 69% of barred Seyfert 1 sample with dust spirals) remains almost the same as for NLS1s (8/12, 67%), we conclude that large-scale stellar bars are the principal driver of the grand-design dust structure. Even though we have only 12 NLS1s in our sample, 9 are barred and we see that 8 of them show grand-design nuclear dust spirals. This lends support to the idea that higher fueling rates in NLS1s are helped by the transfer of gas on a kiloparsec scale via large-scale stellar bars that almost always form grand-design dust spirals within 1 kpc of the nuclei of NLS1s.

During the classification process for nuclear dust structures, we noticed that several galaxies in our sample showed nuclear star formation in the form of stellar nuclear rings or star-forming nuclear spiral arms. ESO 323-G77, IR 1249-131, Mrk 42, Mrk 493, Mrk 530, Mrk 744, Mrk 896, Mrk 1044, NGC 1019, NGC 6212, NGC 7469, TOL 2327-027 and WAS 45 show nuclear star-burst rings (see Figure 3.5). Mrk 334 and Mrk 1044 show nuclear spiral arms with star forming sites embedded in them. Table 3.3 and bar plots in Figure 3.7 show that 42% (5/12) of NLS1s show recent star-formation in nuclear rings. One out of these (Mrk 1044) has star formation in the nuclear spiral instead of the nuclear ring. In comparison only 12% (9/75) BLS1s

show recent nuclear star formation in the form of nuclear rings. Again only one (Mrk 334) shows star formation in the nuclear spiral arms. We have not missed any inner stellar rings due to the presence of luminous point sources, unless they are very small. The size of the saturated point source is typically much less than 0.″5 and at a median z of 0.024; 0.″5 (about 10 pixels) corresponds to about 245 pc. We note that all galaxies that host stellar nuclear rings also show grand-design dust spirals and are barred galaxies; see the NR category in Figure 3.9.

As mentioned previously, the NLS1s and BLS1s in our sample show slight differences in their luminosities (0.73 mag.), inclinations (11.1°) and Hubble stage (2 stages). It is unlikely that these differences have an impact on our ability to detect the nuclear dust morphology and the presence of nuclear rings.

As we have discussed, both observational and theoretical studies show that the presence or absence of a large-scale stellar bar is the principal driver in determining the nuclear morphology. Since it is difficult to detect large-scale bars in highly inclined systems, we tested the robustness of our results by excluding galaxies with inclinations greater than 60°. With this constraint, we have 10 NLS1s and 66 BLS1s. From this reduced sample, 9 out of 10 NLS1s (90%) have nuclear dust spirals. Out of these 9 dust spirals, 7 are grand-design (77%) and one flocculent (11%). In comparison, out of 66 BLS1s, 48 (73%) show nuclear dust spirals, 15 (23%) of these are grand-designs, while 22 (33%) are flocculents. Further, 8/10 (80%) NLS1s are barred compared to 27/66 (41%) BLS1s, showing that NLS1s are more barred than BLS1s as for the whole sample. Of the total of 35 barred galaxies in this reduced sample of 76 galaxies, 21 (60%) have grand-design nuclear spirals, while 4 (11%) are flocculents. Of the 32 unbarred galaxies in this reduced sample, 19 (59%) show flocculent nuclear spiral, while one shows grand-design (3%). Further, 5/10 (50%) NLS1s show nuclear rings, while

only 9/66 (14%) of BLS1s show nuclear rings. Thus the difference in inclination does not seem to contribute to a selection bias for bars.

We noted above that NLS1 and BLS1 samples differ in their absolute blue magnitudes. We suppress the contribution of the nuclear point source when creating the structure maps. Any residual contribution to the magnitude due to the Hubble type of the galaxy or the nature of its bulge will be very much smaller than the initial luminosity difference present in the original image between the point source and the rest of the galaxy. Thus our ability to detect faint dusty structures near point sources has not been affected by the intrinsic magnitude differences between the NLS1 and BLS1 host galaxies.

In conclusion, the trends we see in our original sample of 87 galaxies seem to be robust against small variations in the host galaxy parameters.

3.6 Implications

Our analysis shows that the grand-design nuclear dust spirals are largely present in barred galaxies, which is consistent with previous studies. We have also found that NLS1 galaxies, which are thought to have relatively high accretion rates, tend to show large-scale stellar bars, nuclear rings and grand-design nuclear spirals, which are thought to promote or indicate high fueling rates into the nucleus.

Are grand-design nuclear spirals indeed more efficient in fueling the central nucleus? Here we summarize from the literature the theoretical efforts to answer this question. The linear density wave theory (Goldreich & Tremaine 1978, 1979) forms the theoretical underpinnings of hydrodynamical simulations of gas inflow in barred galaxies. Englmaier & Shlosman (2000) showed that the morphology of the nuclear gas/dust spiral depends on two factors: central mass concentration and sound speed in the gas (*i.e.,* gravitational potential and amount of turbulence present in the gas disk). The pitch angle (angle between the spiral arm and a tangent to a circle intersecting

with the spiral arm at radius R) of the spiral is thus dependent on these two factors and ideally one can probe these factors based on the morphological features of the nuclear disk. We note that such a study has not been done so far. In the presence of a large-scale stellar bar potential, the hydrodynamical simulations from several studies (Englmaier & Shlosman 2000; Patsis & Athanassoula 2000; Jogee et al. 2002; Maciejewski et al. 2002; Maciejewski 2004a,b) show that inflows along leading-edges of the stellar bars form "grand-design" type spiral structures in the central kiloparsec. It seems from the discussions in these papers that the presence of the large-scale stellar bar potential overwhelms the effects of the nuclear gravitational potential and turbulence throughout most of the central kiloparsec. This effect is reflected in the tendency of tightly-wound nuclear spirals to avoid barred galaxies, in agreement with our observations (see FL category in Figure 3.10). The merging of grand-design nuclear spiral arms with the leading-edge bar shocks indicates that the nuclear spiral is not decoupled from the large-scale stellar bar, and that the nuclear spiral pattern is *maintained* by the bar potential.

Maciejewski et al. (2002) show that the velocity field of the gas in grand-design nuclear spirals has a large negative divergence. This is indicative of strong shocks along the curving dust lanes, which are needed to drive gas down to the scale of tens of parsecs. The merging of grand-design spiral arms with leading edges of large-scale bars occurs regardless of underlying nuclear potential or sound speed in gas, hinting at the importance of large-scale bars in driving the grand-design nuclear spiral. Simulations of Maciejewski (2004b) indicate that the average inflow rates at $\sim$ 1 kpc are $\sim 0.7\ M_{\odot}\ \mathrm{yr}^{-1}$, at 250 pc, they decrease to $\sim 0.2\ M_{\odot}\ \mathrm{yr}^{-1}$, and at a distance of 40 pc they are $\sim 0.03\ M_{\odot}\ \mathrm{yr}^{-1}$ in models with both a central SMBH of $10^8\ M_{\odot}$ and a large-scale stellar bar. The inflow at distances of 40 pc is reported to be $\sim$ 20 times smaller in models without a black hole. In the absence of a secondary bar on scales of hundreds of parsecs, one probably needs a strong primary bar potential to drive spiral shocks to distances of tens of parsec.

Since local Seyfert galaxies have mass accretion rates of $\sim 0.01\ M_{\odot}\ \mathrm{yr}^{-1}$ (Peterson 1997), it seems plausible that the analysis of Maciejewski (2004b) may be going in the right direction. Further, in the case of flocculent and tightly-wound nuclear spirals, it is not clear at present if the inflow rates are substantially reduced as compared to those in grand-design nuclear spirals, as detailed simulations are yet to be done.

The presence of strong shocks in the ISM is accompanied by star-formation activity. We noted in the previous section that we see more nuclear rings in NLS1s as compared to BLS1s, and the same is true for a barred *vs.* unbarred comparison. Presence of these bright stellar nuclear rings indicates that the central kiloparsec has been fueled in the last few hundred mega-years. Further, bright star-forming regions are often seen on the outer periphery of the main curving dust lanes in these systems. Studies of the rings in galaxies, have shown that rings are resonance phenomena and are often found in galaxies with a large-scale bar (Buta & Combes 1996). The size of nuclear rings in our sample corresponds with typical values for nuclear rings measured by other observers (Laine et al. 2002; Erwin & Sparke 2002; Martini et al. 2003a), and ranges from about 250 pc to 1 kpc; TOL 2327-027 would be an exception due to its large ($\approx$ 5 kpc) circumnuclear disk (see Appendix B). Laine et al. (2002) mention that the size distribution of nuclear rings peaks at about the same radius as the location of the ILR of the main large-scale bar.

On the whole, we conclude that large-scale stellar bars drive the formation of and maintain grand-design nuclear dust spirals, which plausibly provide sufficient inflow rates to fuel the SMBHs in NLS1s. Recent simulations and the presence of star formation confined in a nuclear ring in the central kiloparsec give support to the idea that the gas loses its angular momentum via nuclear spiral shocks driven by the main bar potential. However, it is not clear what the mass inflow rates in flocculent nuclear spirals are. Since flocculent spirals are not driven by orbital resonances of a non-axisymmetric

gravitational potential like a bar, it is plausible to expect that spiral shocks in flocculent spirals are much weaker, leading to less efficient accretion rates. Observational support for this is that very little star formation is seen in flocculent type nuclear spirals in unbarred galaxies, while grand-design spirals show enhanced star formation on the outer edges of their spiral arms and in stellar nuclear rings (Martini et al. 2003a, see also Appendix B). However inflow rates in flocculent spirals need to be studied using numerical simulations.

3.7 Summary

We have analyzed *HST* broad-band (F606W) images of a sample of 91 Seyfert 1 galaxies to study their nuclear morphology. We employed structure maps to enhance fine dust structure in the nuclear regions. Accompanying images in Figure B.1 provide a good repository to study nuclear dust structures on scales $\lesssim 1$ kpc in Seyfert 1 galaxies.

Our sample contains 12 NLS1 hosts and 75 BLS1 host galaxies. This allowed us to compare the nuclear morphology of NLS1 host galaxies to the BLS1 host galaxies. In Crenshaw et al. (2003a) (CKG03), we had noticed that NLS1s showed more large-scale bars as compared to BLS1s. We have revised the main morphological classification from CKG03 with the aid of structure maps, and conclude that 76% of NLS1 host galaxies are barred as compared to 40% for BLS1 hosts. Overall, almost half (47%) of the spiral Seyfert 1 galaxies from CKG03 are barred.

Here, we find that nuclear dust spirals are the most common kind of morphology in the central kiloparsec of Seyfert 1 galaxies. We find that 80% of the NLS1s have grand-design type nuclear spirals as compared to 32% for BLS1s. Further we see that 69% of barred galaxies have grand-design morphology as compared to 7% for unbarred ones. This is in agreement with the trend noted by Martini et al. (2003b). This is also indicative of the

fact that these nuclear spirals are being driven and maintained by large-scale stellar bars. We also find that most BLS1 host galaxies have multi-arm, flocculent or chaotic nuclear dust spirals.

We find that 42% of the NLS1s have nuclear star formation in the form of nuclear rings as compared to 11% of BLS1s. A similar distribution is seen when one compares barred galaxies with the unbarred ones. This again indicates that the large-scale bar is the main driver of these differences. This strengthens the idea that large-scale bars are important to support high fueling rates in NLS1s. Thus our results here support the fueling scenario for barred *vs.* unbarred galaxies via nuclear dust spirals. Recent simulations of gas and dust inflow in barred galaxies give support to the idea that the galactic disk gas loses its angular momentum via nuclear spiral shocks which are being driven by the main bar potential within the central kiloparsec. Further, numerical simulations have shown that when sufficient mass has been accreted into the inner bulge via the primary stellar bar, that bar will be disrupted on time scales $\sim 10^8$ Myr. It has also been claimed that the SMBH's in NLS1s are under-massive for their bulges (Mathur 2000). Thus, a likely evolutionary scenario is that NLS1s are relatively young AGN accreting at high rates, and that they eventually become BLS1s as they accrete enough matter to disrupt the bar and increase the mass of the SMBH.

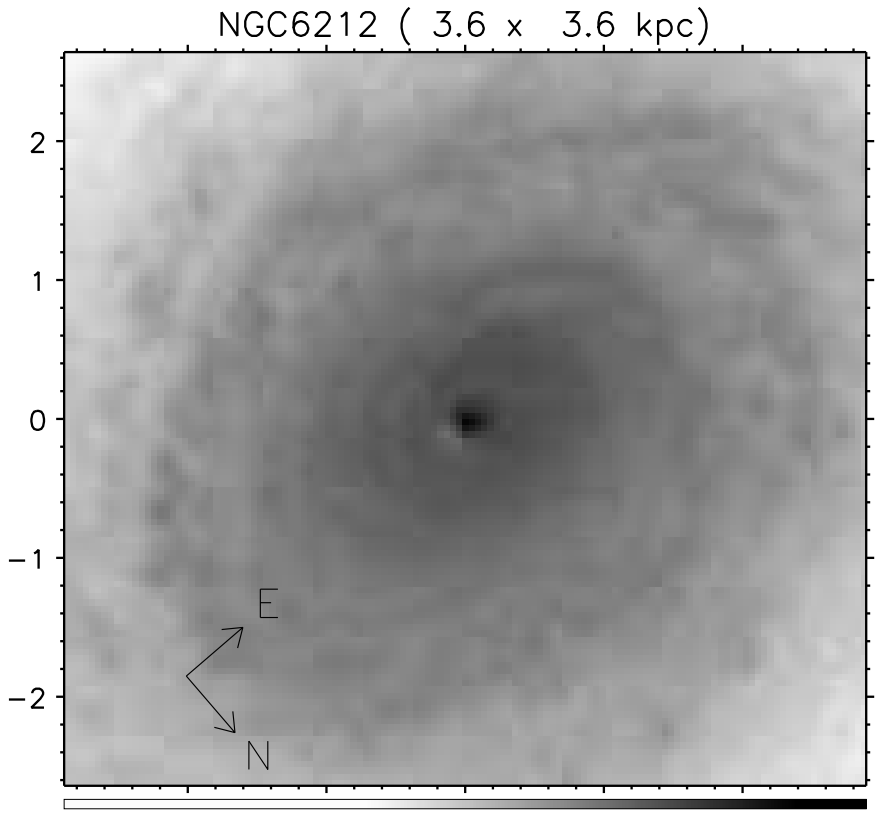

Figure 3.5: Structure Maps of Seyfert 1s: NGC 6212, a flocculent dust spiral (Category: FL).

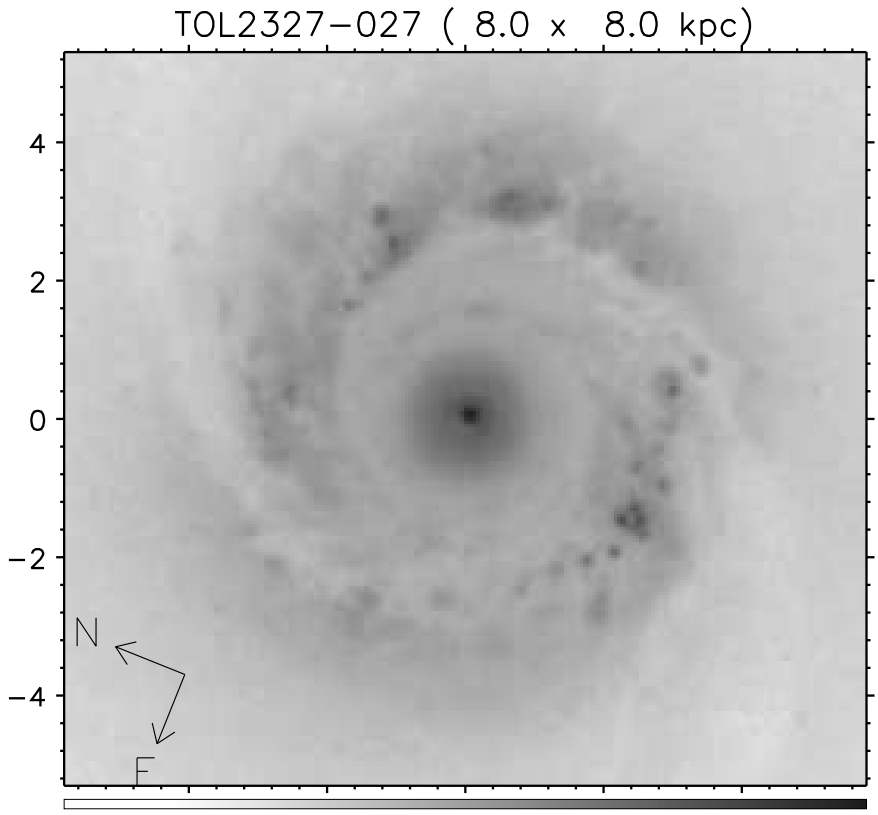

Figure 3.5: Structure Maps of Seyfert 1s: TOL 2327-027, a strongly barred galaxy with a tightly-wound nuclear spiral (Category: GD/TW).

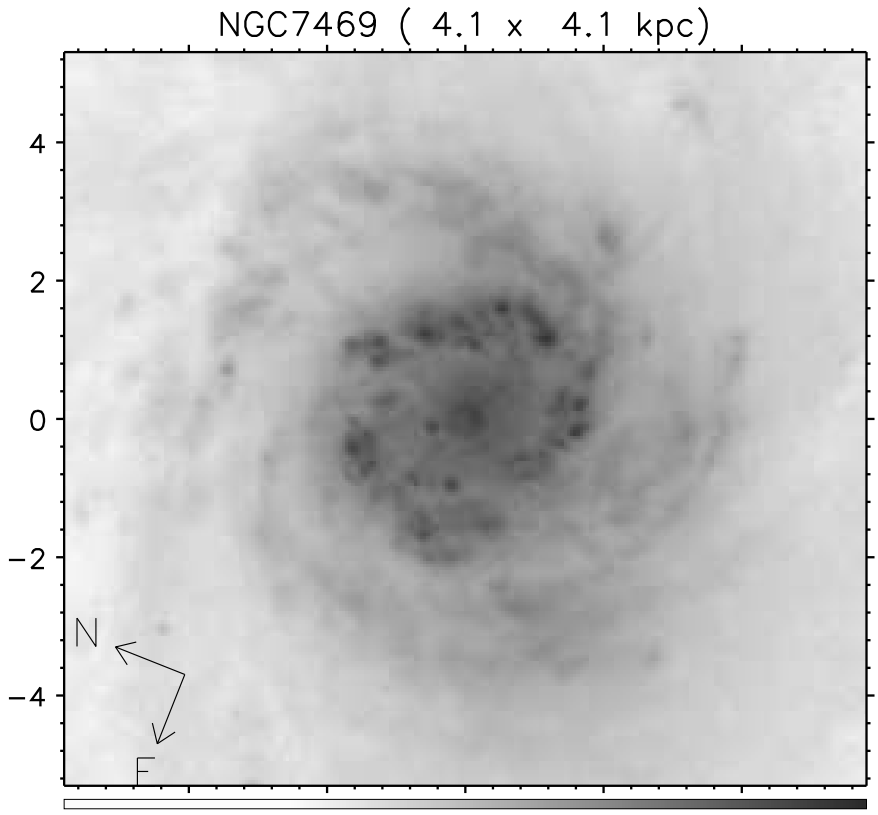

Figure 3.5: Structure Maps of Seyfert 1s: NGC 7469 hosting a multi-arm nuclear spiral with a starburst ring (Category: FL + NR).

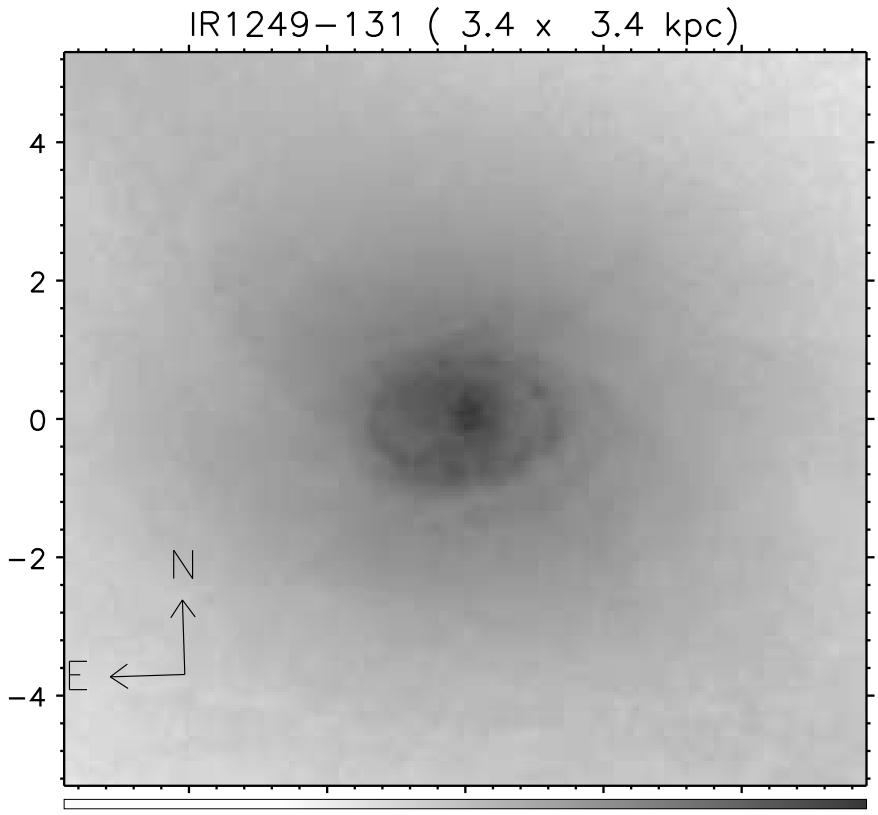

Figure 3.6: Structure Maps of Seyfert 1s: shown above is IR 1249-131; it has a prominent nuclear ring (Category: NR).

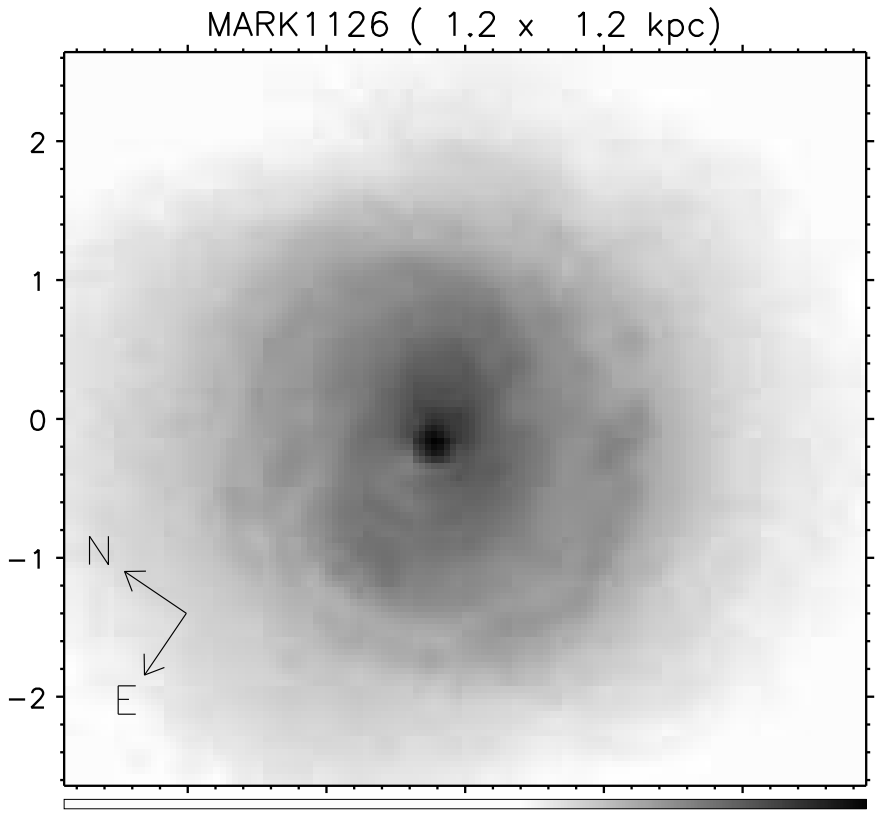

Figure 3.6: Structure Maps of Seyfert 1s: shown above is Mrk 1126 a grand design nuclear spiral with a nuclear ring (Category: GD + NR).

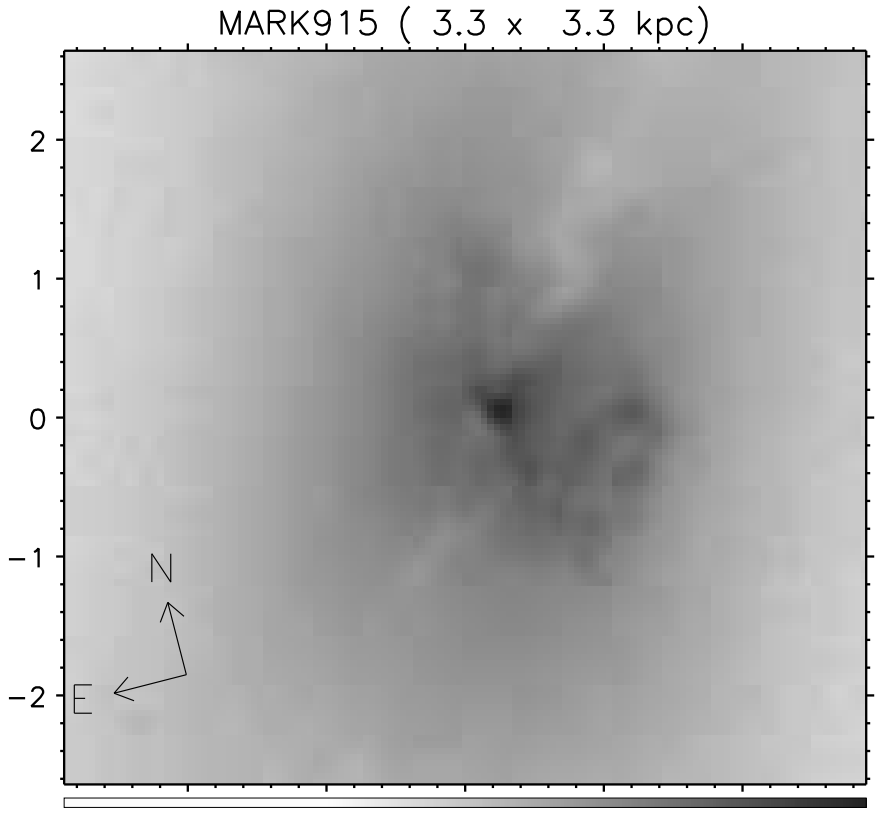

Figure 3.6: Structure Maps of Seyfert 1s: Mrk 915 shows a large-scale dust lane (Category: DL) passing through the nucleus. An emission bicone is clearly visible in this image.

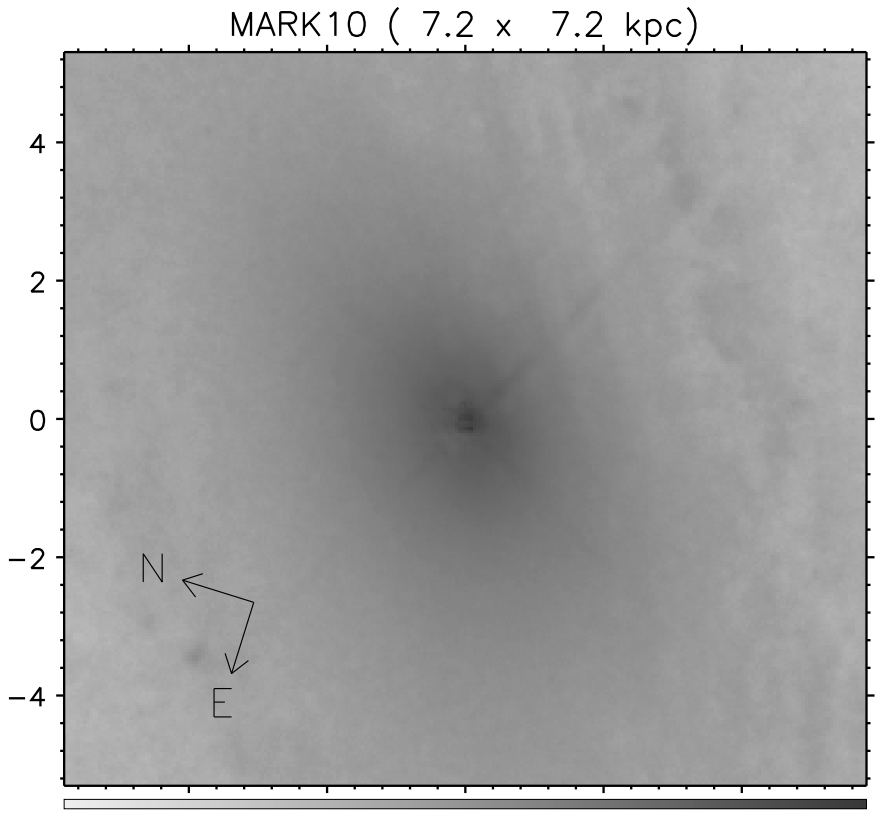

Figure 3.6: Structure Maps of Seyfert 1s: Mrk 10 does not show much dust structure in the nuclear regions (Category: ND).

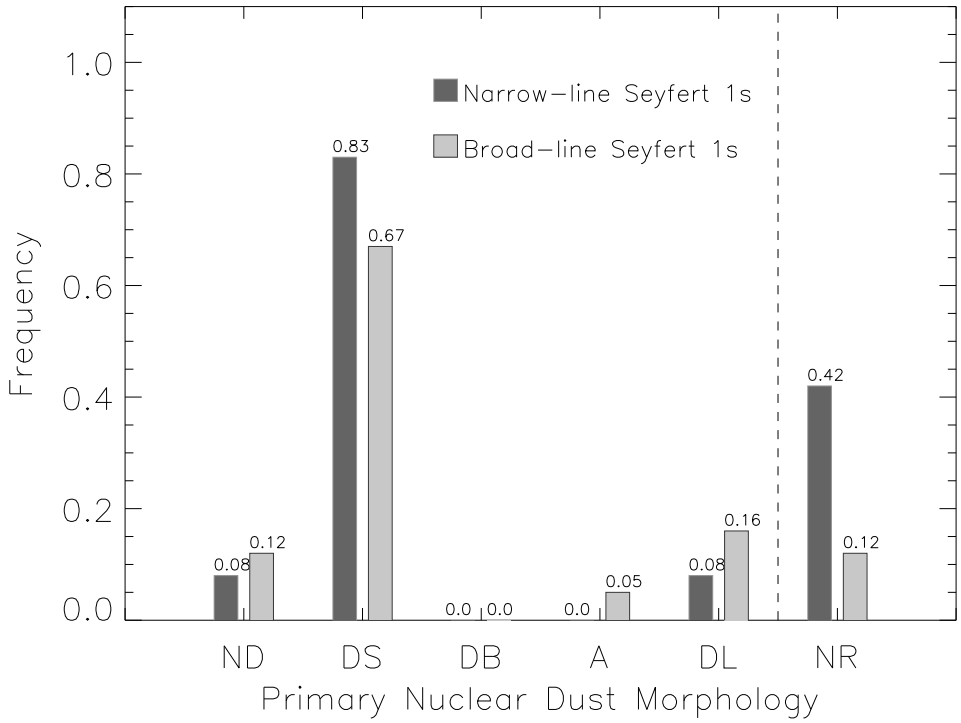

Figure 3.7: Frequency of Nuclear Dust Structures: Figure shows bar plots for various morphological classes shown in Table 3.3. See § 3.4.1 in text for description of morphology classes. Here we compare the NLS1s against BLS1s in their primary nuclear dust morphology. As can be seen dust spirals (DS) is the most common type of morphology.

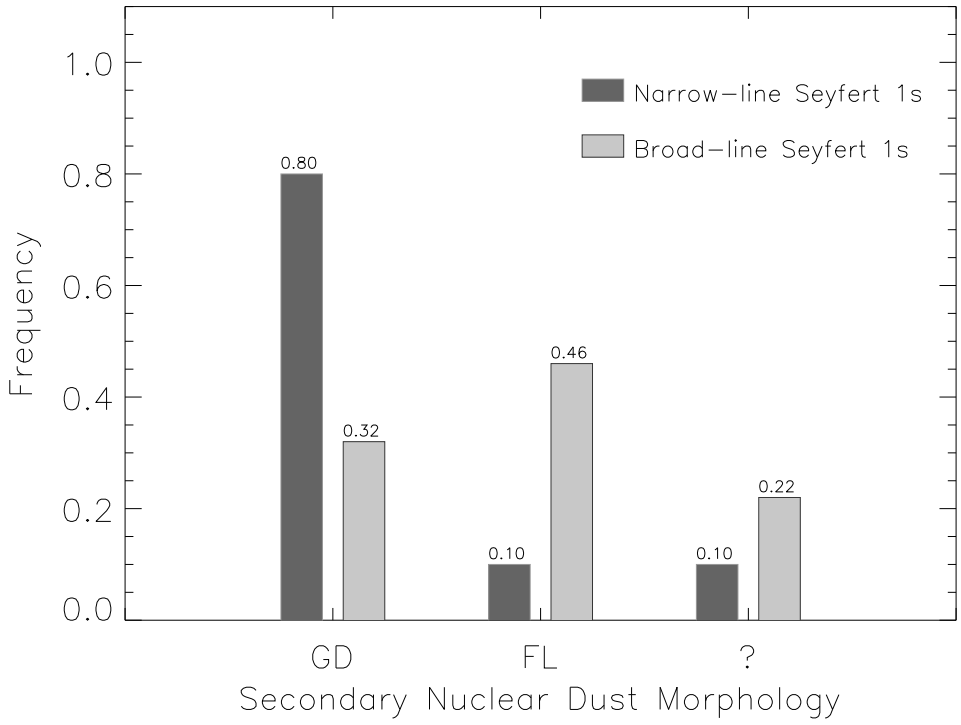

Figure 3.8: Frequency of nuclear dust spirals: Here we compare the NLS1s with BLS1s in the nature of their nuclear dust spirals (secondary nuclear morphology of the DS category in Figure 3.7). NLS1s show mainly GD-type spirals, while BLS1s show mainly FL-type spirals, although BLS1s are more than twice in number than NLS1s.

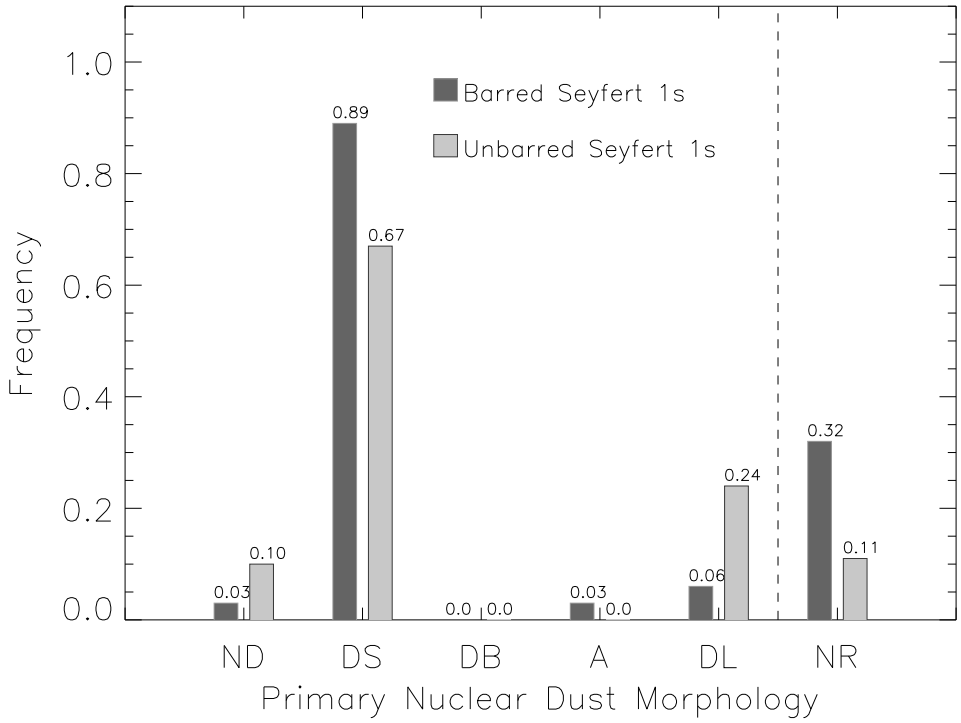

Figure 3.9: Primary Nuclear Dust Structure: barred *vs.* unbarred spirals. Barred galaxies have a slightly higher fraction of grand-design dust spirals.

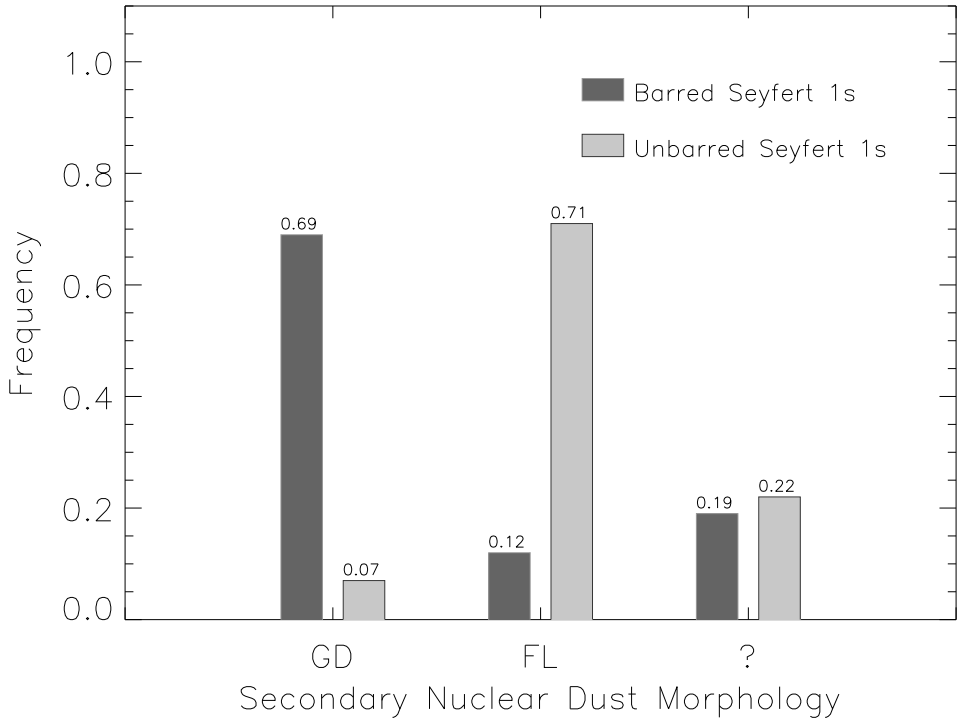

Figure 3.10: Frequency of nuclear dust spirals: barred *vs.* unbarred spirals. This graph clearly shows that the grand-design spiral is driven mainly by large-scale bars, while flocculent spirals exist in unbarred galaxies.

Chapter 4

Mid-IR Spectroscopy of Seyfert Galaxies

As we saw in §1.2.3, we will concentrate on mid-infrared spectroscopy of Seyfert galaxies in this part of the dissertation. In this chapter, we will look at early (1960s–1990s) infrared studies of Seyfert galaxies. We will pay special attention to the spectroscopic results from the *Infrared Space Observatory* (ISO). In Chapter 5, we will describe the *Spitzer Space Telescope* and the Infrared Spectrograph (IRS). In the same chapter we will also cover data reduction procedures for mid-IR spectra from IRS. In Chapter 6, we will look at mid-IR spectra of Seyfert 1.8/1.9s in comparison to spectra of Seyfert 1s and Seyfert 2s. We will describe the morphological characteristics of the spectra. In Chapter 7, we will look at the spectral diagnostics derived from our sample and the archival data.

4.1 Early Infrared Studies

Oke & Sargent (1968) showed that Seyfert galaxies have a power-law spectrum similar to quasars. It was also shown (Neugebauer et al. 1976) that a larger fraction of the stellar radiation contributes to the spectrum in Seyfert

2s than in Seyfert 1s. Rieke & Low (1972) suggested that the bulk of the bolometric luminosity is contained in the infrared. NGC 1068 was recognized as a strong infrared source as early as 1966. Pacholczyk & Wisniewski (1967) studied the broad-band near-IR (up-to 0.22 μm) characteristics for NGC 1068. Further, far-infrared observations of NGC 1068 by Telesco et al. (1976) showed that the spectrum of NGC 1068 shows a turnover (see Figure 4.1) around 100 μm.

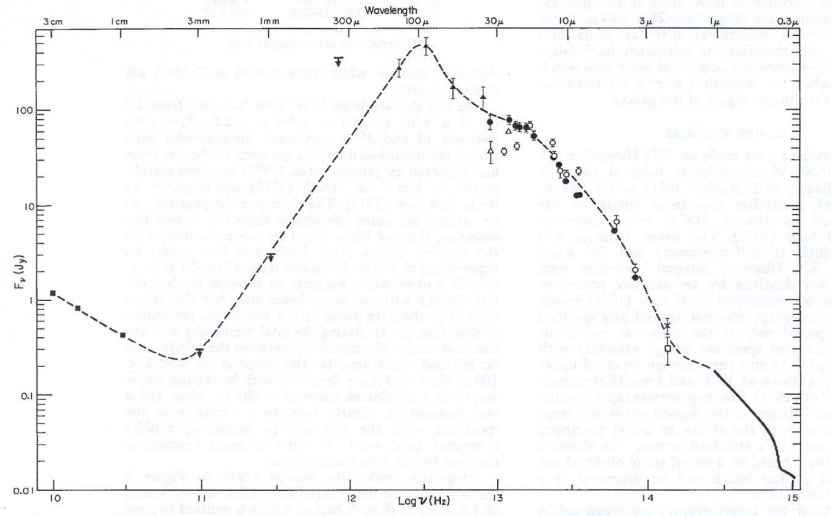

Figure 4.1: Far-IR Turnover in NGC 1068 from Telesco et al. (1976)

Initially, there was uncertainty as to what generated the infrared emission. Is it generated by non-thermal processes like synchrotron radiation, or is it re-radiation from dust in the galaxy? Angel et al. (1976) found that the continuum in NGC 1068 was circularly polarized, thus favoring the idea that scattering and re-radiation from dust is involved in generating the observed strong infrared continuum. This also implied that Seyfert 2 nuclei like NGC 1068 are embedded in envelopes of dust. Further, it was shown that Seyfert galaxies in general are not strong radio sources (Kellermann 1972) and thus should have a weak contribution from the synchrotron process. A number of early infrared observations of Seyfert galaxies also noted the presence of the

10 μm silicate absorption feature (*e.g.,* in Mrk 231, Allen 1976; Gillett et al. 1975; Rieke & Low 1975), indicating that the nuclei of Seyfert galaxies had large quantities of dust. A detailed review of early infrared work on AGN is given in Rieke & Lebofsky (1979).

4.2 The Infrared Continuum

For Seyfert galaxies, Rees et al. (1969) suggested that the emission in the 2.2-22 μm band is produced by dust grains heated by the optical and UV emission from the nucleus. However the continuity observed between the mm-regime and the infrared region for radio-loud objects suggested that some of the Far-IR emission may be non-thermal. Using the CFA sample of 48 Seyfert 2s, Edelson et al. (1987) showed that the turnover around 100 μm is due to dust at a temperature $T \approx 50$ K. They also showed that the mean power-law index for Seyfert 2s was steepest at $\langle \alpha_{2.2\text{–}25\ \mu\mathrm{m}} \rangle = 1.56$. The sub-millimeter break around $\sim$ 100 μm is produced as the emitting efficiency of small dust grains is a sensitive function of frequency, $Q_\nu \propto \nu^\gamma$, with $\gamma \approx 2$ (Draine & Lee 1984), so the emitted spectrum can have a very strong frequency dependence, $F_\nu \propto \nu^{2+\gamma}$, leading to the observed steep spectral indices longward of the sub-millimeter break.

Carleton et al. (1987) studied a sample of hard X-ray selected Seyfert 1s and combined measurements in the optical and the infrared from IRAS. They concluded that the underlying AGN continuum is similar in all Seyferts 1s, but is modified by absorption and reemission by intervening dust. They estimated the radial dependence of the dust temperature, using the prescription of Davidson & Netzer (1979):

$$T = 10^{-6} \left(\frac{L_{eff}}{r^2} \right)^{1/5} \tag{4.1}$$

where the luminosity is in units of erg s^{-1}, the distance r is in parsecs and it is assumed that the dust emissivity is $\propto \lambda^{-1}$. Dust that is responsible for emission at 3.5, 20 and 80 microns, has characteristic temperatures of 1000 K, 180 K and 45 K respectively (Wien's law). For an assumed $L_{eff} = 5 \times 10^{44}$ erg s^{-1}, the dust radiating at above wavelengths is at distances of 0.7 pc, 50 pc and 1600 pc, respectively.

Sanders et al. (1989) have discussed the continuum observations of 105 quasars from the Palomar Bright Quasar (BQS) Survey from 0.3 μm–6 cm. They proposed that the 2 μm–1 mm region is dominated by thermal emission in all AGN except Blazars. They further suggest that the emission at 0.5–5 μm could be produced by hot dust in the outer parts of the accretion disk or a molecular disk a few parsecs in size. They further speculated that the emission in the 5 μm–1 mm region can be produced by heated dust in a warped disk beyond a few parsecs surrounding the nucleus.

Sanders et al. (1989) showed that a local minimum in the infrared SED at ~ 1 μm is a general feature of all AGN. This feature finds a natural explanation in the dust model for infrared emission (Rees et al. 1969). The IR radiation at ~ 1 μm will arise if the dust re-radiates at distances of ~ 0.1 pc from the nucleus, where the temperature will be above ~ 2000 K. At these temperatures the dust grains sublimate. This leads to the minimum in observed flux around 1 μm. Graphite grains have higher sublimation temperatures than silicate grains. Thus, it is expected that dust close to the AGN is composed mainly of graphite grains rather than silicate grains. Barvainis (1987) gives a prescription from the sublimation radius of the graphite grains as

$$r = 1.3 L_{uv46}^{1/2} T_{1500}^{-2.8} \text{ pc}, \tag{4.2}$$

where L_{uv46} is the central source UV luminosity in units of 10^{46} erg s^{-1} and T_{1500} is the grain sublimation temperature in units of 1500 K.

The IR continuum variability was best studied in Fairall 9 (Clavel et al. 1989). The near-IR continuum variations were found to lag behind the UV

continuum variations by $\sim$ 400 days. The IR continuum is thus expected to arise from a distance of $\sim 10^{18}$ cm from the continuum source. These observations support the view that dust is sublimated in a region smaller than this size and survives outside of it. The dust is heated by the incident optical/UV continuum and re-radiates in the infrared region. The far-IR continua of AGN are variable only in radio-loud sources (Edelson & Malkan 1987), which suggests a thermal origin of the far-IR continuum in radio-quiet sources.

Thus, it is now generally accepted that apart from Blazars, the infrared continuum in all AGN is primarily due to reprocessing of the optical/UV continuum by the nuclear dust distribution. This includes heating by the AGN continuum itself, as well as by hot stars in nuclear starbursts, when present.

4.3 ISO Spectroscopy

Studies with IRAS (Beichman 1988; Soifer et al. 1987) revealed many previously known AGN to be more powerful in the infrared than in the visible. In addition, a new population of optically faint but infrared bright galaxies[1] was discovered (luminous infrared galaxies (LIGs) with $L_{IR} > 10^{11}\ L_{\odot}$, Houck et al. 1984). AGN or massive bursts of star formation are the two possible mechanisms that can generate such high infrared luminosities. Quantifying the amount of obscured activity at earlier epochs in the Universe and their contribution to the infrared and X-ray backgrounds remain open issues even today. The *Infrared Space Observatory* (ISO, Kessler et al. 1996) was the first space-based infrared telescope with spectroscopic capabilities. It opened the 2.5–240 μm near-to-far infrared window for astronomical obser-

[1]ULIRGs typically have $L_{IR} > 10^{12}$–$10^{13}\ L_{\odot}$ and Hyper-LIGs have $L_{IR} > 10^{13}\ L_{\odot}$ and were soon discovered after LIGs.

vations. Here we will look at the most important results obtained for nearby active galaxies through ISO spectroscopy.

Within the star forming regions or active nuclei, the incident optical/UV continuum heats the dust grains and they emit in the infrared. The type, size and geometrical distribution of dust grains governs the emission properties of the region, along with the nature of ambient interstellar radiation field. The overall SED in the infrared region is thus a combination of these various components. The dust grain sizes vary from very small ($a \lesssim 10$ nm) to large ($a \sim 30$ μm). The very small grains are heated stochastically, are not in thermodynamical equilibrium, and emit at shorter wavelengths over 3-18 μm (Puget & Leger 1989). But grains emitting at longer wavelengths ($\lambda \gtrsim 25$ μm) appear to be in thermodynamic equilibrium with their surroundings. In strong radio galaxies, the featureless far-IR tail of the SED continues to increase with increasing wavelength, due to non-thermal contribution from the synchrotron radiation spectrum.

4.3.1 IR Continua

There are two prominent continua in the mid-infrared spectra of galaxies: a component that dominates below 5 μm and another above 11 μm. The 3-5 μm continuum likely arises from transient heating of small dust grains (Helou et al. 2000). Transient heating of dust grains dominates in this region but there could also be a component due to direct stellar emission on the short wavelength side. As one moves from shorter wavelengths to the low to mid-IR wavelengths, there is a transition from direct stellar emission to the interstellar dust emission (Boselli et al. 1997; Alonso-Herrero et al. 2001). The mid-infrared region also includes another transition from transient heating of dust grains to the steady-state heating of dust grains. The wavelength at which this transition occurs is determined by the incident radiation field above which a dust grain of a certain size no longer suffers large temperature changes. In the transient heating regime, the mid-infrared con-

tinuum is directly proportional to the underlying radiation field and varies with conditions in the H II regions from which it originates (Boulanger et al. 1998a; Laurent et al. 2000).

For spatially unresolved sources, SED decomposition into these differing continua is the only way to investigate the underlying physical properties. The decomposition approaches go from simple decomposition into a series of black bodies (Haas et al. 1998), to semi-empirical models (Dale et al. 2001), to complex radiative transfer calculations involving multi-grain distributions for dust (Alexander et al. 1999a; Siebenmorgen et al. 2004a). Many active galaxies display a broad and flat (in νF_ν) "hot" continuum that dominates the mid-IR SEDs. Further, de Grijp et al. (1985) showed that galaxy selection based on IRAS color $S_{60}/S_{25} > 0.2$ selects galaxies hosting AGN. The hot mid-IR continuum is produced by grains that are heated up to their sublimation temperatures by the strong radiation from the accretion disk. It is plausible that transient heating of small dust grains plays a significant role in generation of this hot continuum.

In the far-IR, the greater sensitivity and wavelength coverage of ISO over IRAS helped to precisely determine the far-IR turnover in active as well as quiescent galaxies. Quiescent galaxies show a turnover around $\sim$ 150 μm while most star forming galaxies and AGN show a turnover in the $\sim$ 80–100 μm range. This implies the presence of a "cold" component (30–60 K) of dust surrounding the star forming regions in addition to the "warm" component ($\gtrsim$ 60 K) of dust due to starburst activity (Calzetti et al. 2000). In AGN, the fractional contribution of the "warm" component ($\lambda \sim 30$ μm) is much more than that of the "cold" component. A second "very cold" component ($T < 20$ K) was also isolated (Trewhella et al. 2000), which corresponds to the more extended dust and is likely associated with molecular gas in the outer regions of a given galaxy. The "very cold" and the "cold" component together contribute to the far-IR SED and determine the location of the far-IR turnover.

4.3.2 Spectral Features

The mid- to far-IR spectroscopy from ISO enabled study of local AGN and starburst galaxies, *e.g.,* the Seyfert 2 Circinus (Moorwood et al. 1996), the starburst galaxy M82 (Sturm et al. 2000), the Seyfert 2 NGC 1068 (Lutz et al. 1997), and the Seyfert 1.5 NGC 4151 (Alexander et al. 1999b). Three of these active galaxy ISO spectra taken from Verma et al. (2005) are shown in Figure 4.2. The spectra show fine structure lines of low ionization, H-recombination lines, and the thermal continuum that predominantly traces the starburst components. Intermingled with these features are a strong very small grain (VSG) continuum, continuum due to AGN activity and high ionization fine structure lines. In addition to this, the spectra also display rotational lines of H_2, molecular features due to OH, CH, X(CN) (nitrile organic compounds with triple bonds between N and C) and H_2O and very low excitation fine structure lines ([O I] and [C II]) in the far-IR. In Circinus and NGC 1068, we also see the silicate absorption feature at 10 μm.

4.3.3 PAH Features

In the mid-IR region, there are broad emission features in the spectra. These features occur at 3.3, 6.2, 7.7, 8.6 and 11.3 μm. They are always observed in spectra of starburst galaxies and are attributed to PAHs (Leger & Puget 1984; Puget & Leger 1989). These features were also called unidentified infrared bands (UIB) when they were first detected in ISO spectra. They occur in a wide range of celestial sources (Cesarsky et al. 1996a,b; Allamandola et al. 1995) and are common in the spectra of star forming galaxies. The infrared bands are expected to originate in the C-C and C-H bending and stretching vibrational modes in aromatic hydrocarbons and the favored carriers are PAH clusters (Boulanger et al. 1998b). The carriers likely provide a majority of the flux in the 3–12 μm band and show near invariant profiles in a variety of galaxies (Förster Schreiber et al. 2003), although intensity varia-

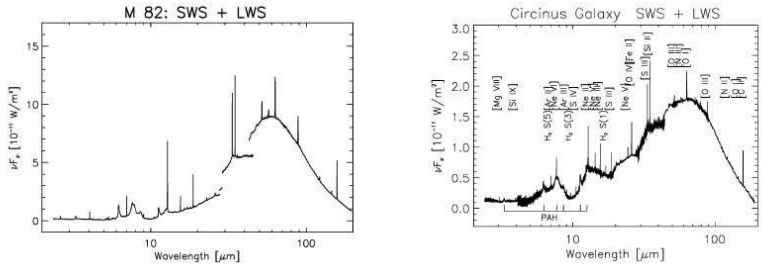

(a) M 82 (Starburst) and Circinus (Seyfert 2 + Starburst)

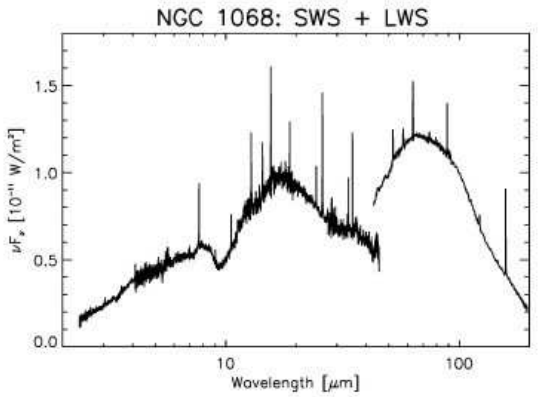

(b) NGC 1068 (Seyfert 2)

Figure 4.2: ISO Spectra of M 82, Circinus and NGC 1068 from Verma et al. (2005). The spectra are plotted as νF_ν *vs.* λ.

tions between PAH bands are observed (but see also Peeters et al. 2003). These broad emission features are well-fit by Lorentzian profiles as opposed to Gaussian profiles (Boulanger et al. 1998b). The mid-infrared spectra of starburst galaxies are generally dominated by these PAH features; these also have a strong continuum from very small grains, which could be stochastically heated PAHs. The PAH emission is expected to arise at the interface of H II regions and molecular clouds, where dust grains are being photo-dissociated due to the UV radiation from newly formed stars (Verstraete et al. 1996; Cesarsky et al. 1996a). In intense radiation fields such as in the vicinity of

super star clusters or AGN, PAH features are weak or absent (Sturm et al. 2000; Le Floc'h et al. 2001; Siebenmorgen et al. 2004b).

4.3.4 Fine Structure Lines

The mid-IR spectral range shows a number of fine structure lines, which are excellent probes of the ionization state of the nebular gas and the intrinsic ionizing continuum. The emission line diagnostics are very useful probes of the physical state of the gas as the line strengths are dependent on the ionization potentials and critical densities of different ionic species. Starburst galaxies commonly show low excitation lines such as [Ar II] λ6.98 μm, [Ar III] λ8.99 μm, [Fe II] λ5.34 μm, [Ne II] λ12.81 μm, and [S III] λ18.71 μm, etc. All of these lines have ionization potentials (IP) between 13.6 eV and $\sim$ 50 eV. High ionization lines with potentials exceeding 50 eV such as [Ne V] λ14.32 μm, [Ne VI] λ7.65 μm, [S IV] λ10.51 μm, [Mg V] λ5.61 μm, [Mg VII] λ5.50 μm, [Mg VIII] λ9.01 μm, and [O IV] λ25.89 μm are mostly seen in AGN or low-metallicity galaxies. The presence of high ionization lines like [Ne V] and [O IV] is often considered to be due to the presence of an active nucleus in unresolved sources. The lines of [O IV] and [S IV] are sometimes also seen in starburst galaxies. The ionization to high energy levels greater than 50 eV is difficult to attain by the UV continuum in typical H II regions. This difference is very useful to separate starburst and AGN contributions in most composite galaxies (Laurent et al. 2000).

Infrared lines are much less affected by extinction than are optical lines and hence are very good probes of the dusty nebular conditions found in AGN outflows. The ratios of two lines of the same species provide information on the electron temperature and densities. The ratio of high to low ionization states of the same element probe the hardness of the incident radiation field. Further, ratios of high to low ionization states of different elements are used as probes of AGN presence and contribute to nebular diagnostics (Genzel et al. 1998; Laurent et al. 2000; Sturm et al. 2002).

4.3.5 Silicate Features

The 10 μm and the 18 μm absorption features arise from the stretching and bending modes of SiO in dust grains. The intrinsic extinction suffered by a galaxy can be estimated by the depth of these features. The 10 μm feature is somewhat difficult to measure due to the presence of PAH features adjacent to it. The 18 μm feature is significantly broader and weaker. This leads to uncertainty in the placement of the local continuum and may affect line measurements (Sturm et al. 2000). Nevertheless, careful placement of the continuum can lead to reasonable estimates of the line-of-sight extinction. In the mid-infrared spectra of local Seyfert galaxies, ISO detected silicate absorption in Circinus and NGC 1068, but silicate emission features were not detected in type 1 AGN like NGC 4151, in contrast to expectations from the compact dusty torus models (Pier & Krolik 1992).

4.3.6 Molecular Features

Apart from fine structure lines and silicate absorptions, molecular features are common in mid-IR spectra. The molecular features trace the warm and cold molecular material. The "warm" features include ro-vibrational lines of molecular hydrogen (H_2) and the "cold" features include ice absorption from cold molecular gas.

The low rotational transitions of hydrogen originate from a warm component ($T \sim$ 100–200 K); higher rotation and ro-vibrational transition arise from gas at much hotter temperatures ($T \sim$ 1000 K). Rigopoulou et al. (2002) surveyed a number of Seyfert and starburst galaxies and showed that the "warm" molecular hydrogen gas was at temperature of $\approx$ 150 K. They detected rotational transitions from S(7) to S(0) in both classes of galaxies. They also note that the fraction of "warm" gas in Seyferts was 2–35% while it is about 10% in starburst galaxies. It is expected that the contribution is due to fairly normal photo-dissociation regions (PDR), low velocity shocks

(as in spiral or collisional shocks between molecular clouds) and X-ray heated gas around the central AGN.

Extragalactic ice features due to H_2O, CH_4 and X(CN) were first detected by ISO (M82 and NGC 253, Sturm et al. 2000). Spoon et al. (2002) studied a heterogeneous sample of 103 active galaxies and suggested that approximately 20% display absorption features attributed to ices. While ices are weak or absent in spectra of starburst and Seyfert galaxies, they are common in ULIRG sources. Spoon et al. (2002) propose a evolutionary scenario for ULIRG sources, where in the obscured phase, ice absorption features dominate the spectrum; as the enshrouded starburst emerges, the PAH features from the PDRs begin to dominate the spectrum. During any of these phases it is possible that an active nucleus remains hidden within the obscuration.

4.4 Ionization/Obscuration in the Mid-IR

A thin accretion disk around a SMBH emits most of its energy in the EUV. This emission longward of the Lyman edge and up to a few hundred eV is called the big blue bump (BBB). Since the BBB is unobservable due to intrinsic and galactic absorption, it is necessary to construct its nature via indirect methods. One such a method is to use high ionization potential (IP) infrared fine structure lines that originate in the NLR and directly probe the EUV SED via photo-ionization modeling. This was attempted for Circinus (Moorwood et al. 1996), NGC 4151 (Alexander et al. 1999b) and NGC 1068 (Alexander et al. 2000). Only Circinus shows the presence of an EUV bump around 70 eV, while the SED of NGC 4151 and NGC 1068 show troughs in the EUV range. This lack of BBB in some sources is thus puzzling.

The differences between Seyfert 1 and Seyfert 2 galaxies are explained based on the orientation of the dusty torus and there is considerable support for this picture. In the mid-IR, the emission due to the torus is expected to be anisotropic (Pier & Krolik 1993). Perez Garcia et al. (1998) noted that

the mid-IR dust temperatures in Seyfert 1s are higher than in Seyfert 2s, supporting unification, since in Seyfert 1s we are presumably looking into the hot inner throat of the torus. Further, Clavel et al. (2000) showed that PAH equivalent widths are larger in Seyfert 2s than in Seyfert 1s. One interpretation of this result is that the PAH emission is isotropic, as it originates in a circum-nuclear starburst that is expected to have more-or-less the same strength in galaxies of both types. The mid-IR AGN continuum is expected to be anisotropic, as it is absorbed by the torus, leading to larger equivalent widths in Seyfert 2s as compared to Seyfert 1s, where they are suppressed by the glare of the AGN-heated continuum.

A test of unification is possible with hard X-ray observations. Hard X-rays are expected to be isotropic as they can penetrate a Compton-thin dusty torus that obscures the optical/UV continuum sources. Lutz et al. (2004) isolate the mid-IR continuum at 6 μm due to the nucleus in a sample of Seyfert 1s and Seyfert 2s, and compare the nuclear 6 μm fluxes to the absorption-corrected hard X-ray fluxes. They find no significant difference in the ratio $f_{6\ \mu\mathrm{m}}/f_{\mathrm{X\text{-}rays}}$ between Seyfert 1s and Seyfert 2s, contrary to the predictions of the unified scheme. Lutz et al. suggest that this apparent uniformity could be due to dilution of the anisotropic mid-IR emission by a dominant mid-IR component (*e.g.,* a starburst continuum) that emits isotropically on the extended scales probed in their study ($\sim$ 100 pc). Further, Kuraszkiewicz et al. (2003) showed that for a sample of hard X-ray selected Seyferts, while Seyfert 2s are redder in their optical colors than Seyfert 1s, their mid-to-far-IR (25 μm/60 μm) colors are similar. They suggest that a clumpy dust disk, a few hundred parsecs in size can reproduce the mid-IR SEDs without requiring a starburst component. Based on the similarity of the mid-to-far-IR colors, they suggest that the AGN continuum can heat the dust located *farther away* ($\sim$ 100 pc) from the center and this "warm" dust can contribute in the mid-IR region. Clumpy torus models (Nenkova et al. 2002) allow such escape of the AGN continuum along the equatorial plane

to heat dust farther from the source, generating milder anisotropy in the mid-IR.

4.5 Diagnostic Diagrams in the Mid-IR

The spectroscopic capability of ISO enabled detailed spectral diagnostics using the infrared fine structure lines. These diagnostics are constructed in the same spirit as the optical diagnostics by Veilleux & Osterbrock (1987). The differences in ionization between AGN and the starburst component are the basis of these diagnostic diagrams. Studies by Genzel et al. (1998), Laurent et al. (2000) and Sturm et al. (2002) established the diagnostics we show below. The main aim of these diagnostic diagrams was to study the excitation of various species in the mid-IR region, to separate the AGN and the starburst components, and estimate the relative fraction of each using measurable spectral features. The diagnostics are based on three easily measured quantities: fluxes of fine structure lines, continuum fluxes and the fluxes of PAH features.

The diagnostic diagrams from Sturm et al. (2002) are shown in Figure 4.3 and Figure 4.4. As we saw before, the high excitation lines ($\gtrsim$ 50 eV) trace the AGN contribution and the [O IV] λ25.89 μm line is ideal to quantify this effect. It is strong in AGN dominated systems, however it is also seen in starburst systems (Lutz et al. 1998). The strength of [O IV] in starburst dominated systems is 10 times weaker than in AGN dominated systems and thus it is possible to use the value of ratio [O IV]/[Ne II] as a simple mixing model to estimate relative AGN fraction in a given system, as shown in Figure 4.3. [Ne II] λ12.81 μm turns out to be a valuable reference line that traces the amount of star formation.

In Figure 4.4, a correlation between L_{MIR} with $L([O\ IV])$ and $L([Ne\ II])$ is shown. The L_{MIR} *vs.* $L([O\ IV])$ correlation shows that at a given L_{MIR} Seyfert 2s show weaker [O IV] luminosities than Seyfert 1s, indicating that the

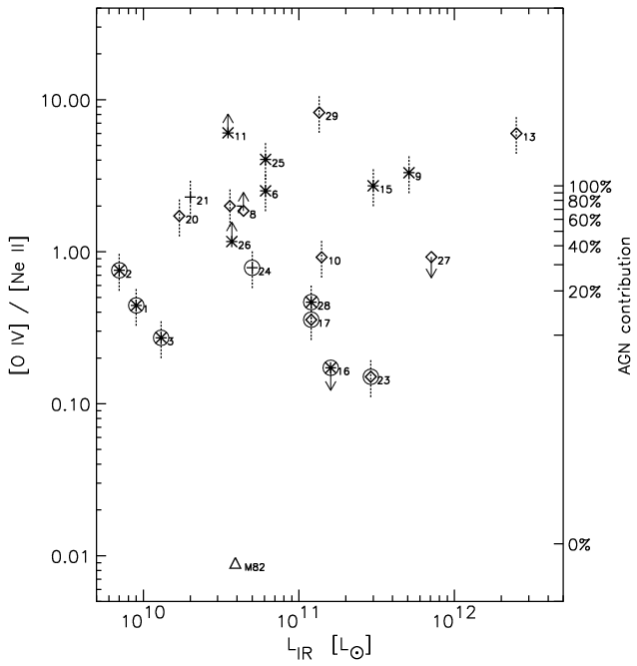

Figure 4.3: Diagnostic Diagrams from Sturm et al. (2002); a simple mixing model for estimating AGN fraction. Seyfert 1s are represented by diamond symbol and Seyfert 2s by asterisks.

NLRs of Seyfert 2s intercept on average weaker AGN continua, against the expectations from the unified model. The L_{MIR} *vs.* $L([Ne\ II])$ correlation shows that both types of Seyfert galaxies seem to have similar amounts of starburst contribution (as measured by the [Ne II] luminosity) at a given L_{MIR}. In the FIR, the [O IV] is not well correlated, but the correlation for [Ne II] becomes stronger for active galaxies and starbursts, indicating a connection between starburst emission as traced by [Ne II] and "cold" dust emission as traced by FIR luminosity.

Genzel et al. (1998) showed that 7.7 μm PAH-to-continuum ratio versus the hardness tracer [O IV]/[Ne II] is a good way to classify ULIRG sources and estimate the amount of AGN contribution to the luminosity of ULIRGs. Laurent et al. (2000) used spectral template fitting to decompose a mid-

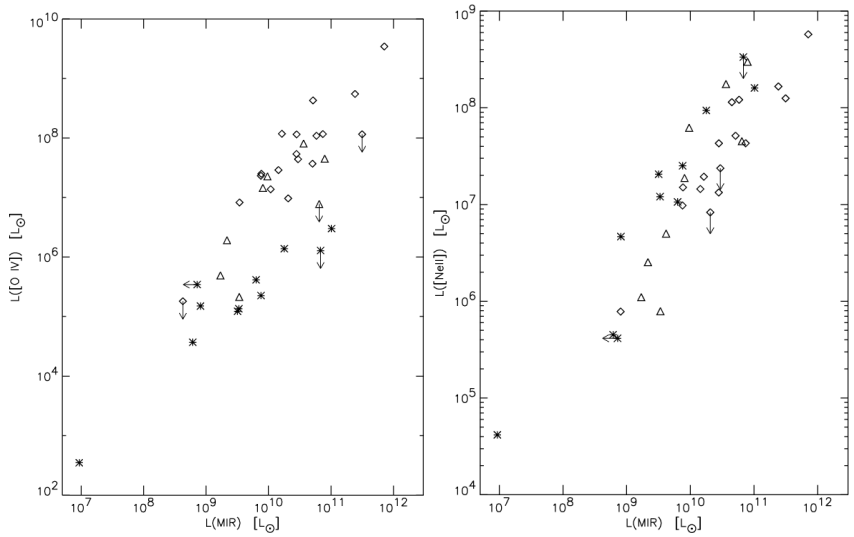

(a)

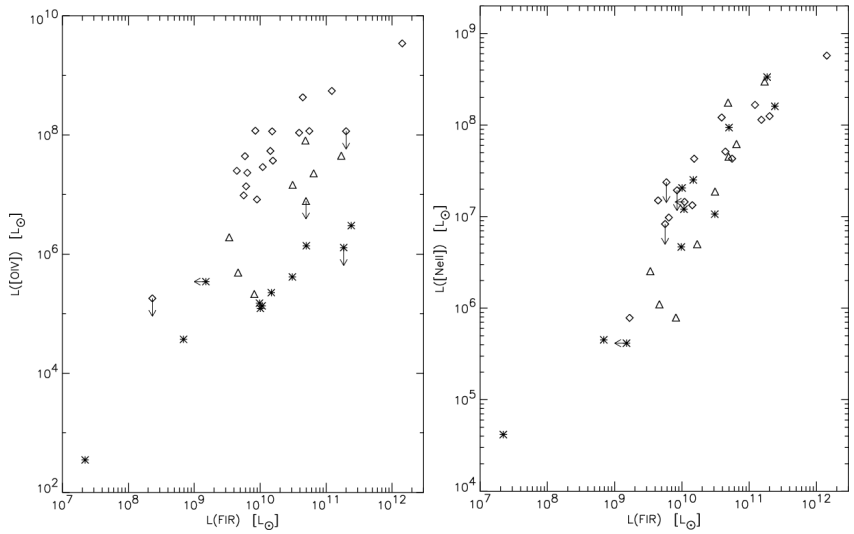

(b)

Figure 4.4: Diagnostic Diagrams from Sturm et al. (2002): (a) L_{MIR} *vs.* $L([OIV])$ and $L([NeII])$, note the separation of Seyfert 1s (diamonds) and Seyfert 2s (asterisks) in the first diagram. (b) L_{FIR} *vs.* $L([OIV])$ and $L([NeII])$, note the better correlation with [Ne II], indicative of strong starburst contribution to FIR luminosities. Composite galaxies are shown with triangle symbols.

IR spectrum into pure AGN (a hot mid-IR continuum), pure H II region (a strong VSG continuum) and a pure PDR contribution (PAH spectrum). They suggest that the ratio of warm ($\sim$ 15 μm) to hot ($\sim$ 6 μm) continuum allows separation between the AGN and the H II component, while the ratio of a PAH feature flux to continuum flux of the underlying continuum allows separation between AGN component and PAH contribution from PDRs. These kinds of diagnostics are invaluable as most mid-IR observations have fairly large-apertures and most distant sources are unresolved, thus requiring a decomposition into different spectral components. As larger fractions of the host galaxy enter the beam of the telescope, the starburst component can dominate the AGN signatures; thus, use of fine structure diagnostics is superior to PAH-based diagnostics when studying effects due to AGN.

The most significant finding from ISO, in relation to Seyfert 1 and 2 galaxies was the mild anisotropy of the mid-IR continuum below $\sim$ 20 μm and its similarity above it. Further, the silicate absorption was detected only in a few nearby type 2 sources, but it is possible that this result was limited by the spectral sensitivity. Nevertheless, the implication is that the torus of the unified models may be more extended than previously thought and/or may be clumpy. The presence of a strong "warm" component in the FIR SEDs of Seyfert galaxies as opposed to presence of stronger "cold" component in FIR SEDs of normal galaxies, implies that Seyferts in general have stronger interstellar radiation fields in their centers. Whether the heating of nuclear dust is primarily due to starbursts or due to effects of the AGN is the key question that is still to be answered. Keeping the ideas discussed in this chapter, we will look at the Spitzer/IRS observations of Seyfert 1.8/1.9s in Chapter 6.

Chapter 5

Spitzer/IRS Instrument and Data Analysis

In this chapter we will look briefly at the *Spitzer Space Telescope* (SST, Werner et al. 2004). We will concentrate on the Infrared Spectrograph (IRS, Houck et al. 2004) and its instrument characteristics.

5.1 Spitzer Space Telescope

SST was launched 2003 August 25, and is one of NASA's Great Observatories, concentrating on infrared astronomy. The spacecraft is in an Earth-trailing solar orbit. An artist's rendering is shown Figure 5.1. *Spitzer* is a cryogenic telescope with good imaging and spectroscopic capabilities with modern IR detector arrays. Its projected cryogenic lifetime is in excess of 5 years. *Spitzer* has three main science instruments: the Infrared Spectrograph (IRS), the Infrared Array Camera (IRAC), and the Multi-band Imaging Photometer for *Spitzer* (MIPS). For broadband imaging and low-resolution spectroscopy, the *Spitzer* instruments have sensitivity close to or at the levels established by the natural astrophysical backgrounds—principally the zodiacal light. *Spitzer* recedes from Earth at a rate of about 0.12 AU yr^{-1}. The principal use of

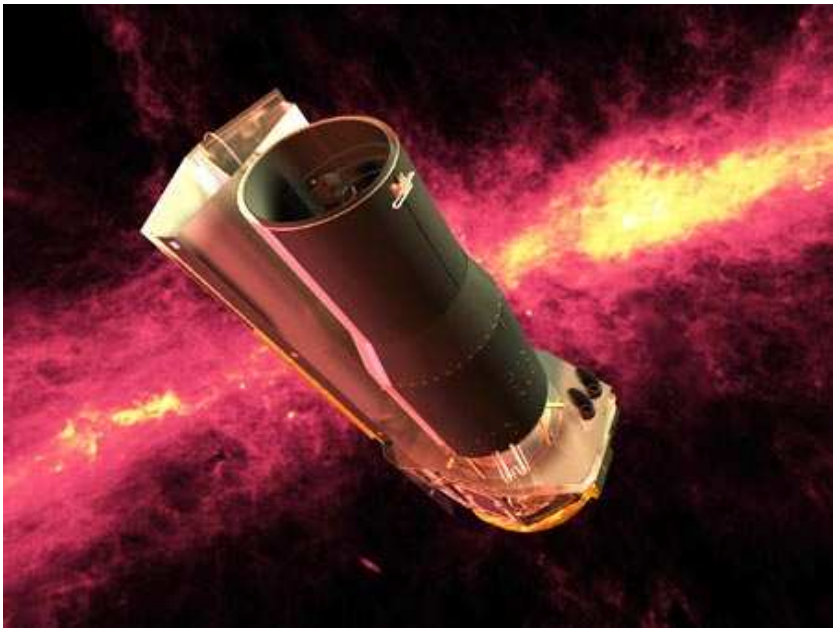

Figure 5.1: An artist's rendering of *Spitzer* space telescope against the infrared sky background. (`http://ssc.spitzer.caltech.edu/`)

the Earth-trailing orbit is to be away from the heat generated by the Earth; this allows radiative cooling of the telescope assisting in the telescope's cryothermal design to be very efficient. The observing time on *Spitzer* is divided among the three major categories of users: General Observers (GO), Legacy Science Teams, and Guaranteed Time Observers (GTO). The GTO's receive 20% of the time for the first 2.5 yr and 15% thereafter. In addition, up to 5% of the observing time can be allocated as Director's Discretionary Time, while the rest of the time is available for GO use. The GO time constitutes about $\sim$ 75% of the available observing time. An overview of instrument wavelength coverage, beam size and detector arrays for all three science instruments is given in Werner et al. (2004).

5.2 IRS Instrument Characteristics

The IRS is described in detail by Houck et al. (2004). The IRS comprises four separate spectrograph modules covering a mid-IR wavelength range of 5.3 to 38 μm with spectral resolutions $\lambda/\Delta\lambda \approx 90$ and 600. The four modules are: Short-Low (SL, short wavelength low resolution), Short-High (SH), Long-Low (LL) and Long-High (LH). The pixel scale, slit width, wavelength coverage and resolution for each of these four modules is given in Table 5.1.

Table 5.1: Instrument Properties of the Infrared Spectrograph.

Module	Array	Pixel Scale (arcsec)	Order	Slit Size (arcsec)	λ (μm)	$\lambda/\Delta\lambda$
Short-Low	Si:As	1.8	SL2	3.6×57	$5.2 - 7.7^a$	80-128
			SL1	3.7×57	$7.4 - 14.5$	64-128
			"Blue" Peak-Up	56×80	$13.3 - 18.7^b$	~ 3
			"Red" Peak-Up	54×82	$18.5 - 26.0^b$	~ 3
Long-Low	Si:Sb	5.1	LL2	10.5×168	$14.0 - 21.3^a$	80-128
			LL1	10.7×168	$19.5 - 38.0$	64-128
Short-Hi	Si:As	2.3	11-20	4.7×11.3	$9.9 - 19.6^a$	~ 600
Long-Hi	Si:Sb	4.5	11-20	11.1×22.3	$18.7 - 37.2^a$	~ 600

[a] The bonus orders cover 7.3–8.7 μm (SL) and 19.4–21.7 μm (LL).

[b] This is the full width at half-maximum of the filter.

The low-resolution modules each contain two sub-slits, one for the first-order spectrum and one for the second-order spectrum. When the source is in the sub-slit for the second order, a short piece of the first order appears on the detector array; this is the "bonus" order (see Figure 5.2). The high-resolution modules are cross-dispersed so that 10 orders (11-20) fall on the detector array.

The IRS supports two modes of operation, the "staring" and "mapping" modes. The "staring" mode is the basic mode of operation and it results in observing the target source at the 1/3 and 2/3 positions along the slit. This results in what is referred to as two "nod" positions per SL/LL exposure. The mapping mode steps the slit parallel and/or perpendicular to the slit according to the number and size of the step requested by the observer. The mapping mode does not perform the "nod" observations that are automatically done in the staring mode. The IRS has two pick-up imag-

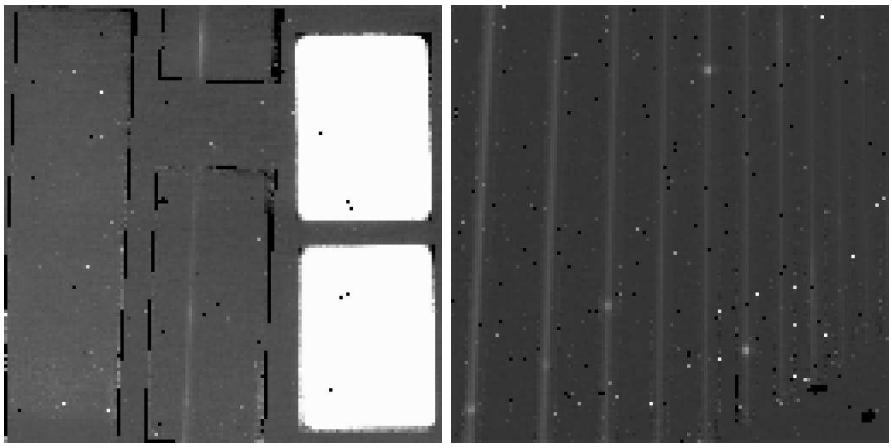

(a) SL and SH Detector Images

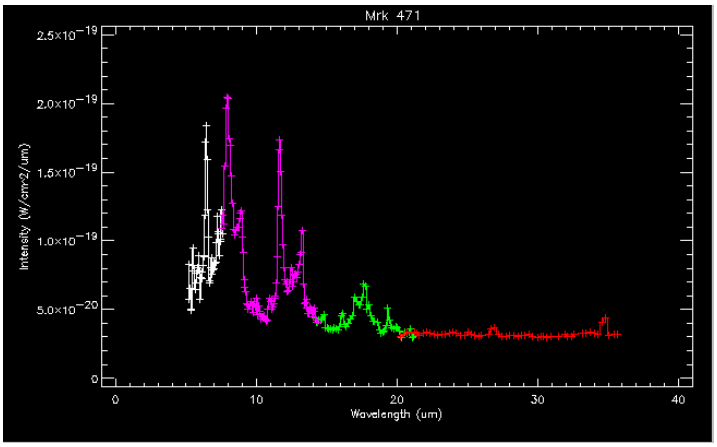

(b) Spectrum of Mrk 471

Figure 5.2: (a) Median-combined SL and SH detector images for Mrk 883 from our data. In the SL image, rectangle on left and middle-bottom delimits the main order, the bonus order falls inside top-middle rectangle. (b) Example spectrum of Mrk 471 showing the SL2 (white), SL1 (Pink), LL2 (Green), LL1 (Red) spectral modules. The data has been cleaned of bad points and bonus orders.

ing fields (bright rectangular fields in Figure 5.2); these are used to improve upon the blind pointing of the telescope based on coordinates specified by the observer. An on-board centroiding algorithm uses the data from pick-up arrays to offset the source position, so that the source is centered within the spectrograph slits accurately.

5.3 Notes on IRS Data Reductions

The IRS observations are stored as `.fits` files and are supplied to the observers from the *Spitzer* Science Center archive via the `leopard` software. The data provided are organized into the following four categories: Engineering Pipeline Data, Basic Calibrated Data (BCD), Browse-Quality Data (BQD), and Calibration Data. Additional files such as processing logs, quality analysis files and detector masks are also available. The entire dataset per target can be retrieved as a compressed Zip file via `leopard`.

The BCD form the basic data files from which scientific data processing can begin. These are 2-D detector images of each Data Collection Event (DCE, or exposure) in units of number of electrons s^{-1}pixel^{-1}. Additional BCD data files include the uncertainty image, the bad pixel mask and other intermediate images generated during pipeline-processing. Additionally, the BCD files can also contain co-added images for those observations with more than one ramp (a detector read pattern) at a target position. As an example of a standard IRS staring mode observation, if the observer has requested three cycles of 30 second integrations on a science target with the SH module, it will result in six DCEs (three integration cycles at each of the two "nod" positions) in Raw data collection mode. Each of the six DCEs has the form of a data cube, where each plane is $128 \times 128 \times n$, and n can be 4, 8 or 16. Here n is the number of read patterns of the full 128×128 detector. The pipeline performs checks for saturation, cosmic rays, dark current subtraction and linearization, before fitting a slope to the sampled detector image pixels

from n read patterns in the cube. Other corrections such as stray light or cross-talk between orders and drifts in dark currents are applied after the slope image is created. Thus, the BCD pipeline will produce six 128×128 DCE slope images, as well as two 128×128 co-added slope images for the "nod" positions. Further, calibration and extraction of the spectrum is then done with software like SPICE and SMART (see Appendix C). The BQD files contain the first-look spectra extracted from two-dimensional BCD images. These are extracted automatically by the post-BCD pipeline by using a search algorithm to trace the spectrum in the two-dimensional image. The spectra are extracted using an aperture that follows the linear expansion of the point spread function (PSF) with wavelength. In the post-BCD pipeline all spectra are extracted as point sources and no sky background subtractions are done. Hence the output spectra are only usable for quick-look purposes.

The post-BCD scientific processing of the data can be done with two tools: *Spitzer* IRS Custom Extraction (SPICE)[1] and Spectroscopy modeling, analysis and reduction tool (SMART). We have used SMART[2] (Higdon et al. 2004) for extraction of our data and the steps described in Appendix C refer to this software package. For mapping mode observations, one can use the CUbe Builder for IRS Spectra Maps, CUBISM[3]. CUBISM and SMART are IDL-based tools, while SPICE is Java-based. Apart from these there are two other software packages that are useful. One is IRSCLEAN[4], which is used to update the bad pixel masks and flag rogue pixels that are not flagged by the automated pipeline. Since the locations of rogue pixels in *Spitzer* detectors vary and increase with time, this has been noted as a pressing issue and should be thus corrected in detector images before attempting extraction. Another tool is IRSFRINGE[5]. This tool is included with the SMART package

[1]SPICE: `http://ssc.spitzer.caltech.edu/postbcd/spice.html`
[2]SMART: `http://ssc.spitzer.caltech.edu/archanaly/contributed/smart/`
[3]CUBISM: `http://ssc.spitzer.caltech.edu/archanaly/contributed/cubism/`
[4]IRSCLEAN: `http://ssc.spitzer.caltech.edu/postbcd/irsclean.html`
[5]IRSFRINGE: `http://ssc.spitzer.caltech.edu/postbcd/irsfringe.html`

and hence separate installation is not necessary. The mid-IR spectral traces show fringing effects and they can be removed using this tool, which attempts to fit multiple sinusoids to flag deviant data points associated with the fringe pattern.

5.4 Data reduction process

The post-BCD analysis and reduction of data can be done with SMART or SPICE. Here we will provide only a brief summary of data reduction steps. A detailed tutorial with step-by-step instructions is given in Appendix C. The basic process of post-BCD analysis is as follows. One loads the BCD image files in the SMART software. Each image is cleaned of bad pixels and/or rogue pixels using the IRSCLEAN tool. This tool also updates the bad-pixel masks, so that the updated information is propagated in the pipeline. The key step after cleaning the images is to perform sky background removal. This is normally achieved by employing the off-source images. The off-source image is subtracted from the on-source image to remove the sky background. The removal of the sky background can also be done after spectra have been extracted, but the former process yields better results. The spectra are then extracted from the background subtracted images for each "nod" position of a given order and module, *e.g.,* nod position 1 for SL1. Thus, per SL module, we have orders 1 and 2, and for each order we have two spectra at the two nod positions. Once all spectra per module are extracted, they are averaged together to form a single spectrum for a given order. Finally, after all spectra have been extracted and combined, we end up with four pieces of the spectrum, SL2, SL1, LL2 and LL1, in order of increasing wavelength from 5.3 to 38 μm. In practice, the response of the spectrum deteriorates beyond ~ 35 μm and below 5.5 μm. These separate module spectra are then stitched together, by estimating the scale factors between the modules. If

the scale factors vary more than $\sim 10\%$, the cause of the variation should be investigated (*e.g.,* the source may be extended in the spectrograph slit).

After the complete spectrum from $5 - 38$ μm is formed, it can be resampled to a common wavelength grid and analyzed using commonly available spectral analysis routines in IDL. We employed the FEATURE routine, which is generic enough to be applied to any spectra. Using the facilities provided by the feature routine, we measured fluxes and equivalent widths. The continuum for the entire spectrum was fit using a spline-fitting routine. The fit was guided by fiducial flux points at 5.5, 14.5, 20 and 30 μm. Additional points were selected if necessary to guide the fit. It should be noted that the fitted continuum was used only during the measurements of the equivalent widths. The measurement of continuum fluxes at the above mentioned fiducial points and the emission feature fluxes was done directly on the complete spectrum. These measurements are reported in Chapter 7.

Chapter 6

Mid-IR Spectra of Seyfert 1.8/1.9s

We saw how *Spitzer* /IRS mid-IR spectra can be reduced in the last chapter. Here we will focus on the mid-IR spectroscopic dataset that we are using in this dissertation. Specifically we will look at the spectra of 12 Seyfert 1.8/1.9s from our accepted GO program. We will also look at some example Seyfert spectra from the *Spitzer* archives and comment on their properties. We will focus on morphology of spectra in this chapter and elucidate points that will lead to the diagnostic relations in Chapter 7.

We have obtained IRS staring mode observations of 12 Seyfert 1.8/1.9 galaxies. The *Spitzer* general observer proposal #3374, PI: Prof. S. Kraemer, proposed mid-IR observations of Seyfert 1.8/1.9s to constrain the location, geometry and the physical properties of the dusty torus. This proposal was based on the premise that under unified schemes, the line of sight to the central continuum source in Seyfert 1.8/1.9s will have a grazing incidence through the torus atmosphere. If so, then multi-wavelength observations of a set of Seyfert 1.8/1.9s should be able to constrain the geometry and scale height of the torus. Further, we saw in Chapter 3 that nuclear regions of type 1 Seyfert galaxies host large quantities of dust. Since large amounts of

dusty material could have a bearing on the observed properties of Seyfert 1.8/1.9s, it was proposed that observing face-on Seyfert 1.8/1.9s, where host galaxy extinction is small, will provide a good handle on the nature of dust very close to the central source. Thus, torus models can be eventually be tested and constrained using these data. Towards this goal, we have obtained low resolution as well as high resolution IRS spectra of 12 roughly face-on nearby ($z \approx 0.01$) Seyfert 1.8/1.9s. At the distances corresponding to this redshift, $1''$ corresponds to ~ 200 pc for $H_0 = 71$ km s^{-1} Mpc^{-1}. Thus, for a full aperture extraction, the SL slit width (see Table 5.1) will sample about 730 pc at z of 0.01.

The 12 galaxies in our sample are listed in Table 6.1 with their respective Seyfert type, the ratio of minor to major axis (b/a) of the host galaxies and their redshifts. The reduced low resolution IRS spectra of these Seyferts are displayed in Figure 6.1. We plot the spectra as F_λ *vs.* λ instead of the customary F_ν *vs.* λ, as it allows us to study the spectral features in the 6–15 μm range in better contrast to the 20–30 μm range. NGC 7603 and NGC 2622 have transitioned from a Seyfert 1.8 to a Seyfert 1.5 state and back several times (Goodrich 1995). As we discuss later, based on the nature of the mid-IR spectra of these objects, we consider them to be in the Seyfert 1.5 state at the time of the Spitzer observations. Also, as we will demonstrate below, based on the mid-IR spectrum, Mrk 622 is a Seyfert 2 rather than a Seyfert 1.9. This leaves a total of 9 galaxies which are Seyfert 1.8/1.9.

To compare our Seyfert 1.8 and 1.9 datasets with the spectra of Seyfert 1s and Seyfert 2s, we obtained the available *Spitzer* archival datasets originally presented in Buchanan et al. (2006) and Weedman et al. (2005). The observations by Buchanan et al. (2006) are IRS spectral maps; hence we have extracted spectra only from the central slit with the nuclear point source. These comprise a total of 19 Seyfert 1–1.5s including NGC 7603, 4 Seyfert 1.8/1.9s (NGC 4579, NGC 4602, NGC 7314 and UGC 7064), and 35 Seyfert 2 galaxies. NGC 7603 and UGC 7064 are common between this dataset and

Table 6.1. Sample of Seyfert 1.8 and 1.9 galaxies.

Galaxy Name	z	b/a	Seyfert Type
Mrk 471	0.034	0.67	Sey 1.8
Mrk 622	0.023	0.95	Sey 2[b]
Mrk 883	0.038	1.00	Sey 1.8
NGC 2622	0.029	0.50	Sey 1.5[a]
Mrk 334	0.022	0.70	Sey 1.8
UGC 7064	0.025	1.00	Sey 1.8
Mrk 609	0.034	0.90	Sey 1.8
NGC 7603	0.030	0.67	Sey 1.5[a]
UM 146	0.017	0.77	Sey 1.9
UGC 12138	0.025	0.88	Sey 1.8
NGC 2639	0.011	0.61	Sey 1.9
NGC 3786	0.009	0.59	Sey 1.8

Note. — The redshift of galaxies (z), the b/a and the Seyfert type are taken from the NASA Extra-galactic Database (NED).

[a]Both these galaxies were originally expected to be Seyfert 1.8 but have likely transitioned to a Seyfert 1.5 class (Goodrich 1995).

[b]Based on the appearance of its mid-IR spectrum we note that this is a Seyfert 2.

our dataset. We take the dataset for Mrk 3 (Seyfert 2) and M82 (starburst) from Weedman et al. (2005). These galaxies are listed in Table 6.2 along with their redshifts and b/a values. Thus the total sample (69) we discuss in this dissertation comprises 20 Seyfert 1/1.5s (with NGC 7603 and NGC 2622 considered as Seyfert 1.5s), 37 Seyfert 2s (with Mrk 622 considered as a Seyfert 2 and Mrk 3 from Weedman et al. 2005) and 12 Seyfert 1.8/1.9s (9 from our datasets, 3 from Buchanan et al. 2006).

Table 6.2. *Spitzer* Archival Datasets: Galaxy properties.

Galaxy	Redshift	b/a	Seyfert Type[a]	*Spitzer* Dataset ID	P.I.
CGCG381-051	0.031	0.67	Sey 2	r1248332	Gallimore
E33-G2	0.018	0.82	Sey 2	r1247308	Gallimore
F01475-0740	0.018	0.83	Sey 2	r1247488	Gallimore
F04385-0828	0.015	0.50	Sey 2	r1244723	Gallimore
F15480-0344	0.030	0.84	Sey 2	r1248025	Gallimore
IC4329A	0.016	0.29	Sey 1.2	r1248000	Gallimore
M-2-33-34	0.015	0.58	Sey 1	r1248128	Gallimore
M-2-40-4	0.025	0.81	Sey 2	r1248153	Gallimore
M-2-8-39	0.030	0.69	Sey 2	r1247692	Gallimore
M-3-34-63	0.021	0.29	Sey 2	r1247769	Gallimore
M-3-58-7	0.031	0.80	Sey 2	r1245798	Gallimore
M-5-13-17	0.013	0.67	Sey 1.5	r1246848	Gallimore
M-6-30-15	0.008	0.60	Sey 1.2	r1245747	Gallimore
Mrk 335	0.026	1.00	Sey 1.2	r1247641	Gallimore
Mrk 348	0.015	0.78	Sey 2	r1247283	Gallimore
Mrk 6	0.019	0.63	Sey 1.5	r1248358	Gallimore
Mrk 79	0.022	0.52	Sey 1.2	r1245363	Gallimore
Mrk 817	0.031	0.80	Sey 1.5	r1246105	Gallimore
Mrk 938	0.020	0.36	Sey 2	r1247385	Gallimore
Mrk 9	0.040	0.80	Sey 1.5	r1248307	Gallimore
NGC 1056	0.005	0.48	Sey 2	r1246489	Gallimore
NGC 1068	0.004	0.85	Sey 2	r1246156	Gallimore
NGC 1125	0.011	0.50	Sey 2	r1245465	Gallimore
NGC 1143-4	0.028	0.89	Sey 2	r1244851	Gallimore
NGC 1194	0.014	0.48	Sey 1	r1247206	Gallimore
NGC 1241	0.014	0.61	Sey 2	r1246822	Gallimore
NGC 1320	0.009	0.32	Sey 2	r1245440	Gallimore
NGC 1667	0.015	0.78	Sey 2	r1245952	Gallimore
NGC 3079	0.004	0.18	Sey 2	r1247513	Gallimore
NGC 3227	0.004	0.67	Sey 1.5	r1245030	Gallimore
NGC 3516	0.009	0.76	Sey 1.5	r1247334	Gallimore
NGC 3982	0.004	0.88	Sey 2	r1244953	Gallimore
NGC 4051	0.002	0.75	Sey 1.5	r1245107	Gallimore
NGC 4151	0.003	0.71	Sey 1.5	r1247078	Gallimore
NGC 424	0.012	0.44	Sey 2	r1244416	Gallimore
NGC 4579	0.005	0.80	Sey 1.9	r1246208	Gallimore

Table 6.2—Continued

Galaxy	Redshift	b/a	Seyfert Type[a]	*Spitzer* Dataset ID	P.I.
NGC 4602	0.008	0.35	Sey 1.9	r1246566	Gallimore
NGC 4922	0.024	0.74	Sey 2	r1247795	Gallimore
NGC 4941	0.004	0.53	Sey 2	r1247155	Gallimore
NGC 4968	0.010	0.47	Sey 2	r1246412	Gallimore
NGC 5005[b]	0.003	0.48	LINER	r1247564	Gallimore
NGC 513	0.020	0.43	Sey 2	r1246771	Gallimore
NGC 5256	0.028	0.89	Sey 2	r1245926	Gallimore
NGC 526A	0.019	0.53	Sey 1.5	r1245491	Gallimore
NGC 5347	0.008	0.76	Sey 2	r1248179	Gallimore
NGC 5548	0.017	0.93	Sey 1.5	r1248102	Gallimore
NGC 5929	0.008	0.78	Sey 2	r1244492	Gallimore
NGC 5953	0.007	0.81	Sey 2	r1247616	Gallimore
NGC 7130	0.016	0.93	Sey 2	r1246361	Gallimore
NGC 7172	0.009	0.56	Sey 2	r1245004	Gallimore
NGC 7314	0.005	0.46	Sey 1.9	r1246950	Gallimore
NGC 7469	0.016	0.73	Sey 1.2	r1247232	Gallimore
NGC 7496	0.006	0.91	Sey 2	r1246233	Gallimore
NGC 7603	0.030	0.67	Sey 1.5	r1245081	Gallimore
NGC 7674	0.029	0.91	Sey 2	r1246873	Gallimore
NGC 931	0.017	0.21	Sey 1.5	r1246003	Gallimore
TOL1238-364	0.011	0.88	Sey 2	r1246643	Gallimore
UGC 11680	0.026	0.39	Sey 2	r1245900	Gallimore
UGC 7064	0.025	0.90	Sey 1.9	r1246745	Gallimore
M 82	0.001	0.38	Sbrst	r7830016	Houck
Mrk 3	0.014	0.89	Sey 2	r3753472	Houck

[a]The Seyfert types and b/a are taken from the NASA Extra-galactic Database (NED).

[b]NGC 5005 is classified as a LINER object and we exclude this object when studying spectral characteristics of the Seyfert sample. This galaxy is not included in plots we present further ahead in Chapter 7

Apart from the low resolution dataset for the 9 Seyfert 1.8/1.9s, 2 Seyfert 1s and 1 Seyfert 2 in our proposal sample, we also have high resolution observations for these systems. These spectra have not been used in the study so far, except to check for line blending, due to their very noisy continua and uncertain flux levels. A future study will be done to characterize these spectra. The archival datasets from Buchanan et al. (2006) do not have high resolution spectra.

6.1 Spectra of Seyfert 1.8/1.9s

Our Seyfert 1.8/1.9s spectra are displayed in Figure 6.1. Immediately apparent from looking at the spectra is the dominance of PAH bands. There appears to be strong starburst contribution. However, some spectra like NGC 7603, NGC 2622, UGC 7064, UM 146, UGC 12138 and NGC 2639 show strong rise in continuum at short wavelengths, the most extreme being NGC 7603. The spectrum of Mrk 622 shows weakening of the continuum in the 5–15 μm range in contrast to the behavior seen in all other spectra. UM 146, UGC 12138 and NGC 2639 appear to show the presence a silicate absorption component around 10 μm; in other sources, it is not clear if the deepness of the continuum around 10 μm is due to the silicate absorption or the presence of PAH complexes. Overall, it seems that the silicate absorption component is weaker than for example detected in the ISO spectrum of NGC 1068. There are several forbidden low-ionization lines like [Ne II] 12.81 μm and [Si II] 34.82 μm that trace the starburst component (Sturm et al. 2002). Apart from these, there are high-ionization lines like [O IV] 25.89 μm, [Ne III] 15.56 μm, [S III] 18.71 μm, [Ne V] 14.32 μm and [Ne V] 24.32 μm, which are all indicators of strongly photo-ionized NLRs by the incident optical/UV nuclear continuum in these systems. The strengths of the high-ionization lines like [O IV] 25.89 μm that arise in the NLR are directly related to the strength of the incident AGN continuum (Melendez, M.B. *et al.*, in preparation; see also Figure 4.4).

6.2 Spectra of Type 1 and Type 2 Seyferts

Recent studies (Hao et al. 2007; Spoon et al. 2007; Buchanan et al. 2006; Weedman et al. 2005) with *Spitzer* have focused on obtaining and analyzing the spectra of local Seyfert galaxies. We display the archival *Spitzer* mid-IR spectra (re-reduced by us from raw data files) of Seyfert 1s listed in Table 6.2

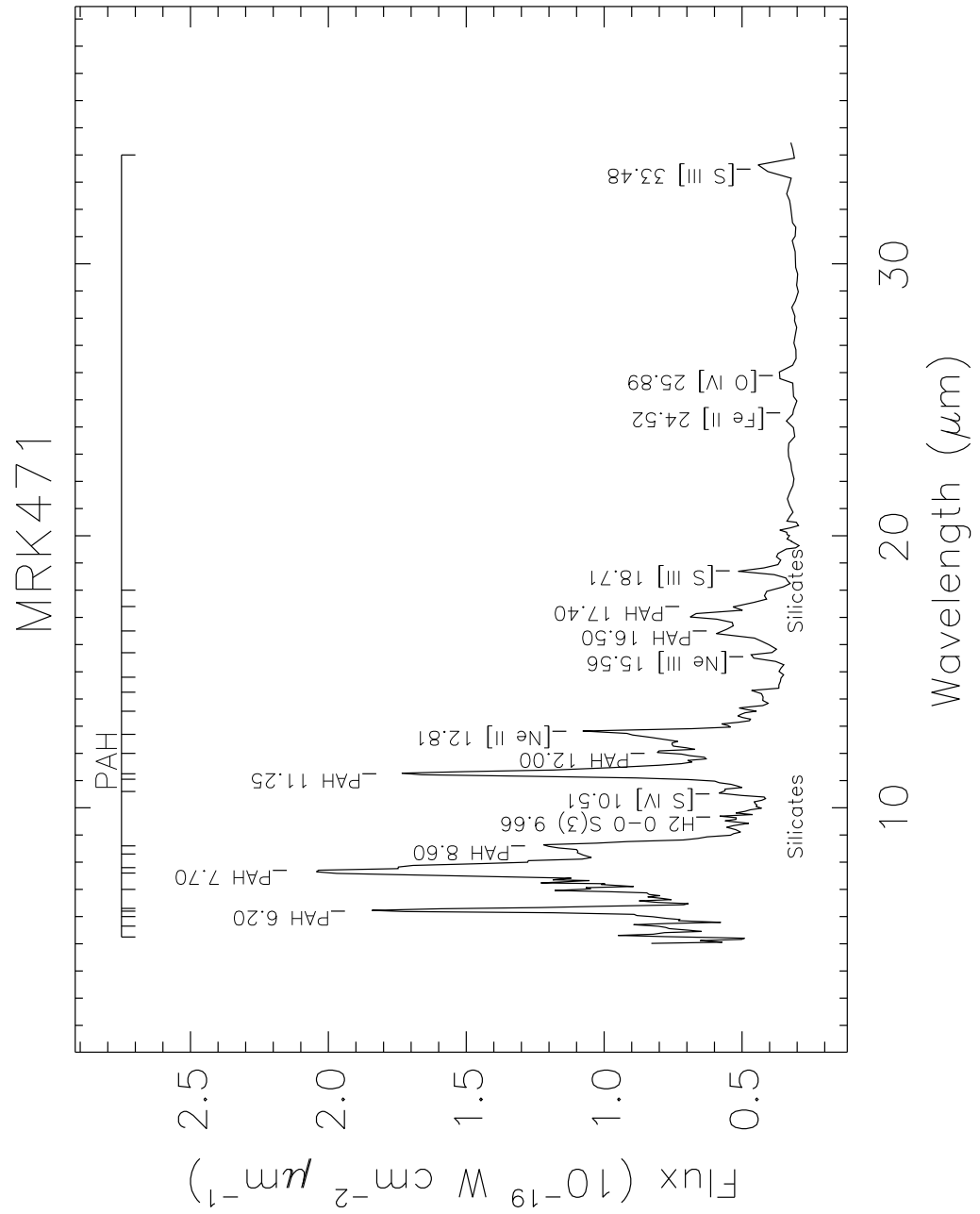

Figure 6.1: *Spitzer* mid-IR spectrum of Mrk 471

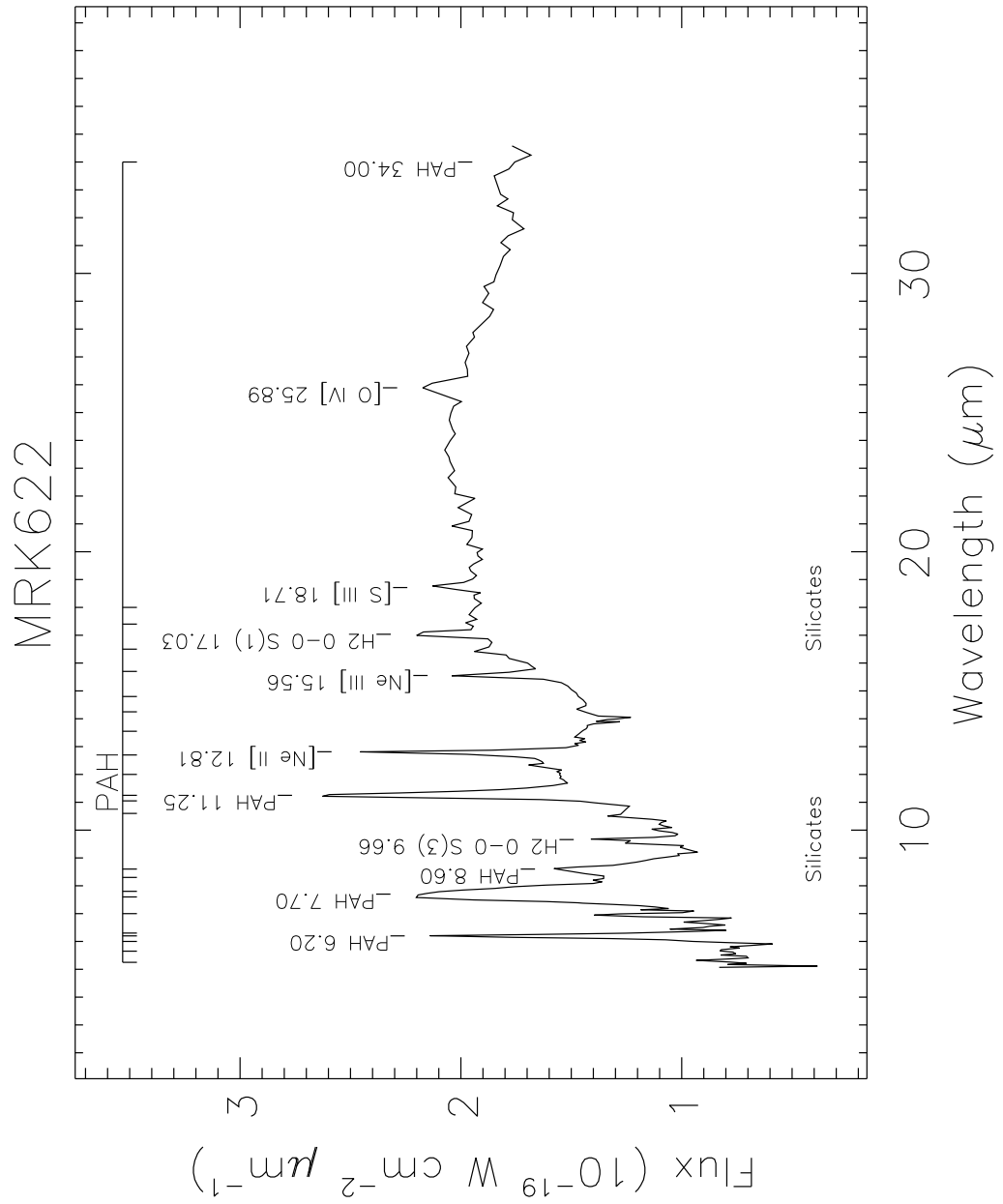

Figure 6.1: *Spitzer* mid-IR spectrum of Mrk 622

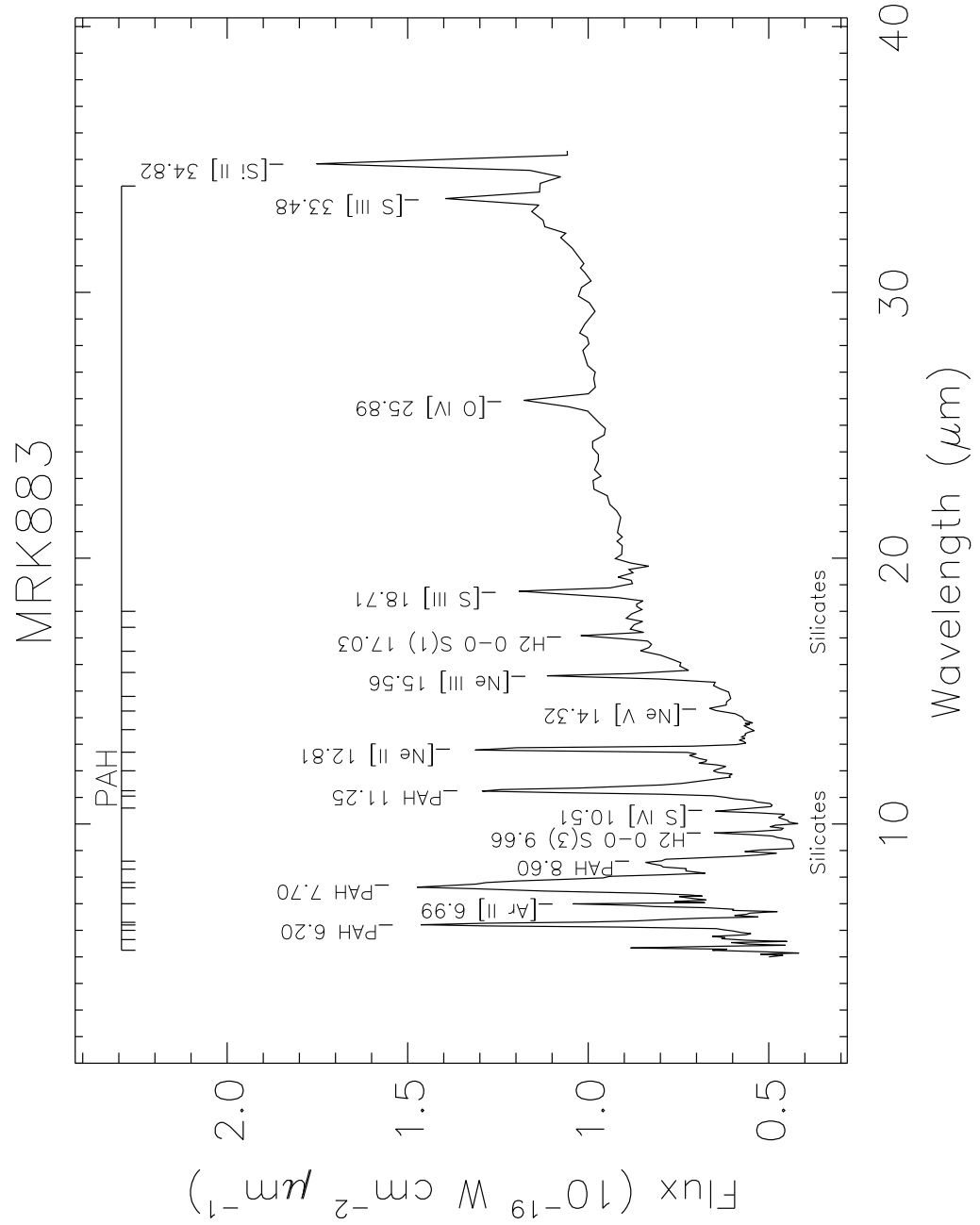

Figure 6.1: *Spitzer* mid-IR spectrum of Mrk 883

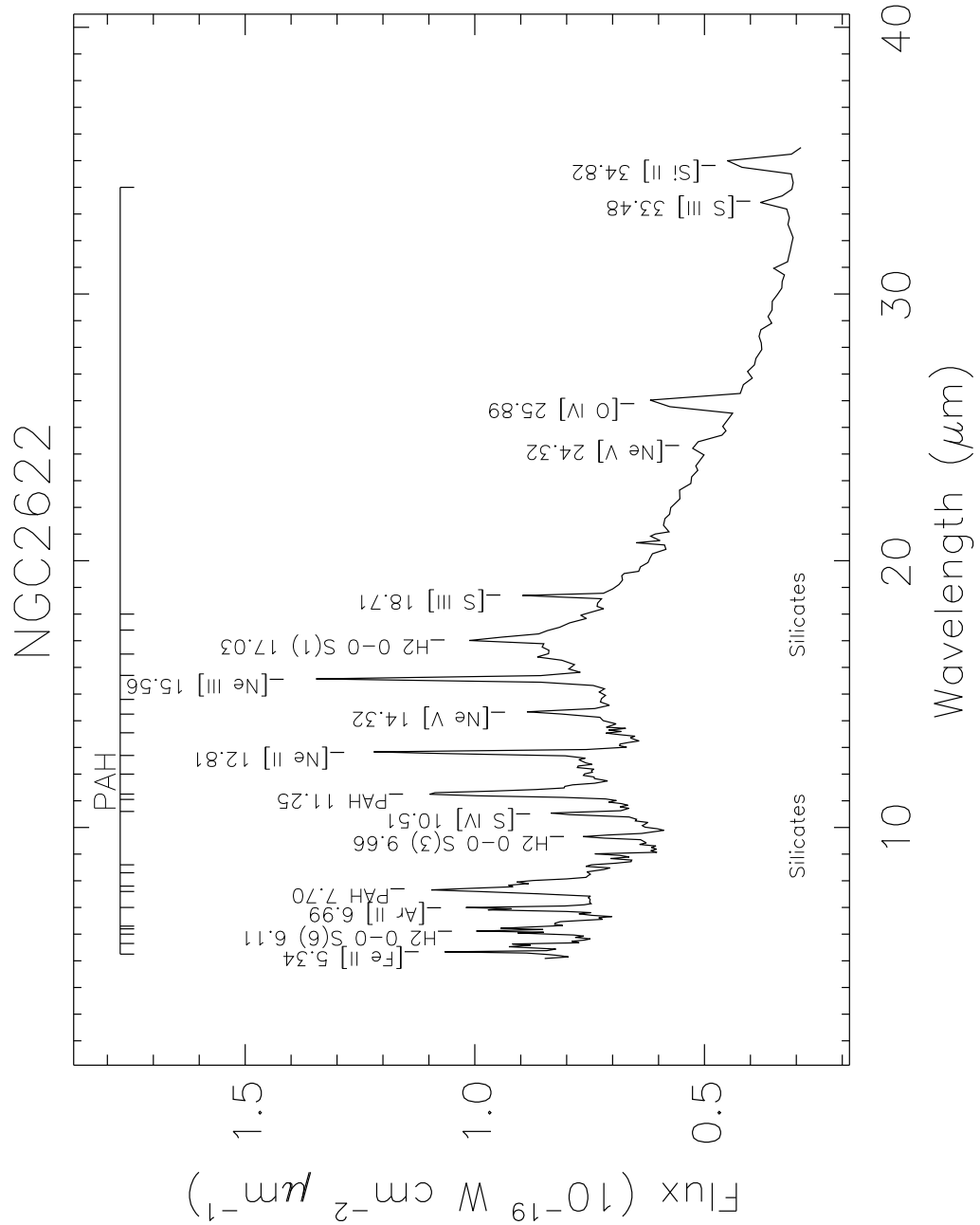

Figure 6.1: *Spitzer* mid-IR spectrum of NGC 2622

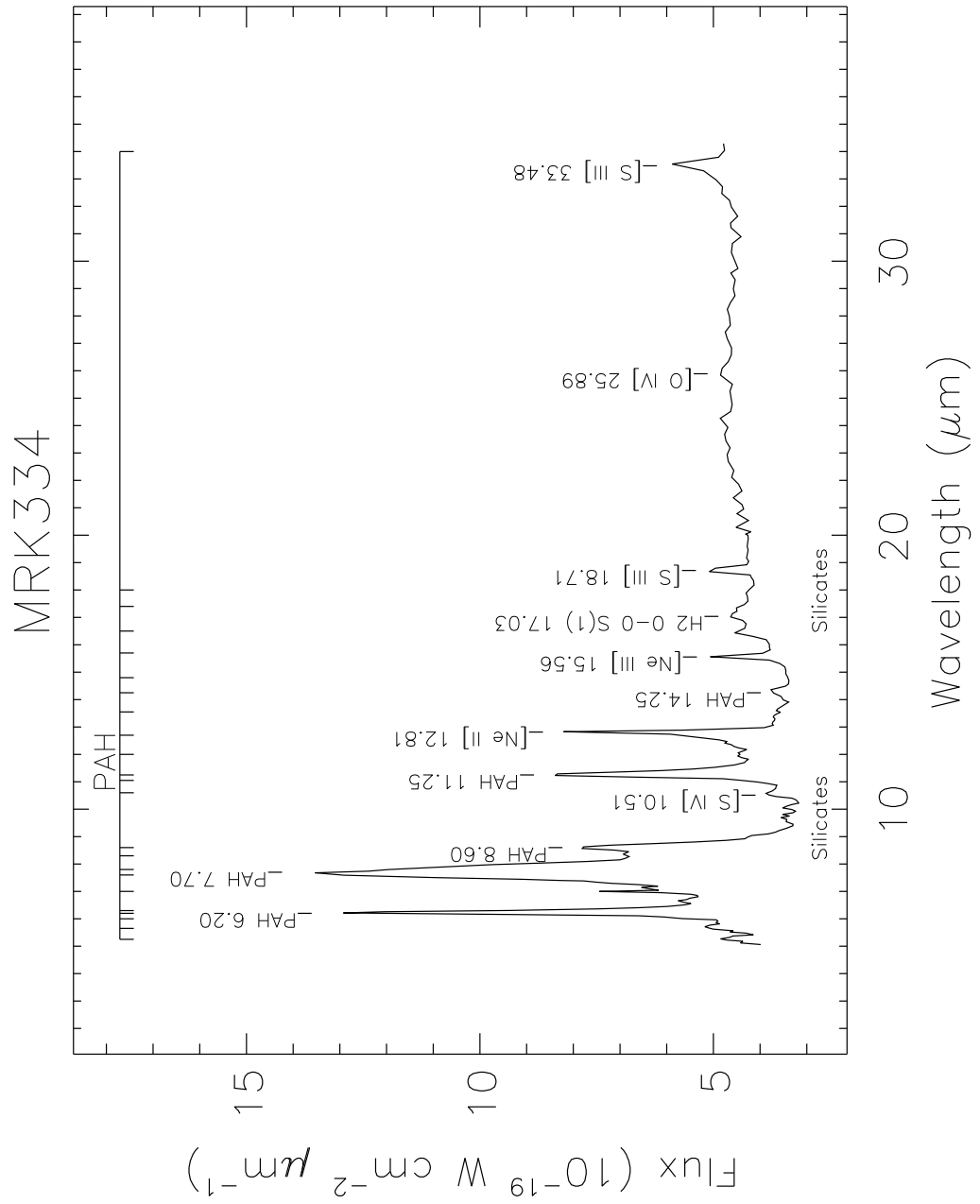

Figure 6.1: *Spitzer* mid-IR spectrum of Mrk 334

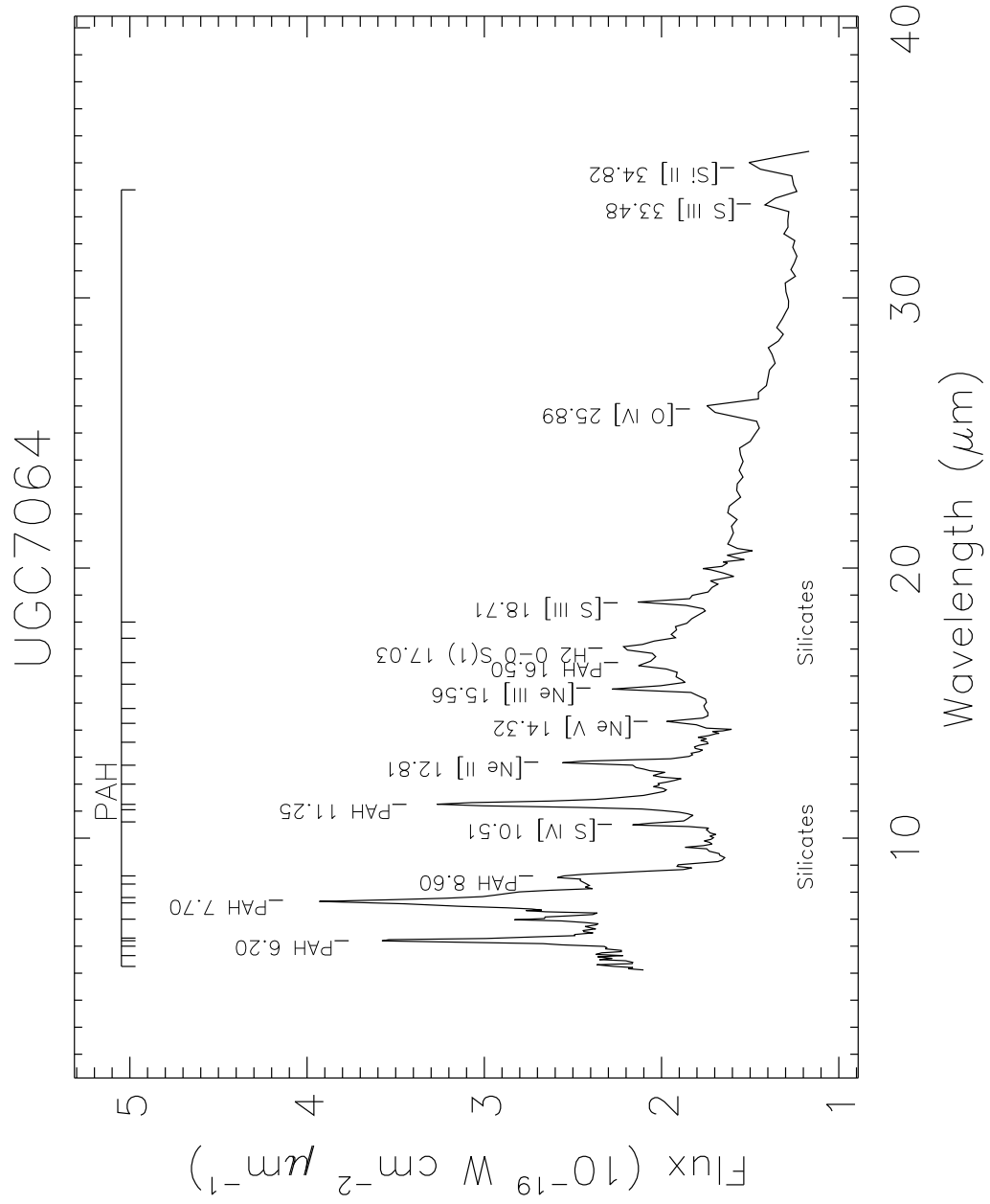

Figure 6.1: *Spitzer* mid-IR spectrum of UGC 7064

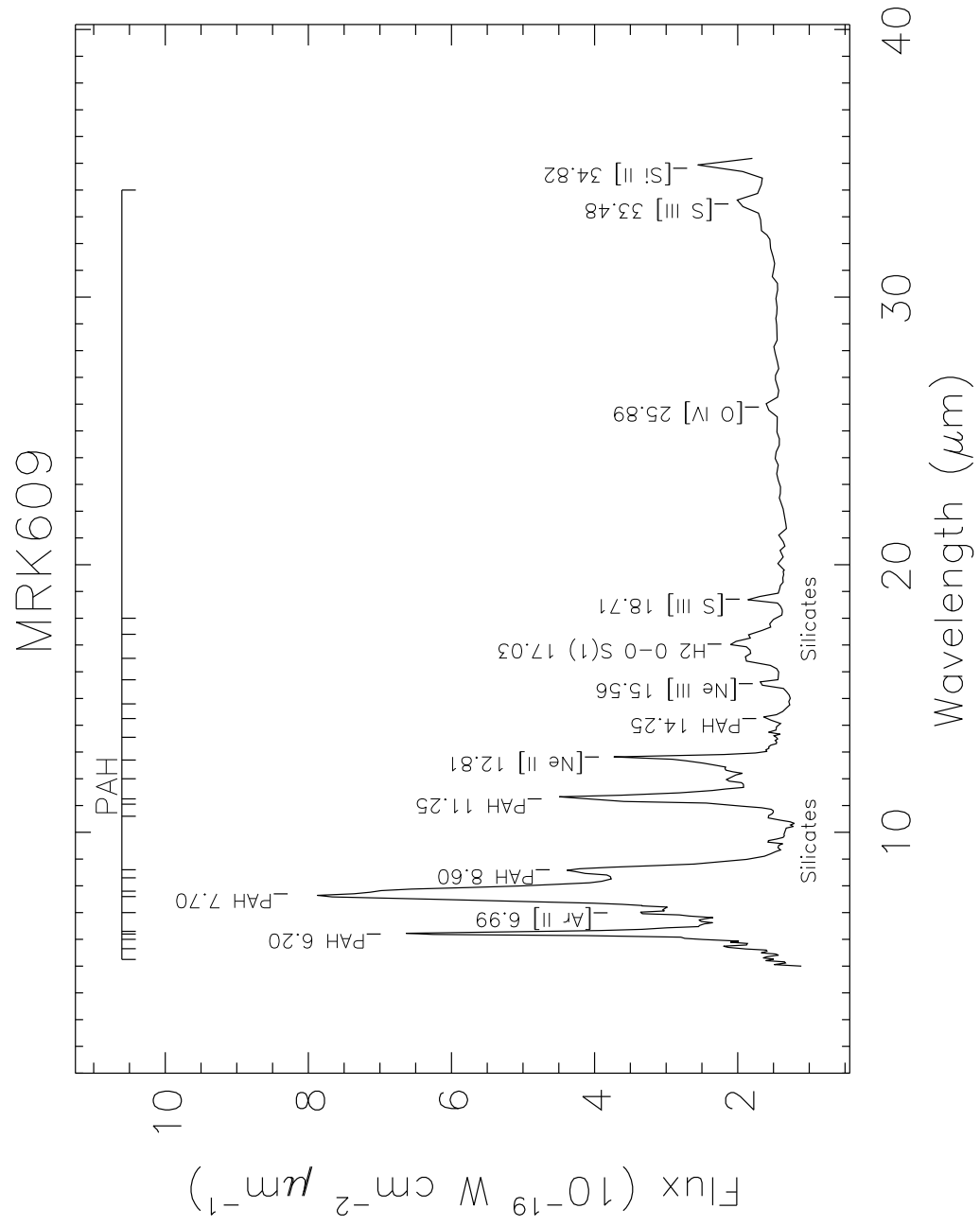

Figure 6.1: *Spitzer* mid-IR spectrum of Mrk 609

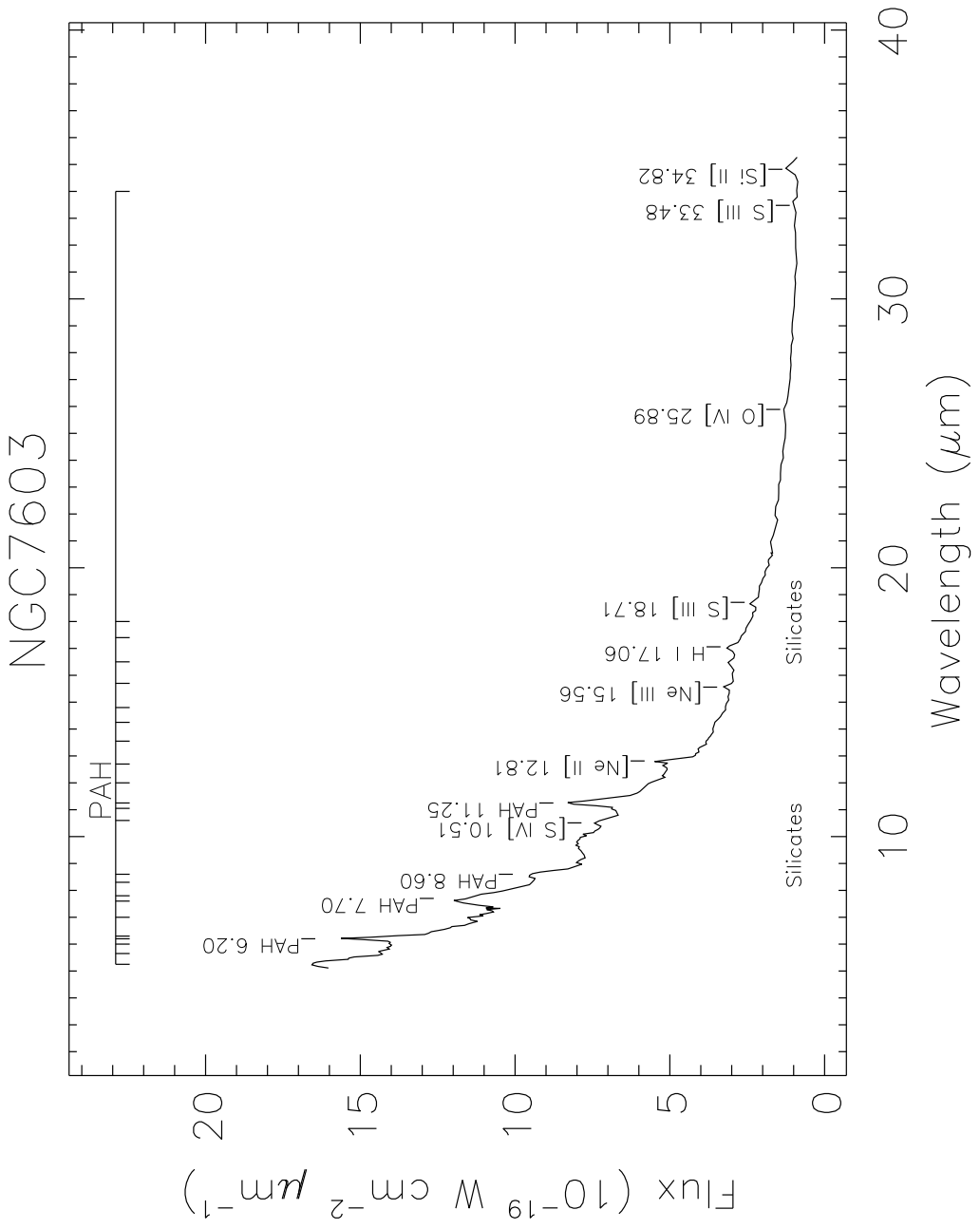

Figure 6.1: *Spitzer* mid-IR spectrum of NGC 7603

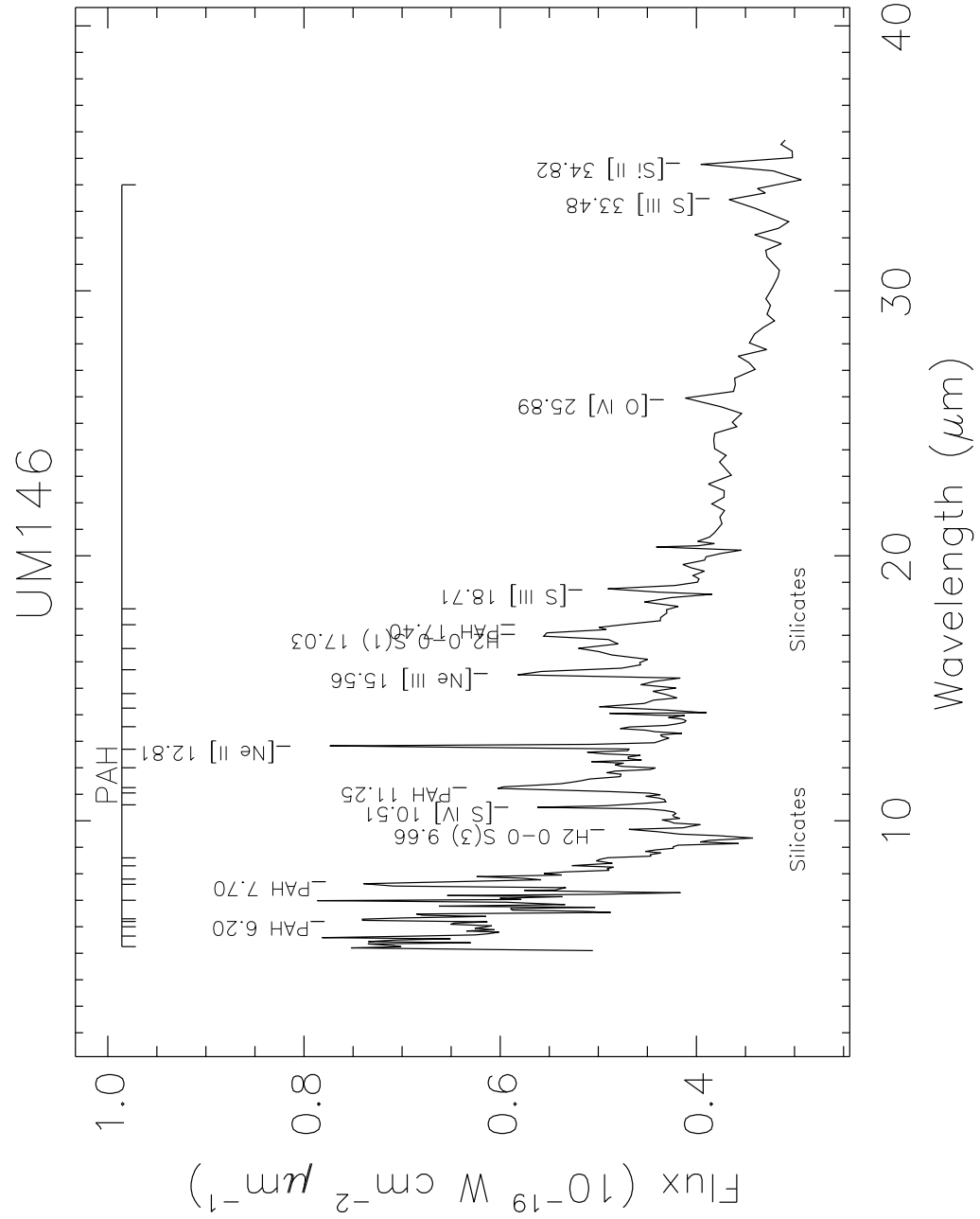

Figure 6.1: *Spitzer* mid-IR spectrum of UM 146

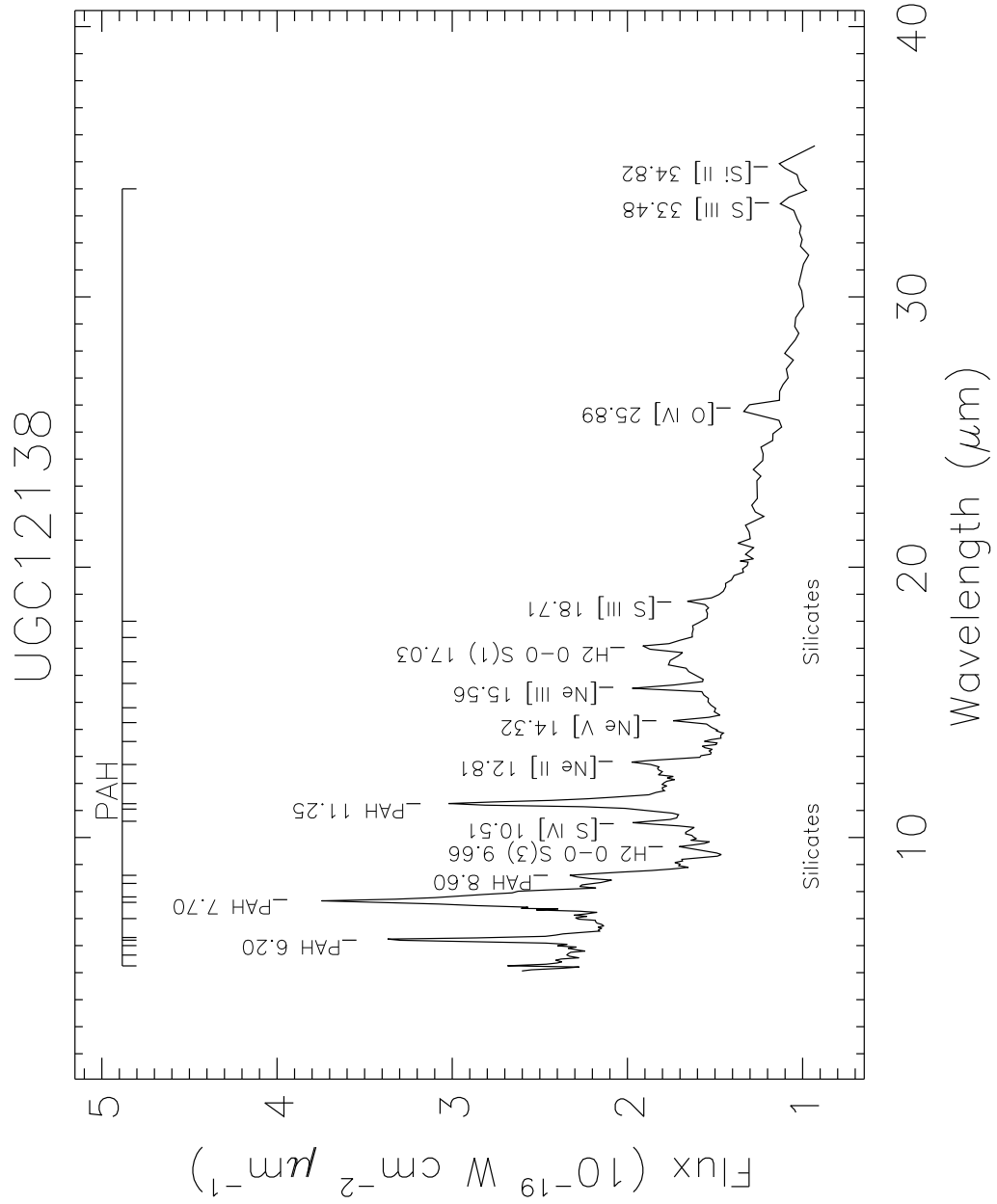

Figure 6.1: *Spitzer* mid-IR spectrum of UGC 12138

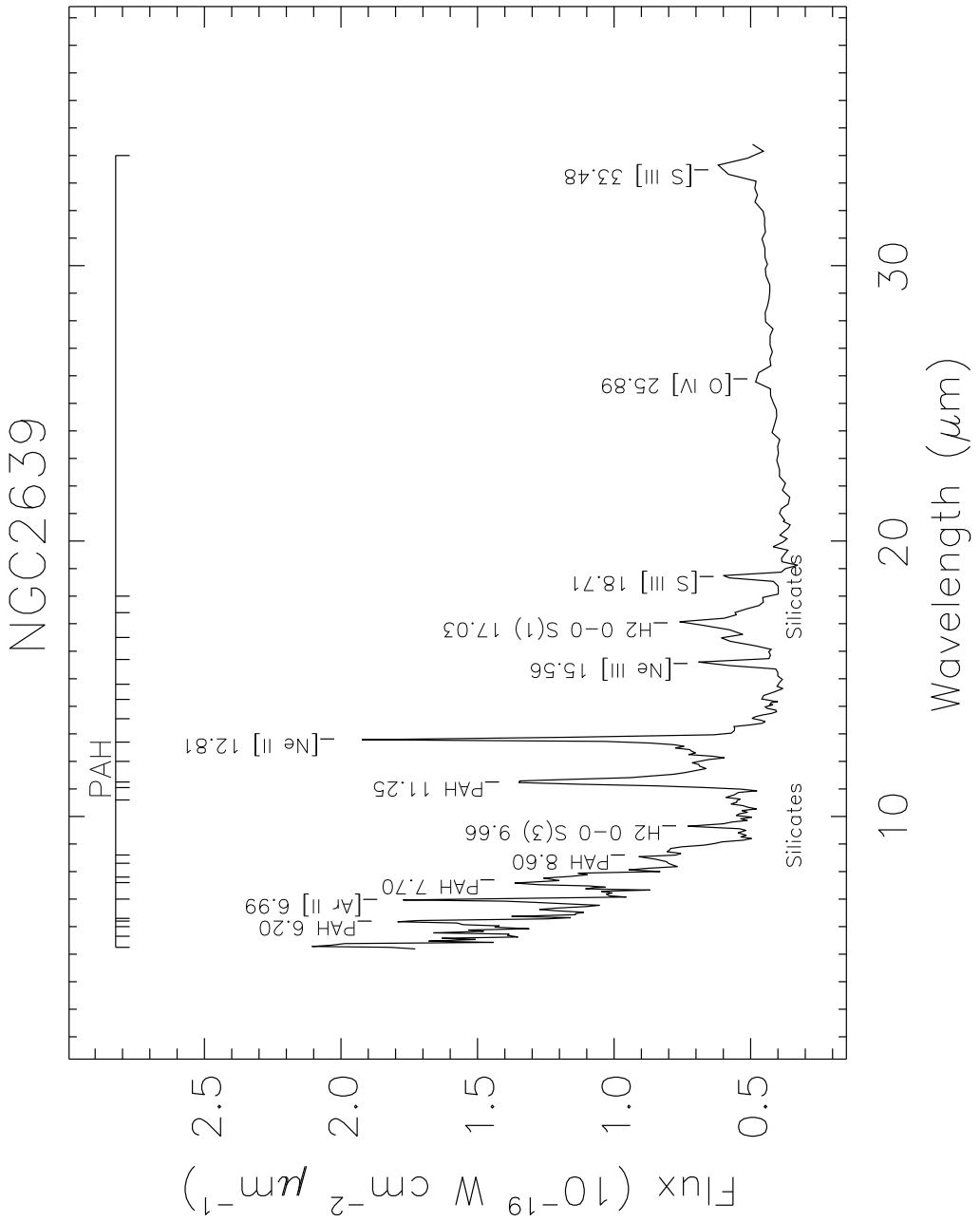

Figure 6.1: *Spitzer* mid-IR spectrum of NGC 2639

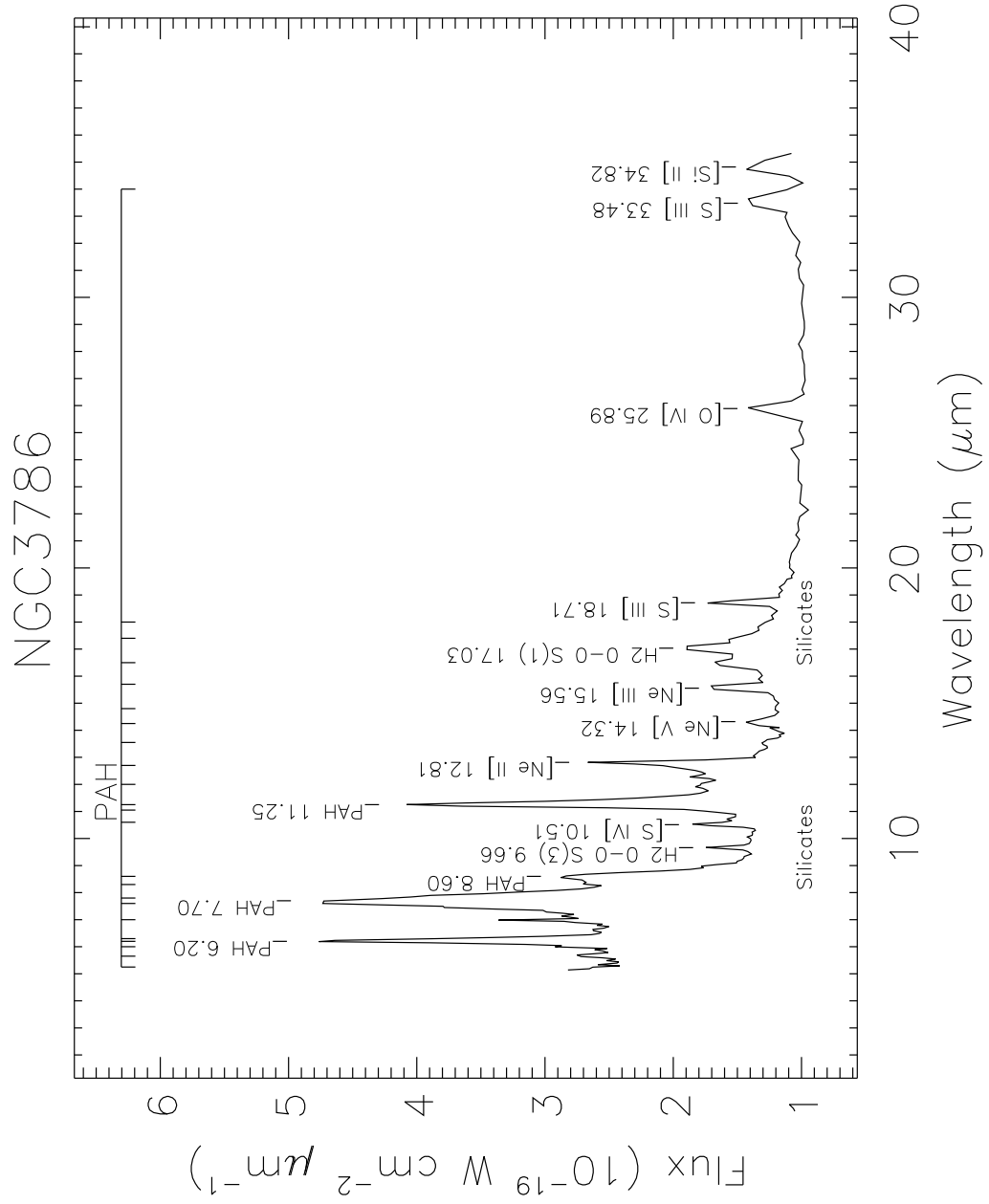

Figure 6.1: *Spitzer* mid-IR spectrum of NGC 3786

in Figures D.1 to D.3. These include objects classified as Seyfert 1s, 1.2s and 1.5s. Archival spectra of Seyfert 2 galaxies are displayed in Figure D.4 to Figure D.9. The listing in Table 6.2 contains 3 Seyfert 1.9s in addition to the 12 Seyfert 1.8/1.9s from our sample in Table 6.1. NGC 7603 and UGC 7064 were observed twice, once in our, and once in Prof. Gallimore's program. The spectra of these two galaxies from the two different programs match very accurately with each other. We display the spectra of the additional 3 Seyfert 1.9s in Figure D.10.

As we saw in Chapter 4, ISO spectroscopy established that, in general, the mid-IR spectra are dominated by three effects (Laurent et al. 2000): the mid-IR AGN continuum, which is the reprocessed optical/UV continuum emission from the torus or other dust structures close to the nucleus, the contribution from circumnuclear starbursts in the form of poly-cyclic aromatic hydrocarbon (PAH) emission bands, and continuum emission from starburst heated dust, including very small dust grains.

The important point immediately evident after looking at these archival Seyfert spectra is that is a wide range in mid-IR continuum shapes. If we separate the Seyfert spectra according to their optical type, as we have done in Figures D.1 to D.3 for Seyfert 1s, Figures D.4 to D.9 for Seyfert 2s and Figure D.10 for Seyfert 1.9s for the archival sample; we see that the majority of Seyfert 1/1.5 spectra show a strong rise at short wavelengths. The situation is not as clear for Seyfert 2s; some show a sharp rise to longer wavelengths, indicating a strong contribution from star formation, others do not. A number of Seyfert 1s and 2s show a broad hump at ~ 20 μm, which appears as a continuum break in F_ν *vs.* ν plots (Weedman et al. 2005). This "hump" or "break" is indicative of warm ($T \approx 170$ K) dust, as we discuss later.

There are obviously cases that do not fit this picture, for example NGC 1194 is classified as a Seyfert 1, but shows strong silicate absorption characteristic of Seyfert 2 objects; on the other hand, there are Seyfert 2s like NGC

424, MCG-3-58-7 and MCG-2-40-4 that show strong mid-IR continua (strong short wavelength emission) characteristic of Seyfert 1s. These cases indicate that Seyfert optical classification may not always agree with the morphology of the spectra in the mid-IR and, as we show below, inclination of the host galaxy also plays an important role (NGC 1194 is highly inclined).

Based on these observations, we suggest that type 1 Seyferts show strong continua that increase from ~ 17 μm to 5 μm. Type 2 Seyferts show weaker continua that diminish from $\sim$ 17 μm to 5 μm. We propose that these two basic trends may be the most fundamental forms of the mid-IR AGN continua. We further propose, that the "hump" around 17 μm noticed by previous workers (Weedman et al. 2005), may be the peak of the black body emission of a dust distribution at a temperature of ≈ 170 K. These fundamental forms of the mid-IR AGN continuum are modified by two processes: (1) the emission/absorption characteristics of the silicate dust distribution and (2) presence of additional PAH features due to star formation. The relative dominance of these processes shapes the type 1 and type 2 continua into the variety we see in the mid-IR spectra of Seyferts. This variety is seen most in the spectra of Seyfert 2s and 1.8/1.9s.

We further note that the continuum shapes are similar for Seyfert galaxies *not* dominated by PAH features in the 20–38 μm wavelength range. Their similarity in the long wavelength range indicates that the mid-IR emission becomes isotropic long-ward of ~ 20 μm. This indicates that in the case of Seyfert galaxies, the emission from the dust distribution close to the nucleus is anisotropic below ~ 20 μm.

The above ideas are shown graphically in Figure 6.2, where all galaxies are normalized to the flux of Mrk 9 around 20 μm for display purposes. The spectra are smoothed by a factor of 10 for clarity of the figure. The 20–30 μm tail gets an increasing contribution from cool ($T \sim 30 - 60$ K) dust as the starburst contribution in the spectrum increases. As the starburst contribution increases, the PAH feature contribution in the 5–20 μm range

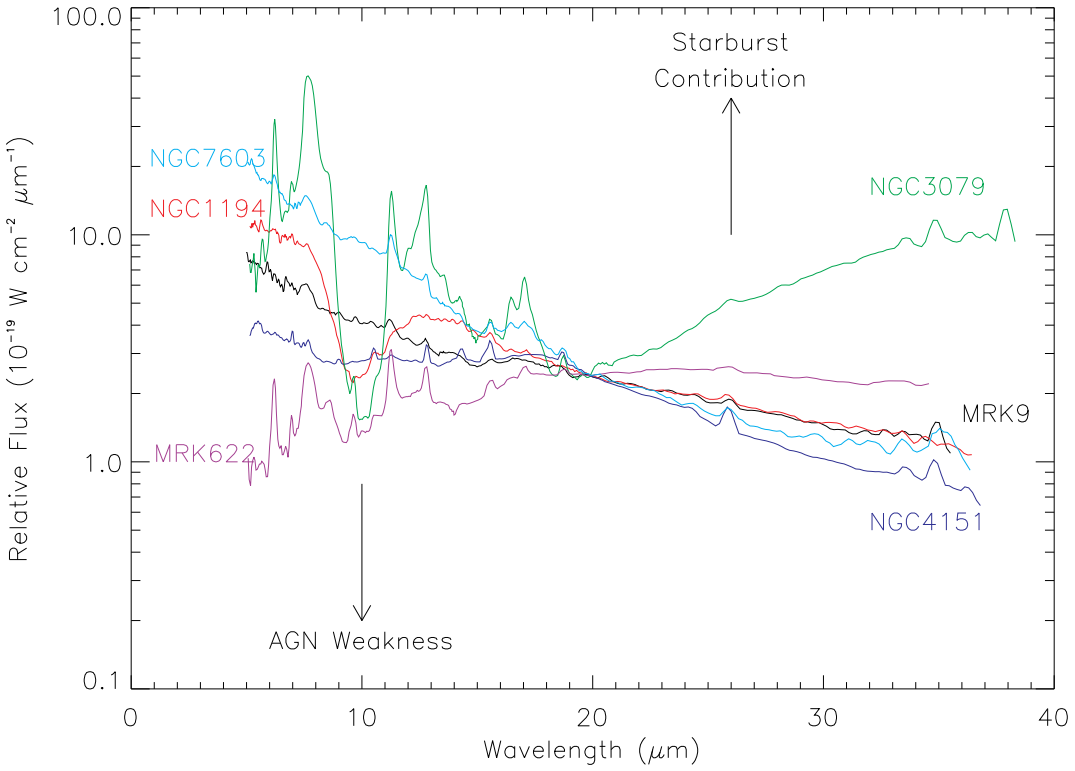

Figure 6.2: Variety in Seyfert mid-IR spectra: NGC 3079—Starburst with external cold dust extinction, NGC 7603—Strong Seyfert 1 continuum + silicate emission + starburst, NGC 1194—Seyfert 1 continuum + silicate absorption, MRK 622—Seyfert 2 continuum + starburst, NGC 4151–Seyfert 1 continuum + moderate silicate emission, Mrk 9—Seyfert 1 continuum + moderate silicate emission.

also increases, as seen in the spectrum of NGC 3079. In addition to the strong starburst contribution, NGC 3079 also shows fairly strong 18 μm silicate absorption, indicating the presence of cold dust outside the starburst region in the line of sight. NGC 7603 shows a very strong Seyfert 1 like mid-IR continuum. NGC 7603 also shows a strong starburst component. The more interesting spectrum is of Mrk 622 (a Seyfert 1.8/2), that shows diminishing

continuum like the Seyfert 2 galaxy, Mrk 3. Unlike Mrk 3, Mrk 622 has an additional starburst contribution. NGC 4151 (a Seyfert 1.5) shows a combination of moderate silicate emission around 10 μm and a strong AGN continuum between 5–9 μm. All Seyfert galaxy spectra show strong NLR fine structure lines with Seyfert 1s showing harder continua and stronger line ratios.

Chapter 7

Spectral Diagnostics from Mid-IR Spectra

In Chapter 6 we presented the mid-IR spectra of Seyfert 1.8/1.9s and archival Seyfert 1 and Seyfert 2 spectra. We saw a few spectral diagnostics derived from ISO spectra in Chapter 4, section 4.5. Similar diagnostic diagrams are possible using Spitzer spectra, and we concentrate on the study of such diagrams in this chapter. Specifically we will compare the properties of Seyfert 1.8/1.9s galaxies with those of the rest of the Seyfert sample. We begin by summarizing the initial results from *Spitzer* spectroscopy of Seyferts by other researchers.

7.1 Spitzer Studies of Seyfert Galaxies

Weedman et al. (2005) published *Spitzer* spectra of nearby classical AGN spanning a broad range in AGN types. They presented both low and high resolution spectra. The AGN selected were NGC 4151 (Seyfert 1), Mrk 3 (Seyfert 2), I Zw I (NLS1), NGC 1275 (BLRG), Centaurus A (NLRG), NGC 7469 (Seyfert 1 with strong starburst), Mrk 231 (ULIRG and BAL AGN) and NGC 3079 (Edge-on low luminosity Seyfert 2). Weedman et al. compared the

overall spectral characteristics, including continuum shapes, emission lines, silicate absorption and emission features, and PAH features. They compared these AGNs to starburst galaxies like NGC 7714 and the low-metallicity compact starburst system SBS 0335-052. They concluded that there are no spectral parameters in their sample that unambiguously distinguish AGNs and starbursts based only on the slopes of continuous spectra. Weedman et al. suggested the use of $f_\nu(30\ \mu\mathrm{m})/\mathrm{f}_\nu(20\ \mu\mathrm{m})$ and $f_\nu(15\ \mu\mathrm{m})/\mathrm{f}_\nu(6\ \mu\mathrm{m})$ flux ratios to parametrize the continuum properties of the mid-IR spectra. The authors also confirm previous results (Genzel et al. 1998) that the strength of the PAH features discriminates between AGN and starburst contributions.

Buchanan et al. (2006) presented *Spitzer* mid-IR a large sample of Seyfert galaxies. In total, they have 87 nearby, 12 μm selected Seyfert galaxies. In Buchanan et al. (2006), they present 51 spectra from this sample. Our archival sample is mainly based on these 51 spectra and a few more additional spectra from their program not included in the paper. We have additionally included a few Seyfert galaxies (NGC 4151, Mrk 3, NGC 7469) from Weedman et al. (2005). Buchanan et al. (2006) use principle component analysis (PCA) to study these spectra. They suggest that the relative contribution of the starburst component is the principle cause of the large variety seen in the mid-IR spectra. They further compare the mid-IR-to-radio flux ratio and find that Seyfert 1s have higher flux ratios than Seyfert 2s by a factor of ~ 2 longward of 15 μm. The difference increases to a factor of ~ 6 around 10 μm. The radio emission is considered isotropic as it is not affected by the dust distribution close to the central source. They suggest that a significant difference between Seyfert 1 and Seyfert 2 ratios is consistent with unified schemes. Further, they suggest that the mid-IR emission is anisotropic, but the level of anisotropy is much weaker than predicted by the compact torus models (Pier & Krolik 1992). Buchanan et al. further suggest, that since their sample is selected based on IRAS 12 μm fluxes, there may be a orientation-dependent bias in the sample as the dust distribution (or

the "torus") may be optically thick at 12 μm; however they do not find that the sample is biased toward more luminous Seyfert 2 galaxies. Further, they suggest that another selection effect may be affecting the sample; Seyfert 2s in the sample appear to have a larger starburst contribution than Seyfert 1s, which contradicts the expectations from the unified scheme. It is possible that the enhanced PAH feature contribution from starburst dominated Seyfert galaxies will lead to this selection effect in the 12 μm selected sample.

Hao et al. (2007) present *Spitzer* spectra of 196 AGN and ULIRGs. They mainly study the silicate feature strength ($S_{10\ \mu\mathrm{m}} = \ln(F_{obs}/F_{cont})$, F_{obs} is observed flux at 10 μm and F_{cont} is flux at 10 μm from the fitted continuum) and conclude that Quasars/QSOs tend to show silicate features in emission, Seyfert 1s show weak emission features, Seyfert 2s show weak absorption features, and ULIRGs show deep silicate absorptions. They further note that the 10 μm silicate strength correlates with the flux ratio $f_\nu(14.5\ \mu\mathrm{m})/\mathrm{f}_\nu(27.5\ \mu\mathrm{m})$, with quasars and Seyfert 1s showing similar weak emission features with flatter (on a F_ν *vs.* λ plot) continuum between $\sim$ 15–30 μm, and Seyfert 2s and ULIRGs showing increasing absorption at 10 μm with steepening continuum between $\sim$ 15–30 μm, respectively. Spoon et al. (2007), using a similar ULIRG, starburst and AGN sample find that for most ULIRGs and starburst galaxies, there is an anti-correlation between the silicate feature strength ($S_{10\ \mu\mathrm{m}}$) and the strength of the 6.2 μm PAH. As the silicate absorption increases, the 6.2 μm PAH gets weaker. In starburst galaxies, when the 6.2 μm PAH is stronger, the silicate absorption is weakest. In contrast, for their AGN sample, the silicate absorption is always weaker and the PAHs are also weaker due to the presence of a harder radiation field for AGN.

These results indicate that silicate features are weak in Seyfert galaxies, compared to expectations from torus models. This was also noted by ISO studies, but has now been established firmly due to the availability of the full mid-IR spectra from *Spitzer* for a large number of local Seyfert galaxies. It is also established (Clavel et al. 2000; Buchanan et al. 2006), that the mid-IR

spectra show anisotropic behavior until the $\sim$ 17 μm "break", hinting that the torus emission is anisotropic in the mid-IR. For more distant sources, larger parts of the galaxy are included in the aperture, leading to greater contribution from extended starburst regions within the host galaxy disk that modify the intrinsic mid-IR continuum from the nucleus.

Our spectral diagnostic results below have been developed contemporaneously with many of the results mentioned above, and we keep these results in mind as we discuss the implications in §7.4.

7.2 Measurements and Data Tables

We have measured three quantities: the emission line fluxes, the equivalent widths of the silicate absorption or emission feature and the PAH features, and the continuum fluxes at 6, 15, 20 and 30 μm for the complete spectra. The continuum fluxes were measured by a weighted average of the flux values in a 1 μm bin centered on the wavelength of interest, with weights being errors on the individual data points. Table 7.1 lists the measured continuum fluxes from the spectra. Table 7.2 lists the equivalent widths of the 6.2 μm PAH and the equivalent widths of the silicate 10 μm feature. Table 7.3 lists the various narrow emission line fluxes measured for each object from the low resolution data.

When measuring the emission line fluxes, we measured the feature with the local continuum points selected on the two sides of the feature. The flux in the feature was measured by interpolating between the two continuum regions selected on either side and then integrating the area under the feature curve above the interpolated continuum. If the feature was blended with other features, we have selected the local continuum points along the spectrum such that only the visible contribution of the feature is measured. This is the best that can be done without deblending the features. The features were measured three times to average out any continuum placement

errors. we estimated errors by taking into consideration the variance of continuum placements and the errors on the integrated fluxes as estimated from the errors on individual data points. The error in continuum placement and the integrated flux was added in quadrature at each measurment cycle and assigned to that corresponding measurement. The final flux and the uncertainity on it was estimated from the mean of these values. We also measured fluxes of PAH features.

The equivalent widths were measured using a similar approach to the flux measurements except that the spectrum was divided by the fitted continuum, and the measurements were done on the continuum-divided spectrum. The uncertainty due to the subjective choice of the continuum contributes to the uncertainty in the measurement of the equivalent width. We did some tests by varying the continuum by small amounts and checking the effects of this on the equivalent widths. Based on these tests we estimate that the uncertainty due to subjective choice of the continuum is $\sim 10\%$. When measuring the equivalent width of the silicate absorption/emission feature, we have not removed the contribution from the 9.66 μm H_2 emission line, which is small in most cases.

Table 7.1. Continuum flux values (in F_λ units) from mid-IR spectra.

Galaxy	Continuum flux (10^{-19} W cm^{-2} μm^{-1}) at 6.00 μm	15.00 μm	20.00 μm	30.00 μm
CGCG381-051	1.66 ± 0.86	1.80 ± 0.06	2.57 ± 0.05	1.92 ± 0.03
E33-G2	6.36 ± 0.49	3.67 ± 0.06	2.66 ± 0.10	1.23 ± 0.04
F01475-0740	2.94 ± 0.59	3.43 ± 0.11	3.55 ± 0.13	2.15 ± 0.05
F04385-0828	15.55 ± 0.61	9.01 ± 0.29	7.92 ± 0.22	6.33 ± 0.10
F15480-0344	2.95 ± 0.28	3.40 ± 0.09	3.48 ± 0.08	2.23 ± 0.04
IC 4329A	35.31 ± 1.83	18.49 ± 0.46	14.30 ± 0.42	6.11 ± 0.13
Mrk 334	6.56 ± 2.38	3.49 ± 0.13	4.31 ± 0.11	4.56 ± 0.06
Mrk 335	8.03 ± 0.52	2.52 ± 0.08	2.00 ± 0.10	1.01 ± 0.03
Mrk 348	8.06 ± 0.33	5.12 ± 0.12	4.14 ± 0.18	1.90 ± 0.07
Mrk 471	0.96 ± 0.35	0.37 ± 0.02	0.32 ± 0.02	0.30 ± 0.02
Mrk 6	8.69 ± 0.72	4.13 ± 0.27	3.88 ± 0.12	2.06 ± 0.05
Mrk 609	2.97 ± 1.44	1.33 ± 0.09	1.38 ± 0.03	1.45 ± 0.01
Mrk 622	1.03 ± 0.40	1.51 ± 0.09	1.93 ± 0.03	1.84 ± 0.02
Mrk 79	11.24 ± 0.64	5.20 ± 0.14	4.26 ± 0.09	2.56 ± 0.06
Mrk 817	7.66 ± 0.46	5.11 ± 0.14	5.37 ± 0.16	3.89 ± 0.07
Mrk 883	0.76 ± 0.27	0.64 ± 0.06	0.89 ± 0.03	1.01 ± 0.01
Mrk 9	6.78 ± 0.51	2.68 ± 0.06	2.38 ± 0.06	1.45 ± 0.04
Mrk 938	10.41 ± 5.42	5.80 ± 0.16	7.68 ± 0.37	14.52 ± 0.16
M-2-33-34	1.84 ± 0.45	1.61 ± 0.27	1.56 ± 0.07	1.17 ± 0.01
M-2-40-4	13.95 ± 0.62	6.03 ± 0.13	4.93 ± 0.10	3.58 ± 0.05
M-2-8-39	2.03 ± 0.30	3.10 ± 0.07	2.39 ± 0.08	0.98 ± 0.04
M-3-34-63	1.09 ± 0.60	0.28 ± 0.04	0.28 ± 0.05	0.37 ± 0.01
M-3-58-7	11.74 ± 0.75	4.93 ± 0.08	4.78 ± 0.08	3.33 ± 0.07
M-5-13-17	3.20 ± 0.44	2.79 ± 0.09	2.67 ± 0.06	1.87 ± 0.03
M-6-30-15	12.17 ± 0.55	5.85 ± 0.10	4.84 ± 0.12	2.50 ± 0.06

Table 7.1—Continued

Galaxy	Continuum flux (10^{-19} W cm^{-2} μm^{-1}) at 6.00 μm	15.00 μm	20.00 μm	30.00 μm
NGC 1056	3.75 ± 2.51	1.34 ± 0.15	1.48 ± 0.11	1.79 ± 0.04
NGC 1125	3.23 ± 0.85	3.12 ± 0.23	3.28 ± 0.08	3.84 ± 0.03
NGC 1194	13.99 ± 0.80	4.90 ± 0.16	3.20 ± 0.08	2.00 ± 0.03
NGC 1241	2.15 ± 0.76	1.27 ± 0.12	1.12 ± 0.12	1.12 ± 0.03
NGC 1320	9.45 ± 0.39	6.36 ± 0.15	5.55 ± 0.17	3.58 ± 0.07
NGC 1667	3.31 ± 1.85	1.16 ± 0.11	1.08 ± 0.04	1.12 ± 0.03
NGC 2622	0.84 ± 0.07	0.74 ± 0.04	0.62 ± 0.02	0.34 ± 0.01
NGC 2639	1.44 ± 0.18	0.41 ± 0.05	0.38 ± 0.02	0.44 ± 0.02
NGC 3079	21.20 ± 11.51	5.54 ± 0.38	3.81 ± 0.23	10.47 ± 0.32
NGC 3227	···	8.61 ± 0.78	8.71 ± 0.20	6.30 ± 0.12
NGC 3516	11.10 ± 0.66	5.12 ± 0.14	4.58 ± 0.10	2.78 ± 0.05
NGC 3786	3.05 ± 0.68	1.23 ± 0.10	1.09 ± 0.02	0.99 ± 0.01
NGC 3982	1.59 ± 0.60	1.28 ± 0.11	1.43 ± 0.06	1.42 ± 0.03
NGC 4051	14.37 ± 0.98	8.77 ± 0.22	7.39 ± 0.32	4.42 ± 0.05
NGC 4151	47.16 ± 2.18	35.85 ± 1.88	30.08 ± 0.97	12.99 ± 0.20
NGC 424	35.01 ± 1.79	14.44 ± 0.25	10.36 ± 0.32	4.42 ± 0.13
NGC 4602	1.34 ± 0.63	0.64 ± 0.04	0.74 ± 0.11	0.78 ± 0.03
NGC 4941	···	1.54 ± 0.15	1.64 ± 0.08	1.24 ± 0.03
NGC 4968	6.13 ± 0.94	6.26 ± 0.22	5.75 ± 0.18	3.37 ± 0.05
NGC 5005	7.91 ± 1.68	2.02 ± 0.16	1.83 ± 0.12	3.40 ± 0.09
NGC 513	1.97 ± 0.41	1.29 ± 0.10	1.24 ± 0.09	1.05 ± 0.03
NGC 5256	4.75 ± 2.79	2.35 ± 0.26	2.75 ± 0.09	3.87 ± 0.01
NGC 526A	···	3.60 ± 0.07	2.67 ± 0.12	0.83 ± 0.02
NGC 5347	4.38 ± 0.43	5.45 ± 0.13	5.04 ± 0.13	2.87 ± 0.07
NGC 5548	···	4.17 ± 0.09	3.68 ± 0.07	1.95 ± 0.06

Table 7.1—Continued

Galaxy	Continuum flux (10^{-19} W cm^{-2} μm^{-1}) at 6.00 μm	15.00 μm	20.00 μm	30.00 μm
NGC 5929	2.73 ± 0.87	0.37 ± 0.10	0.40 ± 0.05	0.48 ± 0.01
NGC 5953	5.23 ± 2.94	2.77 ± 0.22	2.87 ± 0.09	3.42 ± 0.07
NGC 7130	6.26 ± 2.22	6.08 ± 0.27	7.69 ± 0.21	9.36 ± 0.06
NGC 7172	···	3.94 ± 0.25	2.34 ± 0.07	2.86 ± 0.04
NGC 7314	···	2.30 ± 0.15	1.72 ± 0.07	1.33 ± 0.01
NGC 7469	26.83 ± 8.20	19.37 ± 0.47	23.65 ± 0.17	23.83 ± 0.29
NGC 7496	4.38 ± 2.27	4.26 ± 0.12	6.03 ± 0.21	7.31 ± 0.07
NGC 7603	14.11 ± 0.73	3.16 ± 0.08	1.86 ± 0.09	0.97 ± 0.01
NGC 7674	13.19 ± 0.74	9.18 ± 0.33	8.46 ± 0.18	5.78 ± 0.14
NGC 931	14.54 ± 1.11	7.11 ± 0.20	5.70 ± 0.15	3.24 ± 0.07
TOL 1238-364	6.53 ± 1.02	9.56 ± 0.29	10.98 ± 0.27	7.91 ± 0.08
UGC 11680	5.18 ± 0.66	2.45 ± 0.27	2.68 ± 0.42	1.60 ± 0.65
UGC 12138	2.49 ± 0.32	1.55 ± 0.09	1.34 ± 0.04	1.00 ± 0.01
UGC 7064	2.57 ± 0.40	1.79 ± 0.11	1.65 ± 0.06	1.29 ± 0.01
UM 146	0.66 ± 0.05	0.44 ± 0.04	0.39 ± 0.02	0.32 ± 0.02

Table 7.2. Equivalent Widths of PAH and SiO Features

Galaxy	Equivalent Width (in units of 0.1 μm) PAH 6.2 μm	Silicate 9.7 μm[a]
CGCG381-051	-3.73 ± 0.15	-2.43 ± 0.02
E33-G2	-0.31 ± 0.01	-0.35 ± 0.02
F01475-0740	-1.73 ± 0.10	-1.19 ± 0.86
F04385-0828	-0.37 ± 0.03	12.27 ± 0.04
F15480-0344	-0.91 ± 0.02	1.13 ± 0.15
IC 4329A	-0.08 ± 0.01	-3.71 ± 0.14
Mrk 334	-3.13 ± 0.01	3.01 ± 0.04
Mrk 348	-0.12 ± 0.02	3.21 ± 0.05
Mrk 471	-3.69 ± 0.36	0.71 ± 0.43
Mrk 6	-0.22 ± 0.03	-0.27 ± 0.04
Mrk 609	-4.27 ± 0.03	3.90 ± 0.03
Mrk 622	-3.66 ± 0.13	-0.75 ± 0.10
Mrk 79	-0.21 ± 0.02	-0.20 ± 0.07
Mrk 817	-0.52 ± 0.01	-0.28 ± 0.03
Mrk 883	-5.01 ± 0.18	0.55 ± 0.04
Mrk 9	-0.18 ± 0.02	-0.30 ± 0.06
Mrk 938	-5.07 ± 0.12	9.43 ± 0.53
M-2-33-34	-2.83 ± 0.29	-0.00 ± 0.11
M-2-40-4	-0.54 ± 0.02	2.54 ± 0.11
M-2-8-39	-0.38 ± 0.02	-0.82 ± 0.19
M-3-34-63	-19.48 ± 1.26	-15.22 ± 1.39
M-3-58-7	-0.54 ± 0.02	-0.21 ± 0.08
M-5-13-17	-1.45 ± 0.05	-0.43 ± 0.20
M-6-30-15	-0.09 ± 0.02	-0.41 ± 0.14

Table 7.2—Continued

Galaxy	Equivalent Width (in units of 0.1 μm) PAH 6.2 μm	Silicate 9.7 μm[a]
NGC 1056	-10.01 ± 0.26	-4.02 ± 1.01
NGC 1125	-2.95 ± 0.04	12.75 ± 0.20
NGC 1143-4	-2.12 ± 0.03	9.38 ± 0.45
NGC 1194	-0.33 ± 0.07	16.97 ± 0.06
NGC 1241	-5.65 ± 0.13	4.52 ± 0.23
NGC 1320	-0.44 ± 0.02	1.43 ± 0.04
NGC 1667	-8.06 ± 0.04	3.92 ± 0.09
NGC 2622	-1.14 ± 0.01	-0.39 ± 0.06
NGC 2639	-0.83 ± 0.02	-0.45 ± 0.02
NGC 3079	-5.35 ± 0.07	10.27 ± 0.45
NGC 3516	-0.34 ± 0.02	-0.39 ± 0.08
NGC 3786	-1.94 ± 0.02	0.06 ± 0.13
NGC 3982	-0.75 ± 0.04	0.92 ± 0.22
NGC 4051	-0.69 ± 0.01	-0.84 ± 0.15
NGC 4151	-0.09 ± 0.02	0.75 ± 0.12
NGC 424	-0.17 ± 0.01	1.39 ± 0.05
NGC 4579	-0.70 ± 0.02	-1.29 ± 0.10
NGC 4602	-0.58 ± 0.03	1.50 ± 0.08
NGC 4968	-1.10 ± 0.04	2.65 ± 0.11
NGC 5005	-2.27 ± 0.06	3.57 ± 0.38
NGC 513	-1.69 ± 0.04	-0.87 ± 0.20
NGC 5256	-7.24 ± 0.05	9.32 ± 0.08
NGC 5347	-0.74 ± 0.02	1.38 ± 0.14
NGC 5548	···	-1.13 ± 0.07

Table 7.2—Continued

Galaxy	Equivalent Width (in units of 0.1 μm) PAH 6.2 μm	Silicate 9.7 μm[a]
NGC 5929	-0.22 ± 0.02	0.21 ± 0.32
NGC 5953	-5.11 ± 0.09	1.50 ± 0.78
NGC 7130	-3.93 ± 0.18	4.87 ± 0.17
NGC 7469	-2.80 ± 0.05	2.65 ± 0.21
NGC 7496	-5.15 ± 0.07	1.94 ± 0.05
NGC 7603	-0.74 ± 0.01	-1.42 ± 0.06
NGC 7674	-0.44 ± 0.02	2.70 ± 0.21
NGC 931	-0.24 ± 0.01	0.48 ± 0.04
TOL 1238-364	-0.89 ± 0.06	3.49 ± 0.12
UGC 11680	-1.12 ± 0.03	-1.39 ± 0.04
UGC 12138	-1.08 ± 0.02	1.68 ± 0.03
UGC 7064	-1.10 ± 0.11	1.68 ± 0.02
UM 146	-1.34 ± 0.11	0.13 ± 0.02

Note. — Emission features have negative equivalent widths. The errors quoted here are 1-σ measurement errors as propagated from error vectors returned by SMART during spectral reductions. There will be an additional $\sim$ 10% error due to subjective placement of the overall continuum.

[a]The silicate equivalent width includes a contribution from the H_2 emission feature at 9.66 μm. No attempt has been made to subtract this feature.

Table 7.3. Integrated PAH and Line Fluxes.

Galaxy	Integrated line fluxes ($10^{-19} W cm^{-2}$) at						
	PAH 6.2 μm	[S IV] 10.51 μm	[Ne II] 12.81 μm	[Ne V] 14.32 μm	[Ne III] 15.56 μm	[S III] 18.71 μm	[O IV] 25.89 μm
CGCG381-051	0.52 ± 0.04	···	0.17 ± 0.01	···	0.03 ± 0.01	0.09 ± 0.01	0.01 ± 0.01
F01475-0740	0.44 ± 0.04	0.03 ± 0.01	0.16 ± 0.01	···	0.12 ± 0.01	0.09 ± 0.01	0.07 ± 0.01
F04385-0828	0.25 ± 0.02	···	0.24 ± 0.02	···	0.18 ± 0.02	···	0.12 ± 0.02
F15480-0344	···	0.07 ± 0.001	0.07 ± 0.001	0.10 ± 0.001	0.15 ± 0.001	0.09 ± 0.001	0.34 ± 0.001
IC4329A	0.27 ± 0.04	0.46 ± 0.02	0.26 ± 0.01	0.43 ± 0.02	0.70 ± 0.03	0.19 ± 0.02	1.08 ± 0.04
Mrk 3	···	0.51 ± 0.08	0.86 ± 0.12	1.09 ± 0.12	2.07 ± 0.29	0.59 ± 0.11	2.10 ± 0.26
Mrk 334	1.55 ± 0.06	0.11 ± 0.02	0.30 ± 0.08	0.13 ± 0.02	0.26 ± 0.03	0.23 ± 0.05	0.15 ± 0.03
Mrk 335	0.11 ± 0.03	0.07 ± 0.01	0.05 ± 0.02	···	···	···	0.09 ± 0.01
Mrk 348	0.16 ± 0.001	0.06 ± 0.001	0.13 ± 0.001	···	0.25 ± 0.001	0.04 ± 0.001	0.24 ± 0.001
Mrk 471	0.25 ± 0.02	0.03 ± 0.01	0.03 ± 0.01	0.02 ± 0.001	0.03 ± 0.001	0.06 ± 0.01	0.04 ± 0.001
Mrk 6	0.20 ± 0.02	0.22 ± 0.01	0.24 ± 0.01	0.12 ± 0.01	0.47 ± 0.01	0.21 ± 0.01	0.50 ± 0.01
Mrk 609	0.93 ± 0.04	0.05 ± 0.01	0.12 ± 0.02	0.09 ± 0.01	0.09 ± 0.02	0.13 ± 0.02	0.08 ± 0.01
Mrk 622	0.27 ± 0.02	···	0.06 ± 0.02	···	0.08 ± 0.02	0.05 ± 0.01	0.10 ± 0.01
Mrk 79	0.22 ± 0.001	0.11 ± 0.01	0.10 ± 0.001	···	0.20 ± 0.001	0.04 ± 0.001	0.51 ± 0.001
Mrk 817	0.36 ± 0.001	0.09 ± 0.001	0.05 ± 0.001	0.08 ± 0.001	0.04 ± 0.001	0.03 ± 0.001	0.06 ± 0.001
Mrk 883	0.22 ± 0.02	0.03 ± 0.001	0.11 ± 0.01	···	0.08 ± 0.01	0.08 ± 0.02	0.10 ± 0.01
Mrk 9	···	0.07 ± 0.001	0.02 ± 0.001	···	0.01 ± 0.001	···	0.07 ± 0.001
Mrk 938	3.53 ± 0.05	···	0.64 ± 0.02	···	0.20 ± 0.02	···	···
M-2-33-34	0.42 ± 0.04	0.26 ± 0.02	0.14 ± 0.01	0.15 ± 0.01	0.40 ± 0.01	0.06 ± 0.02	0.60 ± 0.01
M-2-40-4	0.73 ± 0.04	0.04 ± 0.01	0.14 ± 0.01	0.12 ± 0.01	0.18 ± 0.02	0.04 ± 0.01	0.18 ± 0.01
M-2-8-39	···	0.05 ± 0.01	0.07 ± 0.01	0.10 ± 0.01	0.10 ± 0.01	0.04 ± 0.01	0.15 ± 0.01
M-3-34-63	0.38 ± 0.10	0.02 ± 0.02	0.19 ± 0.05	···	···	···	···
M-3-58-7	0.55 ± 0.04	0.03 ± 0.02	0.05 ± 0.04	···	0.10 ± 0.01	0.06 ± 0.01	0.12 ± 0.01
M-5-13-17	0.36 ± 0.18	0.08 ± 0.001	0.11 ± 0.001	···	0.13 ± 0.001	0.01 ± 0.001	0.12 ± 0.001
M-6-30-15	0.05 ± 0.02	0.09 ± 0.01	0.04 ± 0.01	···	0.01 ± 0.01	···	0.20 ± 0.02
NGC 1056	2.06 ± 0.05	0.04 ± 0.01	0.23 ± 0.01	···	0.25 ± 0.01	0.28 ± 0.03	···
NGC 1125	0.70 ± 0.06	0.12 ± 0.05	0.27 ± 0.08	···	0.31 ± 0.01	0.18 ± 0.01	0.29 ± 0.01
NGC 1143-4	0.30 ± 0.03	0.07 ± 0.01	0.15 ± 0.01	···	···	···	···
NGC 1194	0.18 ± 0.03	0.19 ± 0.03	0.05 ± 0.02	0.12 ± 0.02	0.09 ± 0.01	···	0.14 ± 0.01
NGC 1241	0.71 ± 0.05	0.13 ± 0.02	0.09 ± 0.01	···	···	···	0.02 ± 0.01
NGC 1320	0.48 ± 0.001	0.13 ± 0.001	0.09 ± 0.01	0.08 ± 0.001	0.09 ± 0.001	0.13 ± 0.01	0.32 ± 0.01
NGC 1667	1.05 ± 0.01	···	0.26 ± 0.01	···	0.19 ± 0.01	0.20 ± 0.001	0.12 ± 0.001
NGC 2622	0.03 ± 0.001	0.03 ± 0.01	0.06 ± 0.01	···	···	0.02 ± 0.01	0.08 ± 0.02
NGC 2639	0.10 ± 0.02	···	0.11 ± 0.02	···	0.06 ± 0.01	0.05 ± 0.01	0.03 ± 0.01
NGC 3079	7.79 ± 0.12	0.16 ± 0.05	1.48 ± 0.09	···	0.28 ± 0.01	0.38 ± 0.02	0.36 ± 0.02
NGC 3516	0.26 ± 0.001	0.17 ± 0.001	0.08 ± 0.001	0.11 ± 0.001	0.26 ± 0.001	0.11 ± 0.001	0.38 ± 0.001
NGC 3786	0.65 ± 0.03	0.08 ± 0.01	0.11 ± 0.01	···	0.12 ± 0.03	0.11 ± 0.01	0.19 ± 0.02
NGC 3982	0.21 ± 0.01	0.06 ± 0.001	0.16 ± 0.001	···	0.05 ± 0.001	0.04 ± 0.001	0.02 ± 0.001
NGC 4051	0.90 ± 0.03	0.03 ± 0.01	0.17 ± 0.02	0.18 ± 0.02	0.23 ± 0.02	0.11 ± 0.02	0.32 ± 0.01
NGC 4151	0.69 ± 0.04	0.86 ± 0.02	1.35 ± 0.03	1.08 ± 0.06	2.50 ± 0.11	1.14 ± 0.05	2.45 ± 0.07
NGC 424	1.16 ± 0.05	0.26 ± 0.01	0.15 ± 0.01	0.11 ± 0.001	0.21 ± 0.001	0.06 ± 0.001	0.18 ± 0.01
NGC 4579	0.26 ± 0.03	···	0.11 ± 0.01	···	···	···	···
NGC 4602	0.14 ± 0.02	···	0.16 ± 0.02	0.04 ± 0.01	···	0.09 ± 0.01	0.05 ± 0.01
NGC 4968	0.65 ± 0.03	0.05 ± 0.01	0.24 ± 0.01	0.17 ± 0.02	0.24 ± 0.05	0.19 ± 0.02	0.30 ± 0.01
NGC 5005	1.63 ± 0.06	···	0.60 ± 0.01	···	0.16 ± 0.01	0.08 ± 0.01	0.18 ± 0.01
NGC 513	0.26 ± 0.03	0.01 ± 0.01	0.11 ± 0.01	···	0.08 ± 0.01	0.09 ± 0.01	0.09 ± 0.01
NGC 5256	2.02 ± 0.08	0.09 ± 0.01	0.76 ± 0.02	···	0.37 ± 0.01	0.26 ± 0.01	0.61 ± 0.01
NGC 5347	0.21 ± 0.03	0.03 ± 0.01	0.03 ± 0.01	···	···	0.03 ± 0.01	0.04 ± 0.01
NGC 5548	···	0.02 ± 0.02	0.04 ± 0.02	0.05 ± 0.02	0.14 ± 0.01	0.04 ± 0.01	0.15 ± 0.01
NGC 5929	0.55 ± 0.17	0.05 ± 0.02	0.21 ± 0.02	0.04 ± 0.01	0.09 ± 0.01	···	0.07 ± 0.01
NGC 5953	1.88 ± 0.05	···	1.05 ± 0.02	···	0.21 ± 0.01	0.61 ± 0.02	0.22 ± 0.01
NGC 7130	1.77 ± 0.08	0.07 ± 0.01	0.71 ± 0.05	0.11 ± 0.02	0.37 ± 0.02	0.37 ± 0.10	0.43 ± 0.03
NGC 7469	5.36 ± 0.15	0.15 ± 0.02	1.68 ± 0.04	···	0.45 ± 0.02	1.24 ± 0.03	1.03 ± 0.16

Table 7.3—Continued

Galaxy	Integrated line fluxes ($10^{-19} W cm^{-2}$) at						
	PAH 6.2 μm	[S IV] 10.51 μm	[Ne II] 12.81 μm	[Ne V] 14.32 μm	[Ne III] 15.56 μm	[S III] 18.71 μm	[O IV] 25.89 μm
NGC 7496	1.41 ± 0.03	0.01 ± 0.01	0.34 ± 0.01	0.05 ± 0.01	0.03 ± 0.001	0.34 ± 0.02	···
NGC 7603	1.10 ± 0.04	0.07 ± 0.01	0.11 ± 0.01	···	0.07 ± 0.01	0.13 ± 0.01	0.07 ± 0.01
NGC 7674	0.50 ± 0.04	0.22 ± 0.01	0.18 ± 0.01	0.31 ± 0.02	0.46 ± 0.02	0.22 ± 0.02	0.46 ± 0.02
NGC 931	0.44 ± 0.10	0.21 ± 0.02	0.08 ± 0.01	0.18 ± 0.02	0.22 ± 0.02	0.09 ± 0.02	0.43 ± 0.02
TOL 1238-364	0.63 ± 0.09	0.05 ± 0.01	0.39 ± 0.02	0.09 ± 0.03	0.34 ± 0.03	0.23 ± 0.02	0.12 ± 0.01
UGC 11680	0.53 ± 0.09	···	0.20 ± 0.04	···	···	···	···
UGC 12138	0.26 ± 0.02	0.06 ± 0.001	0.03 ± 0.001	0.06 ± 0.01	0.08 ± 0.01	0.04 ± 0.01	0.11 ± 0.02
UGC 7064	0.09 ± 0.02	···	0.07 ± 0.01	···	0.10 ± 0.01	0.07 ± 0.01	0.17 ± 0.01
UM 146	···	0.02 ± 0.001	0.03 ± 0.001	0.02 ± 0.01	0.04 ± 0.01	0.02 ± 0.01	0.02 ± 0.001

7.3 Diagnostics with Spitzer/IRS

As shown in Figures D.1 to D.9, the continuum shapes of the entire sample of Seyfert galaxies vary significantly. In general, they can be put into three categories as defined by their continuum colors. Buchanan et al. (2006) classified their spectra into the single power-laws (SP), the broken power-laws (BP) and the starburst dominated with strong red continuum (RC). The single power-laws are straight lines on $\log F_\nu$ *vs.* $\log \lambda$ plots. The broken-power-laws show the "break" at ~ 17 μm, while the starburst dominated spectra show PAH features and strongly rising continua longward of ~ 20 μm.

Most Seyfert 1 type objects show the single power law or the broken power law type spectrum, while many Seyfert 2s show strong red continua and PAH dominated spectra. The broken power-law shape results from a break in the continuum around 17 μm which is seen in several Seyfert 1s, but interestingly there are also type 2 Seyferts with a strong 17 μm break and strongly diminishing (compared to the spectra of most Seyfert 1s) continua toward 6 μm, as mentioned in the last chapter. The mid-IR spectra of Mrk 622 (see Figure 6.1) and Mrk 3 are good examples of this behavior. In starburst-dominated sources, there is a significant contribution at longer wavelengths, giving rise to the red continuum behavior mentioned by Buchanan et al. (2006) (see also NGC 3079 in Figure D.7).

In Figures 7.1–7.4 we show various trends in spectral characteristics and their behavior with Seyfert type. In these graphs, Seyfert 1s are represented with plus symbols, Seyfert 2s are square symbols and Seyfert 1.8/1.9s are represented by filled triangles. All systems with $b/a \leq 0.5$ are circled in red. Fluxes are measured in F_λ units (W cm^{-2} μm^{-1}) and equivalent widths are in microns.

Figure 7.1 is a comparison of 6–15 μm and 20–30 μm continuum spectral indices. The spectral index here is defined as,

$$\alpha_{1-2} = \log(f_1/f_2)/\log(\lambda_1/\lambda_2) \tag{7.1}$$

Note that this is in contrast to the standard definition that uses frequency units. Also, it should be noted that Buchanan et al. (2006) use $\alpha_{1-2} = \log(f_{\nu_1}/f_{\nu_2})/\log(\lambda_1/\lambda_2)$ as they plot their spectra as λ *vs.* F_ν. So individual values of our spectral indices cannot be compared directly to theirs. We prefer the λ *vs.* F_λ plots, as the features in the 6–15 μm range are seen in better contrast to each other as shown in the figures in the last chapter. A positive 20–30 spectral index implies a positive slope on a $log(\lambda)$ *vs.* $log(F_\lambda)$ plot. In this graph the dashed line shows a single power-law. A more positive 6–15 and negative 20–30 (along the arrow labeled BP) results in a broken power law behavior. Note that there are a number of Seyfert 2s with positive 6–15 slopes that have more extreme 6–15 spectral indices than a Seyfert 1 like NGC 4151. A positive 20–30 and a negative 6–15, along the arrow labeled RC, leads towards a starburst type spectrum with strong red continuum and well defined PAH bands. Most Seyfert 1.8s and 1.9s are mid-way (in comparison of spectral shapes) between Seyfert 1 types (broken power law, NGC 4151 and NGC 2622) and starburst type spectra like NGC 3079.

Overall, the graph shows that Seyferts have a wide range of continuum shapes in the mid-IR. One possible interpretation is that the Seyfert 2 galaxies in the upper left corner are dominated by a single component of warm ($T \approx 150$K) dust from the nuclear region (*e.g.,* the torus or the inner NLR). These objects have a rather simple thermal continuum, as shown by Mrk 622 in Figure 6.1, which appears as a broken power-law in ν *vs.* F_ν plots. As one moves down and to the right in Figure 7.1, the red continuum from increased starburst contribution (with dust cooler than $\sim$ 150 K) becomes stronger. As one moves from the upper left to middle left in this diagram, we see a larger contribution from the hotter dust in the 6–15 μm region. This is expected for Seyfert 1s, but several Seyfert 2s occupy this region as well. The majority of Seyfert 1.8/1.9s fall in the region occupied by Seyfert 2s with significant star formation.

Figure 7.2 shows the 10 μm silicate equivalent width (EW) compared

against the 20–30 μm spectral index. Negative EWs imply emission features. The silicate EWs are *small* for most of the Seyferts. The mean emission EW in our sample is -0.16 μm with a median of -0.08 μm. The mean absorption EW in our sample is 0.38 μm with a median of 0.26 μm. Hao et al. (2007) report silicate strengths ($S_{10\ \mu\mathrm{m}} = \ln(F_\lambda/F_{cont})$) for a large sample of quasars, Seyferts and ULIRG galaxies. The quasar and ULIRG silicate strengths bracket the range of $S_{10\ \mu\mathrm{m}}$ for Seyfert galaxies. For quasars, the mean silicate emission strength reported by Hao et al. (2007) is 0.20. For ULIRGS, it is -1.56. For comparison, we measured the apparent silicate optical depth (τ_λ) at the peak of the 10 μm feature for our Seyfert sample. The corresponding mean values of silicate strengths ($S_{10\ \mu\mathrm{m}}$) are -0.07 for Seyfert 1s and -0.35 for Seyfert 2s. The median values are 0.02 and -0.18, respectively.

There are several Seyfert 2s and a Seyfert 1 (NGC 1194) in the upper region of Figure 7.2. All of these objects are significantly inclined ($b/a \leq 0.5$) and/or are merging with companion objects. Their high EWs are probably a result of absorption in the host galaxy disk rather than being intrinsic to the AGN. Along with Seyfert 1s but slightly above are Seyfert 2 galaxies that show silicate absorption (positive EWs) but have a negative 20–30 spectral index, commensurate with strong AGN continua of Seyfert 1s. A more positive 20–30 spectral index takes us toward starburst-like spectra dominated by PAH bands and strong red continua. The most important result from this graph is that Seyferts with inclined or merging host galaxies should be excluded from studies of the circumnuclear regions, because the strong silicate EWs indicate absorption from dust in the plane of the host galaxy. This is a point that has not been generally appreciated. Once these objects are eliminated, the nuclear regions show only weak silicate emission or absorption features.

Figure 7.3 shows the equivalent width for the 6.2 μm PAH emission feature compared to the 20–30 μm spectral index. Again the equivalent widths

are negative for emission features and absolute values are plotted on the graph in logarithmic scale. As can be seen there is a strong correlation between the 20–30 μm spectral index and the 6.2 μm PAH equivalent width. Going down and to the right indicates more starburst contribution to the spectrum. A very positive 20–30 spectral index leads to the galaxies with very red continua, most of which are inclined or merging. Thus, the PAH contribution is strongly correlated with the 20–30 spectral index, which supports our use of this index as a starburst indicator in Figure 7.1. Spoon et al. (2007) show that the PAH 6.2 μm EWs are anti-correlated with silicate absorption strengths for ULIRG and starburst galaxies. In their diagram, most AGN with weak PAH strengths have weak silicate strengths, which agrees with our results in Figure 7.2. Further, Hao et al. (2007) show that the silicate strengths correlate with the ratio of fluxes at 14.5 μm and 27.5 μm for a large sample of Seyfert, ULIRG, starburst and QSO sources. Thus it appears that strong PAHs go together with very red continua toward 30 μm. Along with these properties, the presence of very strong silicate absorption leads to ULIRG-like spectra, while weaker silicate absorption leads to starburst-like spectra. Thus, weak silicate strengths and weak PAH strengths are both strong indicators of presence of an active nucleus. This argues that the observed deep silicate absorption originates primarily in dusty star forming regions on scales of hundreds of parsecs. Thus, highly inclined active galaxies will tend to show deep silicate absorption profiles. Further, in Figure 7.3, Seyfert 1.8-1.9s occupy the same region as Seyfert 2s with strong starburst contributions to their spectra. Seyfert 1s in general have weaker starburst contributions to their spectra. But this does not necessarily imply that they have weaker starbursts on an absolute scale, since a stronger flux at 6–15 μm due to hot dust will necessarily lead to weaker PAH equivalent widths and a more negative 20–30 μm spectral index.

Figure 7.4 shows the [O IV] 25.89 μm to [Ne II] 12.81 μm ratio compared to the [Ne III] 15.56 μm to [Ne II] 12.81 μm ratio. There is a strong correla-

tion, with Seyfert 2s and Seyfert 1.8/1.9s showing mostly low [O IV]/[Ne II] ratios and low [Ne III]/[Ne II] ratios. We see a similar correlation with [Ne V]14.32 μm/[Ne II] in Figure 7.5, although there are fewer data points. Most Seyfert 1s have high [O IV]/[Ne II], [Ne V]/[Ne II] and [Ne III]/[Ne II]. This correlation for Seyfert 1.8-1.9s and Seyfert 2s indicates that their NLRs are subject to similar amounts of ionization, whereas at least a component of the NLR in Seyfert 1s may experience higher ionization states, in general. Another alternative that can lead to the correlation in Figure 7.4 is that Seyfert 1.8, 1.9 and 2s have more star formation than Seyfert 1s on a absolute scale, and hence stronger [Ne II].

7.4 Implications

We have compared the mid-IR spectral properties of Seyfert 1.8/1.9s with those of archival Seyfert 1s and Seyfert 2s from Buchanan et al. (2006) and Weedman et al. (2005). Here we summarize the main results and consider the implications.

The Seyfert mid-IR spectra are dominated by four main components: (1) a hot dust ($T \gtrsim 300$ K) heated by the AGN continuum, (2) warm dust ($T \approx 170$ K) heated by the AGN; (3) cooler dust ($T \approx 60$ K) from surrounding circumnuclear star-forming regions giving rise to the strong red continuum; (4) extinction from cold dust in the host galaxy plane for merging and/or inclined host galaxies. The optical classifications of Seyferts do not always carry over to corresponding spectral shapes in the mid-IR, but there seems to be a general agreement for Seyfert 1s to show mostly single or broken power law type behavior and Seyfert 2s to show mostly PAH and red continuum dominated spectra (see Figure 6.2), in agreement with the trend noted by Buchanan et al. (2006). The simplest mid-IR spectra appear to be those of Seyfert 2 galaxies with little star formation, which are dominated by a single thermal component that peaks at ~ 17 μm. Seyfert 1s tend to have emission

from a hotter component ($T > 300$ K) in the 6–15 μm band and, in many cases, weak silicate emission, in general agreement with the Unified Model prediction that we are looking down the hot throat of the dusty torus in type 1 objects. The quenching of the intrinsic AGN continuum, leading to weaker heating of the dust in the region close to the AGN, plausibly can be the cause of changes in the spectral index in the 6–15 μm band.

AGN type variability and misclassification of Seyfert galaxies may be another reason for a mismatch between the optical Seyfert classification and the expected mid-IR spectral shapes. Some Seyfert 1.8/1.9 galaxies are known to transition to a type 1 or a type 2 class object. As we saw before, the first such detection was for NGC 7603 by Tohline & Osterbrock (1976). They noticed that the broad hydrogen recombination lines changed to narrow lines with a simultaneous increase in the stellar absorption features in the spectrum. The spectrum then recovered the broad lines again. Goodrich (1995, 1989a) found that two of our objects, NGC 7603 and NGC 2622, transitioned from a Seyfert 1.8 to a Seyfert 1.5 class probably as a result of changes in the intrinsic line of sight reddening. In the mid-IR, they show steepening spectra towards short wavelengths (see Figure 6.1 and Figure 6.1) as compared to the rest of our sample, indicative of Seyfert 1/1.5 spectra. The mid-IR spectrum of NGC 2622 is similar in its continuum shape to the mid-IR spectrum of NGC 4151 (see, Weedman et al. 2005, and Figure D.3), except that NGC 2622 shows very strong PAH bands. The mid-IR spectrum of NGC 7603 is, however, markedly different than the rest and has characteristics of a type 1 quasar spectrum with strong emission bands at 10 and 18 μm and very little cool dust emission at longer wavelengths. NGC 7603 does however, have some starburst contribution in the form of PAH bands (see Figure 6.1). Thus, it is important to compare contemporaneous optical and mid-IR spectra when possible to eliminate the possibility of type variability in the spectra. For the specific case of Seyfert 1.8/1.9s in this sample, comparison with contemporaneous optical spectra is being done and results will

be reported in a future publication.

The equivalent width of the 10 μm silicate feature in Seyfert galaxies is much weaker than expected from uniform density compact torus models (see Figure 7.2), confirming previous *Spitzer* results by Shi et al. (2006), Spoon et al. (2007), and Hao et al. (2007). There is a weak trend in our sample for the silicate equivalent width to be correlated with the 20–30 μm spectral index, hinting that some of the silicate absorption may be coming from the cool dusty star forming clouds in the host galaxy disk rather than close to the nucleus. Hao et al. (2007) present a similar trend for a much larger sample of ULIRGs, quasars, and Seyferts, as we mention in § 7.1. Spoon et al. (2007) show that the 6.2 μm PAH equivalent width is correlated with silicate absorption strengths for ULIRGs and starburst galaxies. Further, using radiative transfer calculations, Levenson et al. (2007) suggest that deep silicate absorption, as seen in ULIRG type sources, will occur only if the distribution of dust is both geometrically and optically thick. Thus, we conclude that in Seyfert galaxies, the strength of the 10 μm silicate feature is significantly affected by contamination from dust in the host galaxy and careful deconvolution will be required before torus models can be fully tested.

We find a strong correlation between the 6.2 μm PAH equivalent width and the 20–30 μm spectral index (Figure 7.3). The mid-IR starburst contribution can thus be characterized using either diagnostic. It appears that very strong PAHs go together with very red continua toward 30 μm. Coupled with above mentioned results from Hao et al. (2007) and Spoon et al. (2007), this implies that weak silicate absorption strengths and weak PAH strengths seem to be associated with strong AGN dust continua. The correlation between strong silicate absorption and redder continuum indices for ULIRGs, and the presence of deep silicate absorption in highly inclined or merging galaxies (Figure 7.2) indicates that any deep silicate absorption observed in AGN is likely associated with the dust in the host galaxy plane.

In general, the mid-IR spectra of Seyfert 1.8 and 1.9 galaxies are similar

in shape and PAH strengths (Figure 7.3) to the spectra of Seyfert 2 galaxies with starbursts. This is surprising, since the optical spectra of Seyfert 1.8-1.9s indicate only a modest amount of reddening of the BLR, typically $E_{B-V} = 1$ (Goodrich 1995). This leads to a relatively small extinction in the mid-IR, and therefore one would expect that the *Spitzer* IRS spectra of Seyfert 1.8-1.9s should look more like Seyfert 1s. This may provide an important clue to the geometry of the obscuring "torus", which will be investigated in detail in the future. However, we note that the spectra of some Seyfert 1.8 and 1.9 galaxies look like Seyfert 1 spectra after subtraction of a starburst template (see Chapter 8). This point needs further study.

In Figure 7.4 we showed a strong correlation for Seyfert 2s and Seyfert 1.8-1.9s, which tend to show low [O IV]/[Ne II] and [Ne III]/[Ne II]. There could be three possible scenarios that could give rise to the observed low [O IV]/[Ne II]. (1) The ionization state of the NLR is low in Seyfert 1.8/1.9s and Seyfert 2s as compared to Seyfert 1s. (2) The starburst component as traced by [Ne II] and PAH fluxes is intrinsically stronger in Seyfert 1.8, 1.9 and 2s than in Seyfert 1s. (3) These objects have hidden inner NLRs and are subject to significant obscuration of high-ionization NLR lines. We can rule out the last scenario for Seyfert 1.8-1.9s. The modest amount of extinction observed in the optical for Seyfert 1.8-1.9s suggests that the extinction should be negligible in the mid-IR; thus Seyfert 1.8-1.9s should have [O IV]/[Ne II] ratio similar to those of Seyfert 1s, which is not observed in Figure 7.4. If the starburst contribution is similar between Seyfert 1s and Seyfert 1.8-1.9s, but the intrinsic AGN continuum is weaker in Seyfert 1.8-1.9s, then that hints at an intrinsically low ionization state of the NLRs of Seyfert 1.8-1.9s. Whether this scenario is applicable or not can only be tested after an absolute measure of starburst contribution between different Seyfert types can be done.

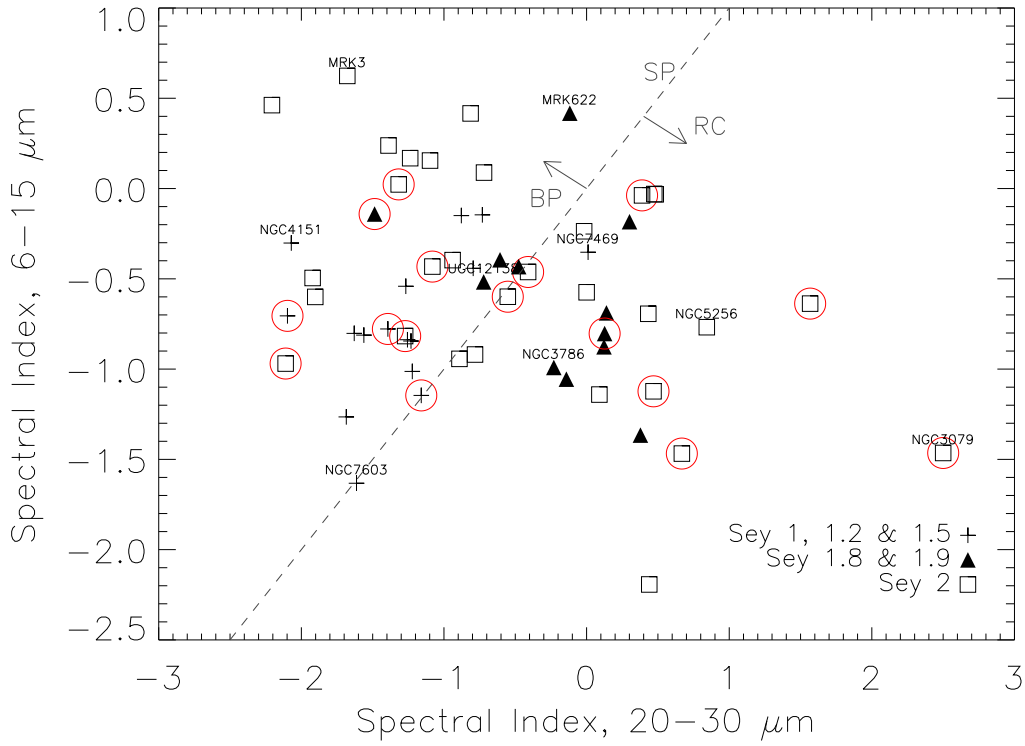

Figure 7.1: The 6–15 μm spectral index *vs.* 20–30 μm spectral index. BP—Broken Power law, SP—Single Power law and RC—Red Continuum. See Figure 6.2 for some of the example spectra. The points circled in red have highly inclined ($b/a < 0.5$) host galaxies and/or are interacting.

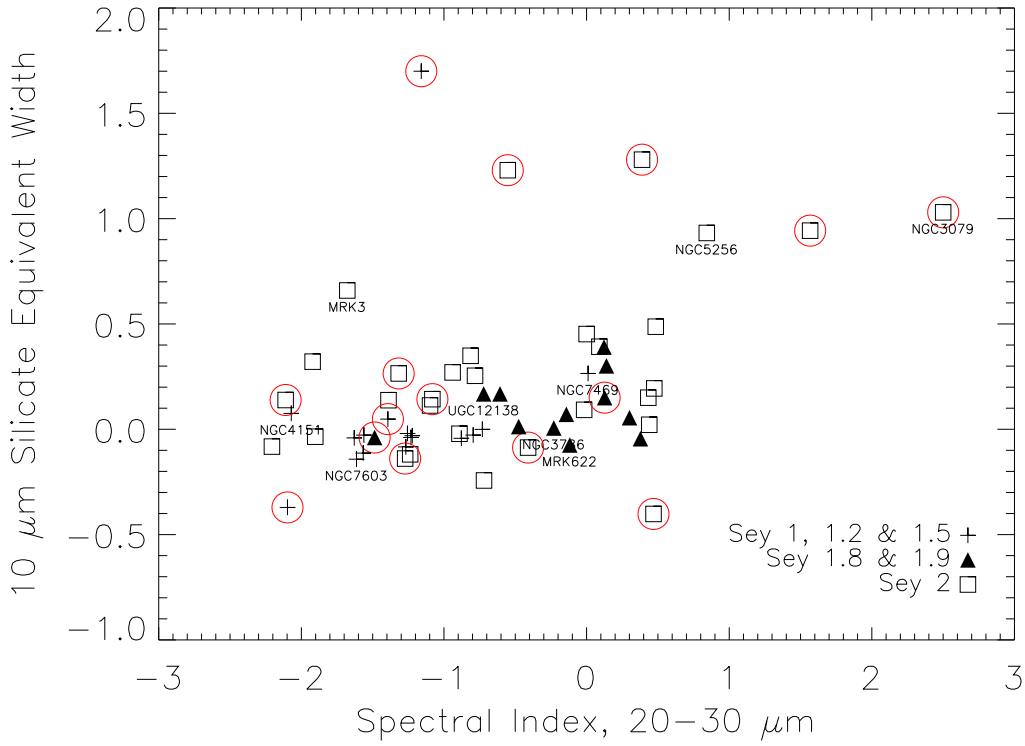

Figure 7.2: The 10 μm Silicate equivalent width (μm) *vs.* 20–30 μm spectral index. The circled symbols have host galaxies with $b/a \leq 0.5$. NGC 5256 has a fairly high equivalent width and is a face-on host galaxy, but is classified as interacting (source: NED).

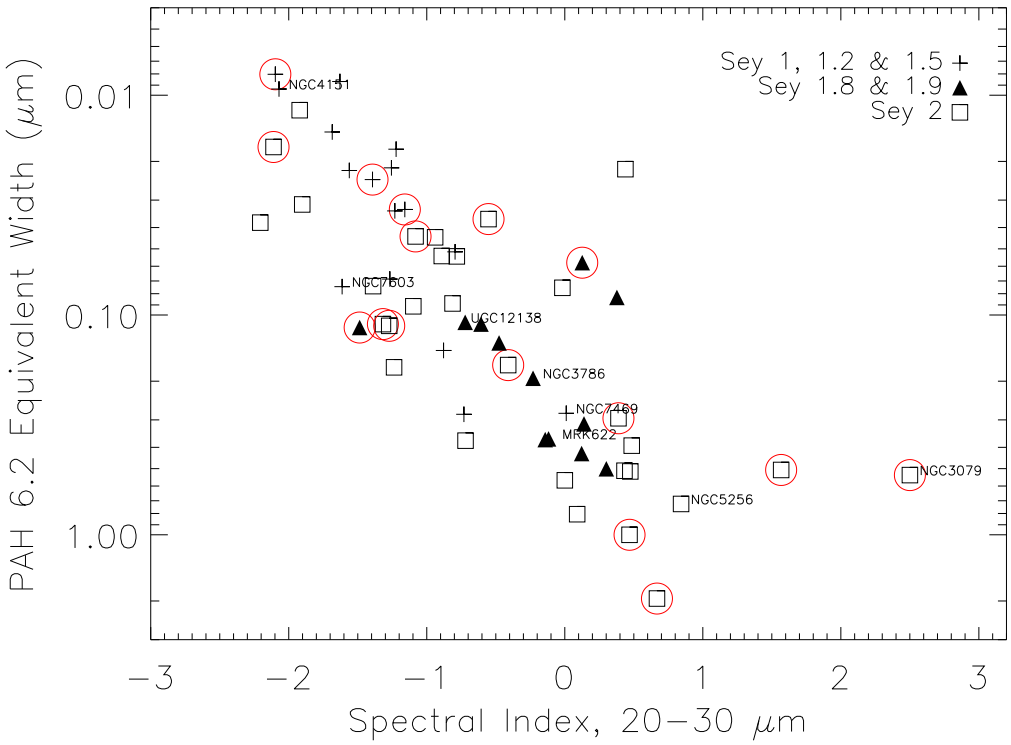

Figure 7.3: The 6.2 μm PAH equivalent width *vs.* the 20–30 μm spectral index. Equivalent widths are negative for emission features and absolute values are plotted here on a log scale. As the spectral index becomes more positive, the starburst contribution to the spectrum increases. High inclination ($b/a < 0.5$) and/or interacting systems are circled in red.

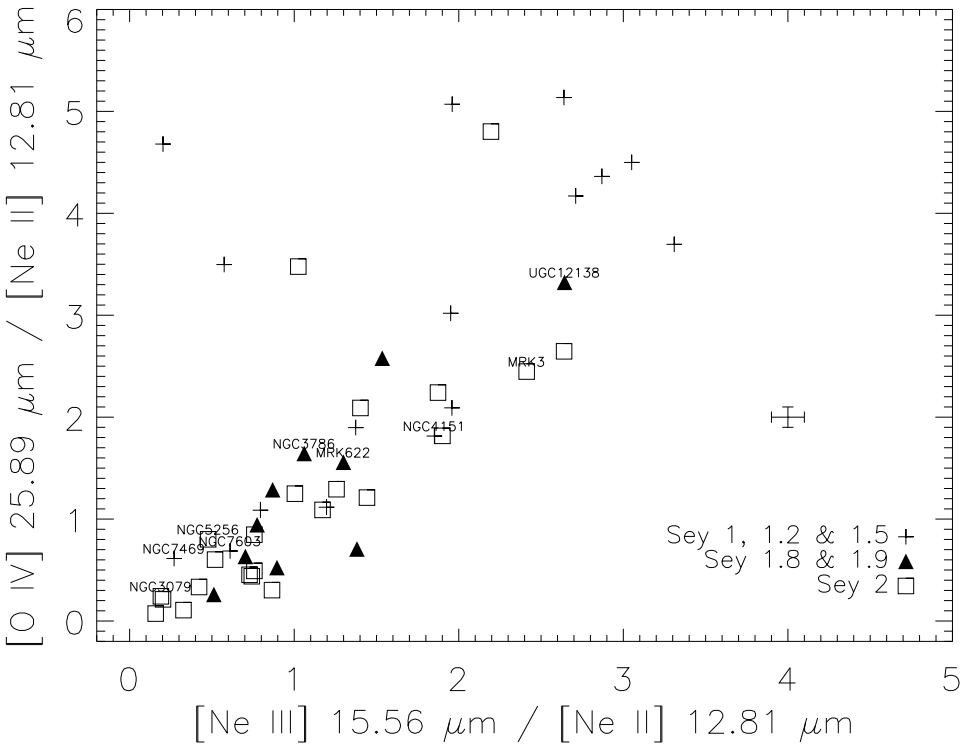

Figure 7.4: The [O IV] 25.89 over [Ne II] 12.81 ratio *vs.* [Ne III] 15.56 over [Ne II] 12.81 ratio. Correlation between Seyfert 1.8-1.9s and Seyfert 2s indicates that both subclasses of Seyfert galaxies have similar amounts of NLR ionization or they have intrinsically stronger starburst contributions as compared to Seyfert 1s. The cross symbol indicates typical error in reported ratios.

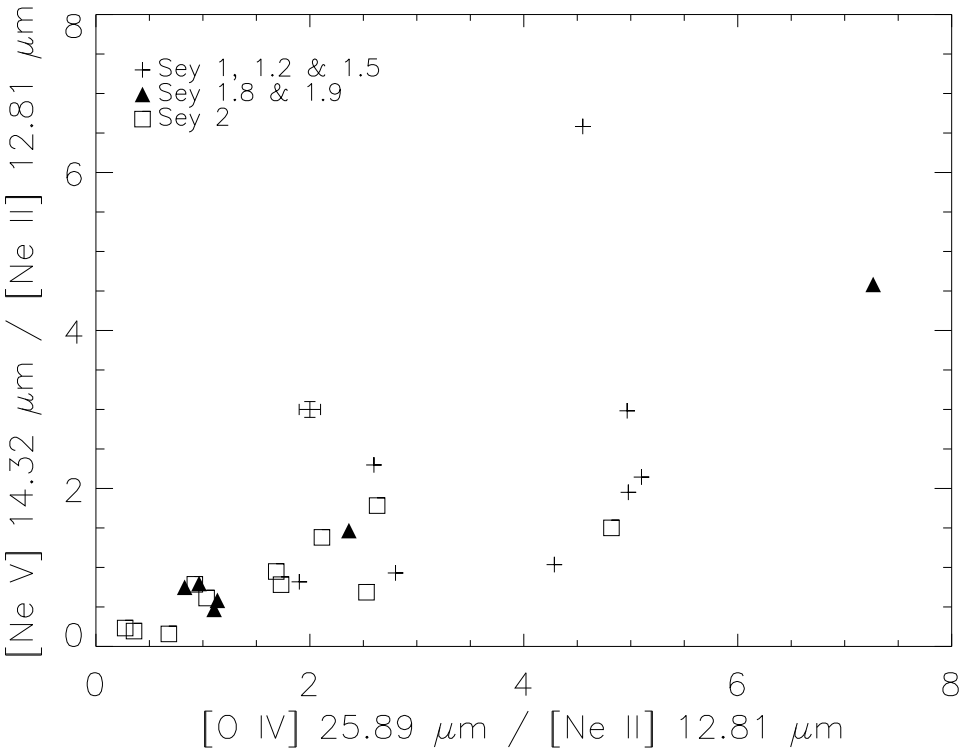

Figure 7.5: The [O IV] 25.89 over [Ne II] 12.81 ratio *vs.* [Ne V] 14.32 over [Ne II] 12.81 ratio. The cross symbol indicates typical error in reported ratios.

Chapter 8

Conclusions

In this chapter, we derive the main conclusions from this dissertation work. We have looked at three things: (1) the geometry of the NLR in relation to the inclination of the host galaxy disk, (2) the nature of the dusty spirals within $\sim$ 500 pc of Narrow-Line Seyfert 1 nuclei and the implications for AGN fueling, and (3) the nature of *Spitzer* mid-IR spectra of Seyfert 1.8/1.9s in comparison to spectra of Seyfert 1s and Seyfert 2s. What key points did we learn from this research?

8.1 Orientation Geometry of the NLR

In Chapter 2 we saw the main motivations for this study. The primary goal was to develop a computer visualization of the orientation of the NLR with respect to the normal to the host galaxy disk. Such a program was implemented in the *Interactive Data Language* and used in a number of studies (Das et al. 2005, 2006; Collins et al. 2005) to facilitate the visualization of the geometry of the NLR. The geometrical system used inside the program was based on the work of Clarke et al. (1998), but we used the NLR orientation and opening angle of the NLR as estimated from NLR kinematics, which provides accurate measures for these quantities. The key difference from pre-

vious studies, which used the weak elongated radio emission or [O III] λ5007 emission line images from *HST* , is that we can determine the inclination angle of the NLR bicone from the kinematics. This allows better constraints to be obtained on the angle (β) between the NLR axis (presumed to be the axis of the accretion disk) and the normal to the galaxy plane. The NLR kinematics are thus a probe of the orientation of the accretion disk with respect to the host galaxy disc in Seyfert galaxies. These geometric constraints can then be applied to the dynamical models of the NLR outflow to constrain them. The simulated orientation geometry can also be used to check the observed properties of extinction in the NLR (Collins et al. 2005) and determine which side of the emission bicone is being extincted by the inclination of the host galaxy.

A key question comes from this study. Is the inclination of the nuclear disk within $\sim$ 500 pc of the nucleus the same as the inclination of the large-scale disk of the host galaxy? If they are different, are they different in sizable numbers of Seyfert galaxies? This question will have some bearing on the formation and the extinction of the ENLR and the NLR, as well as the geometry of the fueling flow from the galaxy to the nuclear regions. The orientation of the NLR bicone axis with respect to the inner nuclear disks (β_{inner}) and with respect to the outer host galaxy disk (β), should be compared. It may be possible to determine the inclination of the nuclear disk with radio VLBI observations of molecular gas. One example is the study of ^{12}CO emission from the central $\sim$ 100 pc of NGC 1068 by Schinnerer et al. (2000), where they suggest that a warped molecular disk of gas can provide the fueling flow to the nucleus, as well as sufficient obscuration to classify NGC 1068 as a Seyfert 2 type object from our line of sight. A result by Hunt & Malkan (2004) also suggests that the nuclear regions of Seyfert 2s are more morphologically disturbed than those of Seyfert 1s. These results hint that the distribution of dust on a scale of hundreds of parsecs in Seyferts may play a role in their optical classifications, in addition to the role played

by the parsec-scale torus near the nucleus.

8.2 NLS1s and Nuclear Dust Spirals

We studied *HST* WFPC2 optical images of a sample of NLS1s and BLS1s. Crenshaw et al. (2003a) had noted an excess of large-scale bars in NLS1s as compared to BLS1s. We studied the nuclear region of this sample of NLS1s and noticed that a number of them show grand-design type nuclear spirals in comparison to BLS1s, which tend to show flocculent multi-arm and tightly-wound nuclear spirals. These results were published in Deo et al. (2006).

A number of previous studies (Martini et al. 2003b; Pogge & Martini 2002) had reported that instead of nuclear dust bars, they detected an excess of nuclear spirals in the centers of active galaxies. Further, these studies also noted that galaxies hosting large-scale stellar bars had grand-design type nuclear spirals at their centers, while those without large-scale bars showed multi-arm tightly-wound nuclear spirals. These studies indicated that large-scale bars drive spiral density shocks to centers of active galaxies.

NLS1s are thought to have smaller black hole masses ($\sim 10^6\ M_\odot$) and higher relative accretion rates. Thus, finding grand-design type nuclear spirals in centers of barred NLS1s supports the scenario whereby the central SMBH is fed efficiently via the nuclear spiral shocks driven by the gravitational potential of the large-scale stellar bars.

Along with the nuclear grand-design spirals in NLS1s, we also found that NLS1s tend to show nuclear rings of star formation. These rings often host massive young star clusters and are resonance phenomena (Buta & Combes 1996). As the gas is driven inward due to large-scale bar shocks, it piles up at the Lindblad resonances, and this leads to massive bursts of star formation, thereby producing the ring-like structures.

These observations show that the central regions of Seyfert galaxies host a large amount of gas and dust, which is often driven there by the presence

of large-scale bars. The different types of nuclear spiral morphology seen in the inner regions of Seyfert galaxies also hints at evolution of the nuclear region due to external triggers, such as bars and minor mergers.

Véron-Cetty & Véron (2001) show that the permitted narrow "broad" lines in NLS1s are better fit by Lorentzian profiles than by Gaussian ones. Dietrich et al. (2005) show that such profiles are also well fit by two component Gaussian profiles, where one component has FWHM $\simeq 3275\pm800$ km s^{-1} while the narrow core has FWHM $\simeq 1200\pm300$ km s^{-1}. Véron-Cetty & Véron (2001) had noted similar trends, indicating that there is broad-line gas with velocities similar to those of BLS1s. Véron-Cetty & Véron (2001) suggest that the intermediate FWHM (~ 1500 km s^{-1}) profiles seen in NLS1s may come from a flattened disk of gas. It has been suggested (Mason et al. 1996) that the observed narrow "broad" lines may arise from an intermediate region between the NLR and the BLR. Significant obscuration of the BLR emission in NLS1s may lead to such narrow permitted lines *and* weaker NLR ionization. Dietrich et al. (2005) however suggests that the NLRs in NLS1s and BLS1s may not have different ionization levels based on similar strengths of optical emission lines that are sensitive to the EUV continuum. It remains to be seen if the weakness of "broad" components in NLS1s is due to an obscuration effect.

8.3 Mid-IR spectroscopy of Seyfert 1.8/1.9s

As we saw in Chapters 6 and 7, Seyfert 1.8/1.9 mid-IR spectra from our sample show a dominant contribution from circumnuclear star formation. Many Seyfert 2 galaxies show the same effect. We show that the simplest mid-IR spectra appear to be those of Seyfert 2 galaxies with little contribution from star formation. These spectra appear to be dominated by a "warm" ($T \sim 170$ K) dust component, and it is likely that this dust component leads to the observed "17 μm" break. Further, Seyfert 1 spectra tend to

have stronger continua in the 6–15 μm range than Seyfert 1.8/1.9s and 2 galaxies. Finally, it is plausible that the deep silicate absorption observed in a few objects originates in cold dust in the host galaxies of high inclination or interacting systems.

The distribution of dusty matter in the nuclear disks of Seyfert galaxies (Malkan et al. 1998; Hunt & Malkan 2004) can play a significant role in this case. The dust associated with the nuclear disks of Seyfert galaxies can then mimic the effects attributed to a compact dusty torus on parsec scales. However, our sample of Seyfert 1.8/1.9s is selected to be face-on and should in principle, have much less contamination due to extinction from the host galaxy. As we noted above, the spectra are dominated by circumnuclear starburst features, and we decided to see how the *HST* images look for Seyfert 1.8/1.9s in our sample. The structure maps of these images are displayed in Figure 8.1 and 8.2. As can be seen, many of them are barred and show disturbed dust morphology and starburst regions in their central kiloparsecs. This nuclear dust morphology is surprisingly similar to NLS1s.

The correlation between the [O IV]/[Ne II] *vs.* [Ne III]/[Ne II] ratio for Seyfert 1.8/1.9s and Seyfert 2s suggests three possibilities: (1) the ionization state of the NLR is low in the mid-IR in Seyfert 1.8/1.9s and Seyfert 2s as compared to Seyfert 1s, (2) the starburst component as traced by [Ne II] and PAH fluxes is intrinsically stronger in Seyfert 1.8/1.9s and Seyfert 2s than in Seyfert 1s, (3) Seyfert 1.8/1.9s have hidden inner NLRs and are subject to significant obscuration of high-ionization NLR lines. The only scenario we can rule out presently is the last one. Since Seyfert 1.8/1.9s are expected to have only a modest amount of extinction in the optical (Goodrich 1995), this suggests that extinction should be negligible in the mid-IR. Thus, Seyfert 1.8/1.9s should rather have similar [O IV]/[Ne II] ratios as Seyfert 1s, which is not true. At the present, without proper separation of the starburst component from the spectra, we can not rule out the second possibility. An absolute measure of the starburst contribution is essential before further

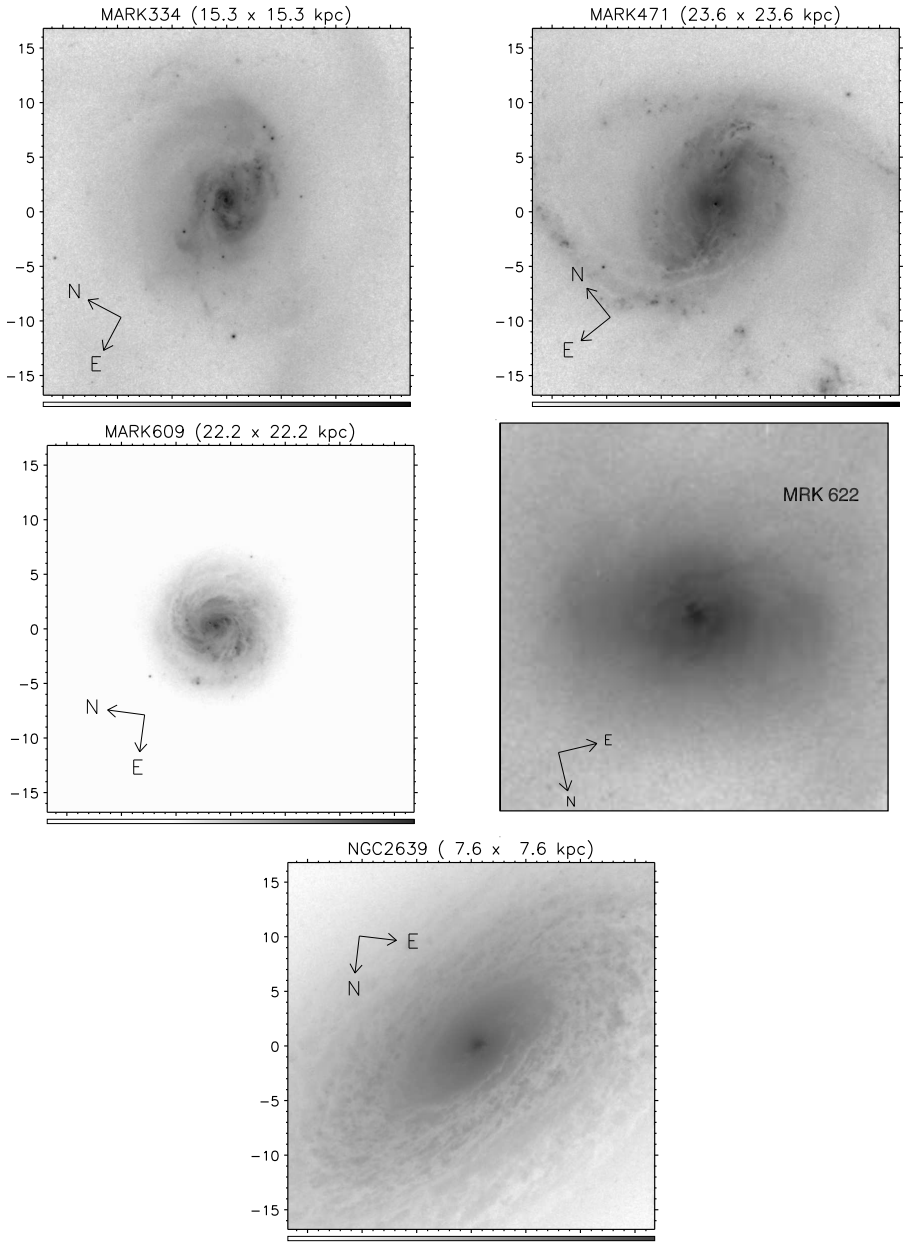

Figure 8.1: Structure maps of Seyfert 1.8/1.9s from our program.

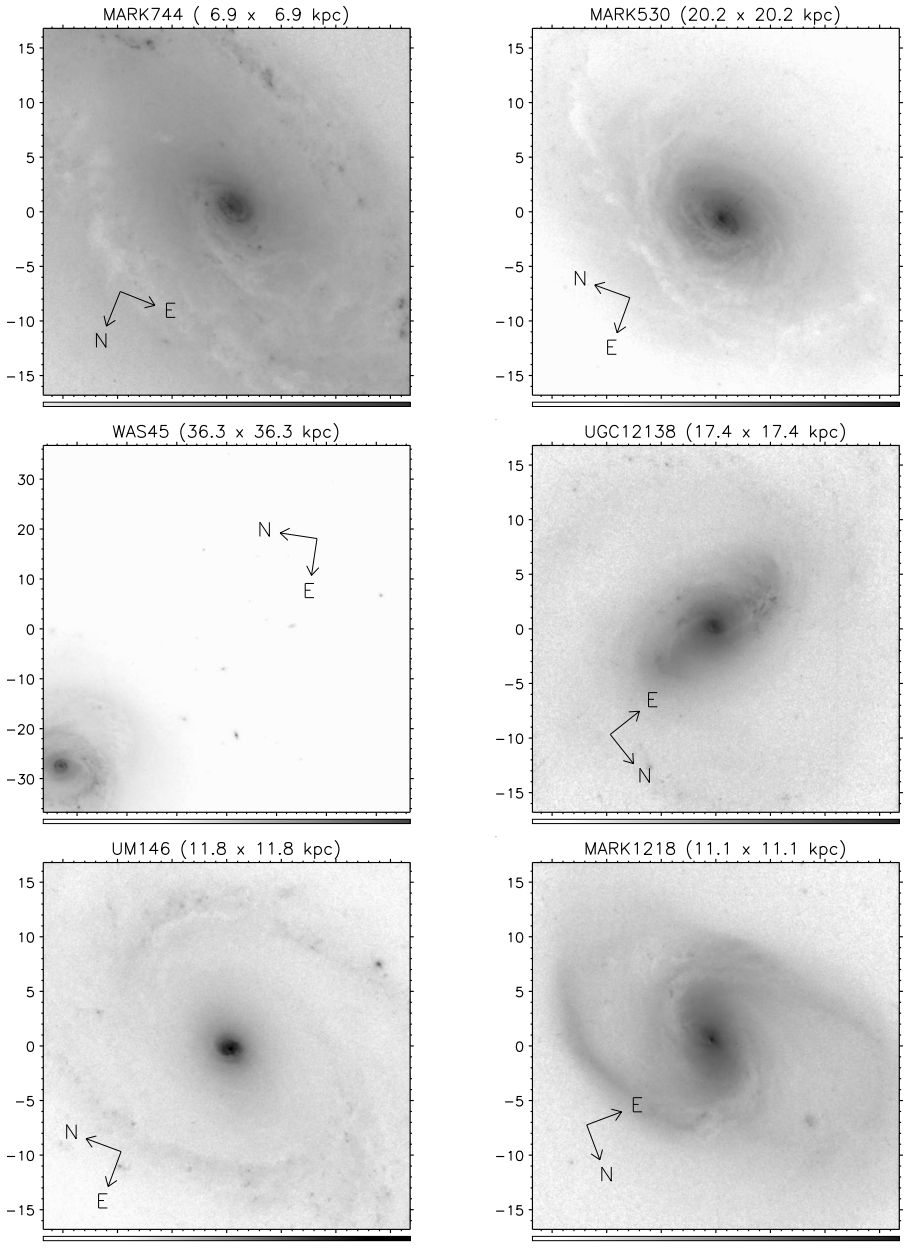

Figure 8.2: Structure maps of Seyfert 1.8/1.9s images from our program.

conclusions can be derived.

8.4 Future Directions

We look at further research ideas based on the current research discussed so far. First, we discuss the simple decomposition of mid-IR spectra into a few components, which we are already actively pursuing. Secondly, we bring together some recent and past results in the literature on the nature of Seyfert 1.8/1.9s and NLS1s to ask new questions.

8.4.1 Decomposition of Mid-IR Spectra

Here we demonstrate decompositions of selected mid-IR spectra into individual spectral components. These components include: (1) a pure Seyfert 1 mid-IR continuum, (2) a pure Seyfert 2 mid-IR continuum, (3) a starburst PAH template, (4) a mid-IR continuum due to starbursts and (5) an emission/absorption spectrum due to the silicate-graphite-PAH (Draine & Li 2007) dust at a given temperature. Here we focus only on the first four components.

Historically, the mid-IR spectrum of M82 has been used as a starburst template. This spectrum does not show any effects due to silicate absorption (Sturm et al. 2002) and hence provides a decent starburst template. Laurent et al. (2000) used the ISO spectrum of NGC 7023, a PDR region in the Galaxy as the PAH template. They supplemented this with the ISO spectrum of M17, an HII region in the Galaxy, to provide the VSG continuum. Laurent et al. (2000) used these templates with nuclear ISO spectrum of Centaurus A as the AGN template to derive their diagnostics mentioned in §4.5. An alternative template based on *Spitzer* spectra of local starburst galaxies is provided by Brandl et al. (2006). In the simple decompositions discussed in next section, we use this spectral template to provide the PAH

features and mid-IR continuum due to starburst. This spectrum template is displayed in Figure 8.3.

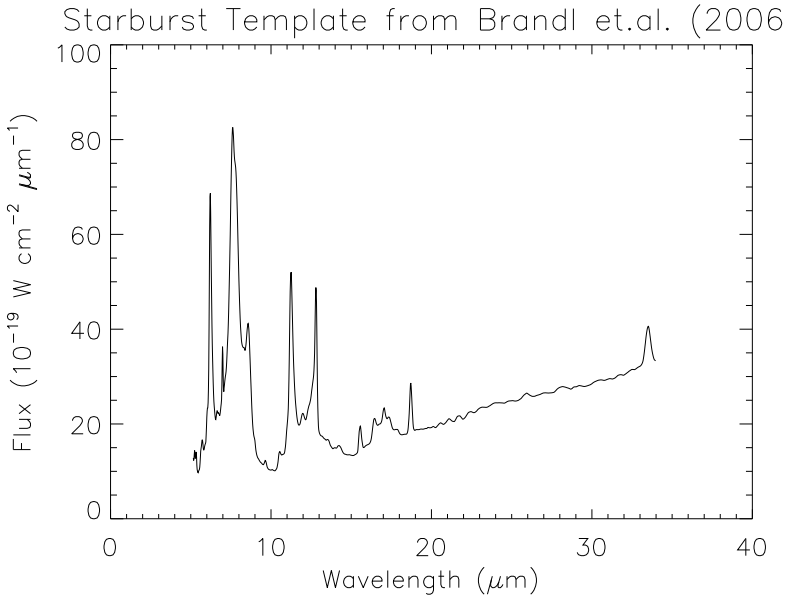

Figure 8.3: Starburst template from Brandl et al. (2006).

We use the spectrum of Mrk 3 as the base Seyfert 2 template that peaks in flux around 17 μm (a black body of ≈ 170 K). Although Mrk 3 shows an additional "hot" ($T \approx 450$ K) dust component in the $5.3 - 7.0$ μm range, to first order the spectrum of Mrk 3, which is devoid of any PAH features, acts as a good Seyfert 2 spectral template. The spectrum of Mrk 3 is displayed in Figure D.5, bottom-left.

Further, we use the spectrum of NGC 4151 derived by subtracting a combination of the Seyfert 2 template (spectrum of Mrk 3) and the starburst template from the spectrum of NGC 4151. This is shown in Figure 8.4. It should be noted that the intrinsic mid-IR AGN continuum is most probably a superposition of several black body spectra that are modified by the emission and absorption processes of the dust distribution in the line of sight.

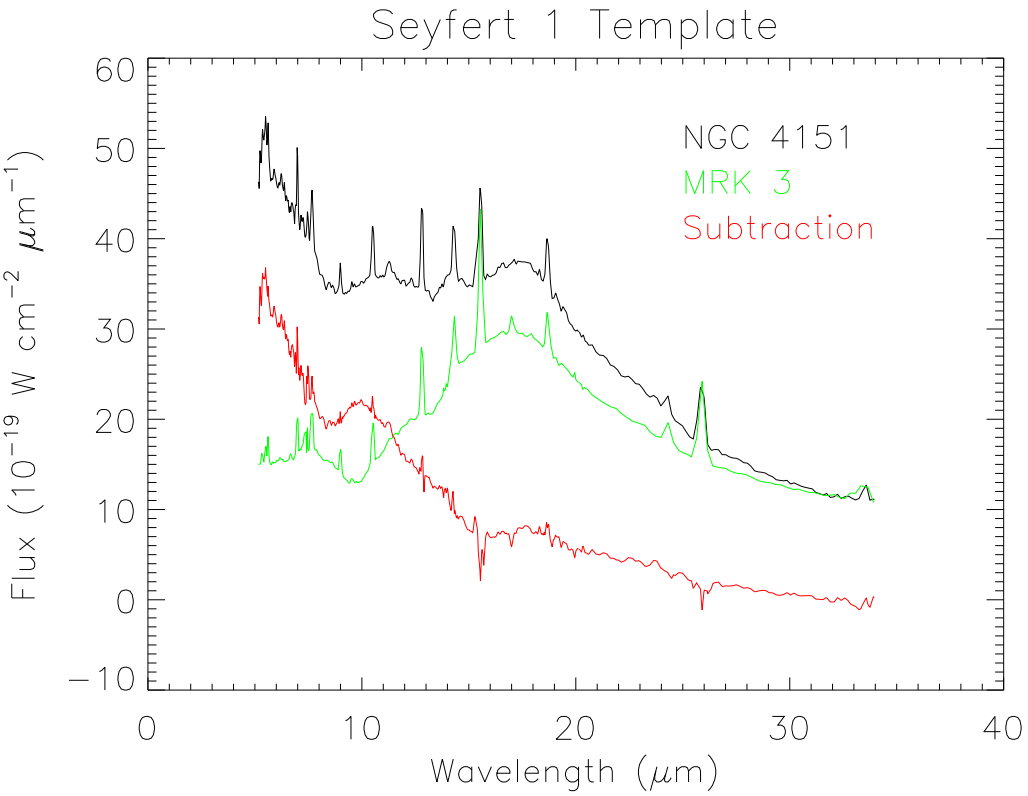

Figure 8.4: A possible Seyfert 1 mid-IR spectral template: The subtraction of Mrk 3 spectrum scaled to match NGC 4151 spectrum around 30 μm brings out the weak silicate emission features in the spectrum of NGC 4151. The underlying AGN continuum rises strongly toward short wavelengths. Both NGC 4151 and Mrk 3 have little contribution from star formation. The emission lines are not fully matched and are over-subtracted in some cases, indicating intrinsically different strengths in the NLRs of Mrk 3 and NGC 4151.

As we noted in § 6.1, almost all of our Seyfert 1.8/1.9s spectra appear to be strongly contaminated by the contribution from circum-nuclear starbursts. Thus it is natural to ask, how will the spectra look if we subtract the starburst component?

We attempted simple template subtractions on Seyfert 1.8/1.9 spectra

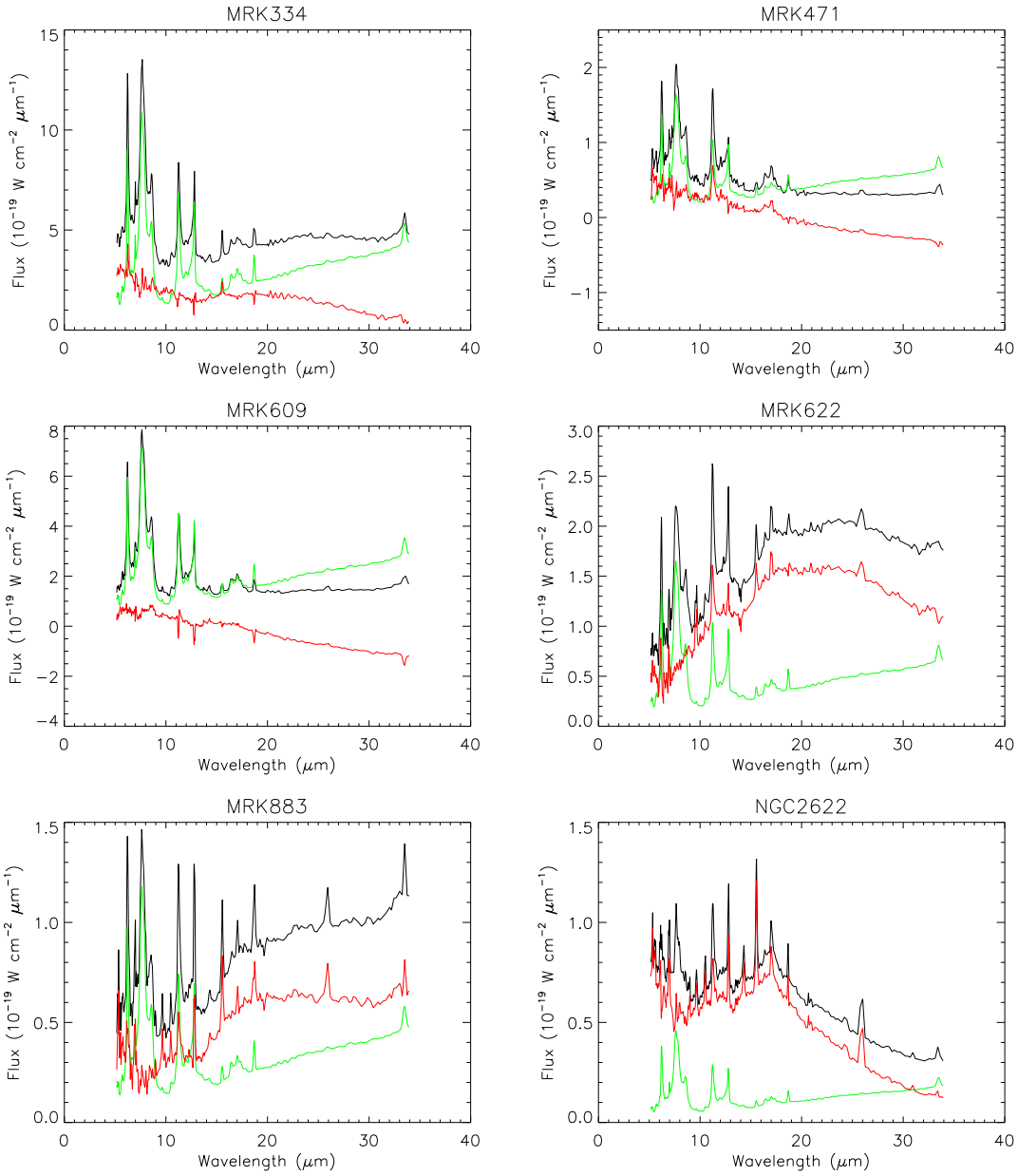

Figure 8.5: Simple subtraction of starburst template from Seyfert 1.8/1.9 Spectra. Black trace–observed spectrum, green–Starburst template, and red–subtraction.

and the results are shown in Figure 8.5. As can be seen, a few Seyfert 1.8/1.9s show Seyfert 1/1.5 like spectra (see Figure 8.4). Although the subtractions are very noisy, the silicate emission features at 10 μm and 18 μm are quite clearly seen in Mrk 334, NGC 3786, NGC 7603, UGC 12138, 4 out of 12 Seyfert 1.8/1.9s in our sample, by using just simple scaling and subtraction of the starburst template. However over- or under-subtractions in these spectra also demonstrate that a monolithic starburst template is probably not a good representation of the starburst contribution in these spectra. More sophisticated approaches involving curve-fitting of PAH features and the underlying continuum are needed. Nevertheless, it is instructive that by combining scaled template spectra, it is possible to retrieve some information about the underlying AGN continuum and the silicate emission features. For example, Figure 8.7 shows the subtraction of the Mrk 3 template and the starburst template from the NGC 2622 spectrum. The residual spectrum is comparable to that of NGC 4151 in Figure 8.4.

Thus, simple template subtraction shows that some Seyfert 1.8/1.9s have a type 1 continuum underneath that is being marginally over-shadowed by the strong circum-nuclear starburst. It will however be much more accurate to fit individual spectral components, such as the PAH features, the starburst continuum, the forbidden emission lines, the "hot", "warm" and "cold" dust continua, and the silicate emission features. We are currently in the process of writing such a piece of code that will combine these various spectral features in the mid-IR and provide a simultaneous multi-component fit to the spectra.

We have derived two primary results from these decompositions. First, it is possible to decompose the mid-IR low resolution spectra into identifiable and measurable components, as discussed above. We show that the intrinsic spectra of some Seyfert 1.8/1.9s are more like Seyfert 1.5s in the mid-IR, but are contaminated by extensive star formation in the circum-nuclear region. Secondly, the $\sim$ 17 μm break noticed in many Seyfert galaxies is a result of presence of a distribution of dust with temperature $T \approx 170$ K. The

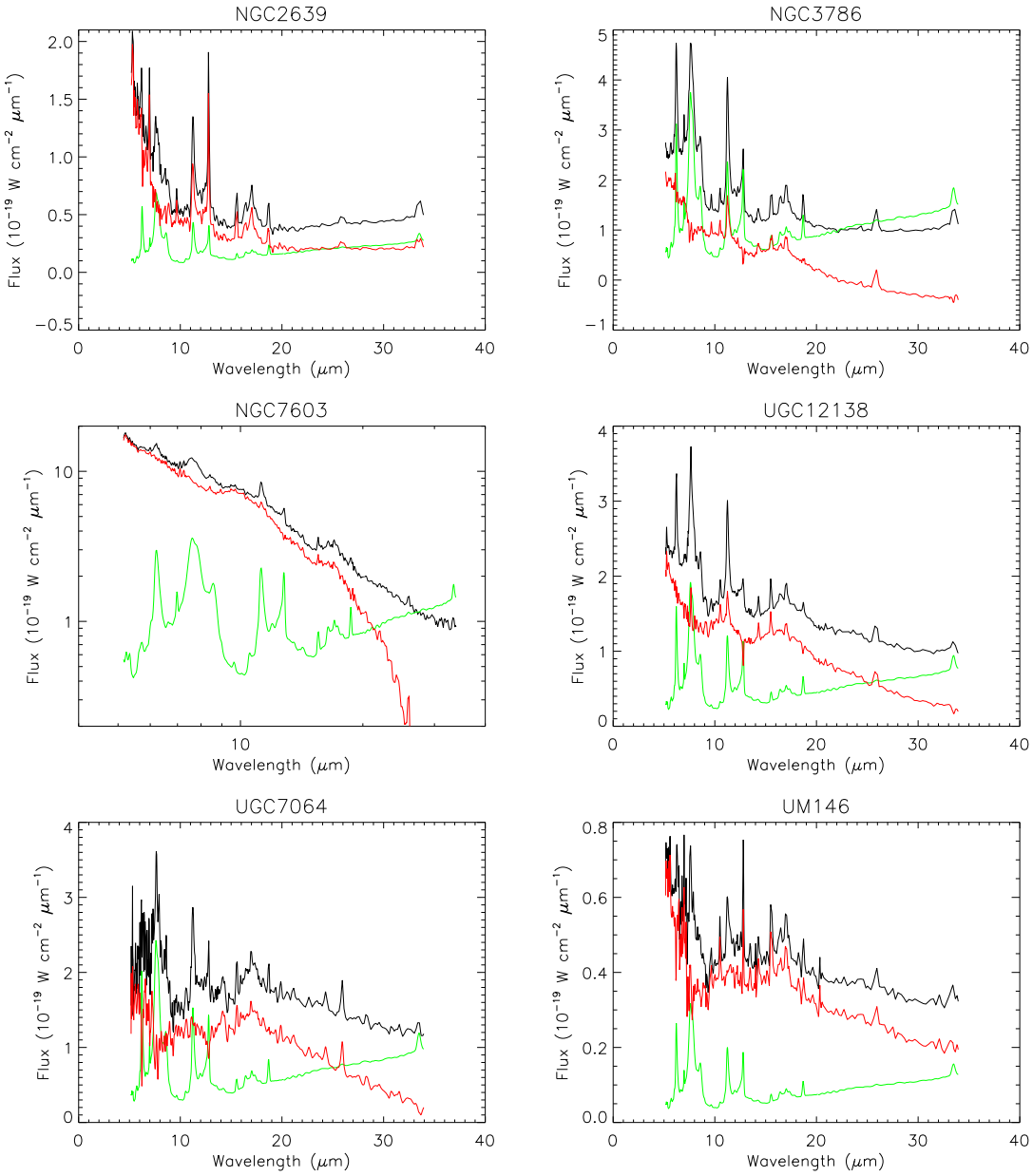

Figure 8.6: Simple subtraction of starburst template from Seyfert 1.8/1.9 Spectra. Black trace–observed spectrum, green–Starburst template, and red–subtraction.

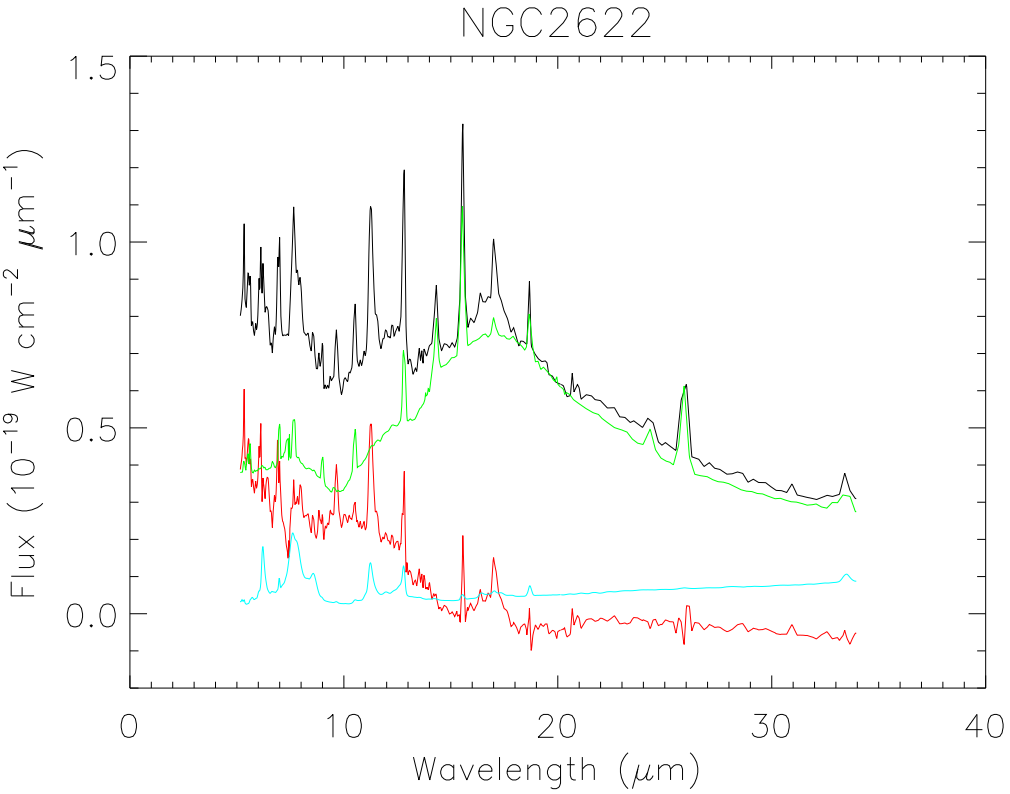

Figure 8.7: Decomposition of NGC 2622 (black) using the Seyfert 2 (green) and starburst template (cyan), note the silicate emission features in the final subtraction (red).

predominant existence of this break in the mid-IR spectra of many Seyfert 1.5 and Seyfert 2 systems indicates common excitation mechanisms and/or distances from the central source for the dust distribution giving rise to this component. The multi-component fits will greatly increase our ability to understand mid-IR Seyfert spectra in the near future.

8.4.2 Type variability of Seyfert 1.8/1.9s and NLS1s

Some Seyfert galaxies (*e.g.,* NGC 7603, Tohline & Osterbrock 1976) show strong variations in their broad emission lines and change their optical Seyfert type over a period of a few years. This variability of broad hydrogen lines was attributed to changes in reddening (Goodrich 1995), but there are indications from long term monitoring ($\sim$ 20 yr, Kollatschny et al. 2000) of NGC 7603 that this may not always be the case. Interestingly, NGC 7603 also shows variations in its Fe II complexes commensurate with changes in $H\alpha$, indicative of variations in a highly dense component of BLR gas from which the Fe II blends are thought to arise. Further, Véron-Cetty et al. (2001), show that objects with strongest Fe II emission have narrower Balmer lines. They also show an anti-correlation between FWHM of Hβ and $R_{4570} = f(\mathrm{FeII}\ \lambda4570)/f(\mathrm{H}\beta)$, where they propose that objects that fall into the NLS1 class have FWHM of Hβ up to 3500 km s^{-1} with $R_{4570} > 0.5$. They also show that for NLS1s, as the strength of the Fe II complex increases, the soft X-ray excess also increases, and that the maximum FWHM of Hβ for NLS1s can be an increasing function of the Hβ luminosity. Further, by using spectropolarimetry of Seyfert 1.8/1.9s (Goodrich 1989a) shows that widths of the polarized broad Balmer components are comparable to those of NLS1s. A number of these intriguing observations lead to the question: **are the Seyfert 1.8/1.9 and the NLS1 phenomena results of associated changes in the active nucleus?** Currently this question is highly speculative, but it seems that a systematic study of a large sample of Seyfert 1.8/1.9s in the optical with a large database of AGN like Sloan Digital Sky Survey, in comparison to the previously studied NLS1s samples such as those of Véron-Cetty et al. (2001), will probe the continuum of properties between these type 1 Seyferts.

Appendix A

Using the Seyfert Visualization Tool

The following sequence of screen captures shows how the visualization tool can be used to simulate the geometry of the NLR and the disk of the host galaxy. We will take the example of NGC 4151 (the parameters are given in Table A.1). The software distribution comes with a UNIX shell script called `run_sim.sh`. The shell script is executed from the command terminal on an X server display. The shell script searches the IDL library paths to initiate some of the base 3-D IDL routines from the IDL demo library and then executes IDL. IDL compiles the routines needed to load the software and a GUI window is displayed on the user's screen. The usage is extremely simple.

The user inputs the position angle (P.A.$_{\rm gal}$) and inclination ($i_{\rm gal}$) of the host galaxy, the position angle (P.A.$_{\rm bicone}$) and inclination (ϕ) of the NLR bicone, and the half-opening angle ($H.A._{\rm bicone}$) of the NLR. The screen of the software will look as in Figure A.1(a). On the panel to the left, the parameters can be typed in to the text-boxes. After that, clicking on the "Build Model" button will construct the model. The screen will look as in Figure A.1(b). After this point, the user can use the mouse pointer to drag

Table A.1: Geometrical Model Parameters for 12 Seyfert Galaxies.

Galaxy Name	Galaxy P.A.	Galaxy Incl.	Bicone P.A.	Bicone Incl.	Bicone H.A.	Closer Side	δ	β
(1)	(2)	(3)	(4)	(5)	(6)	(7)	(8)	(9)
MRK 3	208	33	252	83	23	W	44	62
MRK 573	5	30	118	67	40	SE	113	40
MRK 620	230	39	85	82	23	NW	145	62
NGC 1068	106	40	15	85	35	NE	91	45
NGC 1386	205	68	181	87	23	NW	24	67
NGC 3081	86	34	165	80	40	S	79	47
NGC 3516	236	36	200	23	26	NE	36	28
NGC 4151	22	20	60	50	36	SW	38	40
NGC 5506	91	76	192	68	40	S	101	13
NGC 5643	92	30	260	87	43	S	168	81
NGC 5728	182	52	135	68	35	W	47	40
NGC 7212	222	53	185	76	41	NW	37	52

Notes: The columns (2)–(6) form the input parameters for the visualization program and columns (7)–(9) give the results. The parameters for Mrk 3, NGC 4151 and NGC 1068 listed here are based on slitless spectra; more accurate parameters were derived later by Das et al. (2005, 2006) and Collins et al. (2005) which are listed in Table 2.1

the model in 3-D to visualize the geometry. An example view is shown in Figure A.1(c). The model can be brought back to original sky view by click on the menu "View" and then "Reset model view".

A.1 Advanced usage

When the model is built, each surface in the model is designed as a separate model object in IDL. Thus each surface can be independently transformed to a different coordinate system, via translation, rotation and scaling. This allows the user to scale the components with respect to each other, while

keeping their relative orientations with respect to other components the same. The most disruptive mechanism is changing the rotation transformation, as the simulated geometry can then be anything the user chooses it to be. This is not recommended.

Apart from the main components of bicones, the disk, the software also includes axes as colored lines in the model. The galaxy axes (major and minor) are colored red. The plane of the sky is indicated by red and green colored axes. The LOS is colored blue. The bicone axis is colored yellow. The coloring and shading of all model components can be changed from the "Options" menu. Surrounding the model is a cubical grid, which can be turned off. The north-east compass is fixed on the side of the cube facing the observer. The "Options" menu allows changing the plotting styles of all model objects in the view.

Before modifying a model object in the view, it must be selected. This is done using the mouse pointer and right-clicking on the object of interest. Right-clicking in an empty area of the model, de-selects the selected model. The "Edit" menu allows selection, deletion and restoring of model objects in the current view.

Once the model is configured to the user's liking, the "File" menu allows printing to a postscript file. You can also export the current view as a GIF, JPEG, or a TIFF file. Another interesting option is to export the view as a Virtual Reality Markup Language (VRML) file. The advantage of this option is that one can load this VRML file in a full-fledged 3-D animation software for further editing.

Clicking on the "Quit" button will bring you back to the IDL command prompt. Type "Exit" on it to close the IDL session.

A.2 NLR geometry of 12 Seyfert galaxies

Table A.1 shows 12 Seyfert galaxies for which we modeled the orientation of the NLR with respect to the host galaxy disk. This effort was reported in Deo & Crenshaw (2003). We compiled the listings of P.A. and inclinations ($i = \arccos(b/a)$) of host galaxies from the NASA Extragalactic Database. The inclination angle, the P.A. and the half-opening angle of the [O III] NLR bicones were provided by J. Ruiz from his dissertation. These parameters are derived from slitless spectroscopy. The reduction of slitless spectra to radial velocities is complicated. It is estimated that these are inferior to the measurements done with the long-slit spectroscopy. Nevertheless, these parameters provide a first crude estimate of the NLR geometry. The simulated geometries are shown in Figure A.2 along with the HST/WFPC2 images for their nuclear regions in the light of [O III] λ5007. As can be noted, the ranges of β angles are consistent with random orientations.

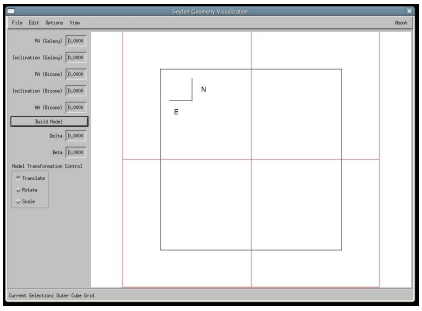

(a) Initial screen

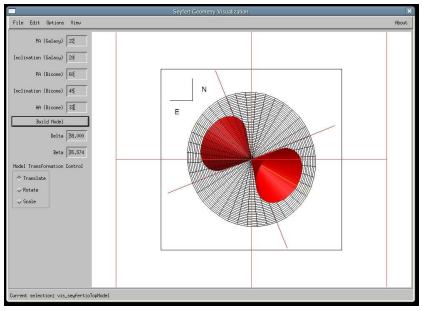

(b) Sky view after the model is built

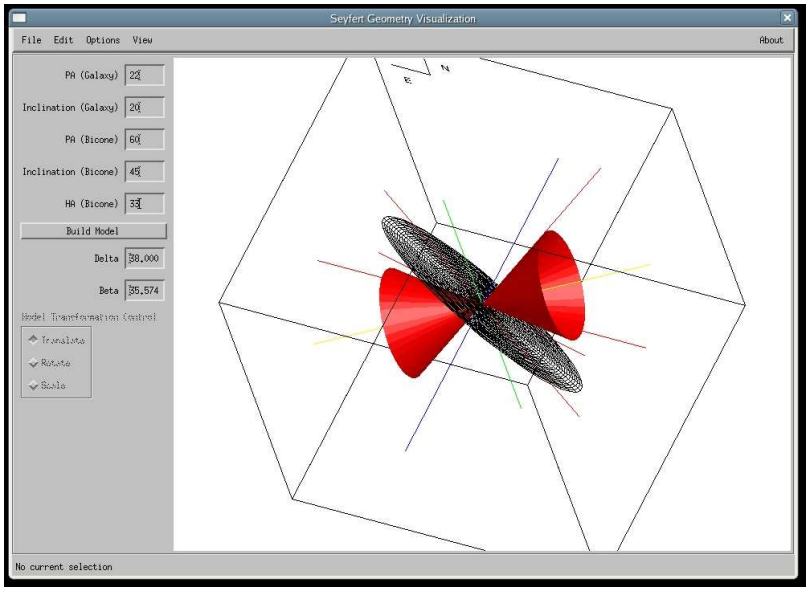

(c) Model rotation in 3-D with mouse

Figure A.1: Screen captures for Seyfert Geometry Visualization software.

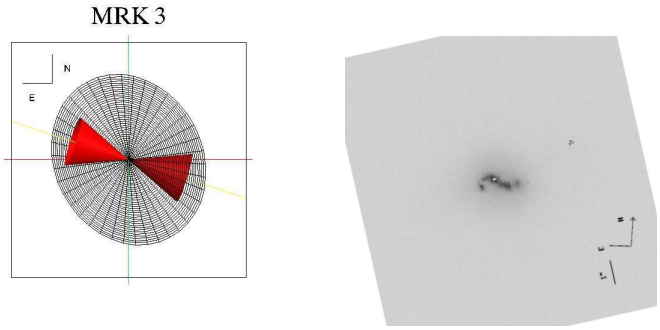

(a) Mrk 3

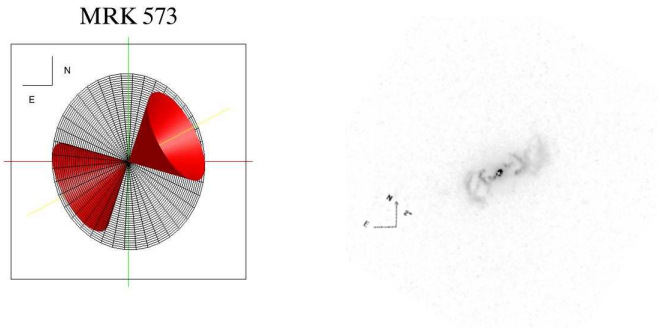

(b) Mrk 573

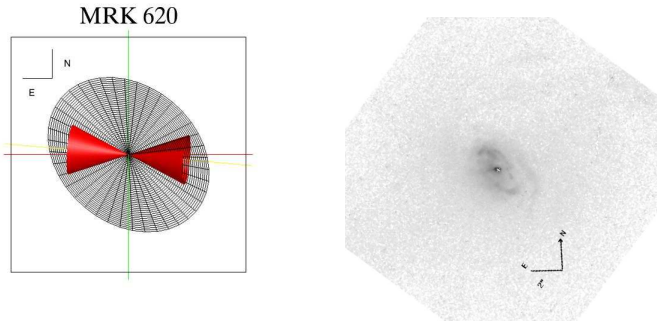

(c) Mrk 620

Figure A.2: NLR orientations of 12 Seyfert galaxies: left column shows models, right column shows the WFPC2 F502N filter ([O III] λ5007) *HST* images.

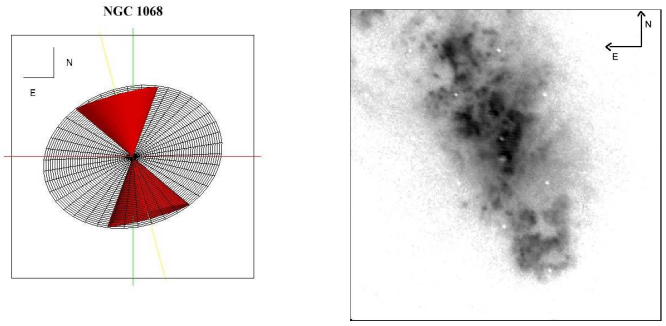

(a) NGC 1068

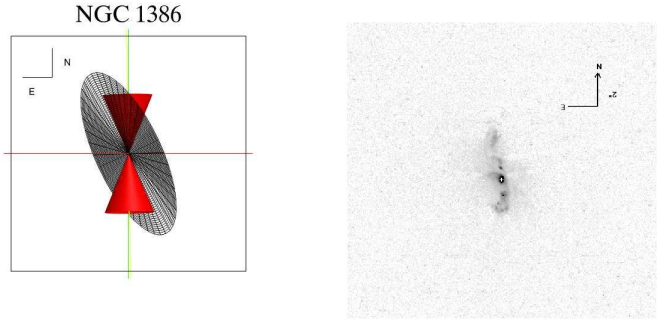

(b) NGC 1386

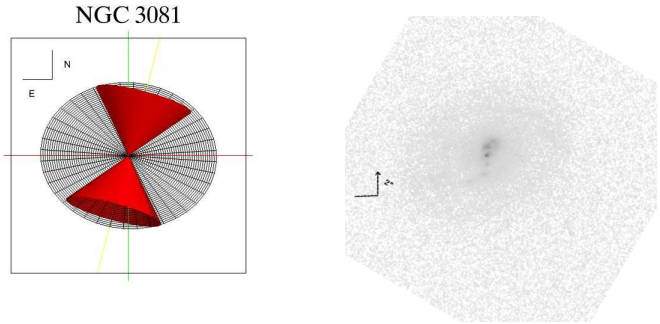

(c) NGC 3081

Figure A.3: NLR Geometries of 12 Seyfert Galaxies: continued

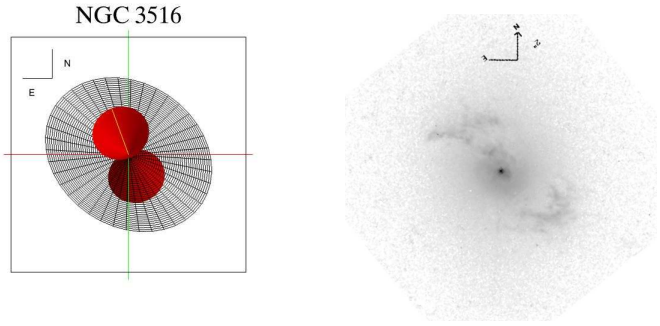

(a) NGC 3516

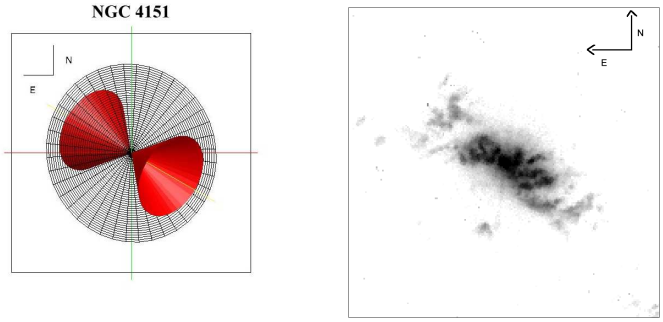

(b) NGC 4151

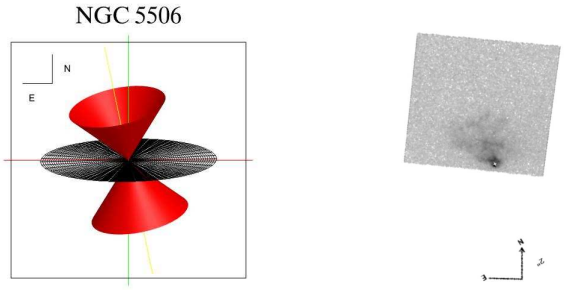

(c) NGC 5506

Figure A.4: NLR Geometries of 12 Seyfert Galaxies: continued

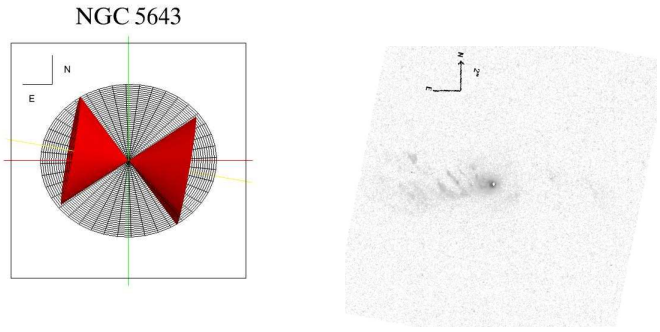

(a) NGC 5643

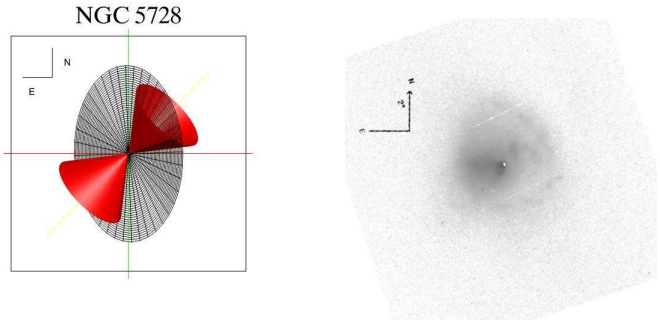

(b) NGC 5728

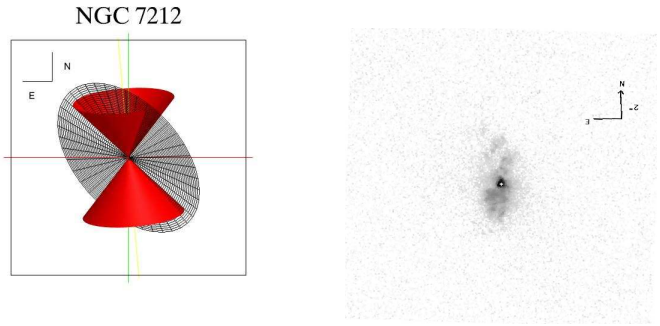

(c) NGC 7212

Figure A.5: NLR Geometries of 12 Seyfert Galaxies: continued

Appendix B

Nuclear Morphology of NLS1s and BLS1s.

In the notes below, we provide reasoning for a particular classification for each galaxy. These can be used with structure maps in Figure B.1 (see also, Deo et al. 2006). We note the various dust features seen and any other comments specific to each galaxy. Some of the galaxies show star-forming regions/stellar clusters in their circumnuclear regions; these appear as small dark globular regions in these value-inverted images and often are associated with the dusty regions in the galaxy. Common sites for star formation are dust lanes along the large-scale bars and in multi-arm loosely-wound spirals. In the case of grand-design spirals most of the star-formation seems to be restricted to the outer edges of the dust lanes curving in to form the spiral. Often these form stellar nuclear rings. Many nuclear rings however seem to be associated with the "loosely-wound" type of nuclear spirals. This is an important differentiator and may be indicative of evolution of nuclear regions of these galaxies. Galaxies with "point source" as the primary nuclear morphology classification do not have structure maps included in Figure B.1 (see Malkan et al. 1998, for original images). The figures are arranged so that on each page there are a total of six galaxies shown. The top two rows

show three galaxies, with the topmost row showing the complete structure map of the PC image, the row below that shows the same galaxy, but zoomed in to show the nuclear spiral structures clearly. All images are labeled with name of the galaxy and the scale of the image. A colorbar at the bottom shows the contrast scaling used. Light structures are dusty, while starlight is dark in these value-inverted images.

ESO 215-G14 (SB:DS:GD, BLS1) This galaxy has a noticeable bar in the structure map, but was originally classified as S (unbarred spiral) in CKG03. The bar is along approximately the east-west direction. Two very faint dust lanes are seen on leading edges of the bar. The structure map reveals a GD dust spiral in the center. Northern arm of the spiral is more clearly visible. The bar structure can be brought out by using a PSF with different size scale; here we chose the one that showed the inner spiral in clearest detail.

ESO 323-G77 (SB:DS:FL, BLS1, NR) Shows a multi-arm flocculent nuclear spiral along with a nuclear ring of star-burst regions encircling the spiral. Multiple large-scale dust lanes connect with the nuclear spiral at the position of the ring. Originally classified as a S (unbarred spiral) in CKG03.

ESO 354-G4 (S:DS:FL, BLS1) Shows filamentary multi-arm spiral structure on kiloparsec scale. Toward the center, nuclear spiral structure is smooth and has distinct puffy gaseous arms with small dust lanes embedded in them. The nuclear spiral is much smoother than the filamentary nature of the outer spiral. Spiral arms on north-west side are more distinct.

ESO 362-G18 (S:DS:FL, BLS1) Shows dust spiral structure in the inner kiloparsec. Half of the galaxy is in the PC chip while the other half in WF2. Mosaic image shows star forming regions interspersed with dusty lanes. On the WF2 side a large-scale dust lane curves in toward the nucleus.

ESO 438-G9 (SB:DS:GD, BLS1) Large-scale dust lanes are apparent in the main spiral arms as well as along the leading-edges of the bar. Prominent star forming regions are seen along the bar edges. Toward the center, the dust lanes curve in to form a grand-design type spiral. The inner regions

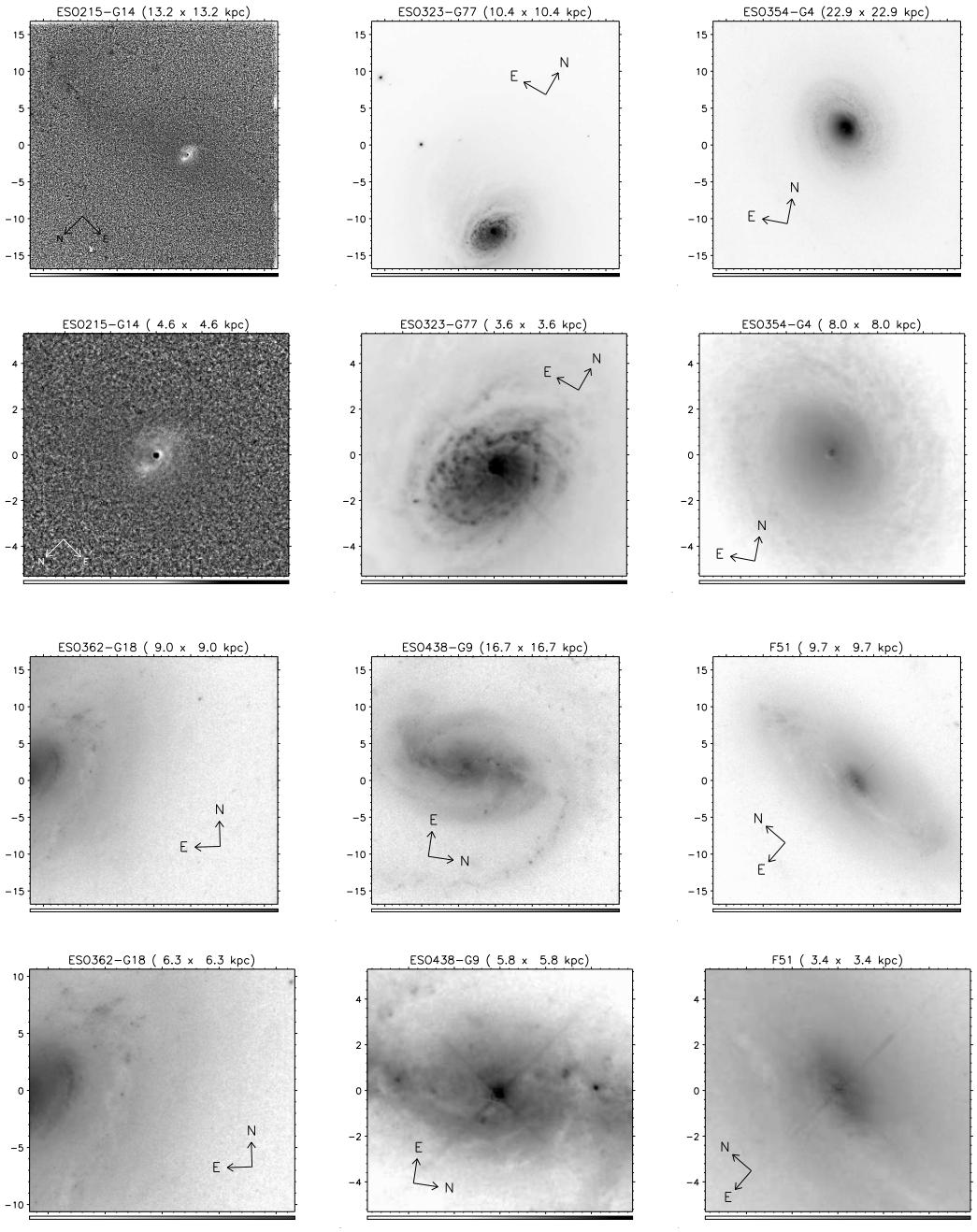

Figure B.1: Structure Maps of Seyfert 1s from Malkan et al. (1998): the images are value-inverted; dusty structures are white, while starlight is dark.

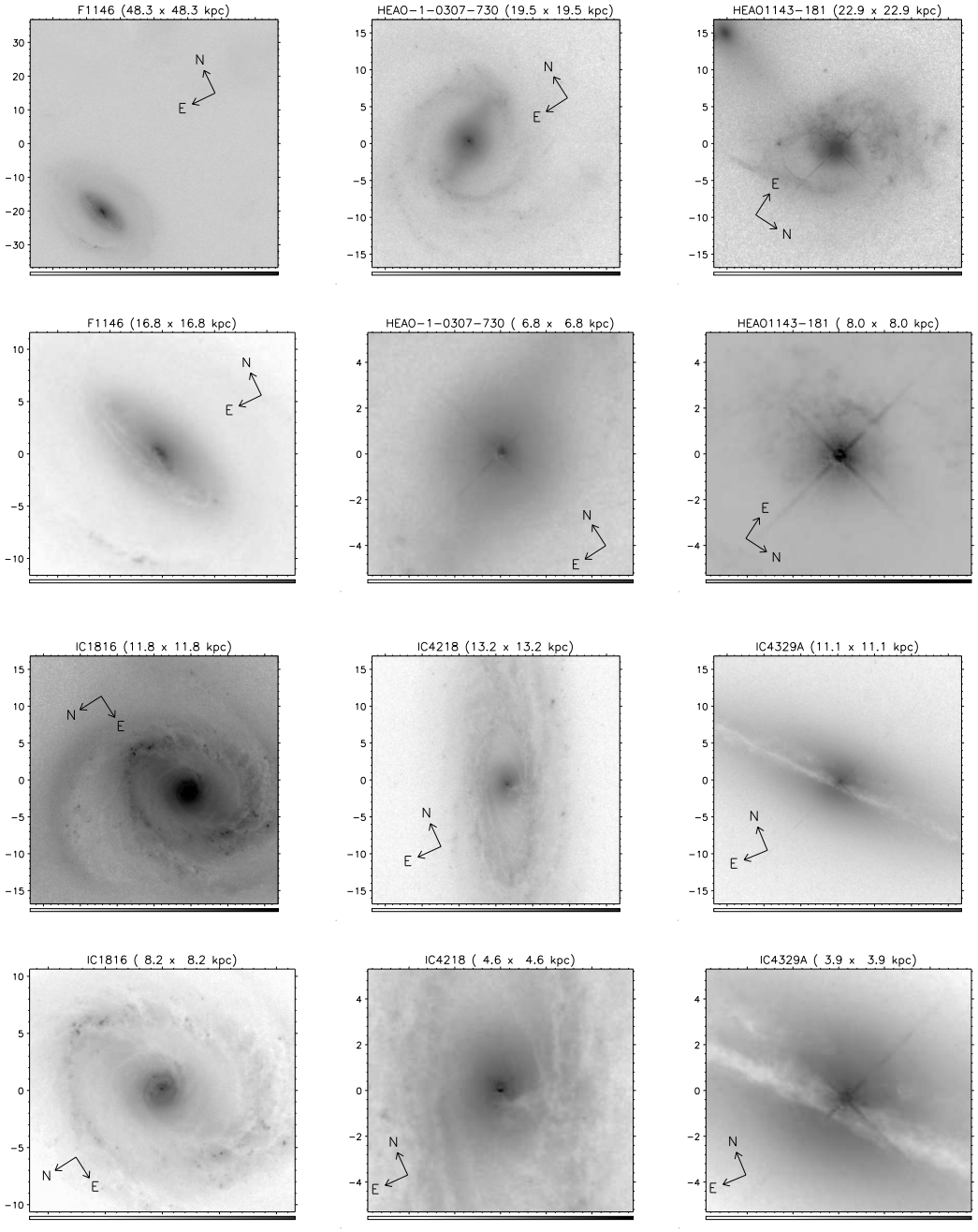

Figure B.2: Structure Maps of Seyfert 1s continued.

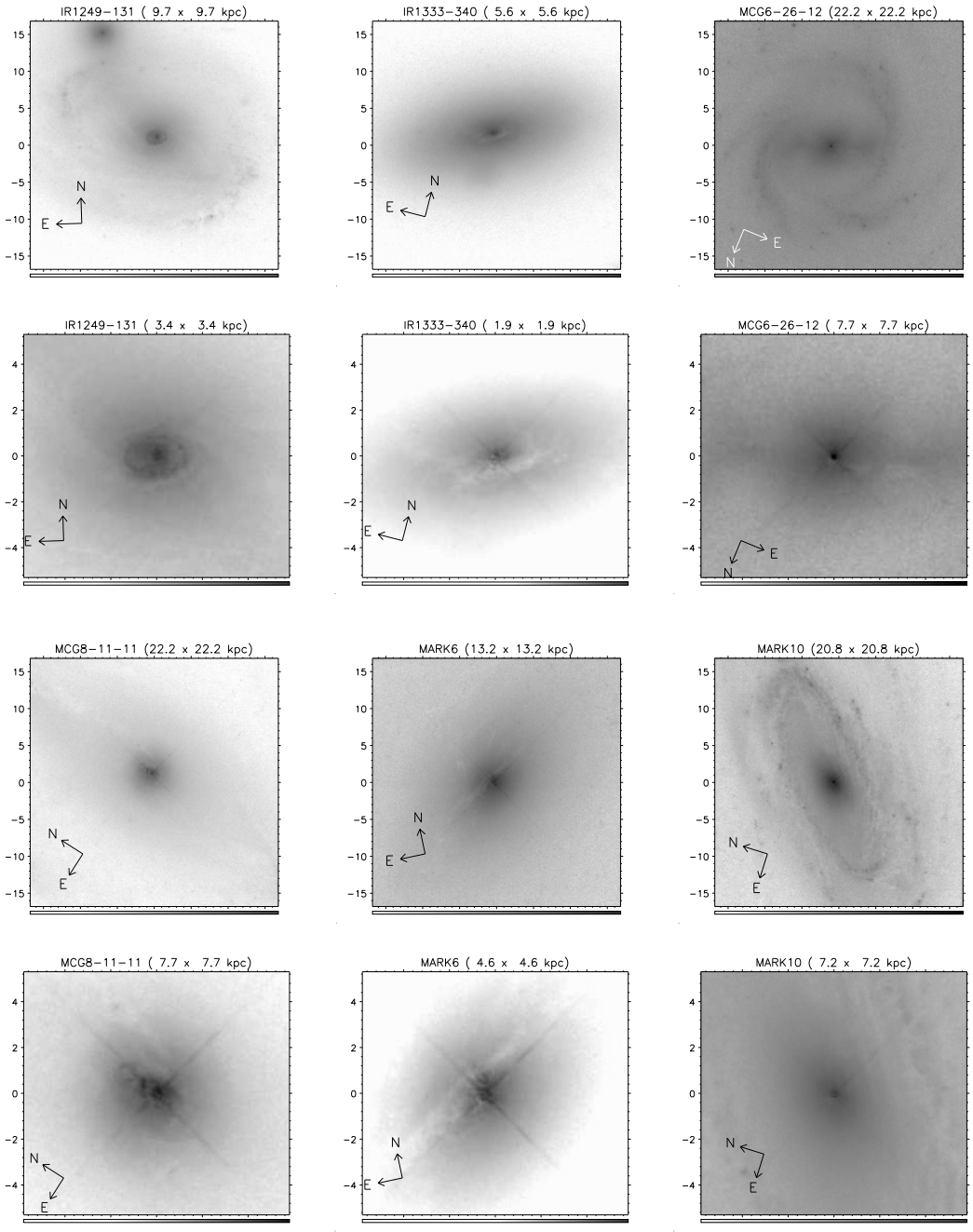

Figure B.3: Structure Maps of Seyfert 1s continued.

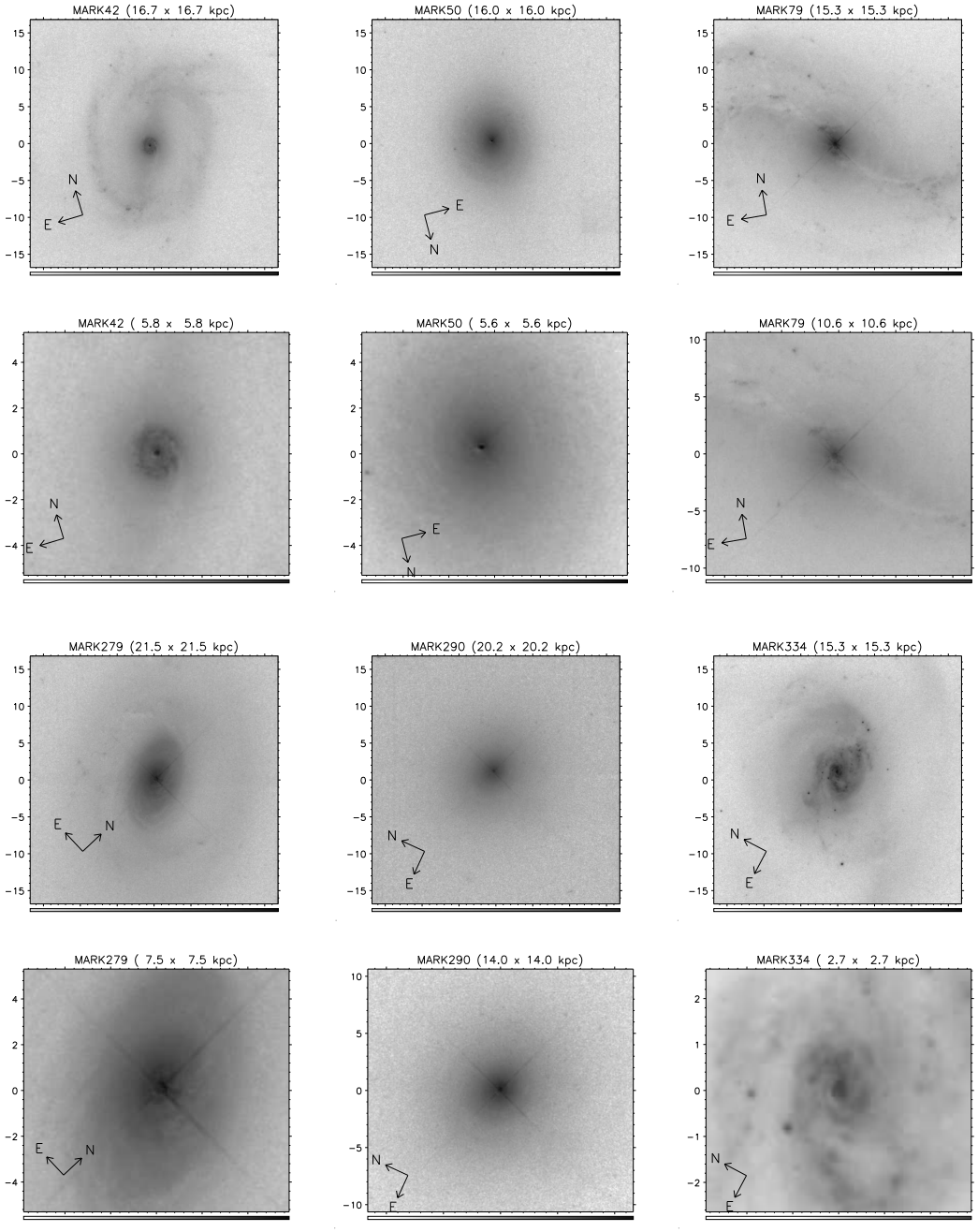

Figure B.4: Structure Maps of Seyfert 1s continued.

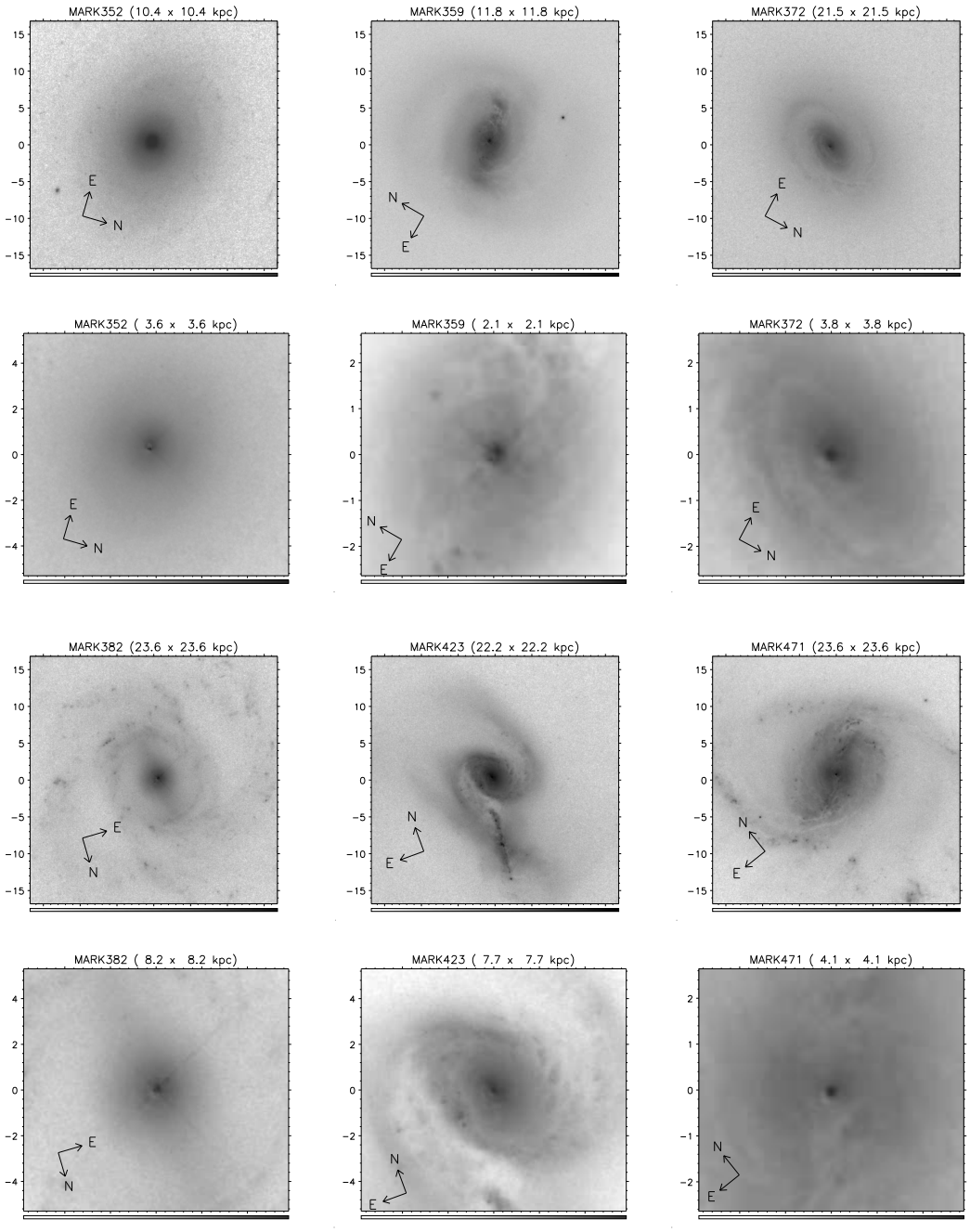

Figure B.5: Structure Maps of Seyfert 1s continued.

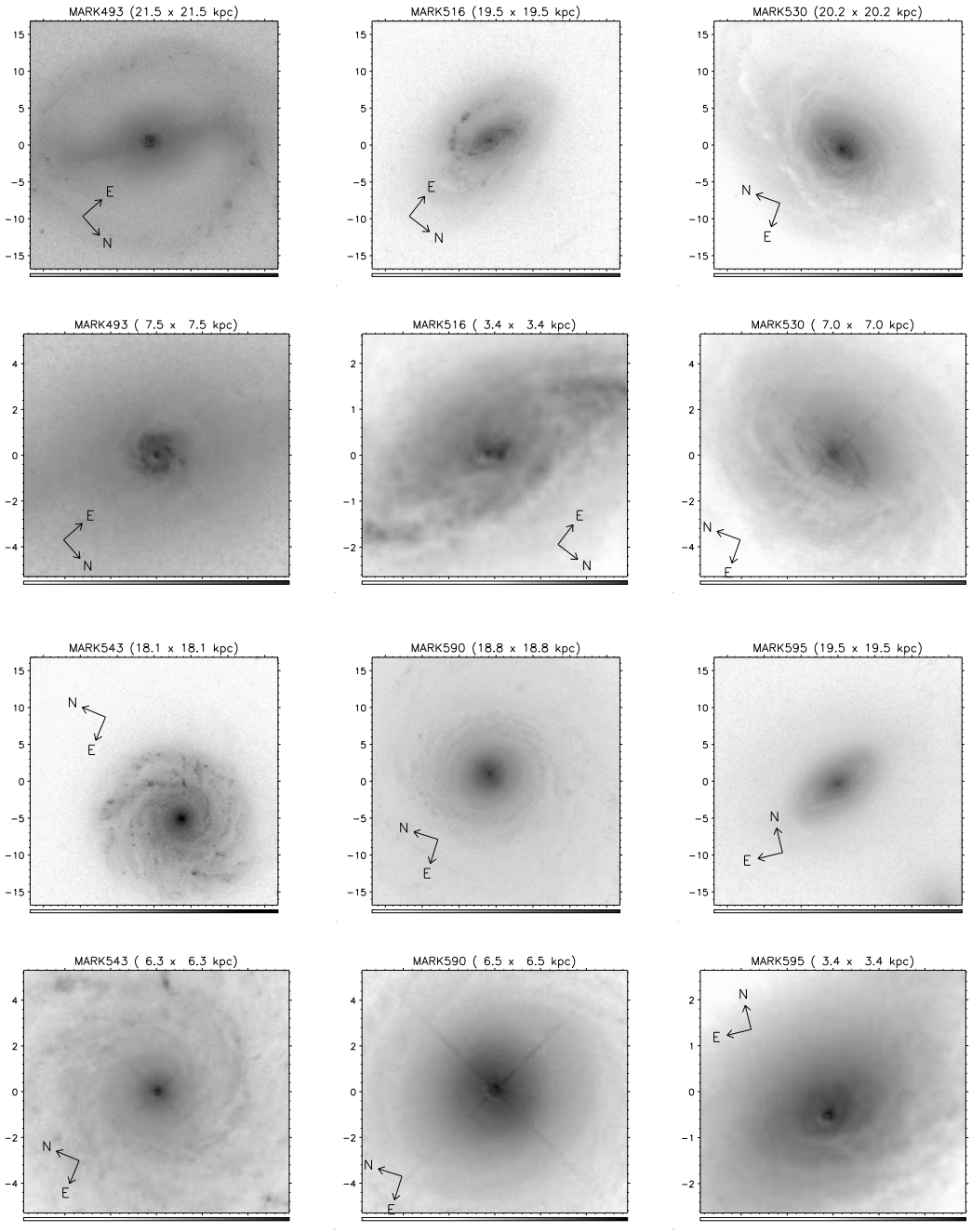

Figure B.6: Structure Maps of Seyfert 1s continued.

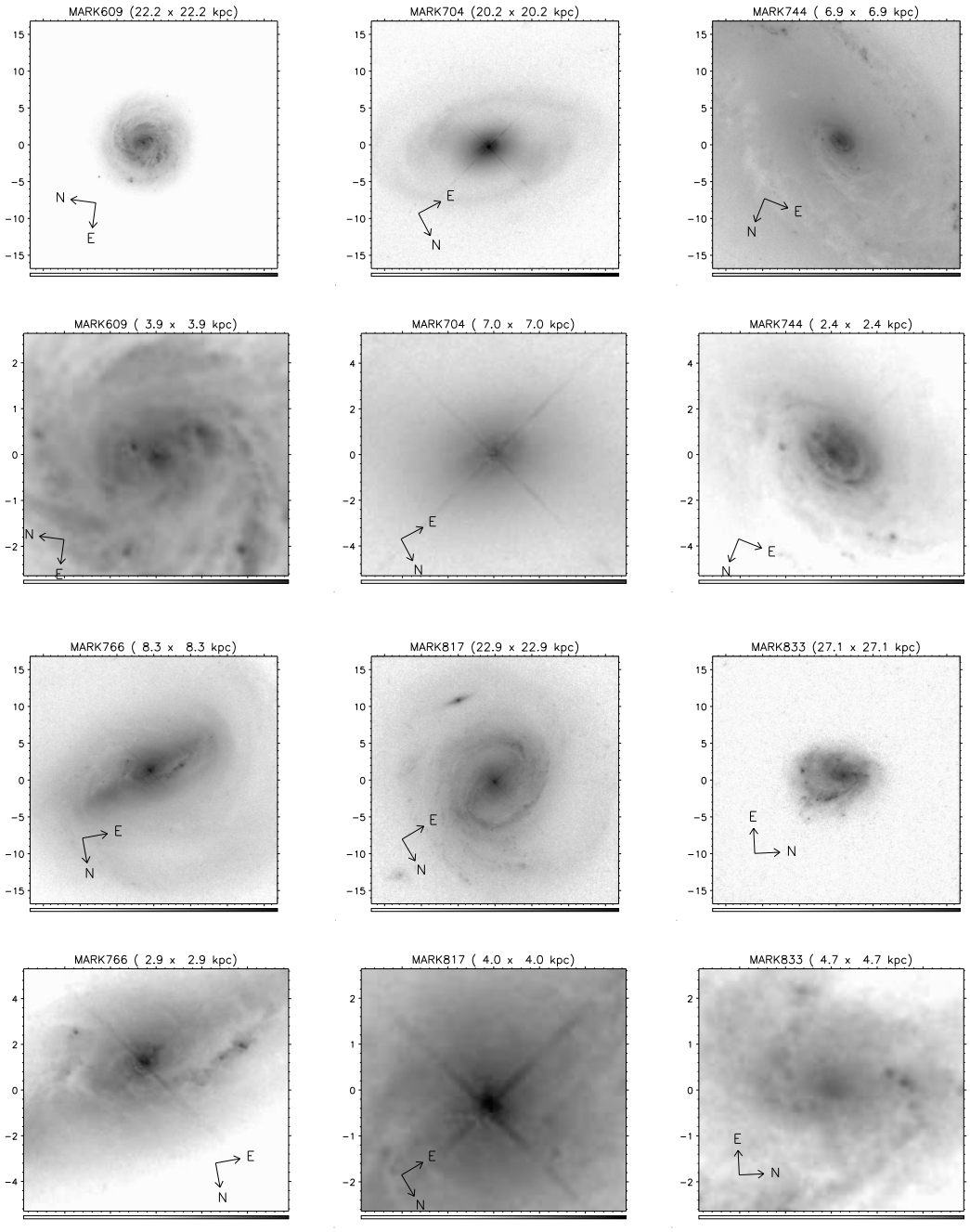

Figure B.7: Structure Maps of Seyfert 1s continued.

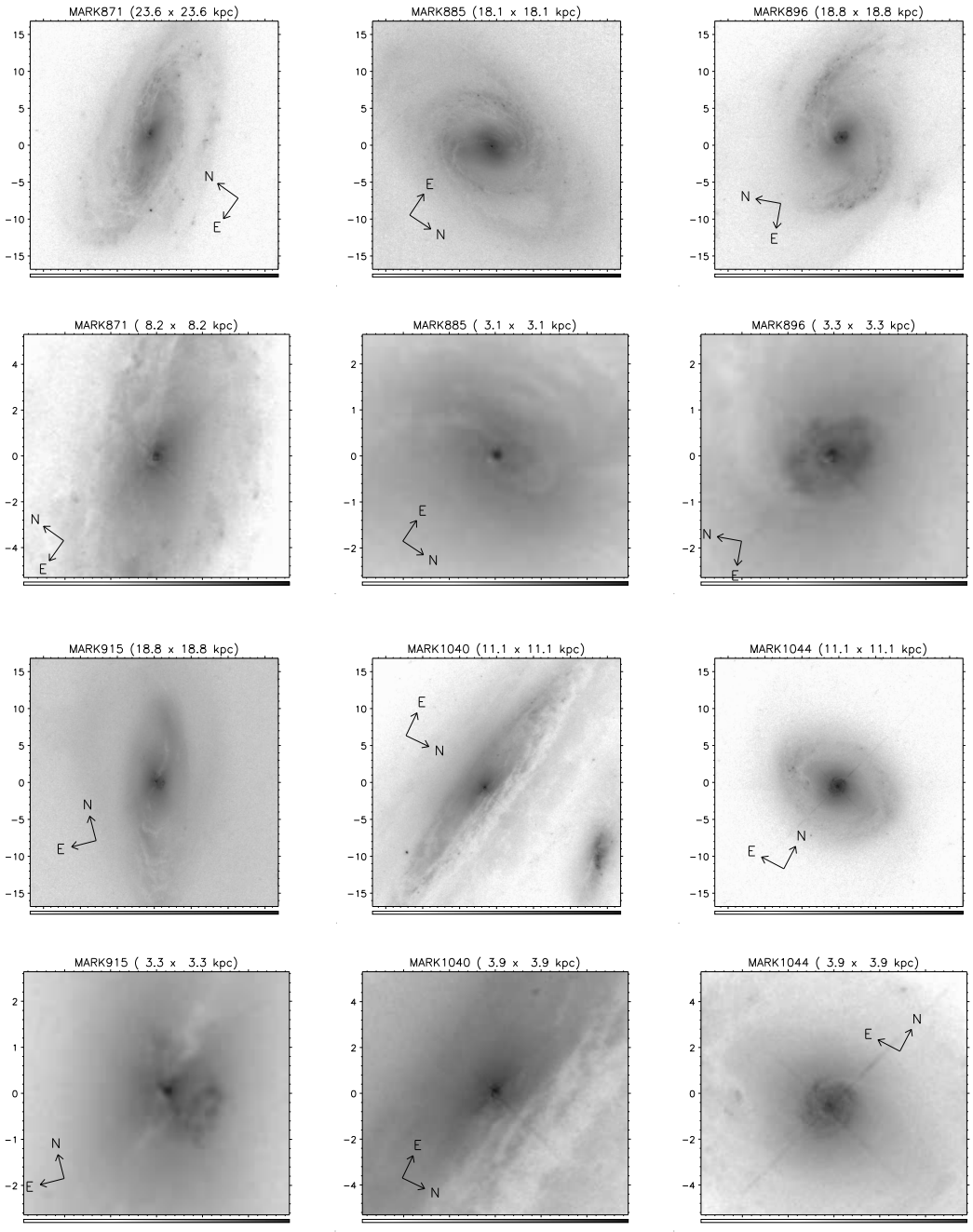

Figure B.8: Structure Maps of Seyfert 1s continued.

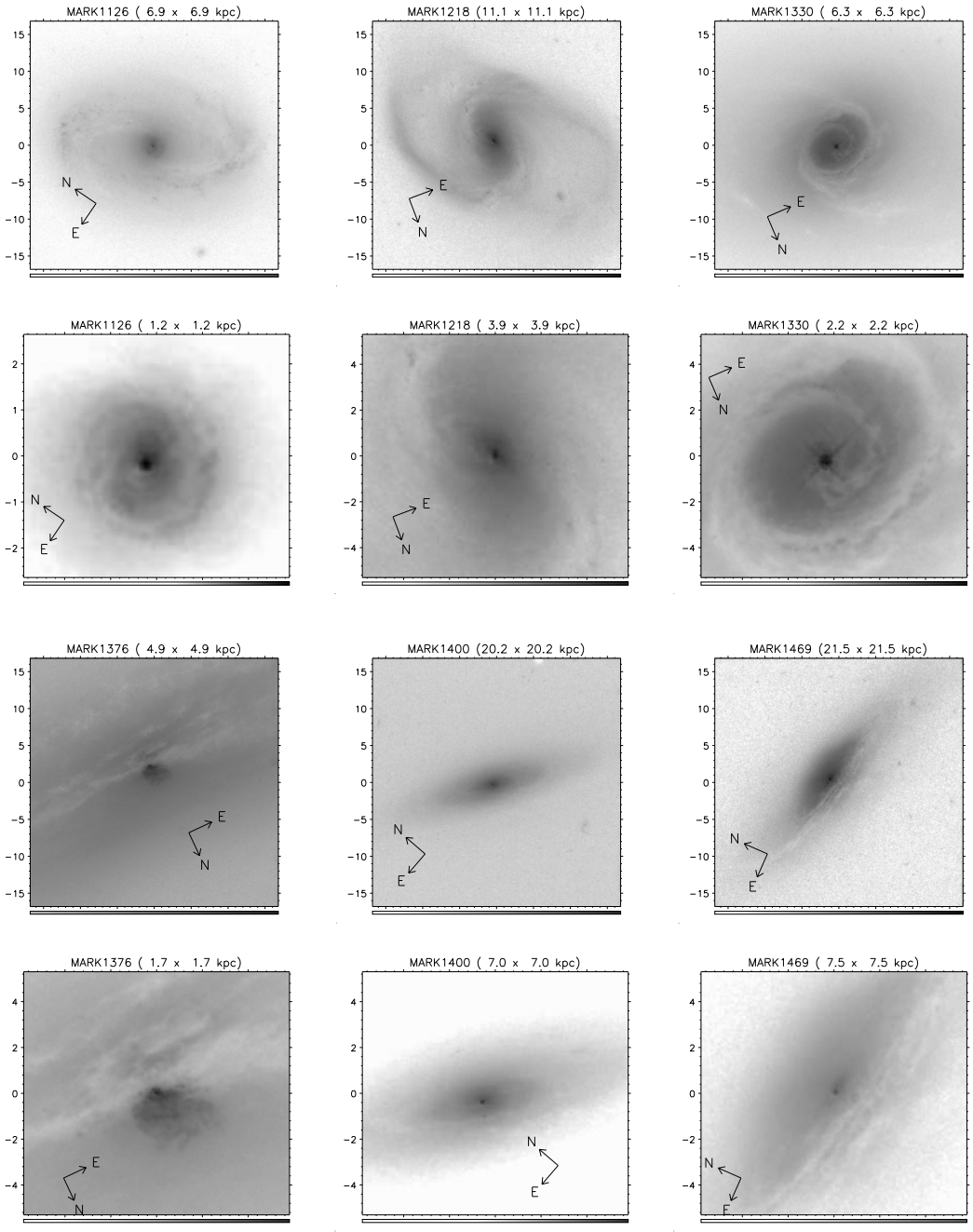

Figure B.9: Structure Maps of Seyfert 1s continued.

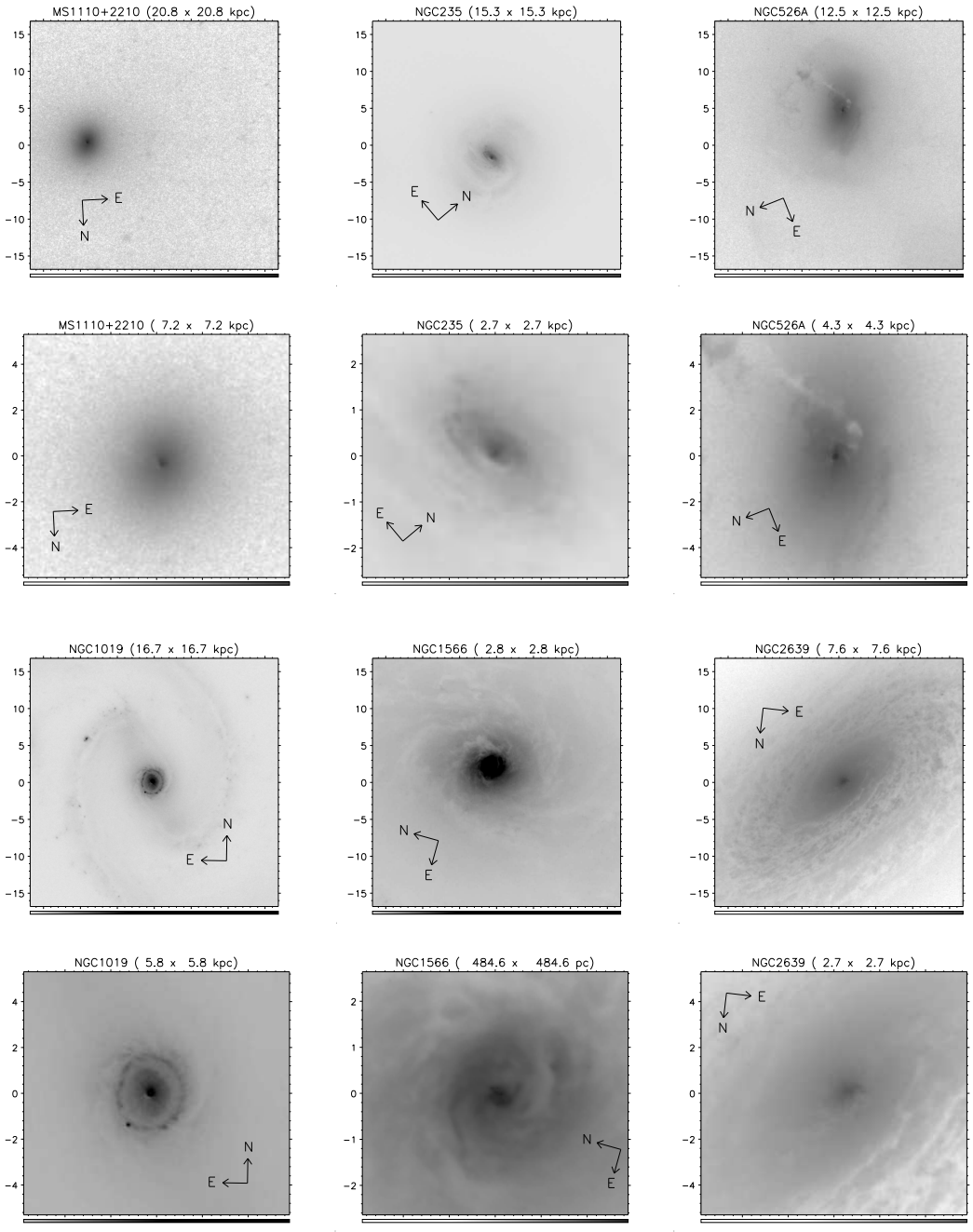

Figure B.10: Structure Maps of Seyfert 1s continued.

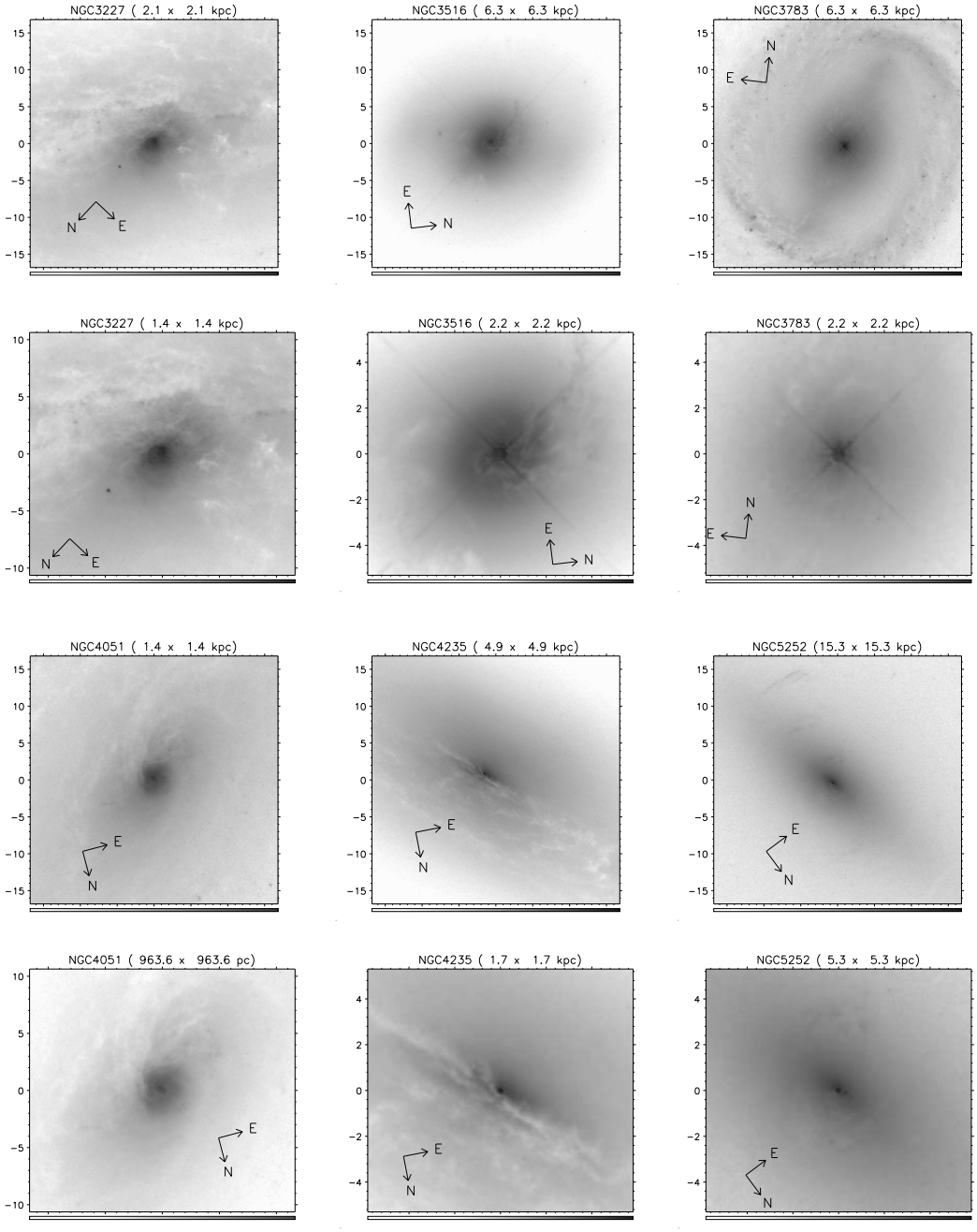

Figure B.11: Structure Maps of Seyfert 1s continued.

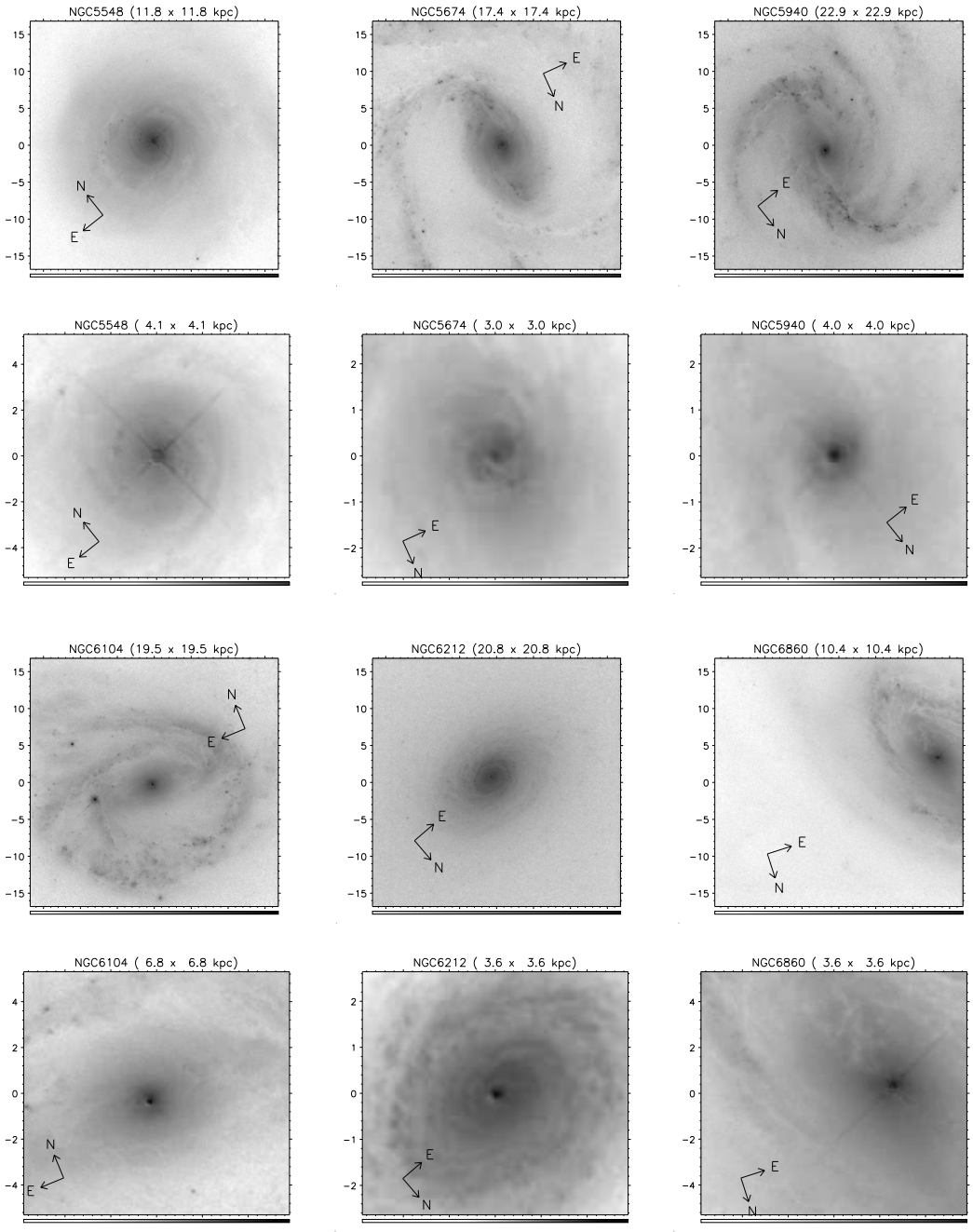

Figure B.12: Structure Maps of Seyfert 1s continued.

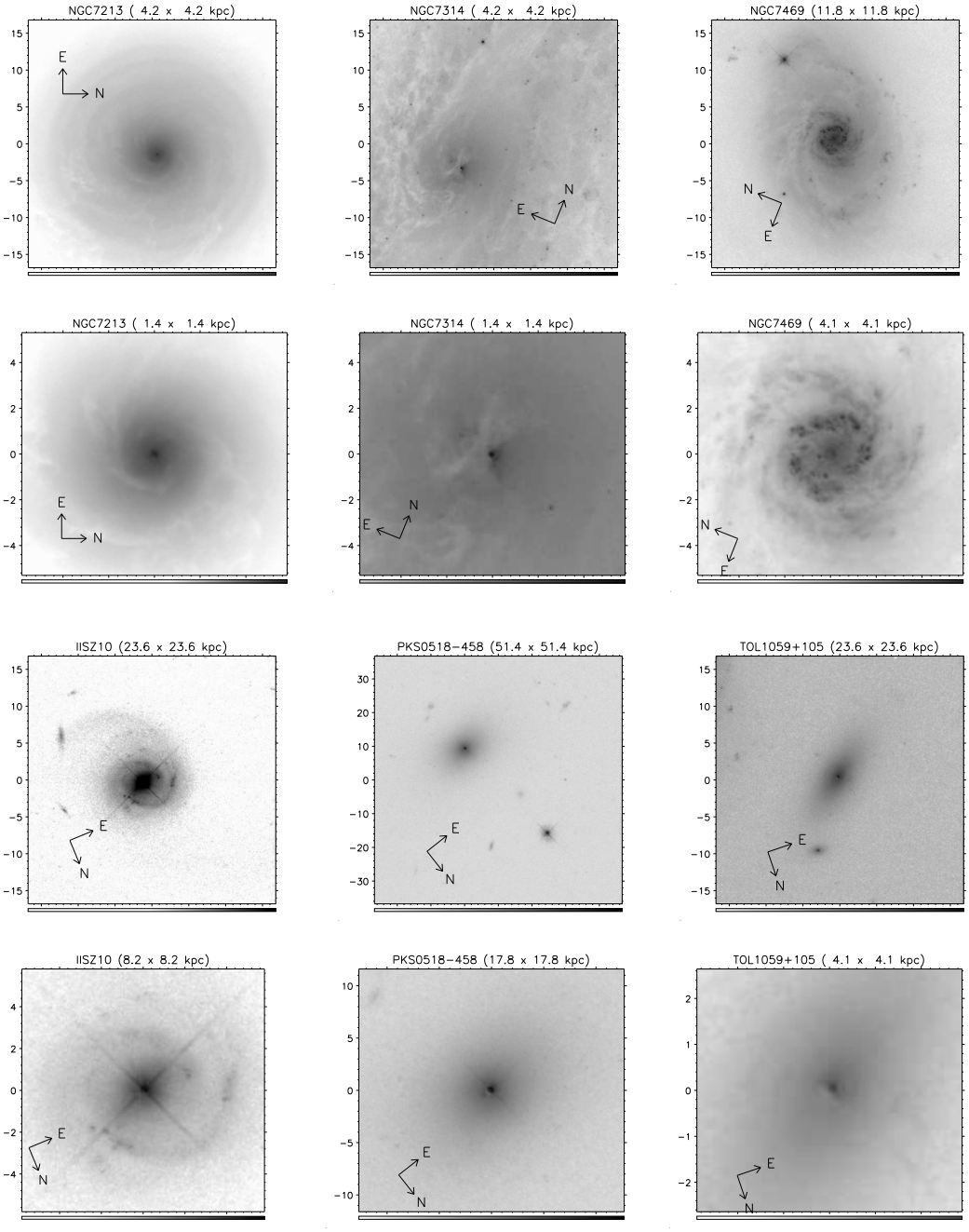

Figure B.13: Structure Maps of Seyfert 1s continued.

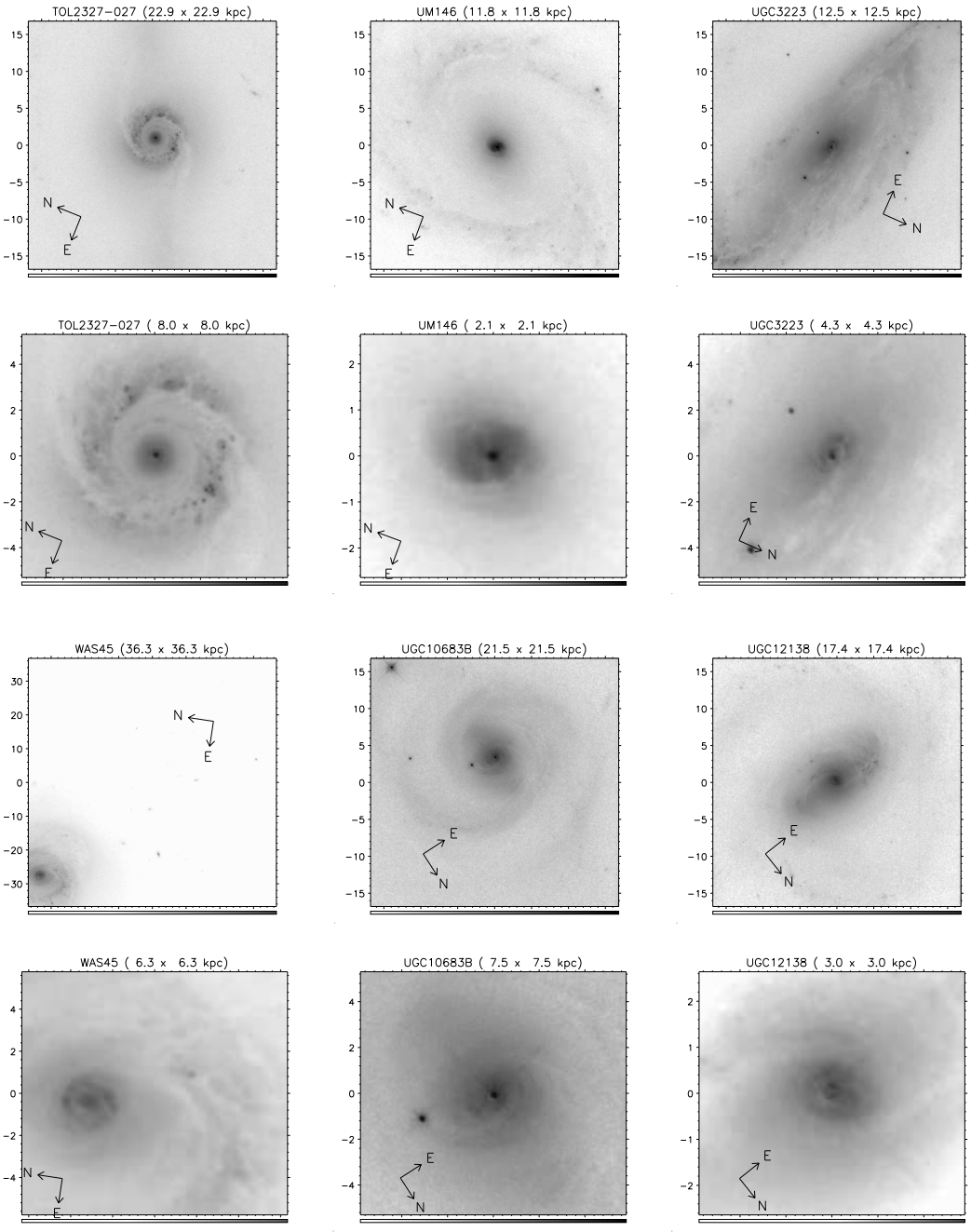

Figure B.14: Structure Maps of Seyfert 1s continued.

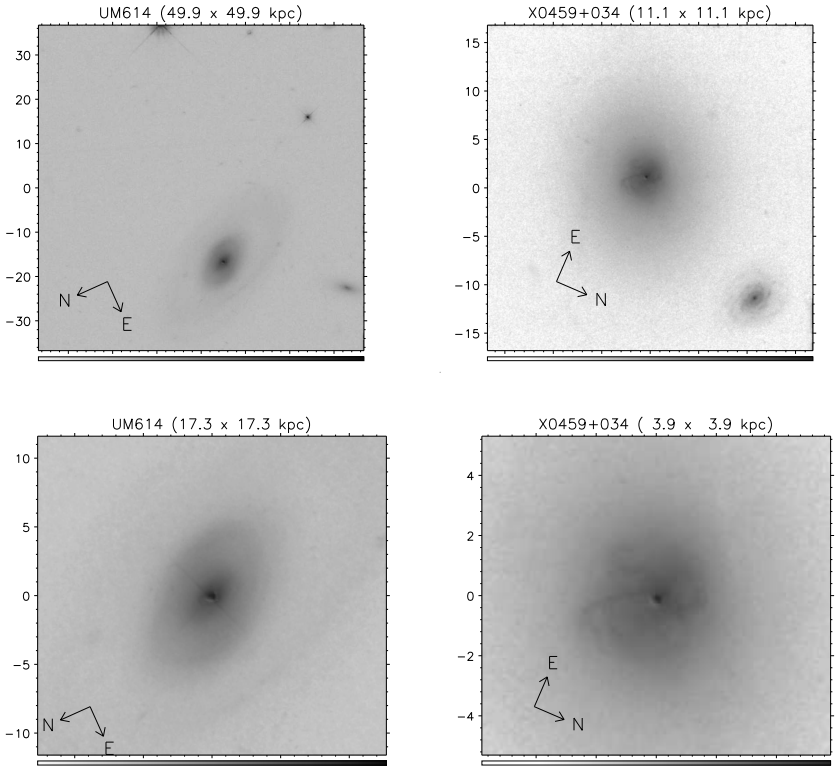

Figure B.15: Structure Maps of Seyfert 1s continued.

of the nuclear spiral itself are lost in the bright saturated core. Both the central kiloparsec as well as the bar structure show chaotic dusty regions. Another galaxy similar to this one is Mrk 766.

F 51 (SB:DS:?, BLS1) This galaxy is highly inclined, with large-scale dust lanes visible. The central kiloparsec shows chaotic dust structure along with bright emission to the west and south-west of the nucleus. Star-forming regions are seen at $\sim$7-8$''$ from the galaxy center, which may be the outer co-rotation radius of the bar. It is not clear if the galaxy has a bar or a warped disk or if this is just a inclination effect.

F 1146 (S:DL:-, BLS1) This galaxy is too distant from us to resolve any nuclear features. But it has a large dusty disk ($\approx$ 8 kpc) that is partially blocking the central AGN.

HEAO 1-0307-730 (SB:ND:-, BLS1) A prototype barred galaxy with two distinct spiral arms. It is again too distant to resolve nuclear structures. However the central 2-3 kpc look devoid of dust.

HEAO 1143-181 (I:A:?, BLS1) An Irregular galaxy, with emission line gas filaments visible; however, it is too distant to resolve nuclear regions.

HEAO 2106-098 (P:ND:-, BLS1) Classified in CKG03 as a point source, it seems this galaxy is probably a SB type, as the bar is noticeable in the structure map. However the galaxy is too distant to see any nuclear structure.

IC 1816 (SB:DS:?, BLS1) This one shows spectacular dust morphology on all scales. We see a nuclear dust spiral with two distinct arms that seem to open as the spiral travels inward eventually forming what looks like a bar-like structure. Curving dust lanes are prominent. This nuclear spiral has two distinct arms but is not the prototype GD, hence we have chosen to not include it in the GD category. The dust structure in the inner 500 pc along the north-south direction looks very similar to a gaseous/dust bar.

IC 4218 (S:DL:-, BLS1) Prominent dust lanes are seen in the main galactic disk. However, the inner 1-2 kpc are devoid of dust and are smooth. A single dust lane is seen all the way to the nucleus on the west side of the galactic disk. There is a hint of spiral (main) dust inflow along the inner side of this dust lane. Overall the galaxy is quite inclined.

IC 4329A (S:DL:-, BLS1) This is an edge-on galaxy with a large dust lane crossing the line of sight to the central source. No nuclear structures are visible.

IR 1249-131 (NGC 4748) (S:DS:GD, NLS1, NR) The large-scale structure shows a faint stellar bar extending from NE to SW. A curving dust lane from the NE side merges with the nuclear ring within the central 1-2″. Inside the nuclear star-burst ring, a two arm nuclear dust spiral can be seen. The structure of the nuclear region is very similar to that of IC 1816, but we see a star-burst ring at about the same radius as the dust spiral arms. The star forming regions and/or emission regions are on the inside edges of the dust lanes. Much of the rest of the central region seems to be chaotic. We chose to give it a GD classification as the dust lanes merge with fainter dust lanes along the large-scale bar.

IR 1319-164 (S:-:-, BLS1) This galaxy was excluded from analysis as most of it is outside the PC chip on the sawtooth side of WFPC/2 field of view.

IR 1333-340 (S:DL:-, BLS1) This one shows strong dust content within the central kiloparsec. However it is not clear if there is any spiral structure, hence we classify this as a DL, for dust lane.

MCG 6-26-12 (SB:DS:GD, NLS1) This is a typical SB galaxy. Even though the central nuclear region is unresolved, we see curving dust lanes close to the central saturated core that connect to the straight dust lanes along the leading-edges of the large-scale bar. Hence this is classified as a GD.

MCG 8-11-11 (SB:DS:?, BLS1) This galaxy was classified as a S in CKG03 but is a SB. One can clearly see a dust lane approaching the nucleus on the

north side, eventually curving to the inner nuclear regions. Since we do not see the second dust lane on the opposite side of the bar, we haven't given it a GD classification.

MARK 6 (S:DL:-, BLS1) A strong dust lane passes close to the nucleus; much of the rest of the galaxy shows little dust structure.

MARK 10 (S:ND:-, BLS1) Very little dust is noticeable in the inner kiloparsec. The morphology is similar to IC 4218.

MARK 40 (?:ND:-, BLS1) This shows very little dust content in the nucleus, and seems to be an interacting system with a tidal tail. (Not displayed in Figure 2.)

MARK 42 (SB:DS:GD, NLS1, NR) A prototype barred galaxy with grand-design nuclear spiral and a star-burst nuclear ring. Curving dust lanes can be traced for slightly more than π radians.

MARK 50 (S:DS:FL, BLS1) Outer multi-arm spiral structure is too faint compared to the central source to be directly seen, but it is seen in the structure map. This galaxy probably hosts a flocculent nuclear spiral. There is not much dust content visible close to the nucleus. There are hints of winding dust lane features within $1''$ of the nucleus.

MARK 79 (SB:DS:GD, BLS1) Two dust lanes along leading edges of the large-scale bar, curving toward the nucleus are seen. Nuclear structure is not prominent; mostly emission line gas filaments are visible.

MARK 279 (S:DS:FL, BLS1) Multi-arm flocculent nuclear spiral structure is visible. More dust structures are clearly visible on NW side of the nucleus.

MARK 290 (E:ND:-, BLS1) No significant dust in the nuclear region is visible. Mistakenly written as a unbarred spiral in CKG03, this galaxy is probably elliptical.

MARK 334 (S:DS:?, BLS1, SBS) Chaotic dust structures are seen on all scales. The central kiloparsec shows a distinct inverted S shaped spiral. The region

connecting the two arms may also be interpreted as a dust bar. This galaxy may host a weak large-scale bar approximately along the NE-SW line. Much of the nuclear spiral probably hosts sites of star formation. The spiral arms are relatively bright compared to other nuclear spirals.

MARK 335 (PG 0003+199) (P:-:-, NLS1) This galaxy is like a point source; no nuclear structure can be discerned.

MARK 352 (E:ND:-, BLS1) We see no significant dust in the nuclear region.

MARK 359 (SB:DS:GD, NLS1) Shows a very chaotic gaseous and dusty large-scale bar but the dust lanes are not clearly demarcated from rest of the structure.

MARK 372 (S:DS:FL, BLS1) Shows a prototypical flocculent multi-arm nuclear dust spiral very similar to galaxies from class TW of Martini et al. (2003a)

MARK 382 (SB:DS:?, NLS1) Probably hosts a GD dust spiral, but the central source is too bright to see it clearly. A curving dust lane NW of nucleus, along leading-edge of the large-scale bar is seen. We choose to not give it a secondary classification.

MARK 423 (S:DS:FL, BLS1) This galaxy is probably merging with its edge-on companion and shows a curious mirror-inverted "?" like view. There is extensive star-formation going on in the disk of the galaxy along with a disturbed dust morphology. We see chaotic gas structures with dust lanes in the central kiloparsec. A distinct two arm structure connected by a dust lane passes through the nucleus.

MARK 471 (SB:DS:GD, BLS1) We see chaotic dust structures within the large-scale bar. These dust lanes connect together and eventually curve toward the center to form a GD type structure. Dust can be traced all the way down to about $0.2''$ of the nucleus.

MARK 493 (SB:DS:GD, NLS1, NR) Another prototypical galaxy with strong large-scale bar with leading-edge dust lanes feeding a central nuclear ring

and a grand-design spiral toward the center. Also notable in this image is the presence of multiple dust spiral arms outside the nuclear ring. The nuclear ring is broken in places where these dust spiral arms connect with inner structure. These arms probably are the four-armed spiral outside the outer ILR of the large-scale bar (see, Maciejewski 2004b).

MARK 516 (S:DS:FL, BLS1) We see that the nuclear dust morphology is chaotic and extensive star-formation is going on. The nuclear region shows two bright nuclei.

MARK 530 (S:DS:FL, BLS1, NR) This galaxy shows dust content on all scales, and the nuclear spiral has multiple dust arms and is of flocculent (FL) type. To the SW of the nucleus just on the outer edge of the curving dust arm, a star-burst region is prominent.

MARK 543 (S:DS:FL, BLS1) Shows dust on large scales. Multiple spiral arms littered with star forming regions are seen. However the central 1-2 kpc appear to be smooth and devoid of dust.

MARK 590 (S:DS:FL, BLS1) This galaxy is similar to MARK 543, but this time the central regions are much more clearly visible. One can see multiple dust spiral arms intermingled with puffy-looking smooth emission. It is at about the same distance as MARK 543, but the star forming regions and multiple dust arms are located on the outer edges of the galactic disk as compared to MARK 543.

MARK 595 (S:DS:FL, BLS1) Shows a multi-arm flocculent dust spiral. One also sees a nuclear emission ring-like structure close to the central source crossed by a straight dust lane, which connects on one side with a dusty spiral arm. The spiral pattern is not seen north of the nucleus.

MARK 609 (S:DS:FL, BLS1) Shows multiple dust spiral arms on all scales. The overall look is that of a chaotic spiral.

MARK 699 (E:ND:-, NLS1) This galaxy is like a point source and almost no structure is visible.

MARK 704 (SB:A:?, BLS1) This is a SB galaxy with very little dust structure visible due to the bright nucleus, however there is dust structure that appears to be curving dust lanes just near the point source.

MARK 744 (S:DS:?, BLS1, NR) This galaxy shows a dusty and gaseous nuclear spiral and large dust lanes are seen on Northern side of the galactic disk. The central spiral has multiple dusty arms that wind by more than 2π. A nuclear ring may be forming at about $1''$ distance from the nucleus.

MARK 766 (SB:DS:GD, NLS1) This is a prototype barred NLS1 with large amount of dust in the large-scale bar along with the curving dust lanes toward the center that eventually form a grand-design type of nuclear spiral.

MARK 817 (SB:DS:GD, BLS1) Another prototypical barred galaxy with leading-edge dust lanes culminating in grand-design nuclear spiral.

MARK 833 (I:A:?, BLS1) This is an irregular galaxy with a hint of formation of spiral structure and a bar along its NW direction. The dust structure is mostly amorphous.

MARK 871 (S:DL:-, BLS1) This is a spiral galaxy with large dust lanes and a smooth inner disk. A large dust lane is traveling all the way to the central source on the NW side of nucleus. A similar dust lane is absent on the SE side; however, dust lanes seem to be curving toward the nucleus, about $6.5''$ from the nucleus.

MARK 885 (SB:DS:GD, BLS1) This is a barred galaxy, with leading-edge dust lanes along the bar. However they do not form a typical GD structure in the central kiloparsec. The dust lanes south of the nucleus seems to merge partly with a dust lane from the other side of the bar on the NE side of the nucleus. The curved dust structure on the north side of the nucleus extends until it merges toward the nucleus.

MARK 896 (SB:DS:GD, NLS1, NR) This is another prototype barred galaxy showing grand-design nuclear spiral with a nuclear ring. Originally classified as a S (unbarred spiral) in CKG03.

MARK 915 (S:DS:GD, BLS1) This is a spectacular example of a dust lane tracing all the way to the nucleus. The galaxy also shows cone-shaped NLR emission regions which are almost perpendicular to the inflowing dust structures. The galaxy is highly inclined.

MARK 1040 (S:DL:-, NLS1) Another spectacular example of a large-scale dust lane obscuring the central regions. Not much can be inferred from the nuclear regions.

MARK 1044 (SB:DS:FL, NLS1, SBS) This is a interesting galaxy showing large-scale dust lanes along leading-edges of the main bar, feeding what looks like a multi-arm flocculent type spiral. However the dust lanes can be traced for about 2π radians before they disappear in the central saturated PSF core. The multi-arm stellar spiral could be the four-armed spiral that forms at the outer ILR. Originally classified as a S (unbarred spiral) in CKG03.

MARK 1126 (SB:DS:GD, BLS1) This is another prototype barred galaxy with a distinct grand-design nuclear dust spiral in the center. The inner extension of the spiral may be interpreted as a dust bar. However the change in pitch angle of the spiral is quite strong and it seems that a similar change on the west side of the nucleus is being masked by the strong emission from the nucleus in that direction. Originally classified as an unbarred spiral (S) in CKG03.

MARK 1218 (SB:DS:GD, BLS1) This is a flocculent spiral that is being fed by large-scale dust lanes. In the nuclear regions, the dust structure is mostly chaotic. The galaxy is probably barred.

MARK 1330 (SB:DS:GD, BLS1) Shows a gaseous and dusty nuclear spiral. The single spiral arm is spectacular and travels all the way to the nucleus, where the flow seems to disintegrate into chaotic gas and dust clouds. We earlier classified it as a FL based only on the PC image, but after looking at the mosaic image one can see that the dust extensions on the north and south side of the nuclear spiral connect to the dust lanes on leading edges

of the large-scale bar. Hence we reclassified it as a GD. Originally classified as a S (unbarred spiral) in CKG03.

MARK 1376 (S:DL:-, BLS1) This galaxy is highly inclined and hence it is impossible to see the nuclear dust structure. An ionization cone like structure is emanating from the nucleus almost perpendicular to the dust lanes. Originally not classified (category ?) in CKG03.

MARK 1400 (S:DS:?, BLS1) The central structure of MARK 1400 is smooth and very little dust structure is seen. There is hint of a dust spiral in the central 2-3 kpc.

MARK 1469 (S:DL:-, BLS1) This galaxy is highly inclined with only large-scale dust lanes visible.

MS 1110+2210 (E:ND:-, BLS1) This galaxy is completely featureless, with no detectable dust structure close to the nucleus.

NGC 235 (S:DS:FL, BLS1) This galaxy shows a flocculent tightly winding nuclear dust spiral.

NGC 526A (I:DL:-, BLS1) This is peculiar galaxy with a large veil-like dust structure in front of the central nucleus. We classified this as a dust lane type (DL).

NGC 1019 (SB:DS:GD, BLS1, NR) This is a spectacular galaxy showing two large-scale spiral arms with dust lanes, a large-scale bar with leading-edge dust lanes, and a distinct nuclear star-forming ring at about 1 kpc from the nucleus. There is a dust lane traveling all the way to the nucleus from the SE side inside the nuclear ring. The inner disk appears featureless and mostly devoid of dust except for the faint dust lanes visible on North and SE of the nucleus. The SE lane connects with the curving dust lane of the northern arm of the large-scale bar. Faint multi-arm spiral extensions are seen around the nuclear ring; these are probably similar to the four-armed type spiral patterns seen in other barred galaxies with an outer ILR.

NGC 1566 (S:DS:FL, BLS1) This is a Sbc galaxy having a flocculent dusty nuclear spiral. Very close to the nucleus the spiral shows a curious inverted S shaped structure in the inner 1″.

NGC 2639 (S:DS:FL, BLS1) This is a spectacular galaxy showing multi-arm flocculent dust spiral structure on large-scales. In the inner 5″ from the nucleus the disk becomes much smoother with two dust lanes traveling toward the nucleus. The puffy nuclear gas disk probably has 3 or 4 spiral arms.

NGC 3227 (SB:DL:-, BLS1) The inner disk is highly inclined and hence we can only see dust lanes crossing it on the SW side. Looking at the WFPC2 mosaic image, these dust lanes are the inner parts of the leading-edge dust lanes of the large-scale bar. The dust within the large-scale bar is also chaotic. We are not seeing the other edge of the bar on the SE side in the WFPC2 image. Emission line gas is seen near the nucleus and perpendicular to the disk plane. Since we cannot see the nuclear structure clearly, we choose to classify this as a DL. Originally not classified (category ?) in CKG03.

NGC 3516 (SB:DL:-, BLS1) This is a spiral galaxy with a large chaotic dust lane traveling toward the nucleus. There are more dusty regions south of the nucleus. The large-scale structure is not clearly seen, but it seems like the galaxy is a SB type in the WFPC1 mosaic image, and the bar may lie on NW-SE line with respect to the nucleus. It is unclear what is generating the large-scale chaotic dust lane. Originally classified as a S (unbarred spiral) in CKG03.

NGC 3783 (SB:DS:FL, BLS1) This is a typical barred galaxy, with a large-scale star+dust ring at the outer co-rotational radius of the bar. The dust lanes along the bar edges are faint. We can see curving dust lanes from the bar edges, but apart from that there are multiple dust lanes, so we choose to go with the FL category for this galaxy.

NGC 4051 (SB:DS:GD, NLS1) This shows a gas and dust rich nuclear region. We choose to classify this galaxy as a GD based on the dust lane NE of the nucleus which connects to the large-scale leading-edge dust lane of the bar.

This is not immediately apparent from the PC image due to proximity of the galaxy.

NGC 4235 (S:DL:-, BLS1) This galaxy is highly inclined and we only see the large-scale dust lane.

NGC 5252 (S:DS:?, BLS1) This is a curious galaxy with dust filaments stretching in arcs all the way out to 15″ and a stellar bar like structure which is completely devoid of dust, stretching along the NS line. One sees a tightly wound spiral structure NW of the nucleus. Since we could not properly classify this we chose to only give it the primary classification of DS.

NGC 5548 (S:DS:FL, BLS1) This one shows a inwardly winding nuclear dust spiral. The overall morphology is similar to NGC 7213.

NGC 5674 (SB:DS:GD, BLS1) This is a prototype barred spiral with spectacular grand-design nuclear spiral. Dust content is seen on all scales.

NGC 5940 (SB:DS:GD, BLS1) This is another barred spiral with a spectacular grand-design nuclear spiral. Dust content is again prominent on all scales.

NGC 6104 (SB:DS:?, BLS1) Dust content is prominent on all scales. A strong large-scale bar is visible, but only one leading-edge dust lane is visible on the NE side of the nucleus. This lane curves and moves toward the nucleus; however, since we do not see the other lane we choose to not give it a secondary classification. This is probably a GD.

NGC 6212 (S:DS:FL, BLS1, NR) This is a spectacular example of a multi-arm flocculent spiral structure for the outer disk and a tightly wound multi-arm structure for the nuclear disk. This is what would be a prototype class TW nuclear spiral from the classification of Martini et al. (2003a). It also shows a nuclear star-forming ring at between 2″ and 3″ from the nucleus.

NGC 6860 (S:DS:FL, BLS1) This galaxy is partly out of the PC chip, but one can see the dust lanes that connect the outer dusty disk with the nucleus. Most of the nuclear disk is smooth.

NGC 7213 (S:DS:FL, BLS1) This a prototype galaxy for a multi-arm flocculent inwardly winding nuclear dust spiral. The dust spiral can be traced all the way to the nucleus. The nuclear disk is packed with large quantities of gas and dust.

NGC 7314 (S:DS:FL, BLS1) The inclined nuclear disk shows chaotic dust content and hence is classified as FL.

NGC 7469 (S:DS:?, BLS1, NR) Shows a good example of a multi-arm nuclear spiral with a nuclear star-burst ring.

II SZ 10 (S:ND:-, BLS1) This is a barred spiral but is too distant to search for nuclear structures. This was mistakenly written as II ZW 10 in CKG03 as the MAST fits header gives 'IIZW10' as the value of 'TARGNAME' parameter.

PKS 0518-458 (E:ND:-, BLS1) This is an elliptical galaxy but too distant to look for nuclear structures.

TOL 1059+105 (S:ND:-, BLS1) This galaxy has bright emission line filaments near its nucleus, but shows no dust content.

TOL 2327-027 (SB:DS:GD, BLS1, NR) This is a spectacular example of a nuclear grand-design spiral. It can be questioned if we can call the spiral that starts at ≈ 5 kpc a nuclear spiral. We can trace winding dust lanes all the way down to 200 pc from the nucleus. At about ≈ 2 kpc the winding of large dust lanes halts and the galaxy seems to have formed a gaseous disk; small dust lanes continue through this disk toward the nucleus. All the star forming regions seem to form in a ring-like structure and are on the outer side of the curving dust lanes. Originally classified as a S (unbarred spiral) in CKG03.

UM 146 (S:DS:?, BLS1) The dust structure in this galaxy is quite faint in the nucleus which is dominated by the optical emission of the nuclear gas disk. One can see small dust lanes crossing the disk. It is possible that the disk is being fueled via large-scale dust lanes, but these are not clearly visible, except on the east side of the nucleus.

UGC 3223 (SB:DS:FL, BLS1) This one shows a flocculent multi-arm disk in the nuclear region. Dust is distributed on large scales in the galaxy and one can see a dust lane traveling toward the nucleus from the north side of the galaxy. This dust lane eventually curves to become the nuclear spiral. There is a ring-like structure around the nucleus. Originally classified as a S (unbarred spiral) in CKG03.

WAS45 (SB:DS:GD, BLS1, NR) This galaxy probably has a grand-design nuclear spiral and is similar in morphology to MARK 1044. A nuclear stellar ring is clearly visible.

UGC 10683B (SB:DS:?, BLS1) This one shows a dusty tightly wound nuclear spiral.

UGC 12138 (SB:DS:GD, BLS1) This one shows a grand-design nuclear dust spiral. The bar is probably not strong as the leading-edge dust lanes are not straight, but rather curved.

UM 614 (S:ND:-, BLS1) Very little dust is seen in the nuclear regions of this galaxy.

X 0459+034 (E:A:-, BLS1) This galaxy shows extended emission line gas filaments but no dust structure is detectable in the nuclear region.

Below we give the table from the Third Revised Catalogue of Galaxies (RC3) that describes the coding of morphological types of galaxies, including the value of T.

Table B.1: The Revised Hubble Classification of Galaxies from RC3.

Classes	Families	Varieties	Stages	T	Type	Code
Ellipticals		Compact		-6	cE	cE...
			Ellipt.(0-6)	-5	E0	.E.0.
			Intermediate	-5	E0–1	.E.0+
		"cD"		-4	E+	.E+..
Lenticulars					S0	.L
	Non-barred				SA0	.LA
	Barred				SB0	.LB
	Mixed				SAB0	.LX
		Inner Ring			S(r)0	.L.R
		S-shaped			S(s)0	.L.S
		Mixed			S(rs)0	.L.T
			Early	-3	$S0^-$	.L..-
			Intermediate	-2	$S0^o$	.L..0
			Late	-1	$S0^+$	.L..+
Spirals	Non-barred				SA	.SA
	Barred				SB	.SB
	Mixed				SAB	.SX
		Inner ring			S(r)	.S.R
		S-shaped			S(s)	.S.S
		Mixed			S(rs)	.S.T
			0/a	0	S0/a	.S..0
			a	1	Sa	.S..1
			ab	2	Sab	.S..2
			b	3	Sb	.S..3
			bc	4	Sbc	.S..4
			c	5	Sc	.S..5
			cd	6	Scd	.S..6
			d	7	Sd	.S..7
			dm	8	Sdm	.S..8
			m	9	Sm	.S..9
Irregulars	Non-barred				IA	.IA
	Barred				IB	.IB
	Mixed				IAB	.IX
		S-shaped			I(s)	.I.S
			Non-magellanic	90	I0	.I.0
			Magellanic	10	Im	.I.9
		Compact		11	cI	cI
Peculiers				99	Pec	.P
Peculiarities			Peculiarity		pec	.....P
(All types)			Uncertain		:	....*
			Doubtful		?	....?
			Spindle		sp	...../
			Outer ring		(R)	R.....
			Pseudo-outer R		(R′)	P.....

Appendix C

Data Reduction Tutorial for Spitzer Spectra

The post-BCD analysis and reductions can be done with SMART, and the steps below describe how to generate a complete 5.3–38 μm spectrum from a set of BCD files.

1. SMART works with 3-plane BCD files (called `.bcd3p.fits`) and includes an IDL routine to generate these files. The files contain the data plane, the uncertainty place and the bad pixel mask plane. The IDL procedure is called `make_3plane`. A typical invocation is as below,

```
[deo@bok data]$ ls r10868992/
ch0  ch1  ch2  ch3  QualityAnalysis_10868992.README

[deo@bok data]$ ls r10868992/ch0
bcd  cal  pbcd  raw

[deo@bok data]$ tcsh # Run csh
deo@bok ~> smart com # and begin smart in command line mode.
...
SMART Initialization messages
...
IDL> make_3plane, 'r10870272/ch0/bcd/', /pu
making ...bcd3p.fits
...
IDL> smart_project ; Begin GUI
IDL>
```

The '/pu' keyword indicates that pick-up array data should be ignored when making 3plane files in sub-directory ch0/bcd. This keyword should be included only if the dataset contains the pickup array data. Note that it will be present only for the low-resolution data in the ch0 sub-directory.

2. After the 3plane files have been generated, they can be loaded in to SMART via the Project Manager GUI.

3. All operations within the SMART GUI are tied to the Dataset Manager. The dataset manager window shows the list of files loaded in your project. All intermediate image and spectrum products are processed and can be saved to the dataset manager. They can be retrieved on demand whenever SMART is restarted. It is a good idea to save all intermediate data products to the dataset manager.

4. SMART is a collection of image processing and spectral analysis tools. For image display, it uses a modified version of Aaron Barth's ATV image display tool. The feature set of ATV is similar to ds9. For spectral analysis, SMART uses a modified version of the ISAP software tool. ISAP was written for ISO/SWS spectral analysis and thus has the same look and feel. SMART contains many other routines that do various things such as unit conversions, data I/O in various formats, spectral line fitting, continuum fitting, etc.

5. Each image file is cleaned and hot pixels are identified with IRSCLEAN, updating the bad pixel masks.

6. After the bcd3p image files have been loaded, difference DCEs per "nod" position are median combined. For example, if there are two DCEs for SL2, then these are median combined into one exposure per "nod" position.

7. As there are no independent sky observations taken by default, sky background needs to be subtracted from the DCEs. This can be accomplished as follows. Subtract the off-source slit image from the on-source slit image; *e.g.,* if you are trying to subtract sky background from SL2 "nod" position 1, median combine the SL1 "nod" position 1 DCEs and subtract that from the SL2 "nod" position 1 image (which is a median combined image of SL2 DCEs itself). An alternate way is to extract the sky spectrum from the off-source image and then subtract that from the on-source extraction. In practice, sky background is better subtracted at the image-level and results in a cleaner extraction.

8. After the background is subtracted, spectral extraction is performed on the cleaned image for "nod 1" and "nod 2" positions. For point source spectra, "Automatic Tapered Column Point Source" extraction option is used. The extraction process is displayed on the screen via plots. Finally the ISAP window is displayed with the extracted spectrum loaded in the window. The ISAP window should be left open while you extract the rest of the modules and orders. Each time you extract a spectrum, SMART will prompt you to load the new dataset into the existing ISAP window. To view the datasets already loaded, click on a button titled "Store". A window will pop-up displaying the stored datasets in the memory cache of ISAP.

9. In the ISAP software, the spectrum displayed in the main display area is called the 'Prime Spectrum'. One can think of this spectrum as the reference spectrum. After all the modules have been extracted and loaded into the ISAP window, one begins by selecting a spectrum (say SL2) from the 'Store' menu as the reference spectrum. Each of the module spectra can then be plotted in the display area independently and the deviant data points flagged and masked. After cleaning all

the module spectra, we can begin 'stitching' the complete spectrum together.

10. Before the 'stitching' process can be done, "nod 1" and "nod 2" spectra for say SL2 must be averaged together to get a single spectrum for SL2. Continue to do this for rest of the modules.

11. The 'stitching' process involves making one of the modules the prime spectrum (say LL1) and then 'merging' the rest of the module spectra (LL2, SL1, and SL2) to this reference spectrum.

12. Normally all module spectra should match in their flux levels in the region of overlap (see Figure 5.2). This however is not often the case. There is a small flux mismatch ($\sim 5\%$) between the LL and SL modules due to their different slit widths. Since the LL1 slit width is widest, the rest of the modules are often scaled to the flux level of LL1 spectrum. This can be done by multiplying the module spectra with a scale factor greater, than but close to, unity.

13. Finally the complete reference spectrum can be re-sampled and any spurious features due to averaging at the merging edges removed. The final spectrum and its parts can then be saved back to the dataset manager window. The final spectrum can be exported out of SMART into a `.fits` file or as a `ASCII` table with a header. The extracted and calibrated spectrum is generally in $\lambda(\mu\mathrm{m})$ *vs.* $F_\nu(\mathrm{Jy})$ units, but the units can be changed if needed.

14. We performed further spectral analysis outside of SMART with commonly available IDL programs to measure equivalent widths and fluxes of lines. The continuum was fit using a spline fitting technique. Since the mid-IR spectra are very feature rich, defining the continuum is a bit of a subjective process.

The above steps required to produce a publication quality spectrum are by no means a complete description, but it provides the most important tips that will be useful when reducing the spectrum using SMART. Readers are advised to read the SMART User Manual and the Data Reduction Cookbooks on the *Spitzer* Science Center's website[1].

The key to extracting good quality high S/N spectra is to clean the images of hot pixels with IRSCLEAN and to perform the sky subtraction at the image level properly. In exceptional cases, when the source is not really a point source, it may be necessary to use manual extraction within SMART instead of the automated routine provided.

[1] `http://ssc.spitzer.caltech.edu/postbcd/irs_reduction.html`

Appendix D

Archival Spitzer Spectra

Here we display the 58 *Spitzer* spectra from the archival sample (Weedman et al. 2005; Buchanan et al. 2006) that we have used in our research. The archival BCD files were retrieved and the spectra extracted using procedures described in Appendix C. The properties of these galaxies are listed in Table 6.2.

We have separated the spectra according to their optical Seyfert types as noted in Table 6.2. Figures D.1 to D.3 show the Seyfert 1 spectra. Figures D.4 to D.9 show the Seyfert 2 spectra. And, Figure D.10 shows the spectra of an additional three Seyfert 1.8/1.9s from the archival sample. As can be seen the Seyfert 2 spectra show the largest variety in continuum shapes, while Seyfert 1 spectra tend to show more continuum emission at short wavelengths. The 17 μm "hump" expected to arise due to warm ($T \sim 170$ K) dust is also prominent in many spectra.

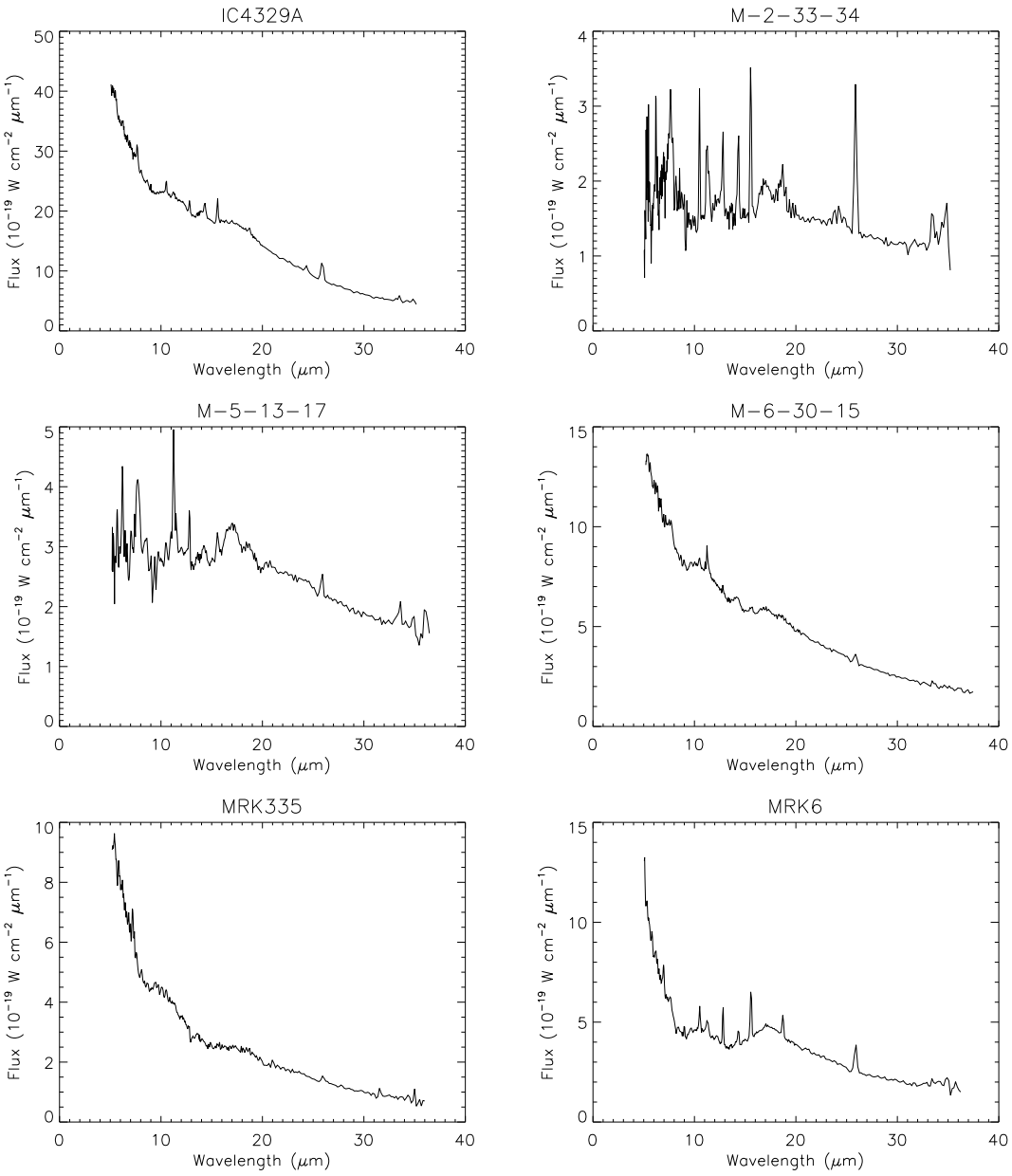

Figure D.1: *Spitzer* spectra of Seyfert 1s, 1.2s and 1.5s from Table 6.2.

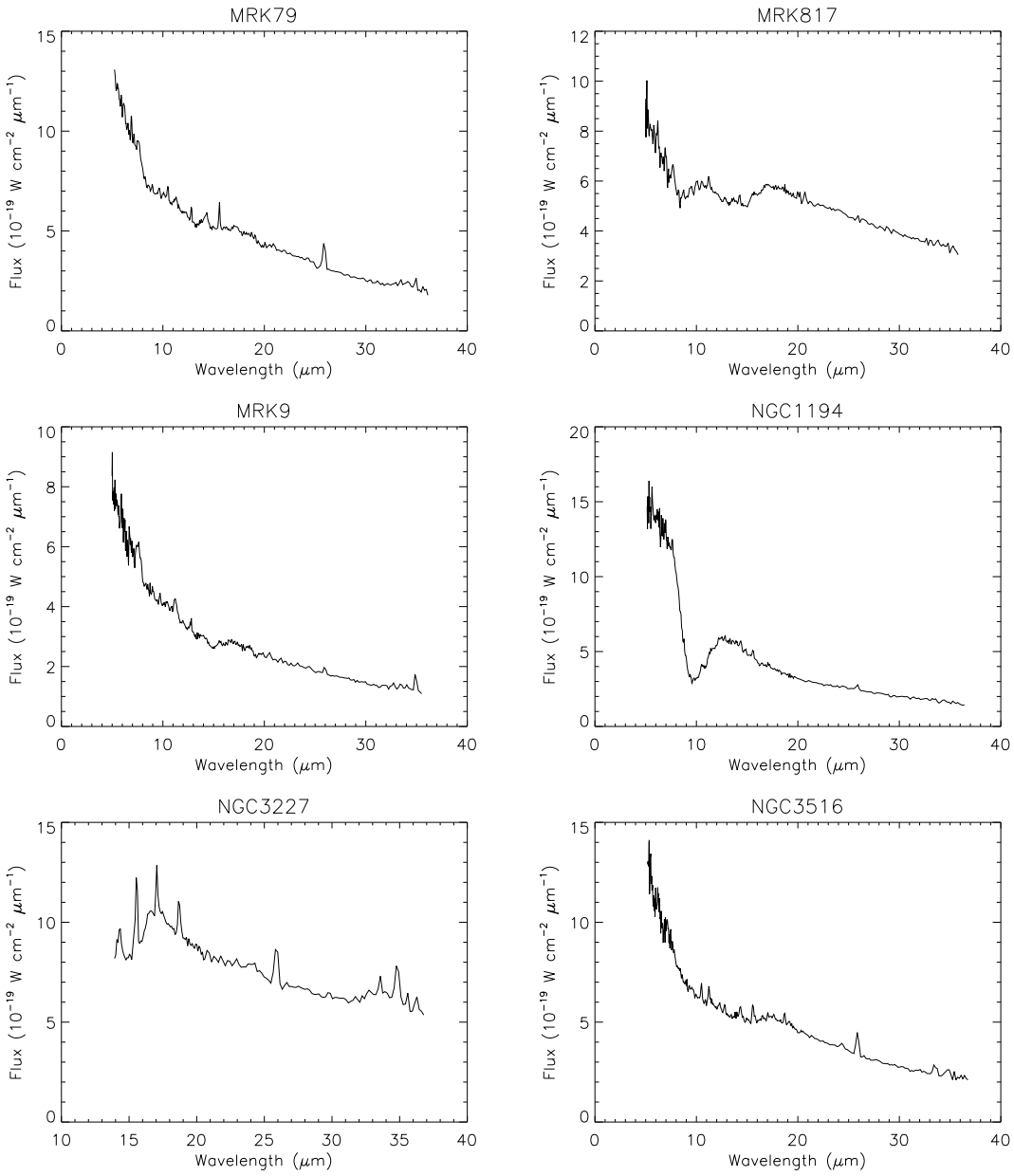

Figure D.2: *Spitzer* spectra of Seyfert 1s: continued

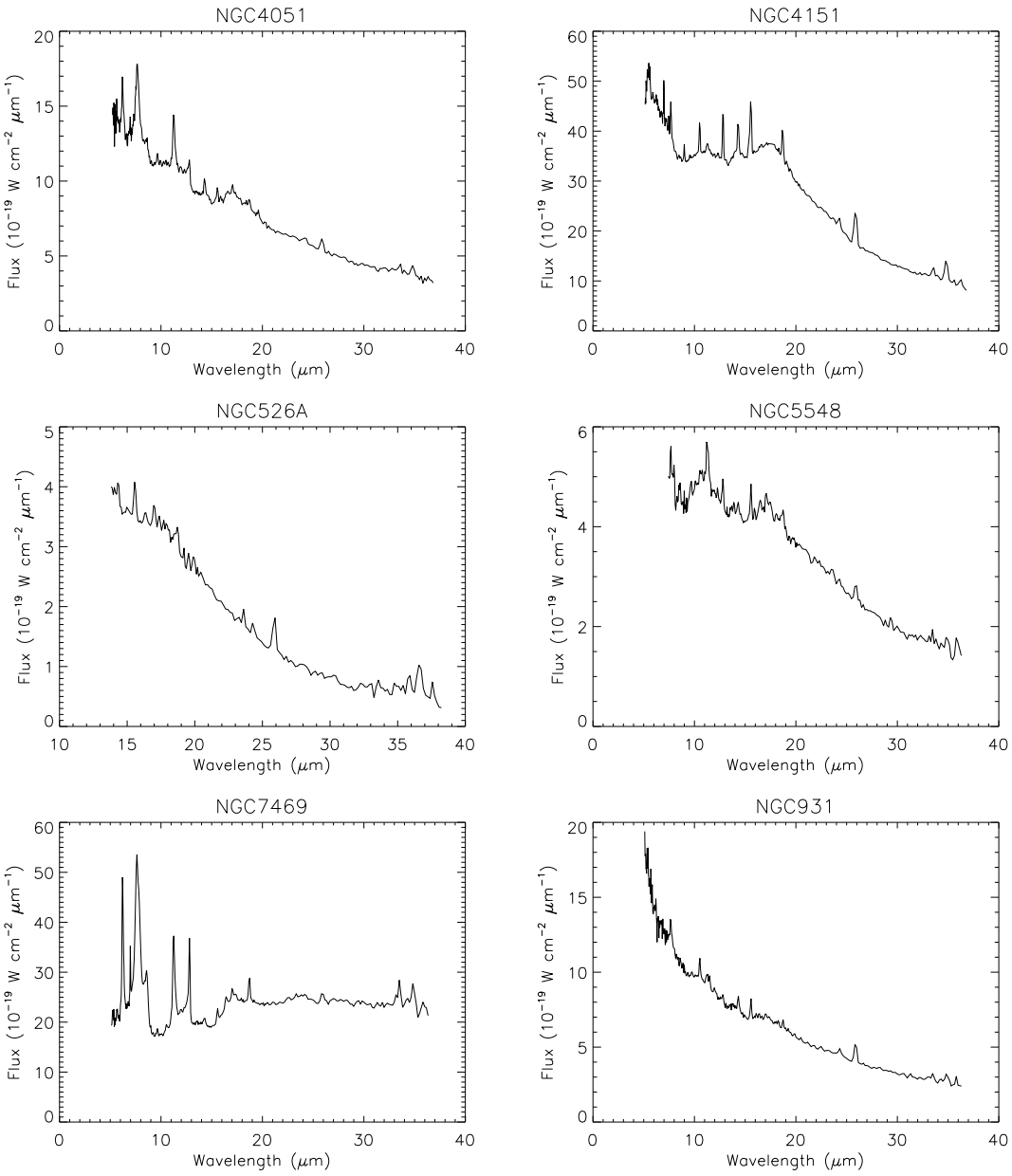

Figure D.3: *Spitzer* spectra of Seyfert 1s: continued

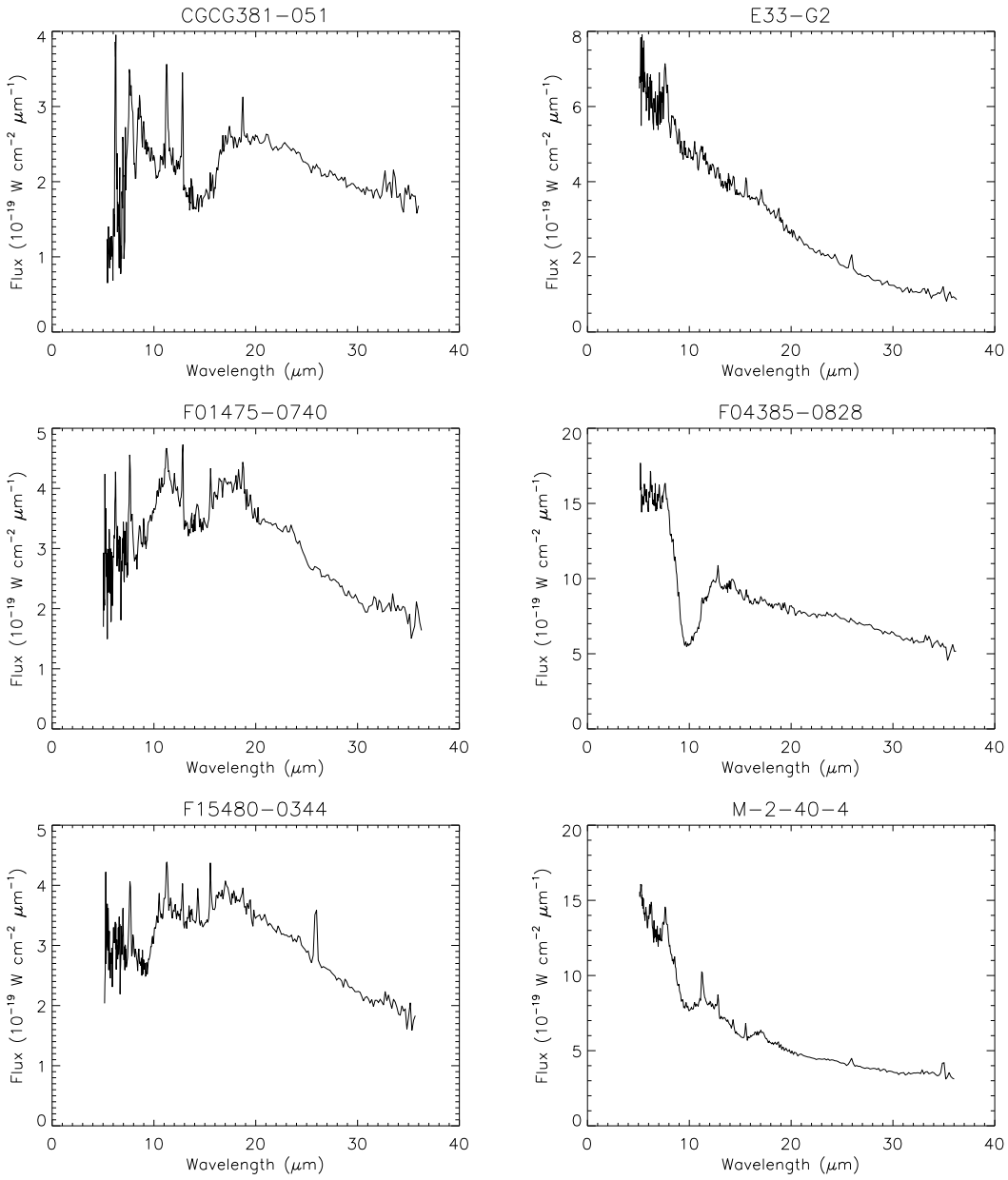

Figure D.4: *Spitzer* spectra of Seyfert 2 galaxies.

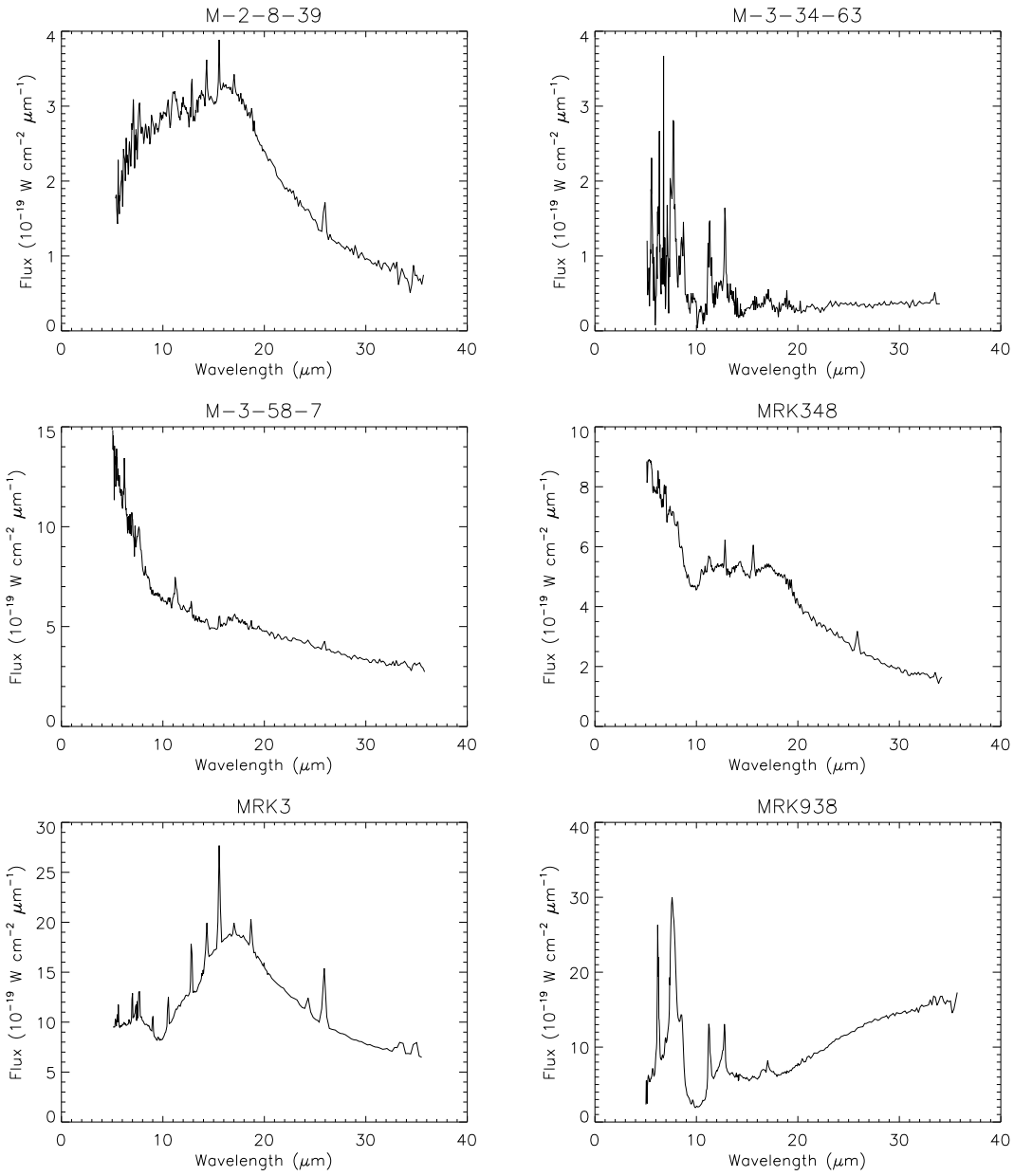

Figure D.5: *Spitzer* spectra of Seyfert 2 galaxies: continued

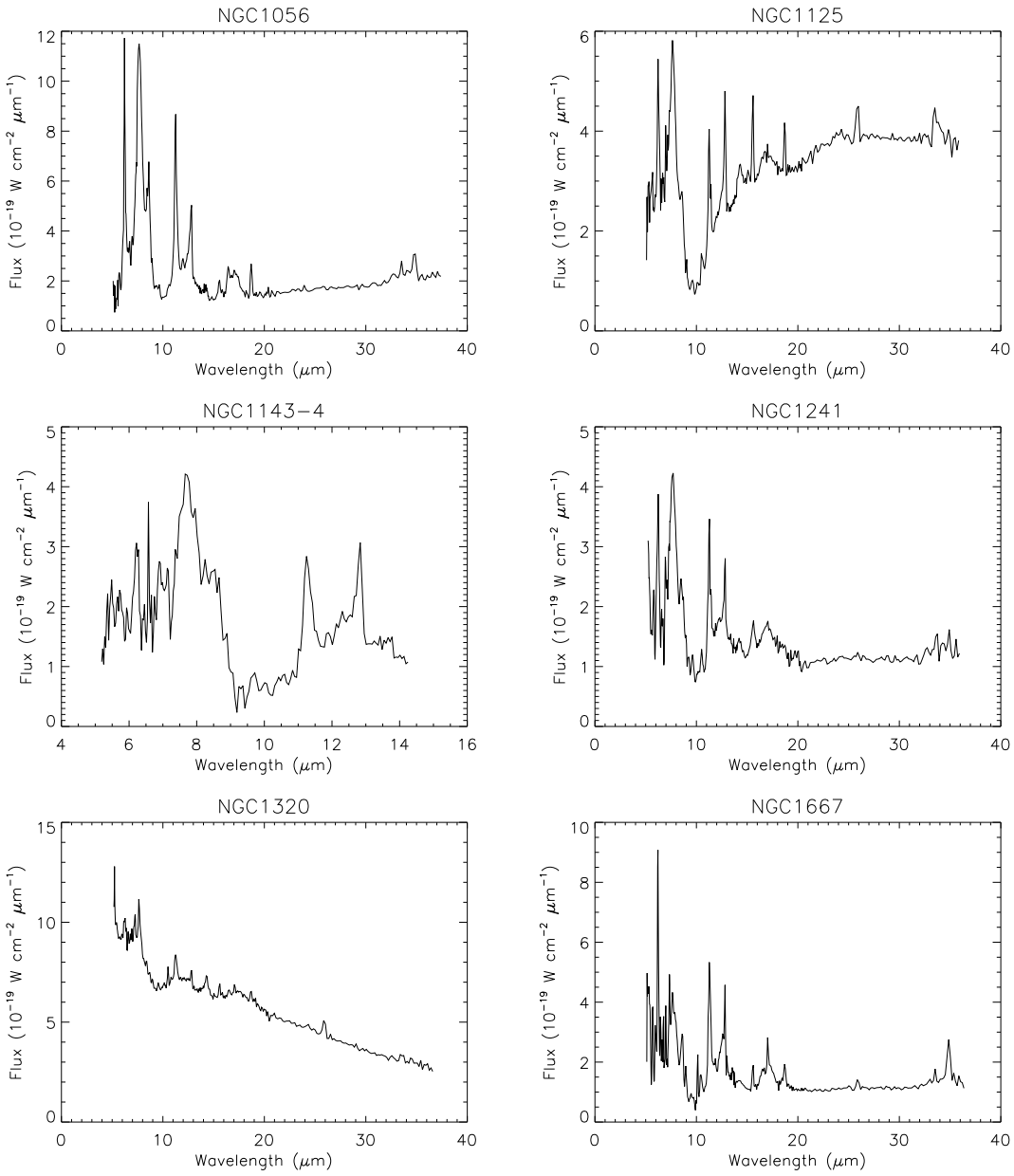

Figure D.6: *Spitzer* spectra of Seyfert 2 galaxies: continued

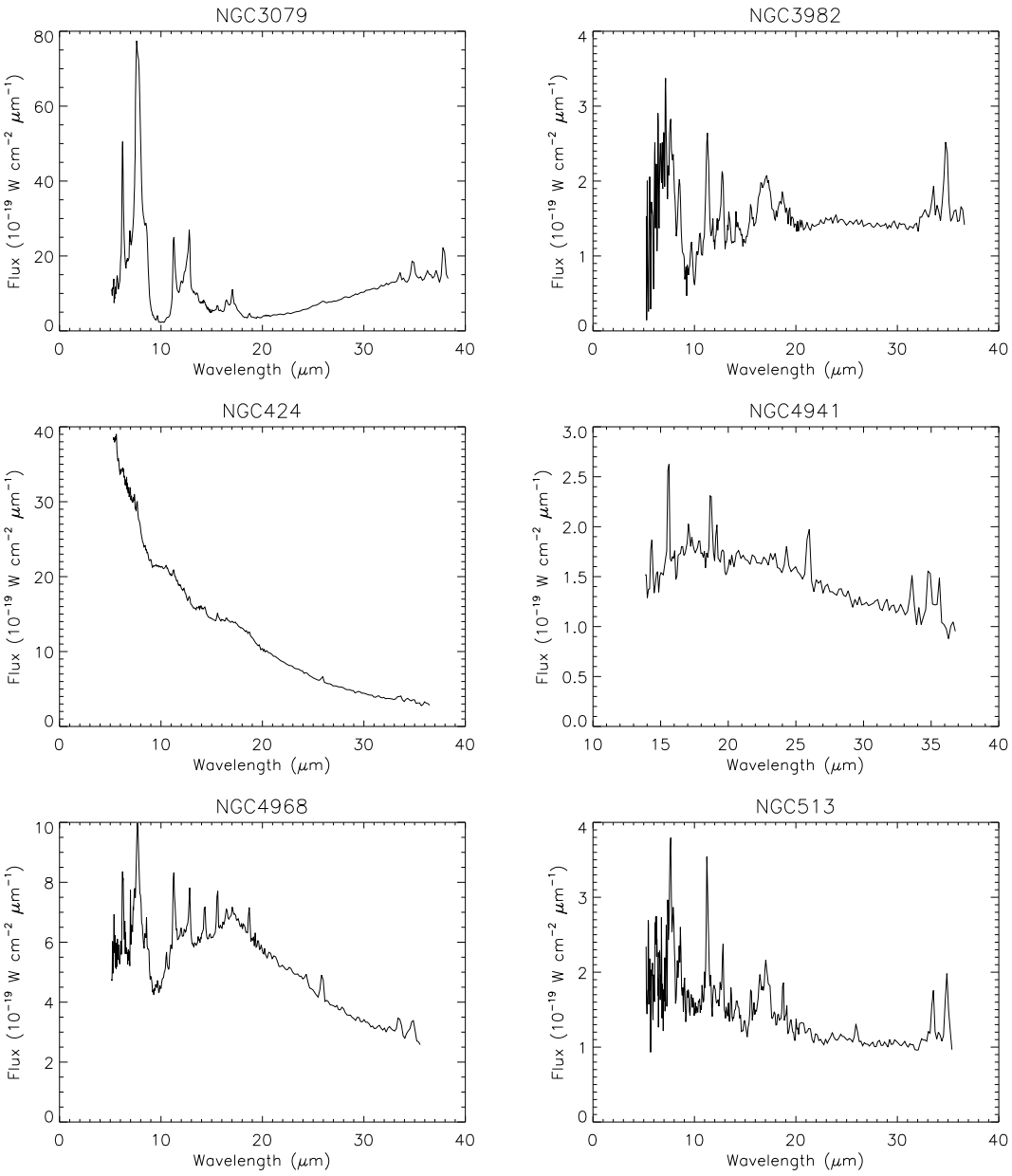

Figure D.7: *Spitzer* spectra of Seyfert 2 galaxies: continued

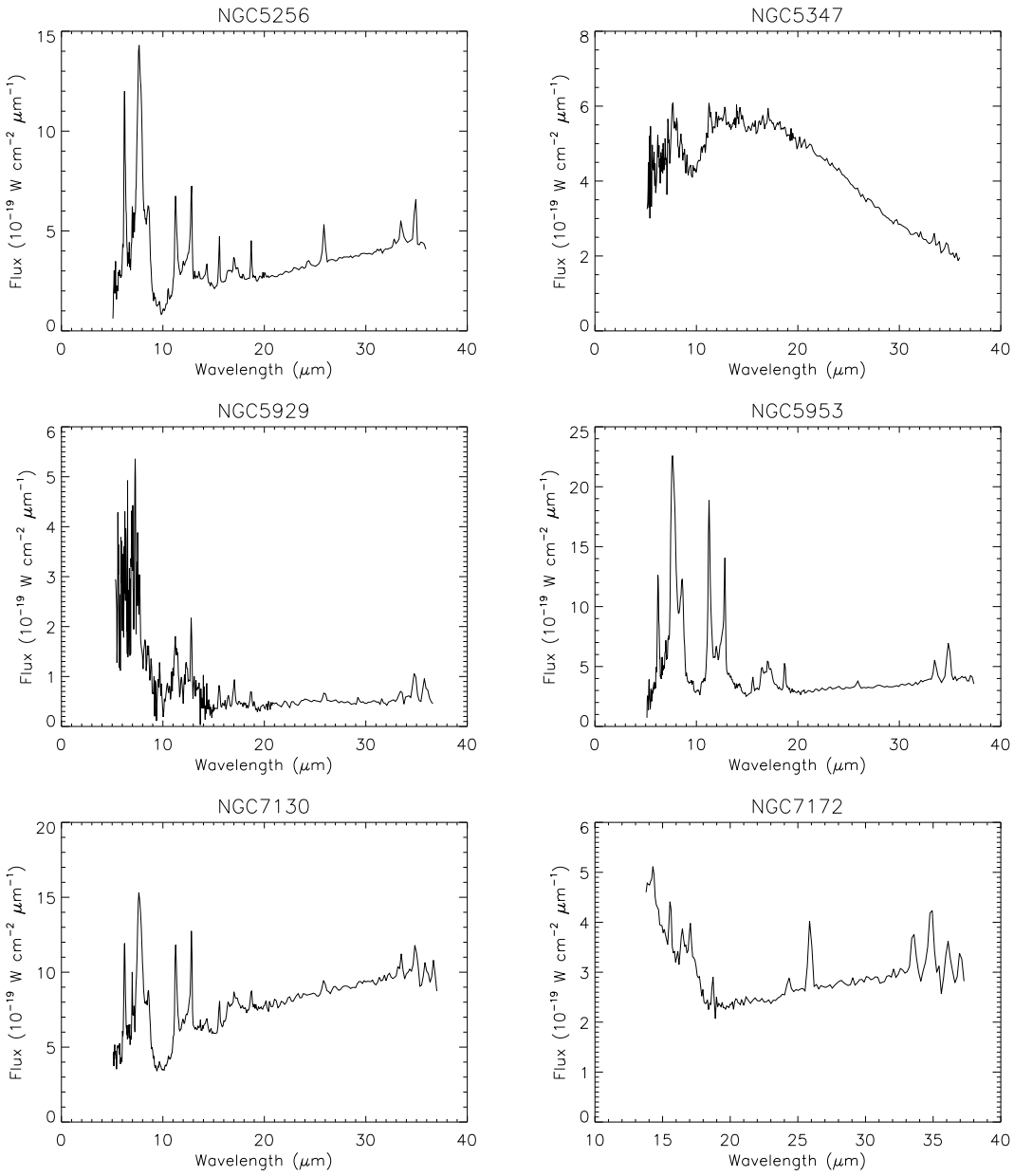

Figure D.8: *Spitzer* spectra of Seyfert 2 galaxies: continued

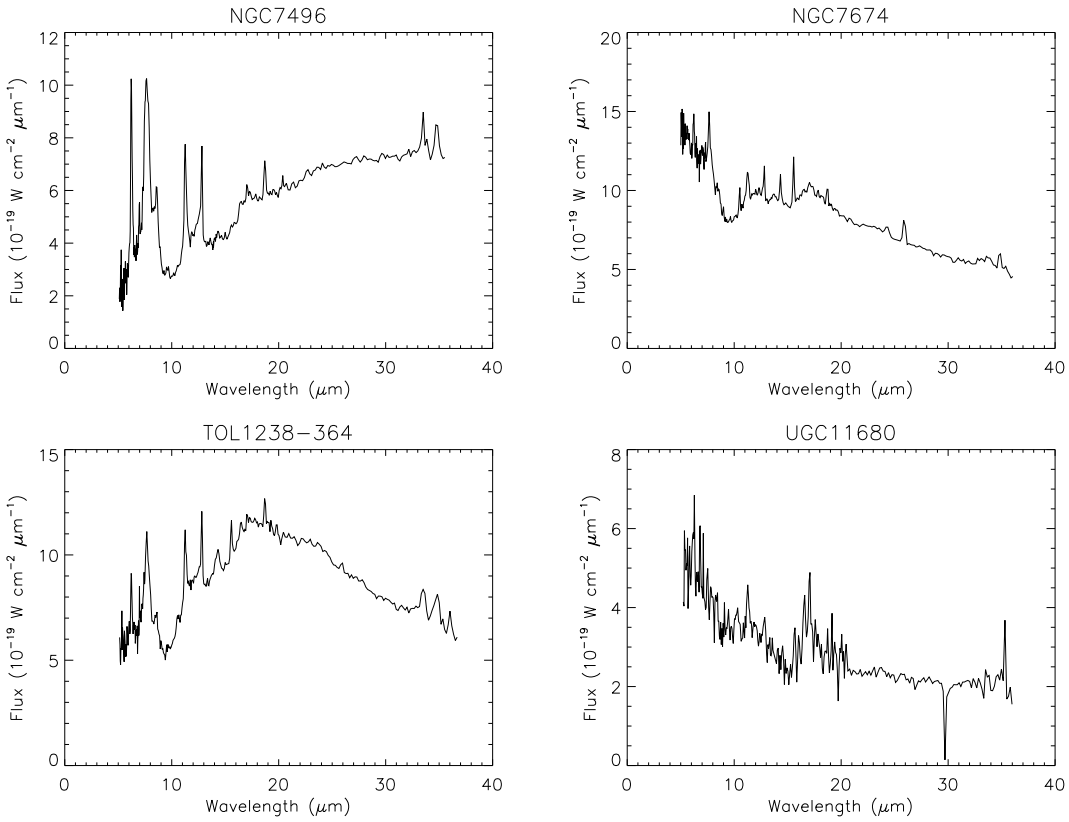

Figure D.9: *Spitzer* spectra of Seyfert 2 galaxies: continued

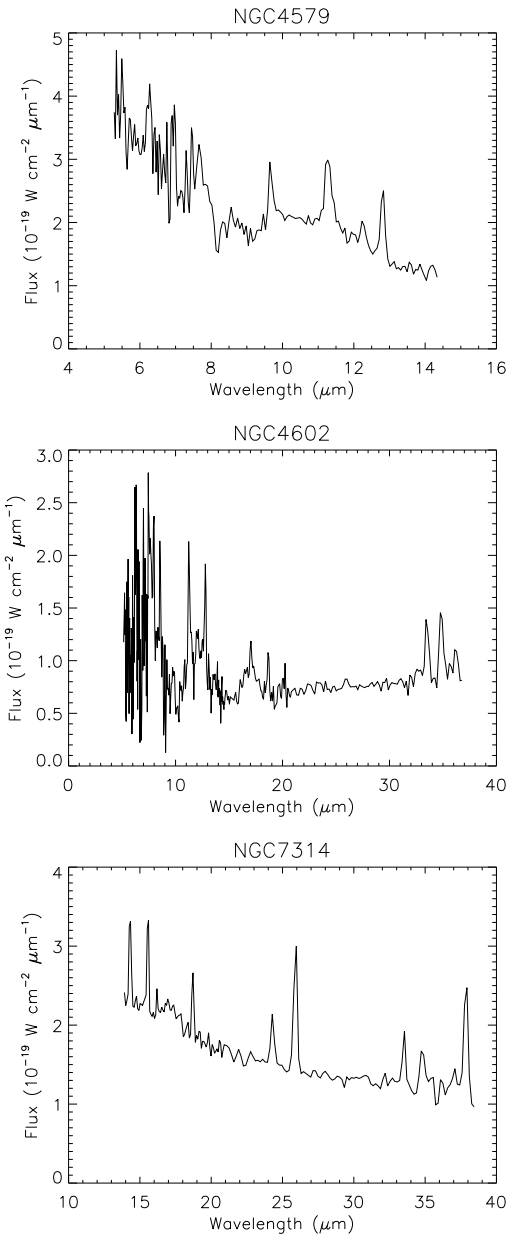

Figure D.10: *Spitzer* spectra of 3 Seyfert 1.9s galaxies from Table 6.2.

References

Adams, T. F. 1977, ApJS, 33, 19

Alexander, D. M., Efstathiou, A., Hough, J. H., Aitken, D. K., Lutz, D., Roche, P. F., & Sturm, E. 1999a, MNRAS, 310, 78

Alexander, T., Lutz, D., Sturm, E., Genzel, R., Sternberg, A., & Netzer, H. 2000, ApJ, 536, 710

Alexander, T., Sturm, E., Lutz, D., Sternberg, A., Netzer, H., & Genzel, R. 1999b, ApJ, 512, 204

Allamandola, L. J., Sandford, S. A., Hudgins, D. M., & Witteborn, F. C. 1995, in Astronomical Society of the Pacific Conference Series, Vol. 73, From Gas to Stars to Dust, ed. M. R. Haas, J. A. Davidson, & E. F. Erickson, 23

Allen, D. A. 1976, ApJ, 207, 367

Alonso-Herrero, A., Quillen, A. C., Simpson, C., Efstathiou, A., & Ward, M. J. 2001, AJ, 121, 1369

Angel, J. R. P., Stockman, H. S., Woolf, N. J., Beaver, E. A., & Martin, P. G. 1976, ApJ, 206, L5

Antonucci, R. 1993, ARA&A, 31, 473

Antonucci, R. R. J., & Miller, J. S. 1985, ApJ, 297, 621

Athanassoula, E. 1992, MNRAS, 259, 345

Baldwin, J. A., Phillips, M. M., & Terlevich, R. 1981, PASP, 93, 5

Barvainis, R. 1987, ApJ, 320, 537

Beichman, C. A. 1988, Astrophysical Letters Communications, 27, 67

Binney, J., & Merrifield, M. 1998, Galactic astronomy (Princeton, NJ : Princeton University Press, 1998.)

Blandford, R. D., & Rees, M. J. 1978, Phys. Scr, 17, 265

Bohlin, R. C., Savage, B. D., & Drake, J. F. 1978, ApJ, 224, 132

Boller, T., Brandt, W. N., & Fink, H. 1996, A&A, 305, 53

Boroson, T. A., & Green, R. F. 1992, ApJS, 80, 109

Boselli, A. et al. 1997, A&A, 324, L13

Boulanger, F. et al. 1998a, in Astronomical Society of the Pacific Conference Series, Vol. 132, Star Formation with the Infrared Space Observatory, ed. J. Yun & L. Liseau, 15

Boulanger, F., Boisssel, P., Cesarsky, D., & Ryter, C. 1998b, A&A, 339, 194

Brandl, B. R. et al. 2006, ApJ, 653, 1129

Bridle, A. H., & Perley, R. A. 1984, ARA&A, 22, 319

Buchanan, C. L., Gallimore, J. F., O'Dea, C. P., Baum, S. A., Axon, D. J., Robinson, A., Elitzur, M., & Elvis, M. 2006, AJ, 132, 401

Buta, R., & Combes, F. 1996, Fundamentals of Cosmic Physics, 17, 95

Buta, R., Corwin, Jr., H. G., & Odewahn, S. C. 2002, in Astronomical Society of the Pacific Conference Series, Vol. 275, Disks of Galaxies: Kinematics, Dynamics and Peturbations, ed. E. Athanassoula, A. Bosma, & R. Mujica, 102

Calzetti, D., Armus, L., Bohlin, R. C., Kinney, A. L., Koornneef, J., & Storchi-Bergmann, T. 2000, ApJ, 533, 682

Carleton, N. P., Elvis, M., Fabbiano, G., Willner, S. P., Lawrence, A., & Ward, M. 1987, ApJ, 318, 595

Cesarsky, D., Lequeux, J., Abergel, A., Perault, M., Palazzi, E., Madden, S., & Tran, D. 1996a, A&A, 315, L309

——. 1996b, A&A, 315, L305

Clarke, C. J., Kinney, A. L., & Pringle, J. E. 1998, ApJ, 495, 189

Clavel, J. et al. 2000, A&A, 357, 839

Clavel, J., Wamsteker, W., & Glass, I. S. 1989, ApJ, 337, 236

Code, A. D. et al. 1993, ApJ, 403, L63

Cohen, R. D., Antonucci, R. R. J., Kishimoto, M., Hurt, T. W., Kay, L. E., Krolik, J. H., & Allen, R. G. 2000, in Bulletin of the American Astronomical Society, Vol. 32, , 1456

Collins, N. R., Kraemer, S. B., Crenshaw, D. M., Ruiz, J., Deo, R., & Bruhweiler, F. C. 2005, ApJ, 619, 116

Crenshaw, D. M., & Kraemer, S. B. 2000, ApJ, 532, L101

——. 2001, ApJ, 562, L29

Crenshaw, D. M., Kraemer, S. B., & Gabel, J. R. 2003a, AJ, 126, 1690

Crenshaw, D. M., Kraemer, S. B., & George, I. M. 2003b, ARA&A, 41, 117

Crenshaw, D. M. et al. 2000, AJ, 120, 1731

Dale, D. A., Helou, G., Contursi, A., Silbermann, N. A., & Kolhatkar, S. 2001, ApJ, 549, 215

Das, V. et al. 2005, AJ, 130, 945

Das, V., Crenshaw, D. M., Kraemer, S. B., & Deo, R. P. 2006, AJ, 132, 620

Davidson, K., & Netzer, H. 1979, Reviews of Modern Physics, 51, 715

de Grijp, M. H. K., Miley, G. K., Lub, J., & de Jong, T. 1985, Nature, 314, 240

De Robertis, M. M., & Shaw, R. A. 1990, ApJ, 348, 421

De Robertis, M. M., Yee, H. K. C., & Hayhoe, K. 1998, ApJ, 496, 93

de Vaucouleurs, G., de Vaucouleurs, A., Corwin, Jr., H. G., Buta, R. J., Paturel, G., & Fouque, P. 1991, Third Reference Catalogue of Bright Galaxies (Volume 1-3, XII, 2069 pp. 7 figs.. Berlin: Springer-Verlag)

de Zotti, G., & Gaskell, C. M. 1985, A&A, 147, 1

Deo, R. P., & Crenshaw, D. M. 2003, in Bulletin of the American Astronomical Society, Vol. 35, , 759

Deo, R. P., Crenshaw, D. M., & Kraemer, S. B. 2006, AJ, 132, 321

Dietrich, M., Crenshaw, D. M., & Kraemer, S. B. 2005, ApJ, 623, 700

Draine, B. T., & Lee, H. M. 1984, ApJ, 285, 89

Draine, B. T., & Li, A. 2001, ApJ, 551, 807

——. 2007, ApJ, 657, 810
Edelson, R. A., & Malkan, M. A. 1987, ApJ, 323, 516
Edelson, R. A., Malkan, M. A., & Rieke, G. H. 1987, ApJ, 321, 233
Elitzur, M., & Shlosman, I. 2006, ApJ, 648, L101
Englmaier, P., & Shlosman, I. 2000, ApJ, 528, 677
Erwin, P., & Sparke, L. S. 2002, AJ, 124, 65
——. 2003, ApJS, 146, 299
Evans, I. N., Tsvetanov, Z., Kriss, G. A., Ford, H. C., Caganoff, S., & Koratkar, A. P. 1993, ApJ, 417, 82
Fanaroff, B. L., & Riley, J. M. 1974, MNRAS, 167, 31P
Fathi, K., Storchi-Bergmann, T., Riffel, R. A., Winge, C., Axon, D. J., Robinson, A., Capetti, A., & Marconi, A. 2006, ApJ, 641, L25
Förster Schreiber, N. M., Sauvage, M., Charmandaris, V., Laurent, O., Gallais, P., Mirabel, I. F., & Vigroux, L. 2003, A&A, 399, 833
Genzel, R. et al. 1998, ApJ, 498, 579
Gillett, F. C., Kleinmann, D. E., Wright, E. L., & Capps, R. W. 1975, ApJ, 198, L65
Goldreich, P., & Tremaine, S. 1978, ApJ, 222, 850
——. 1979, ApJ, 233, 857
Goodrich, R. W. 1989a, ApJ, 340, 190
——. 1989b, ApJ, 342, 224
——. 1990, ApJ, 355, 88
——. 1995, ApJ, 440, 141
Goodrich, R. W., & Osterbrock, D. E. 1983, ApJ, 269, 416
Grupe, D., Beuermann, K., Reinsch, K., Thomas, H.-C., & Fink, H. H. 1994, in IAU Symposium, Vol. 159, Multi-Wavelength Continuum Emission of AGN, ed. T. Courvoisier & A. Blecha, 508
Haas, M., Chini, R., Meisenheimer, K., Stickel, M., Lemke, D., Klaas, U., & Kreysa, E. 1998, ApJ, 503, L109+
Halpern, J. P., & Oke, J. B. 1987, ApJ, 312, 91

Hao, L., Weedman, D. W., Spoon, H. W. W., Marshall, J. A., Levenson, N. A., Elitzur, M., & Houck, J. R. 2007, ApJ, 655, L77

Heckman, T. M. 1980a, A&A, 87, 142

——. 1980b, A&A, 88, 365

Helou, G., Lu, N. Y., Werner, M. W., Malhotra, S., & Silbermann, N. 2000, ApJ, 532, L21

Higdon, S. J. U. et al. 2004, PASP, 116, 975

Ho, L. C. 1996, in Astronomical Society of the Pacific Conference Series, Vol. 103, The Physics of Liners in View of Recent Observations, ed. M. Eracleous, A. Koratkar, C. Leitherer, & L. Ho, 103

Ho, L. C., Filippenko, A. V., & Sargent, W. L. W. 1994, in IAU Symposium, Vol. 159, Multi-Wavelength Continuum Emission of AGN, ed. T. Courvoisier & A. Blecha, 275–278

Ho, L. C., Filippenko, A. V., & Sargent, W. L. W. 1997, ApJ, 487, 591

Houck, J. R. et al. 2004, ApJS, 154, 18

——. 1984, ApJ, 278, L63

Hunt, L. K., & Malkan, M. A. 1999, ApJ, 516, 660

——. 2004, ApJ, 616, 707

Jogee, S., Shlosman, I., Laine, S., Englmaier, P., Knapen, J. H., Scoville, N., & Wilson, C. D. 2002, ApJ, 575, 156

Keel, W. C. 1980, AJ, 85, 198

Kellermann, K. I. 1972, in IAU Symposium, Vol. 44, External Galaxies and Quasi-Stellar Objects, ed. D. S. Evans, D. Wills, & B. J. Wills, 190

Kembhavi, A. K., & Narlikar, J. V. 1999, Quasars and active galactic nuclei : an introduction (Cambridge, U.K. : Cambridge University Press, c1999.)

Kessler, M. F. et al. 1996, A&A, 315, L27

Khachikian, E. Y., & Weedman, D. W. 1974, ApJ, 192, 581

Kinney, A. L., Schmitt, H. R., Clarke, C. J., Pringle, J. E., Ulvestad, J. S., & Antonucci, R. R. J. 2000, ApJ, 537, 152

Kishimoto, M., Kay, L. E., Antonucci, R., Hurt, T. W., Cohen, R. D., & Krolik, J. H. 2002, ApJ, 565, 155

Kollatschny, W., Bischoff, K., & Dietrich, M. 2000, A&A, 361, 901

Konigl, A., & Kartje, J. F. 1994, ApJ, 434, 446

Kormendy, J., & Richstone, D. 1995, ARA&A, 33, 581

Krist, J. E., & Hook, R. N. 1999, The Tiny Tim User's Guide (Baltimore: Space Telescope Science Institute)

Krongold, Y., Dultzin-Hacyan, D., & Marziani, P. 2001, AJ, 121, 702

Kuraszkiewicz, J. K. et al. 2003, ApJ, 590, 128

Laine, S., Shlosman, I., Knapen, J. H., & Peletier, R. F. 2002, ApJ, 567, 97

Laurent, O., Mirabel, I. F., Charmandaris, V., Gallais, P., Madden, S. C., Sauvage, M., Vigroux, L., & Cesarsky, C. 2000, A&A, 359, 887

Lawrence, A., & Elvis, M. 1982, ApJ, 256, 410

Le Floc'h, E., Mirabel, I. F., Laurent, O., Charmandaris, V., Gallais, P., Sauvage, M., Vigroux, L., & Cesarsky, C. 2001, A&A, 367, 487

Leger, A., & Puget, J. L. 1984, A&A, 137, L5

Levenson, N. A., Sirocky, M. M., Hao, L., Spoon, H. W. W., Marshall, J. A., Elitzur, M., & Houck, J. R. 2007, ApJ, 654, L45

Li, A., & Draine, B. T. 2001, ApJ, 554, 778

Lutz, D., Genzel, R., Kunze, D., Spoon, H. W. W., Sturm, E., Sternberg, A., & Moorwood, A. F. M. 1998, in Astronomical Society of the Pacific Conference Series, Vol. 132, Star Formation with the Infrared Space Observatory, ed. J. Yun & L. Liseau, 89

Lutz, D., Maiolino, R., Spoon, H. W. W., & Moorwood, A. F. M. 2004, A&A, 418, 465

Lutz, D., Sturm, E., Genzel, R., Moorwood, A. F. M., & Sternberg, A. 1997, Ap&SS, 248, 217

Maciejewski, W. 2004a, MNRAS, 354, 883

——. 2004b, MNRAS, 354, 892

Maciejewski, W., Teuben, P. J., Sparke, L. S., & Stone, J. M. 2002, MNRAS, 329, 502

Maiolino, R., Alonso-Herrero, A., Anders, S., Quillen, A., Rieke, M. J., Rieke, G. H., & Tacconi-Garman, L. E. 2000, ApJ, 531, 219

Maiolino, R., & Rieke, G. H. 1995, ApJ, 454, 95

Malkan, M. A., Gorjian, V., & Tam, R. 1998, ApJS, 117, 25

Martini, P., & Pogge, R. W. 1999, AJ, 118, 2646

Martini, P., Regan, M. W., Mulchaey, J. S., & Pogge, R. W. 2003a, ApJS, 146, 353

——. 2003b, ApJ, 589, 774

Mason, K. O., Puchnarewicz, E. M., & Jones, L. R. 1996, MNRAS, 283, L26

Mathis, J. S. 1990, ARA&A, 28, 37

Mathur, S. 2000, MNRAS, 314, L17

Mathur, S., Kuraszkiewicz, J., & Czerny, B. 2001, New Astronomy, 6, 321

Miller, J. S., & Antonucci, R. R. J. 1983, ApJ, 271, L7

Miller, J. S., & Goodrich, R. W. 1990, ApJ, 355, 456

Moorwood, A. F. M., Lutz, D., Oliva, E., Marconi, A., Netzer, H., Genzel, R., Sturm, E., & de Graauw, T. 1996, A&A, 315, L109

Mulchaey, J. S., & Regan, M. W. 1997, ApJ, 482, L135+

Mulchaey, J. S., Regan, M. W., & Kundu, A. 1997, ApJS, 110, 299

Murayama, T., Taniguchi, Y., & Nagao, T. 2001, in Astronomical Society of the Pacific Conference Series, Vol. 222, The Physics of Galaxy Formation, ed. M. Umemura & H. Susa, 375

Nagar, N. M., & Wilson, A. S. 1999, ApJ, 516, 97

Nenkova, M., Ivezić, Ž., & Elitzur, M. 2002, ApJ, 570, L9

Neugebauer, G., Becklin, E. E., Oke, J. B., & Searle, L. 1976, ApJ, 205, 29

Oke, J. B., & Sargent, W. L. W. 1968, ApJ, 151, 807

Osterbrock, D. E. 1978, Proceedings of the National Academy of Science, 75, 540

——. 1981, ApJ, 249, 462

Osterbrock, D. E., & Dahari, O. 1983, ApJ, 273, 478

Osterbrock, D. E., & Pogge, R. W. 1985, ApJ, 297, 166

Pacholczyk, A. G., & Wisniewski, W. Z. 1967, ApJ, 147, 394

Padovani, P., & Urry, C. M. 1992, ApJ, 387, 449

Patsis, P. A., & Athanassoula, E. 2000, A&A, 358, 45

Peeters, E., van Diedenhoven, B., van Kerckhoven, C., Hony, S., Tielens, A. G. G. M., Allamandola, L. J., Hudgins, D. M., & Bauschlicher, C. W. 2003, in Astrophysics of Dust, ed. A. N. Witt, Colorado: Astrophysics of Dust Conference, Estes Park, 41

Perez Garcia, A. M., Rodriguez Espinosa, J. M., & Santolaya Rey, A. E. 1998, ApJ, 500, 685

Peterson, B. M. 1993, PASP, 105, 247

——. 1997, An Introduction to Active Galactic Nuclei (Cambridge: Cambridge University Press)

Peterson, B. M. et al. 2004, ApJ, 613, 682

Pier, E. A., & Krolik, J. H. 1992, ApJ, 401, 99

——. 1993, ApJ, 418, 673

Pogge, R. W. 2000, New Astronomy Review, 44, 381

Pogge, R. W., & Martini, P. 2002, ApJ, 569, 624

Pounds, K. A., Done, C., & Osborne, J. P. 1995, MNRAS, 277, L5

Prendergast, K. H. 1983, in IAU Symposium, Vol. 100, Internal Kinematics and Dynamics of Galaxies, ed. E. Athanassoula, 215

Puget, J. L., & Leger, A. 1989, ARA&A, 27, 161

Quillen, A. C., Shaked, S., Alonso-Herrero, A., McDonald, C., Lee, A., Rieke, M. J., & Rieke, G. H. 2000, ApJ, 532, L17

Rees, M. J., Silk, J., Warner, M. W., & Wickramasinghe, N. C. 1969, Nature, 223, 788

Regan, M. W., & Mulchaey, J. S. 1999, AJ, 117, 2676

Rice, M. S., Martini, P., Greene, J. E., Pogge, R. W., Shields, J. C., Mulchaey, J. S., & Regan, M. W. 2006, ApJ, 636, 654

Rieke, G. H., & Lebofsky, M. J. 1979, ARA&A, 17, 477

Rieke, G. H., & Low, F. J. 1972, ApJ, 176, L95+

——. 1975, ApJ, 197, 17

Rigopoulou, D., Kunze, D., Lutz, D., Genzel, R., & Moorwood, A. F. M. 2002, A&A, 389, 374

Rudy, R. J. 1984, ApJ, 284, 33

Rudy, R. J., Cohen, R. D., & Ake, T. B. 1988, ApJ, 332, 172

Rudy, R. J., Cohen, R. D., & Puetter, R. C. 1985, ApJ, 288, L29

Rudy, R. J., & Rodriguez-Espinosa, J. M. 1985, ApJ, 298, 614

Rudy, R. J., & Willner, S. P. 1983, ApJ, 267, L69

Ruiz, J. R., Crenshaw, D. M., Kraemer, S. B., Bower, G. A., Gull, T. R., Hutchings, J. B., Kaiser, M. E., & Weistrop, D. 2005, AJ, 129, 73

Sanders, D. B., Phinney, E. S., Neugebauer, G., Soifer, B. T., & Matthews, K. 1989, ApJ, 347, 29

Savage, B. D., & Mathis, J. S. 1979, ARA&A, 17, 73

Schinnerer, E., Eckart, A., Tacconi, L. J., Genzel, R., & Downes, D. 2000, ApJ, 533, 850

Schmitt, H. R., Antonucci, R. R. J., Ulvestad, J. S., Kinney, A. L., Clarke, C. J., & Pringle, J. E. 2001, ApJ, 555, 663

Schmitt, H. R., Donley, J. L., Antonucci, R. R. J., Hutchings, J. B., Kinney, A. L., & Pringle, J. E. 2003, ApJ, 597, 768

Schmitt, H. R., & Kinney, A. L. 1996, ApJ, 463, 498

Schmitt, H. R., Kinney, A. L., Storchi-Bergmann, T., & Antonucci, R. 1997, ApJ, 477, 623

Sellgren, K. 1984, ApJ, 277, 623

Seyfert, C. K. 1943, ApJ, 97, 28

Shi, Y. et al. 2006, ApJ, 653, 127

Shlosman, I. 2002, in Astronomical Society of the Pacific Conference Series, Vol. 275, Disks of Galaxies: Kinematics, Dynamics and Peturbations, ed. E. Athanassoula, A. Bosma, & R. Mujica, 231

Shlosman, I., Begelman, M. C., & Frank, J. 1990, Nature, 345, 679

Shull, J. M., & van Steenberg, M. E. 1985, ApJ, 294, 599

Siebenmorgen, R., Freudling, W., Krügel, E., & Haas, M. 2004a, A&A, 421, 129

Siebenmorgen, R., Krügel, E., & Spoon, H. W. W. 2004b, A&A, 414, 123

Simkin, S. M., Su, H. J., & Schwarz, M. P. 1980, ApJ, 237, 404

Soifer, B. T., Neugebauer, G., & Houck, J. R. 1987, ARA&A, 25, 187

Spergel, D. N. et al. 2003, ApJS, 148, 175

Spoon, H. W. W., Keane, J. V., Tielens, A. G. G. M., Lutz, D., Moorwood, A. F. M., & Laurent, O. 2002, A&A, 385, 1022

Spoon, H. W. W., Marshall, J. A., Houck, J. R., Elitzur, M., Hao, L., Armus, L., Brandl, B. R., & Charmandaris, V. 2007, ApJ, 654, L49

Sturm, E., Hasinger, G., Lehmann, I., Mainieri, V., Genzel, R., Lehnert, M. D., Lutz, D., & Tacconi, L. J. 2006, ApJ, 642, 81

Sturm, E., Lutz, D., Tran, D., Feuchtgruber, H., Genzel, R., Kunze, D., Moorwood, A. F. M., & Thornley, M. D. 2000, A&A, 358, 481

Sturm, E., Lutz, D., Verma, A., Netzer, H., Sternberg, A., Moorwood, A. F. M., Oliva, E., & Genzel, R. 2002, A&A, 393, 821

Telesco, C. M., Harper, D. A., & Loewenstein, R. F. 1976, ApJ, 203, L53

Tohline, J. E., & Osterbrock, D. E. 1976, ApJ, 210, L117

Toomre, A., & Toomre, J. 1972, ApJ, 178, 623

Trewhella, M., Davies, J. I., Alton, P. B., Bianchi, S., & Madore, B. F. 2000, ApJ, 543, 153

Urry, C. M., Padovani, P., & Stickel, M. 1991, ApJ, 382, 501

Veilleux, S. 1989, PhD thesis, University of California, Santa Cruz

Veilleux, S., & Osterbrock, D. E. 1987, ApJS, 63, 295

Verma, A., Charmandaris, V., Klaas, U., Lutz, D., & Haas, M. 2005, Space Science Reviews, 119, 355

Véron-Cetty, M.-P., & Véron, P. 2001, A&A, 374, 92

Véron-Cetty, M.-P., Véron, P., & Gonçalves, A. C. 2001, A&A, 372, 730

Verstraete, L., Puget, J. L., Falgarone, E., Drapatz, S., Wright, C. M., & Timmermann, R. 1996, A&A, 315, L337

Wandel, A. 2002, ApJ, 565, 762

Weedman, D. W. et al. 2005, ApJ, 633, 706

Werner, M. W. et al. 2004, ApJS, 154, 1

Whittet, D. C. B. 1992, Dust in the Galactic Environment (Bristol: Institute of Physics (IOP) Publishing)